

***Supramolecular Systems Based On Trisamides  
With Linear Perfluorinated Side Chains***

DISSERTATION

zur Erlangung des akademischen Grades eines  
Doktors der Naturwissenschaften (Dr. rer. nat.)  
an der Fakultät für Biologie, Chemie und Geowissenschaften  
der Universität Bayreuth

vorgelegt von

***Steffen Czich***

*aus Heidenheim a. d. Brenz*

Bayreuth, 2020



Die vorliegende Arbeit wurde experimentell in der Zeit von September 2012 bis Oktober 2016 am Lehrstuhl für Makromolekulare Chemie I der Universität Bayreuth unter Betreuung von Herrn Professor Dr. Hans-Werner Schmidt angefertigt.

*Vollständiger Abdruck der von der Fakultät für Biologie, Chemie und Geowissenschaften der Universität Bayreuth genehmigten Dissertation zur Erlangung des akademischen Grades eines Doktors der Naturwissenschaften (Dr. rer. nat.).*

Dissertation eingereicht am: 02.06.2020

Zulassung durch die Prüfungskommission: 01.07.2020

Wissenschaftliches Kolloquium: 12.11.2020

Amtierender Dekan: Prof. Dr. Matthias Breuning

Prüfungsausschuss:

Prof. Dr. Hans-Werner Schmidt	(Gutachter)
Prof. Dr. Andreas Greiner	(Gutachter)
Prof. Dr. Georg Papastavrou	(Vorsitz)
Prof. Dr. Thomas Scheibel	



## Danksagung

An dieser Stelle möchte ich mich bei allen Personen bedanken, die mir zur Erstellung dieser Arbeit mit Rat und Tat zur Seite gestanden, sowie allen, die mir Vertrauen und Zuspruch in schwierigen Phasen gespendet haben.

Ein ganz herzlicher und besonderer Dank gilt meinem Doktorvater, Herr Prof. Dr. Hans-Werner Schmidt, für die Aufgabenstellung und die Bereitstellung eines perfekt ausgestatteten Arbeitsplatzes, sowie die Freiheit den zu erforschenden Themenbereich in verschiedene Richtungen ausdehnen zu können. Viele motivierende und anregende Diskussionen und Gespräche trugen dazu bei, dass ich mich mit dem neu gestellten Thema sehr gut identifizieren und viel Spaß bei der Arbeit entwickeln konnte. Den wichtigsten Dank jedoch will ich für die Hilfe, Unterstützung und Wertschätzung, ganz besonders auf menschlicher Ebene, innerhalb und auch in Folge sehr schwieriger Zeiten aussprechen, ohne die diese Arbeit für mich nicht möglich gewesen wäre.

Großer Dank gebührt auch Dr. Andreas Timme, der mir durch die Einführung in diverse Messtechniken und die offene und bereitwillige Weitergabe seines praktischen und theoretischen Wissens über Trisamide im Allgemeinen, sowie im Bereich der flüssigkristallinen Materialien den Einstieg in das Thema sehr vereinfacht hat.

Ich danke auch unseren Technikerinnen des Lehrstuhls Sandra Ganzleben, Jutta Failner und Doris Hanft für die Synthese und Bereitstellung der zu untersuchenden Substanzen. Bei Doris bedanke ich mich auch für viele unterhaltsame Gespräche und das gute Laborklima.

Vielen Dank an Dr. Klaus Kreger für sein fundiertes Wissen und viele Gespräche in jedem Themenbereich, in dem ich eine Inspiration oder Unterstützung benötigte. Mein Dank gilt auch Dr. Reiner Giesa, vor Allem für seine Hilfe im Bereich des Elektrosplinnens, und Dr. Christian Neuber für diverse organisatorische Angelegenheiten.

Großer Dank gebührt Petra Weiss und Christina Wunderlich für ihre unermüdliche administrative und organisatorische Arbeit am Lehrstuhl, aber auch ihre offene und optimistische Art sowie ein nettes Lächeln jeden Morgen. Vielen Dank auch an Alexander Kern, der in jeglicher Art von Software- und Hardwareproblemen jederzeit mit voller Unterstützung zur Seite stand.

Ich möchte mich sehr bei meinen Laborkolleginnen und Kollegen, Dr. Julia Singer, Christian Bartz, Andreas Schedl, Hannes Welz, Minde Jin und Astrid Rauh bedanken. Ohne sie wäre der Laboralltag um vielfaches eintöniger gewesen und mir deutlich schwerer gefallen. Vor allem an Tagen, an denen die Chemie wieder einmal nur das machte was sie wollte.

Danke an Martina Heider für die stundenlange Einweisung in die Messtechnik des REM, sowie Dr. Beate Förster und Werner Reichstein für ihre Unterstützung. Alle hatten immer passende und hilfreiche Tipps um meine REM Aufnahmen noch zu verbessern, aber auch ein offenes Ohr für jegliche andere Dinge des Alltags.

Ich danke auch meinen ehemaligen Hilfswissenschaftlern und Praktikanten Dominik Dörr, Eva Fürsattel, Sonja Dziwior, Matthias Burgard, Florian Dresel, und Laura Schwinger für ihren Fleiß und ihre Mitarbeit am Thema meiner Doktorarbeit im Rahmen von Mitarbeiterpraktika.

Des Weiteren möchte ich mich auch bei allen anderen Mitarbeiterinnen und Mitarbeitern des Lehrstuhls bedanken, mit denen ich in meiner Zeit am Lehrstuhl zu tun haben durfte. Danke für Geräteeinweisungen, sachliche und private Gespräche und Diskussionen, gemeinsame Grillabende und andere Aktivitäten, sowie die große Hilfsbereitschaft für jegliche Art von Problemen und deren Bewältigung.

Danke auch an das das Team der „University of Bayreuth Graduate School“ für die Finanzierung und die Hilfe zur reibungslosen Abwicklung für meine Konferenzteilnahme im Ausland.

Ein immens wichtiger Dank gebührt meiner Familie, die immer wie eine Wand hinter mir steht und die mich in jeder Situation auffängt, wenn es nötig ist, aber mir auch jederzeit die Freiheit lässt, die ich für mich selbst zur persönlichen Entfaltung und für volle Arbeitspower brauche. Danke, dass ihr sichtbar und unsichtbar hinter mir steht! Immer so, wie ich es gerade brauche.

Außerdem will ich meinen engsten Freunden danken, für die Begleitung durch eine teilweise sehr schwere Zeit. Danke, dass ihr immer zu mir haltet und mich unterstützt, egal wie weit die Distanz zwischen uns ist! Um es in einer Metapher dieser Doktorarbeit zu sagen: Ihr seid die Fluoratome an meiner Kernverbindung, ohne die das Gesamtmolekül nicht die atemberaubenden Eigenschaften innehaben würde, die ich finden konnte





*“If we knew what it was we were doing,*

*It would not be called research,*

*would it?”*

*Albert Einstein, (1879-1955), Physicist*



<b>1. Introduction</b> .....	<b>1</b>
1.1 FLUORINE CHEMISTRY .....	1
1.2 LIQUID CRYSTALS AND PLASTIC CRYSTALS .....	5
1.3 SUPRAMOLECULAR CHEMISTRY .....	11
<b>2. Objectives of the thesis</b> .....	<b>19</b>
<b>3. Thermal properties, mesophase behavior and structure property relations of two series of 1,3,5-benzenetrisamides with linear perfluorinated side chains</b> .....	<b>21</b>
3.1 MOLECULAR STRUCTURE OF THE TRISAMIDES .....	21
3.2 CHARACTERIZATION METHODS .....	22
3.3 PHASE BEHAVIOR OF 1,3,5-BENZENETRISAMIDES WITH LINEAR PERFLUORINATED SIDE CHAINS BASED ON 1,3,5-TRIAMINOBENZENE .....	31
3.3.1 BTA based on 1,3,5-triaminobenzene with heptafluoropropyl side chains (1a).....	31
3.3.2 BTA based on 1,3,5-triaminobenzene with nonafluorobutyl side chains (1b).....	35
3.3.3 BTA based on 1,3,5-triaminobenzene with undecafluoropentyl side chains (1c).....	38
3.3.4 BTA based on 1,3,5-triaminobenzene with tridecafluorohexyl side chains (1d).....	41
3.3.5 BTA based on 1,3,5-triaminobenzene with pentadecafluoroheptyl side chains (1e).....	44
3.3.6 BTA based on 1,3,5-triaminobenzene with heptadecafluorooctyl side chains (1f).....	49
3.3.7 Comparison within this series.....	52
3.4 PHASE BEHAVIOR OF 1,3,5-BENZENETRISAMIDES WITH LINEAR PERFLUORINATED SIDE CHAINS BASED ON TRIMESIC ACID .....	56
3.4.1 BTA based on trimesic acid with pentafluoropropyl side chains (2a) .....	56
3.4.2 BTA based on trimesic acid with heptafluorobutyl side chains (2b) .....	60
3.4.3 BTA based on trimesic acid with nonafluoropentyl side chains (2c).....	63
3.4.4 BTA based on trimesic acid with undecafluorohexyl side chains (2d).....	66
3.4.5 BTA based on trimesic acid with tridecafluoroheptyl side chains (2e).....	69
3.4.6 BTA based on trimesic acid with pentadecafluorooctyl side chains (2f) .....	73
3.4.7 Comparison within this series.....	77
3.5 PHASE BEHAVIOR OF A 1,3,5-CYCLOHEXANETRISAMIDE WITH LINEAR PERFLUORINATED SIDE CHAINS .....	81
3.6 SUMMARY .....	88

<b>4. Melt electrospinning of trisamides with linear perfluorinated side chains*</b> .....	<b>91</b>
4.1 EXPERIMENTAL PROCEDURE .....	95
4.2 CHARACTERIZATION METHODS .....	95
4.3 SELECTED TRISAMIDES .....	97
4.4 MELT ELECTROSPINNING EXPERIMENTS WITH THE AIM TO OBTAIN THIN FIBERS.....	97
4.4.1 <i>Electrospinning of the BTA with undecafluoropentyl side chains (1c)</i> .....	98
4.4.3 <i>Electrospinning of the CTA with tridecafluoroheptyl side chains (3a)</i> .....	110
4.5 MELT ELECTROSPINNING EXPERIMENTS WITH THE AIM TO OBTAIN THICK FIBERS .....	115
4.5.1 <i>Experimental procedure</i> .....	115
4.5.2 <i>Selected materials</i> .....	116
4.5.3 <i>Results of the melt electrospinning to thick fibers</i> .....	117
4.5.4 <i>Summary</i> .....	122
4.5.5 DETERMINATION OF THE SURFACE PROPERTIES BY WETTABILITY MEASUREMENTS.....	123
4.7 SUMMARY .....	125
<b>5. Self-assembly of 1,3,5-benzenetrisamides with perfluorinated side chains and co-self-assembly of structurally related 1,3,5-benzenetrisamides from solution</b> .....	<b>127</b>
5.1 SELF-ASSEMBLY OF BTAS WITH LINEAR PERFLUORINATED SIDE CHAINS .....	128
5.1.1 <i>Experimental procedures</i> .....	130
5.1.2 <i>Characterization methods</i> .....	131
5.1.3 <i>Selected solvents</i> .....	131
5.1.4 <i>Self-assembly of BTAs based on 1,3,5-triaminobenzene</i> .....	132
5.1.5 <i>Self-assembly of BTAs based on trimesic acid</i> .....	144
5.2 CO-SELF-ASSEMBLY OF TWO DIFFERENT 1,3,5-BENZENETRISAMIDES FROM SOLUTION .....	148
5.2.1 <i>Selected benzenetrisamides</i> .....	150
5.2.2 <i>Support materials</i> .....	150
5.2.3 <i>Selected solvents</i> .....	151
5.2.4 <i>Self-assembly procedure and parameters</i> .....	153
5.2.5 <i>Results of the self-assembly of individual compounds from a solvent or a solvent mixture</i> .....	154
5.2.6 <i>Results of the co-self-assembly from a solvent mixture</i> .....	159

Table of contents	III
5.3 SUMMARY .....	165
<b>6. Summary .....</b>	<b>167</b>
<b>7. Appendix .....</b>	<b>171</b>
7.1 APPENDIX I: ANALYTICAL EQUIPMENT AND PROCEDURES .....	171
7.2 APPENDIX II: ADDITIONAL DATA .....	174
7.2.1 <i>Additional data to chapter 3</i> .....	174
7.2.2 <i>Additional data to chapter 4</i> .....	184
7.2.3 <i>Additional data to chapter 5</i> .....	202
<b>8. References .....</b>	<b>205</b>



## 1. Introduction

The introduction to this thesis contains the necessary basics for supramolecular chemistry based on trisamides with linear perfluorinated side chains. It starts with an overview of fundamentals of fluorine chemistry in general, followed by a description of liquid and plastic, calamitic and discotic liquid crystals, with focus on particular fluorinated molecules. In addition, supramolecular chemistry with special emphasis on trisamides based on benzene and cyclohexane cores is addressed.

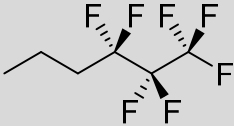
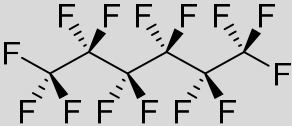
### 1.1 Fluorine chemistry

Molecules containing fluorine draw a lot of attention since it was investigated that they exhibit a unique set of unusual and sometimes extreme physical and chemical properties.<sup>1</sup> Fluoroorganic molecules received increasing attention in a lot of research and application fields including pharmaceutical chemistry, life science and material science.<sup>2-8</sup> Perfluorinated molecules and materials based on perfluorinated substructures exhibit extraordinary properties and find commercial use in a lot of applications such as fire-fighting chemicals, lubricants, polymers with anti-stick and low-friction properties, and fluorosurfactants just to mention a few.<sup>3</sup> Furthermore, in the pharmaceutical and agrochemical industry it is reported that a lot of the products possess fluorine atoms and the number of fluorine containing drugs in the market is expected to continue to grow.<sup>9,10</sup>

Two main properties of the fluorine atom cause the extraordinary differences between perfluorinated and non-fluorinated alkanes. Fluorine has the highest electronegativity among all chemical elements (3.98)<sup>11</sup>, a slightly increased size compared to a hydrogen atom, and an excellent match between the  $2s$  or  $2p$  orbitals with the corresponding orbitals of the carbon atom. The nearly optimum overlap of the orbitals is the main reason for the high stability of the C-F bond and increasing with the number of fluorine atoms bound to the same carbon atom.<sup>3,12</sup> The high electronegativity of the fluorine atom reduces the polarizability<sup>13</sup> and intermolecular interactions of completely perfluorinated molecules. For example, a comparison of n-hexane **1**, 1,1,1,2,2,3,3-heptafluorohexane **2** and perfluorohexane **3** with regard to the physicochemical properties, especially their heats of evaporation and their dielectric constants, are summarized in table 1. With increasing fluorine content and molecular weight  $M$ , the boiling temperature  $T_b$  and the surface tension  $\gamma^{25}$  are decreasing while the density  $d^{25}$ , viscosity  $\eta^{25}$  and compressibility  $\beta$  are increasing. In the case of the heat of vaporization  $\Delta H_v$  and the dielectric constant  $\epsilon$ , **2** exhibits the highest, while for the refractive index  $n_D^{25}$  it shows the lowest value of all three molecules.

The increased atom size of fluorine compared to hydrogen increases not only the entire volume and surface area of a fluorinated molecule, but also influences the molecular conformation, reduces the flexibility of linear fluorocarbon chains, and increases the kinetic stability derived from the steric shielding by a densely surrounded carbon atom with fluorinated substituents.<sup>3</sup> While linear hydrocarbons have a zigzag conformation, linear perfluorocarbons form a helical structure with a twisting angle of about 12-15 ° around each carbon-to-carbon bond for long perfluorinated chains<sup>14-16</sup> as consequence of the steric repulsion of the increased volume and high electron density (figure 1). This results in a less flexible backbone and a more rigid appearance for the perfluorocarbon molecules. This makes molecules bearing long fluorinated substituents ( $C_nF_{2n+1}$  with  $n = 4 - 12$ ) suitable for example as liquid crystals.<sup>12,17</sup> The increased stiffness of perfluorinated chains compared to alkyl chains results further in an increased viscosity, e.g. perfluorohexane compared to n-hexane, and facilitates chain stacking and crystallization.<sup>18</sup>

Table 1: Comparison of selected physicochemical properties of n-hexane (**1**), 1,1,1,2,2,3,3-heptafluorohexane (**2**) and its perfluorinated (**3**) analog [table modified from reference <sup>3</sup>] (boiling temperature  $T_b$ ; heat of vaporization  $\Delta H_v$ ; density  $d^{25}$ ; viscosity  $\eta^{25}$ ; surface tension  $\gamma^{25}$ ; compressibility  $\beta$ ; refractive index  $n_D^{25}$ ; dielectric constant  $\epsilon$ )<sup>3</sup>

Property	<b>1</b>	<b>2</b>	<b>3</b>
			
$M$ (g/mol)	86	212	338
$T_b$ (°C)	69	64	54
$\Delta H_v$ (kcal/mol)	6.9	7.9	6.7
$d^{25}$ (g/cm <sup>3</sup> )	0.655	1.265	1.672
$\eta^{25}$ (cP)	0.29	0.48	0.66
$\gamma^{25}$ (dyn/cm)	17.9	14.3	11.4
$\beta$ (10 <sup>-6</sup> /atm)	150	198	254
$n_D^{25}$	1.372	1.190	1.252
$\epsilon$	1.89	5.99	1.69

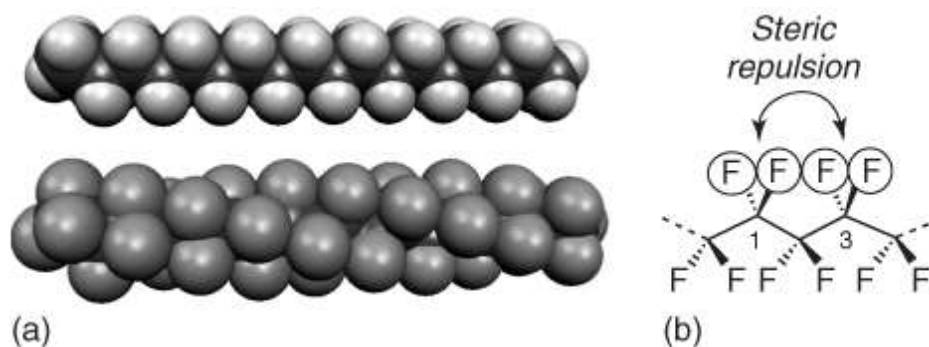


Figure 1: (a) The zigzag conformation of octadecane in the solid state (top left) compared to the helical perfluorooctadecane (bottom left), (b) model of the steric repulsion effect of completely perfluorinated linear alkanes. Figure modified from reference.<sup>3</sup>

The chain length is critical for the intermolecular interaction between fluorocarbons. Shorter perfluoroalkanes have higher boiling temperatures and higher vaporization enthalpies than their non-fluorinated counterparts.<sup>19</sup> However, the boiling temperatures and the vaporization enthalpies get lower than those of related hydrocarbons at a chain length of  $n > 4$  and  $n > 5$ , respectively. The difference increases with increasing chain length. The intermolecular separation of the neighboring carbon atoms is a main effect in the intermolecular separation which is similar for  $\text{CF}_4$  and  $\text{CH}_4$  (0.40 and 0.38 nm)<sup>20</sup> and increases for  $\text{C}_3\text{F}_8$  up to 0.48 nm. For longer n-alkanes (e.g.,  $\text{C}_3\text{H}_8$  0.40 nm)<sup>21</sup> it remains nearly constant.<sup>12</sup> However, it is interesting to point out that for example n-hexane and  $\text{CF}_4$  have about the same molecular mass ( $M(\text{CF}_4) = 88 \text{ g/mol}$ ,  $M(\text{C}_6\text{H}_{14}) = 86 \text{ g/mol}$ ) but the boiling temperature of the hydrocarbon is about 200 K higher than that of the perfluorinated species ( $T_b(\text{C}_6\text{H}_{14}) = 69 \text{ }^\circ\text{C}$ ,  $T_b(\text{CF}_4) = -128 \text{ }^\circ\text{C}$ ).<sup>3</sup>

Another unique property of perfluorinated alkanes is their very low surface tension, which gives the possibility to wet nearly any kind of surface.<sup>22</sup> Not only liquids but also solid perfluorocarbon surfaces for example poly(tetrafluoroethylene) exhibit extremely low surface tension (18.5 dyn/cm) resulting in anti-stick and low-friction properties. The materials with extremely low surface energy are those of fluorinated graphites with about 6 dyn/cm which is likely to be due to a densely fluorine covered surface.<sup>23</sup> In the case of poly(tetrafluoroethylene) (PTFE), this effect can be seen by comparison among polymers with lower fluorine density. For example, poly(difluoroethylene) has a higher surface tension of 25 dyn/cm, polyfluoroethylene a surface tension of 28 dyn/cm and polyethylene only a value of 31 dyn/cm. Another proof for the requirement of a densely covered surface with fluorine for the extremely low surface tension is a comparison with poly(chlorotrifluoroethylene). Here a more polarizable chlorine atom replaces one fluorine atom. The surface energy of a

poly(chlorotrifluoroethylene) surface is 31 dyn/cm which is the same value as for a polyethylene (PE) surface.<sup>3</sup>

Furthermore, fluorine atoms in organic compounds can not only change the hydrophobicity but also the lipophobicity and gives the ability to develop hydrogen bonding.<sup>3</sup> The increased hydrophobicity and lipophobicity is the reason that fluorocarbons and hydrocarbons tend to segregate, which is chain length dependent.<sup>12</sup> A parameter to quantify the immiscibility of liquids is the Upper Critical Solution Temperature (UCST) which strongly depends on the length for hydrocarbon chains but is much less sensitive for perfluorinated chains with different lengths in a  $F_n + H_m$  mixture.<sup>24,25</sup> For example the UCST for a  $F_7 + H_5$  mixture is 9.2 °C, that for a  $F_7 + H_{15}$  mixture is 194.1 °C whereas the UCST for a  $F_3 + H_6$  mixture is 2.4 °C and for a  $F_7 + H_6$  mixture is 30.1 °C.

Although, the lipophilicity is always increased with longer perfluorinated substituents and the hydrophilicity is reduced.<sup>12</sup> For an alkyl chain with a  $CF_3$  unit at one end, a reduction of lipophilicity and an enhancement of the hydrophilicity was found, mainly due to the relatively stronger dipole moment provided by the  $CH_2-CF_3$  unit.<sup>7</sup> Although, the perfluorinated alkanes show weak intermolecular interactions, some partially fluorinated hydrocarbons have quite strong interactions because of local, non-compensated carbon-fluorine dipole moments.<sup>3</sup> They play an important role for the mesophase behavior of fluorinated liquid crystals for example in active matrix liquid crystal display (AM-LCD) technology.<sup>17</sup> Mostly they arise from carbon atoms which are bound directly to fluorine and hydrogen and this results in hydrogen bonding with the polarized H-C bonds as donor and the fluorine as acceptor. Furthermore, it might be expected that fluorine as the element with the highest electronegativity can also form very strong hydrogen bonds. Shimoni and Glukster showed for example that in the presence of oxygen and nitrogen atoms, the C-F unit fails to compete as hydrogen bond acceptor and only in the absence of oxygen and nitrogen atoms it can form weak hydrogen bonds.<sup>26</sup> This was also supported by Dunitz and Taylor with studies on hydrogen bonding between O-H, N-H and C-F units.<sup>27</sup> Their conclusion indicated that the covalently attached fluorine has a low capability to form hydrogen bonds because of its low proton affinity, low polarizability and its inability to modify this by intramolecular electron delocalization or intermolecular cooperative effects. In any event, the inter- and intramolecular interactions involving fluorine in hydrogen bonding has been subject of study for over decades<sup>2,28</sup>, and the non-covalent interactions involving fluorine is still a subject of debate amongst scientific communities.<sup>12</sup>

## 1.2 Liquid crystals and plastic crystals

The liquid crystalline phase is a phase between the solid state and the isotropic phase of a material combining order and mobility.<sup>12,29–34</sup> Therefore, liquid crystalline phases are also called mesophases (greek: mesos = between).<sup>35</sup> The property of a low molecular weight molecules or a polymer to form liquid crystalline phases depends on the molecular architecture, attractive interactions such as hydrogen bonding and dipol-dipol interactions, or repulsive interactions such as segregation of different parts of the molecule.<sup>12,36</sup>

Liquid crystals can be divided into *thermotropic* and *lyotropic liquid crystals*. Thermotropic liquid crystals develop a mesophase when the material is heated up from the solid state into the molten state. The isotropic phase is reached at higher temperatures. Upon cooling, the mesophase is formed before the material crystallizes into the solid state again. Lyotropic liquid crystals only develop their mesophases in suitable solvents under appropriate conditions of concentration and temperature.<sup>34</sup>

Spherical molecules do not form liquid crystalline phases because they have similar attractive forces along all three dimensions, which could be easily destroyed above reaching the melting transition when enough energy is given into the system. This is not the case for rod-like molecules. Their molecular shape leads to anisotropic properties and therefore they exhibit anisotropic intermolecular interactions.<sup>12</sup> When an increasing energy amount is given into the molecular system, the weakest intermolecular bonds are breaking first, leaving a still ordered phase due to the other still present intermolecular interactions. In this state, the rod-like molecules are not completely free to move in any direction but their possibility for rotation or translation is increased. It is also possible that different attractive interactions such as hydrogen bonds or ionic interactions hold the molecules together as well. At a specific amount of energy, all the remaining intermolecular bonds break and the molecules are free to move and rotate isotropically without restrictions. This state is called the isotropic phase where physical properties are not dependent on any direction.

### ***Calamitic liquid crystals***

Rod-like molecules are able to form liquid crystalline phases because of their anisometry.<sup>12</sup> This kind of liquid crystalline phase is termed calamitic liquid crystalline phases. It is necessary that part of the molecules are straight and rigid. Long and mobile side chains lower the melting temperature and allow the development of the liquid crystalline phase. This calamitic liquid crystalline phases can be differentiated into the nematic phase (N), the cholesteric phase (N\*) and different smectic (S) phases. The smectic phases are the states with the highest intermolecular order in a calamitic liquid crystalline phase. The rod-like molecules are ordered parallel to each other in different layers, in which they are able to move freely. This

results in a mesophase with a two-dimensional order having higher viscosities than the other calamitic phases due to a more pronounced existence of an orientation direction and a long-range positional order. In a nematic phase the orientational order is still present but there is no positional order in layers resulting in a one dimensional ordered state while the molecules are statistically arranged.<sup>12</sup> Because of the lack of the positional order in layers, the molecules can move alongside their longest dimension resulting in a lower viscosity of this phase. The third calamitic liquid crystalline phase is the cholesteric phase, which only exists in the presence of chiral molecules. In this case, the molecules are not directly parallel to each other; they change their position for a specific angle resulting in a helical arrangement alongside the material layers. The cholesteric phase has no long-range positional order in layers and behaves in some aspects very similar to a nematic phase.

### ***Fluorinated calamitic liquid crystals***

The introduction of fluorine in liquid crystals provides materials with high positive (terminal substitution) or negative (lateral substitution on the rigid part of the molecule) dielectric anisotropy due to the high polarity of the C-F bond.<sup>12</sup> The fluorinated liquid crystalline materials also have low ion-solvation capability due to the low polarizability which is, in combination with the high dielectric anisotropy, a key requirement of all commercial liquid crystalline mixtures used in liquid crystal displays.<sup>17</sup> Fluorine substitution reduces the elastic constants and increase the dielectric anisotropy.<sup>17,37</sup> A lot of different molecular architectures and positions of fluorine substitutions at different parts of liquid crystalline molecules were investigated and reviewed by Hird.<sup>38</sup> Particularly fluoro-lateral substituents are frequently employed in liquid crystalline structures to modify the melting temperature, liquid crystalline transition temperatures and mesophase morphology. Fluorine and other small substituents in calamitic liquid crystals are also employed when a chiral center is required or as terminal units. They are also introduced to modify physical properties to enable their use in applications.<sup>38</sup>

### ***Discotic liquid crystals***

There exists another type of thermotropic material which forms liquid crystalline mesophases: discotic liquid crystals.<sup>39-41</sup> Discotic molecules are disc shaped. By stacking discotic molecules, they can build up columnar (rod-like) aggregates. This doctoral thesis is only concerned with columnar materials. Therefore, the possible aggregation states, the mesophases and their differentiation is explained in more detail.

In figure 2, the possible states of discotic liquid crystalline materials are shown ordered by their decreasing molecular order. In the crystalline state, the molecules are highly long and

short range ordered, building a regular 3D arrangement without molecular movements. When a liquid crystalline material is heated above its melting temperature ( $T_m$ ), it is possible that mesophases develop. The most ordered kind of mesophases are the plastic mesophases.<sup>12,40-42</sup> In a plastic mesophase the molecules are still highly 3D ordered as in the crystalline state, but some rotational mobility of single discs is possible. The plastic mesophase can be identified by deformation of the material under polarized optical microscopy (POM). The developed textures are not breaking as crystals and characteristic textures are formed. In X-ray diffraction (XRD), the plastic crystalline mesophase is similar to the crystalline state with only slight changes in the patterns. The transition from a crystalline state into a plastic crystalline mesophase requires only low energy due to only minimal changes in the structure, resulting in a very low transition enthalpy.

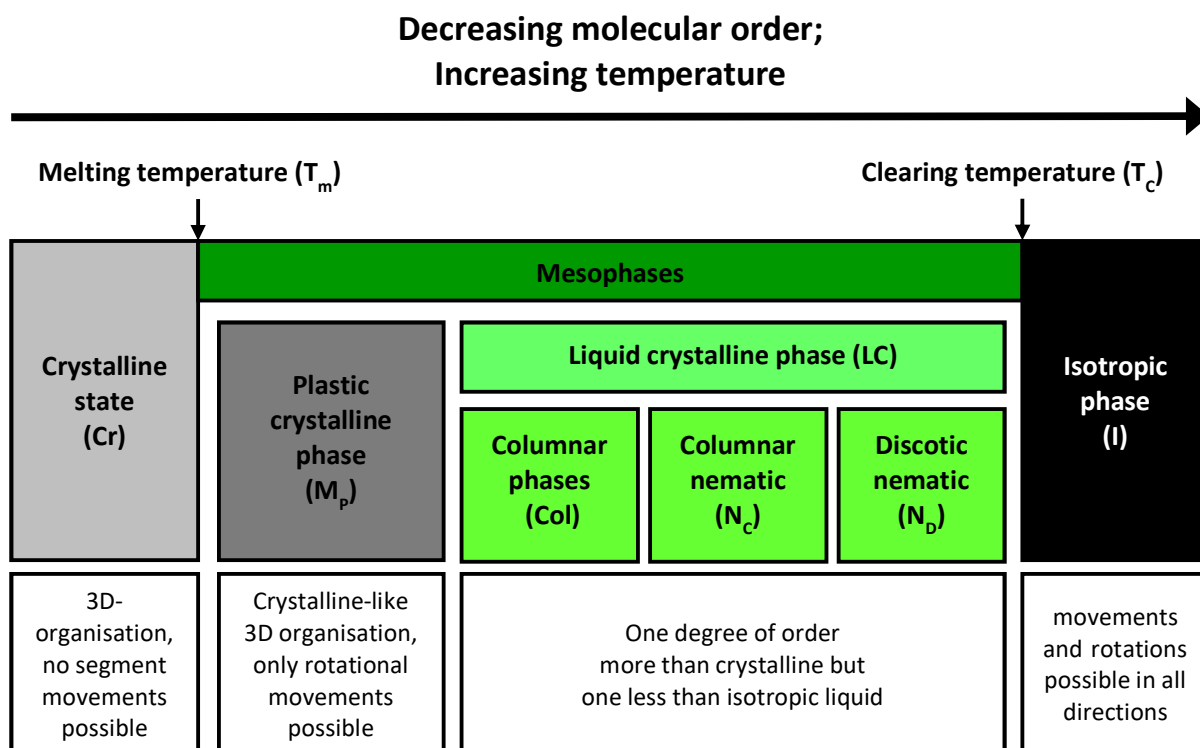


Figure 2: Schematic illustration of the main possible material states and phases of discotic liquid crystals with increasing temperature and decreasing molecular order.

With increasing temperature, thermotropic discotic liquid crystals can develop two kinds of liquid crystalline phases, the columnar (Col) and nematic (N) phases. The higher ordered phase is the columnar phase.<sup>41,43</sup> The discotic molecules are stacked in a columnar structure. The columns can form, beside the one-dimensional liquid organization, also two-dimensional

structures by parallel organization. The columns are statistically shifted to each other and there is no positional order alongside the columns, which is preventing a 3D organization of the crystalline state. The more ordered structures result in higher viscosities of the material than in phases at higher temperatures such as the isotropic phase. It is also possible that the material is not changing into a crystalline state at cooling and is freezing into a glass-like state, which is called mesomorphic glass state. There are different possible arrangements of the columns, some examples are shown in figure 3.

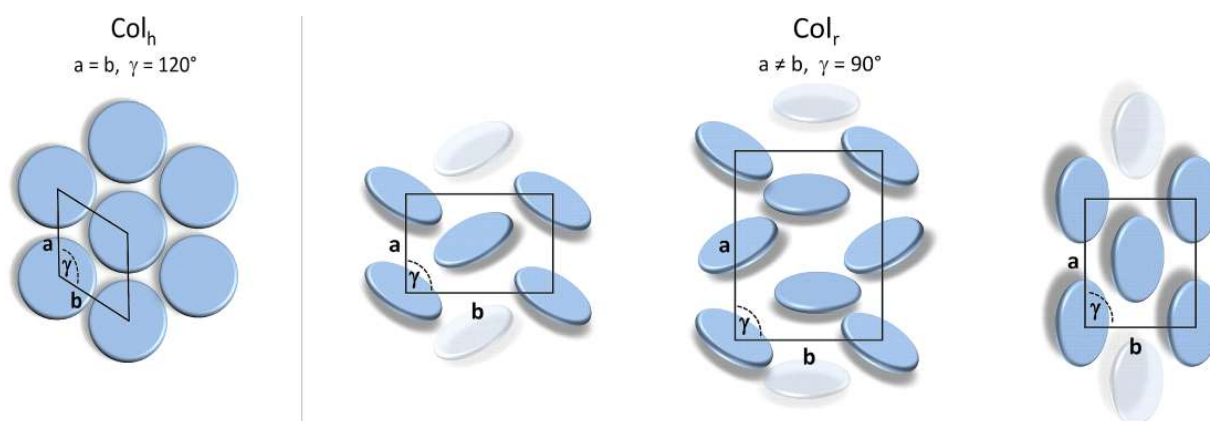


Figure 3: Schematic illustration of the two dimensional structure of the unit cell of the hexagonal and rectangular phases.<sup>44,45</sup>

The arrangement with the lowest system energy for a nearly cylindrical cross section of the columns is the hexagonal columnar phase ( $Col_h$ ). Columns with different lateral interactions or non-symmetrical cross sections can develop rectangular columnar phases ( $Col_r$ ) with a rectangular unit cell. Both  $Col_h$  and  $Col_r$  phases can be identified by typical signals in an XRD measurement as well as typical textures with POM. The single molecules in the columnar stacks are connected by physical bonds. Different strength of the physical bonds can influence the short-range order of the molecules. Therefore, the columnar structure can be differentiated between ordered and disordered columnar phases. In disordered columnar phases, the possibility to move, rotate and translate of the single molecules in their position is higher, while in ordered columnar phases the molecules are more fixed to their position. In the more ordered case, the phases are described as  $Col_{ho}$  for an ordered columnar hexagonal phase. Also,  $Col_{hd}$  for a disordered columnar hexagonal phase exists. There is no clear differentiation if a columnar phase is ordered or disordered because both show no clear translation order which could be found in a plastic crystalline mesophase. Columnar plastic liquid crystalline phases are not dependent on their degree of order and can be regarded as one dimensional fluids.<sup>41</sup> Figure 4 shows a schematic illustration of the molecular

arrangement in an ordered, disordered and plastic columnar phase. It is possible to distinguish an ordered from a disordered phase by the presence of a clear signal for the intermolecular distance of the single molecules at high angles in an XRD measurement. In a disordered phase, the molecules are moving with higher degree of freedom in their position and the signals become broader or not noticeable.

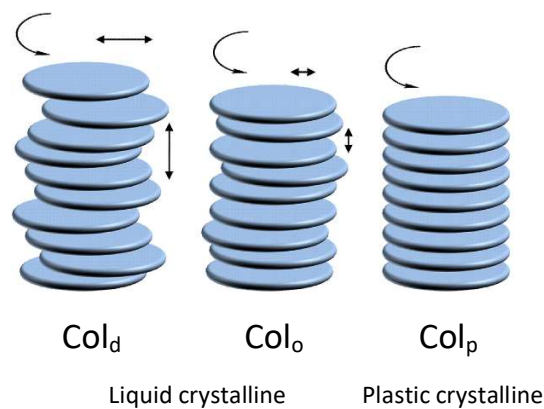


Figure 4: Schematic illustration of the columnar stacking of discotic molecules in an ordered, disordered and plastic columnar phase. Figure modified from reference<sup>44,45</sup>

A decrease of order can be found in discotic nematic mesophases. There are two different nematic phases for discotic liquid crystals, the columnar nematic ( $N_C$ ) and the discotic nematic ( $N_D$ ) mesophase, which are schematically illustrated in figure 5. The higher ordered phase, the  $N_C$  phase, still develops columns of discotic molecules with a typical fluidic short range order.<sup>41</sup> The columns have directional order.<sup>41,42</sup> The nematic phase behaves as a fluid and forms a typical *schlieren* texture indicating a nematic mesophase of the columns. In an XRD experiment, the  $N_C$  phase shows a typical pattern for liquids with a strongly developed diffuse halo but also includes the signal at high scattering angles for the intermolecular interactions in the individual columns. This is not the case in a pattern of the  $N_D$  mesophase due to the non-existence of columnar structures. In this type of nematic mesophase, the discotic molecules are only directional ordered. This is the least ordered liquid crystalline discotic phase. The clearing temperature separates the mesophases from the isotropic phase. The discotic molecules are normally completely unordered in an isotropic phase and can move and rotate freely. This phase can be identified as completely black image between crossed polarizers by POM.

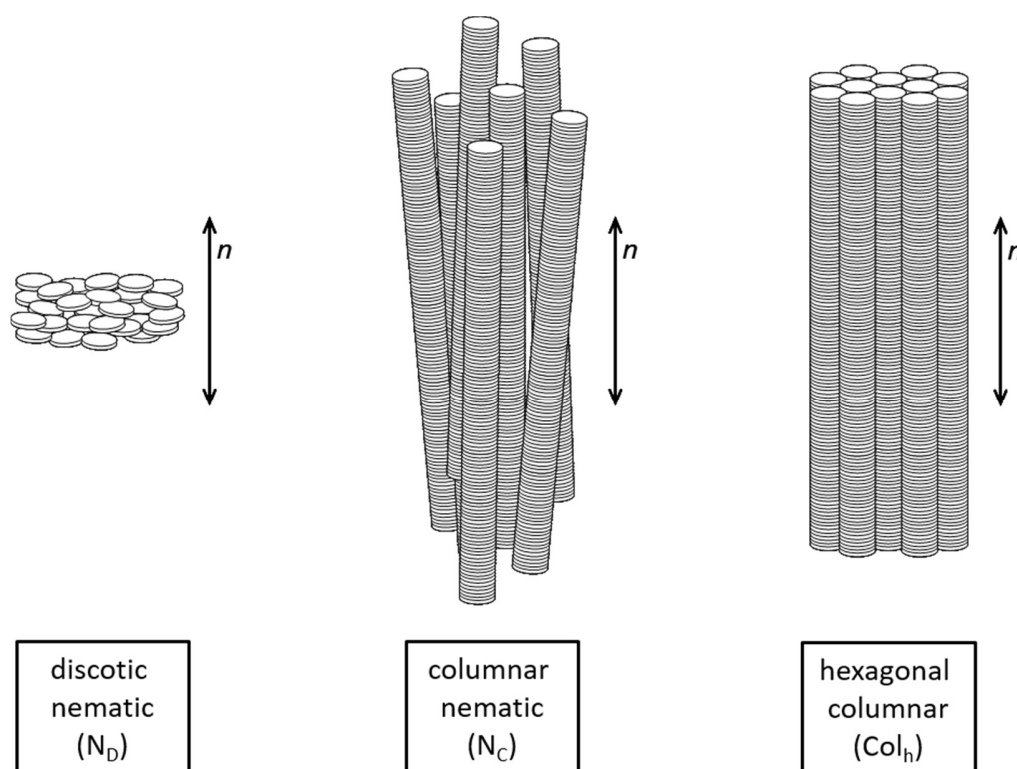


Figure 5: Schematic illustration of the columnar hexagonal  $Col_h$ , the columnar nematic  $N_C$  and the discotic nematic  $N_D$  liquid crystalline mesophases.<sup>45</sup>

### Fluorinated discotic liquid crystals

One of the most commonly used core in discotic liquid crystalline materials are 2,3,6,7,10,11-hexasubstituted triphenylenes with identical peripheral units.<sup>46</sup> The substitution of only one peripheral hydrocarbon unit with a fluorinated chain markedly reduces the columnar phase stability due to the incompatibility with the other five hydrocarbon chains.<sup>47</sup> When all six peripheral chains are substituted, the material shows an extremely high columnar phase stability. Even a single trifluoromethyl group at the end of each chain provides a significant phase stabilization effect.<sup>48</sup> A fluorine substitution in the plane of the core increase the molecular breadth slightly and reduces the melting temperature significantly.<sup>49</sup> Nevertheless, the columnar stability is higher than for the non-fluorinated system due to an enhancement of the intermolecular interactions caused by the higher amount of space necessary for a fluorine substituent. In the case of hexa-*peri*-hexabenzocoronenes with fluorinated chains at the periphery compared to non-fluorinated species, the columnar phase stability leads to a columnar order.<sup>50</sup> The insertion of a *p*-substituted phenyl ring, which seems to increase the linearity and rigidity of the fluorinated chains, leads to formation of smectic and not columnar mesophases.<sup>51</sup> By reducing the fluorinated part with elongation of the alkyl spacer, the

smectic phase can be changed to a hexagonal columnar structure. Another class of disc-like molecules, based on a pentakis(phenylethynyl)phenoxy core, form nematic phases which can be stabilized with the substitution of only one fluorinated chain.<sup>52</sup> The nematic phase is made of a cybotactic cluster due to a local lamellar organization of the molecules caused by the segregation of the fluorinated chains and their tendency to align parallel to each other.

The stabilization and modification of the self-assembly by the fluorophobic and the steric effects of perfluorinated chains was used for other disc-like  $\pi$ -conjugated aromatics<sup>53</sup> such as coronene diimides<sup>54</sup> and porphyrins<sup>55,56</sup>. Also perylene diimides<sup>57-59</sup>, naphthalene tetracarboxylic diimides<sup>60,61</sup>, pyromellitic diimides<sup>62</sup> with fluorinated chains were reported.<sup>12</sup>

### 1.3 Supramolecular chemistry

Supramolecular chemistry was defined as chemistry of molecular assemblies and intermolecular bonds by Jean-Marie Lehn in 1978.<sup>63</sup> In contrary to the traditional chemistry, which deals with covalent chemical bonding, supramolecular chemistry is a matter of chemical interactions between molecules. These non-covalent interactions determine the spatial organization of molecules, which can lead to the formation of larger supramolecular objects. Examples for non-covalent interactions are hydrogen bonds,  $\pi$ - $\pi$ -stacking, van-der-Waals forces or dipolar, ionic and coordination metal interactions.<sup>45,64</sup> In the supramolecular approach, molecules are able to self-assemble reversibly to supramolecular objects. The properties of these objects are controlled by the molecular structure of the single molecules, which are influenced by side chains, functional groups or shape and size.<sup>65</sup> Therefore, the supramolecular approach includes the design of the individual molecules, the architecture of the supramolecular constructions as well as the study of the properties of the final supramolecular objects.

The work in modern supramolecular chemistry encompasses the construction of molecular devices, machines, and molecular recognition, by self-assembly and self-organization.<sup>66</sup> In self-organization processes, energy is required to achieve a non-equilibrium state while self-assembly systems reach their equilibrium without any external force. The self-organization is one of the basic attributes in supramolecular chemistry because it depends on intermolecular interactions. The interactions of the molecules are based upon the molecular complementarity. The interacting molecules complement one another by their interacting groups and their shape, in a way that they can interact with each other.<sup>67</sup> It is possible that one molecule combines with a second or more of the same molecule, which is called self-complementary process. When several molecules have assembled, it is often referred to as supramolecular object or macromolecule. Because of the non-covalent bonding of the self-assembled supramolecular object or macromolecule, it resides in a thermodynamic

equilibrium.<sup>68</sup> Liquid crystals, as described before, are also part of the supramolecular chemistry world. The liquid crystalline behavior is dependent on the interactions between the single molecules.<sup>64</sup> Discotic molecules can be self-complementary objects and build up columnar structures connected by non-covalent forces. The forces in the column are much stronger than in all other spatial dimensions and therefore, it can be understood as supramolecular.<sup>68</sup>

### ***1,3,5-Benzenetrisamides and 1,3,5-cyclohexanetrisamides***

In the field of supramolecular chemistry and the self-assembly to supramolecular objects, 1,3,5-benzenetrisamides (BTA) and 1,3,5-cyclohexanetrisamides (CTA) became one of the most investigated class of molecules because of their possibility to develop well defined non-covalent bonds in a self-complementary fashion. The chemical structure is based on a benzene or cyclohexane core with three amide groups directly connected at the 1, 3 and 5 position. The core is responsible for symmetry and planarity while the amide groups can form three strong hydrogen bonds between the single molecules, which result in one-dimensional self-assembly. 1,3,5-Benzenetrisamides can be synthesized with different position of the amide groups, in one case the core is directly connected to the carbonyl group which can be achieved by synthesis based on the core molecule bearing three acid groups at the 1,3 and 5 position. It is also possible that the synthesis bases on a 1,3,5-triamine core unit resulting in amid groups directly connected to the core with their nitrogen side. Molecules with mixed amide connectivity are also possible.<sup>69</sup> In the case of a self-assembly process, the amide groups are arranged in such way that the molecules are self-complementary units and therefore the three chains develop hydrogen bonds as strong attractive intermolecular interactions. With proper substituents such as long alkyl chains, a lot of BTAs and CTAs develop a columnar mesophase, which can not only be related to the anisotropy of the disc-shaped molecules but also on the strong hydrogen bonding.<sup>68,70-73</sup> The nature of the peripheral substituents is very important for the properties, in particular with respect to solubility, thermal behavior, and crystal structure. With only slight changes, the self-organization, the thermal properties, and mesophase behavior is influenced.

The structural BTA motif allows BTAs to form physical gels<sup>73-75</sup>, to be used as additives to improve the electret performance of polypropylene<sup>76</sup>, to improve the clarity of isotactic polypropylene<sup>69,77</sup>, and the nucleation of poly(vinylidene fluoride)<sup>78</sup> and poly(terephthalate).<sup>79</sup> Another field of application are supramolecular fibers formed by self-assembly of BTAs from solvents<sup>80-82</sup> or by electrospinning<sup>83</sup>.

**1,3,5-Benzenetrisamides based on trimesic acid:** In 1986 Matsunaga et al. first reported on liquid crystalline 1,3,5-benzenetrisamides based on a trimesic acid core, with the amide groups directly connected to the core with their carbonyl units, and long alkyl side chains.<sup>84</sup> In 1999 it was proven by Lightfoot et al. via crystallographic investigations that N,N',N''-tris-(2-methoxyethyl)-1,3,5-benzenetricarboxamide self-assembles into columnar structures.<sup>71</sup> The columns were built up by stacked molecules, which were held together by strong, threefold hydrogen bonds. To achieve strong hydrogen bonds, it is necessary that the amide groups are turning out of the coplanarity with an angle as high as possible. The conjugation to the phenyl group is the reason why the amide groups can only turn in angles between 36.8 ° to 45.5 °, which causes the adjacent molecules to undergo a turn of 60 ° to strengthen the hydrogen bonds. All the amide groups are now pointing into the same direction, resulting in a helical arrangement of the hydrogen bonds.

Ten years later in 2009 Kristiansen et al. found two different helical assemblies in the columnar structures of 1,3,5-benzenetricarboxamides with bulky tert-butyl substituents, the up and down configuration.<sup>72</sup> They originate from the orientation of the oxygen atoms in the formed columns, which had a triple-helical bonding pattern along the column axis. In the developed hexagonal structure, build up by the BTA columns, the columns with different configurations arranged in an antiparallel fashion to lower the energy of the whole supramolecular arrangement.

Beside this most common three dimensional columnar arrangement of BTAs, it is also possible that only two dimensional structures such as rosettes<sup>85</sup>, T-shaped<sup>86</sup> or sheet structures<sup>87</sup> were formed. Generally, trisamides which form intermolecular hydrogen bonds with adjacent molecules have a flatter geometry than trisamides which form intramolecular hydrogen bonds.<sup>88</sup>

However, the nature of the side chains plays a very important role for the formation of the crystal structure and the mesophase behavior. Timme et al. investigated a series of 1,3,5-benzenetricarboxamides with linear and branched alkyl substituents with respect to their phase behavior and mesophase structure.<sup>89</sup> He found, for a series of benzene tricarboxamides, different columnar hexagonal and rectangular mesophases of liquid crystalline and plastic crystalline nature. Linear substituted benzene tricarboxamides showed broader liquid crystalline mesophases with increasing side chain length. They showed smaller intercolumnar distances than the branched species. Branched benzene tricarboxamides had higher transition temperature to the isotropic phase. With increasing temperature, the intercolumnar interactions became weaker and get completely lost by further heating, while the intermolecular forces were still intact. At even higher temperatures, the single columns were transformed into smaller aggregates. It is possible that this small aggregates are still

present above the clearing temperature of the material and upon further heating a molecular isotropic phase can be obtained.<sup>89</sup>

Within one column of the supramolecular aggregates, the hydrogen bonds are pointing into one direction causing a macrodipole along the columnar structure with the sum of at least all individual dipole moments generated by each single molecule.<sup>90</sup> It was shown by Albuquerque et al. that the dipole moment per 1,3,5-benzenetrisamide molecule increases with increasing molecule number within a supramolecular column resulting in a macrodipole higher than the sum of the single molecule dipoles.<sup>91</sup> Another group proved this cooperative nature of self-assembly in the case of 1,3,5-benzenetrisamides by simulations regarding the free energy change dependent on the oligomer size.<sup>92</sup>

In dilute solutions the self-assembly mechanism of various asymmetric 1,3,5-benzenetricarboxamides with chiral substituents was investigated by Stals et al. using temperature dependent circular dichroism (CD-) and ultraviolet and visible (UV-Vis) analysis.<sup>93</sup> A highly cooperative mechanism called nucleation-growth model was developed by van der Schoot<sup>94</sup> which was modified from the original model from Oosawa and Kasai.<sup>95</sup> It includes two regimes: a nucleation regime in which all molecules are molecularly dissolved and an elongation regime where the aggregate grows rapidly. The self-assembly process of 1,3,5-benzenetrisamides is illustrated in figure 6. The BTA from synthesis is dissolved in a particular solvent and the molecules self-assemble upon cooling into supramolecular nanofibers, the side chains facing to the surface. Upon further cooling, supramolecular nanofiber bundles and assemblies of fiber bundles are formed. This self-assembly process is thermally reversible.

Further investigations showed that the intermolecular hydrogen bonds become stronger with an increasing length of the column. This cooperative mechanism is caused by electrostatic interactions, which interaction energy decreases with increasing number of monomers indicating that larger aggregates are more favorable.<sup>96,97</sup> This cooperative self-assembly mechanism was found to be also valid for partially fluorinated 1,3,5-benzenetrisamides.<sup>98</sup>

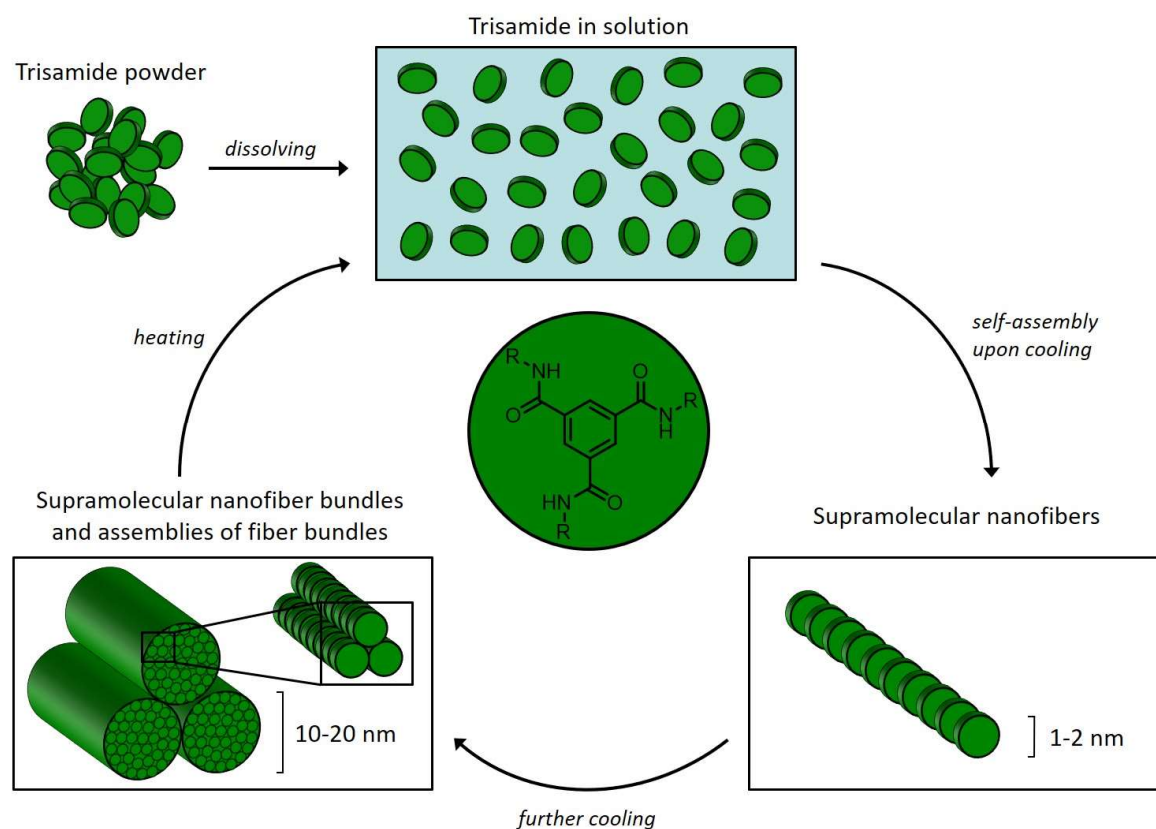


Figure 6: Schematic concept of the cooperative self-assembly mechanism of 1,3,5-benzenetrisamides in dilute nonpolar solutions. Scheme modified from reference.<sup>99,100</sup>

**1,3,5-Benzenetrisamides based on 1,3,5-triaminobenzene:** Instead of using trimesic acid as core unit, it is possible to use 1,3,5-triaminobenzene as well. This results in BTAs with amide groups directly connected to the core with the nitrogen part.

As it was the case for the BTAs based on trimesic acid, all three oxygen atoms of the amide group could be found to point to the same direction in columnar packing for BTAs based on 1,3,5-triaminobenzene.<sup>101</sup> A difference could be found in the hydrogen bonding strength. Compared to the species based on trimesic acid, weaker hydrogen bonds are formed for BTAs based on 1,3,5-triaminobenzene because of the more planarized amide groups with respect to the benzene core, leading to a decrease of the macrodipole.<sup>91</sup> This could also be found in dilute systems.<sup>81</sup> In dilute alkane solutions, the BTAs self-assemble into one-dimensional aggregates via helical hydrogen bond formation. The formed columns were found to be less stable than the columns of their comparable BTA species based on trimesic acid because of the lower hydrogen bonding strength.<sup>81</sup> Wegner et al. simulated the self-assembly behavior in solid state of a BTA based on trimesic acid and a BTA based on 1,3,5-triaminobenzene with

methyl groups as substituents.<sup>102</sup> They found a significantly different packing for the BTA based on 1,3,5-triaminobenzene due to a symmetry breaking. This means that only two of the amide groups point into one direction with respect to the benzene core while the third one points to the opposite direction. Therefore, it is not possible to form the typical symmetric columnar arrangement of the hydrogen bonds, as it is the case for the BTAs based on trimesic acid.

Regarding the formation of fibers from BTAs based on 1,3,5-triaminobenzene, Abraham investigated the self-assembly of 1,3,5-tris(2,2-dimethylpropionylamino)benzene with respect to the fiber formation at different BTA concentration and cooling rates. By lowering the cooling rate, a broader fiber size distribution was observed for all concentrations while at constant cooling rate and decreasing BTA concentration, the fiber size distribution got narrower and shifted down to the nanometer range.<sup>103</sup> The same molecules were self-assembled from 2,2,4,4,6,8,8-heptamethylnonane as solvent with the result of supramolecular fibers with significant aspect ratios (>1000:1).<sup>72</sup> The self-assembly mechanism is highly cooperative and therefore, the nucleation-growth model shown in figure 6 is also valid for the self-assembly of BTAs based on 1,3,5-triaminobenzene.<sup>81</sup>

***Influence of fluorine on the crystal structure of BTAs:*** In 2017, Zehe et al. published the results of investigations on structure and disorder of four columnar 1,3,5-benzenetrisamides, one of them bearing a fluorine substitution, determined by X-ray scattering and density functional theory calculations. It was demonstrated that the column orientation, and thus the columnar dipole moment, is receptive to geometric frustration if the columns aggregate in hexagonal rod packing.<sup>104</sup> For a 1,3,5-benzenetrisamide based on 1,3,5-benzenetricarboxylic acid, each stack has a 50 % probability to be either in the up or the down state, while a stripe-type macrodipole arrangement for a similar trisamide based on 1,3,5-triaminobenzene, and honeycomb patterns for different 1,3,5-benzenetrisamides with longer side chains or a fluorine substitution, were found. The four different molecules were expected to have varying ratio of macrodipole and steric interactions, which was proven by analysis via XRD and quantum-mechanical calculations on finite clusters of single-crystal structures. The fluorinated molecule showed the lowest molecular dipole moment because of the *anti*-alignment of the C-F and C=O bonds which is induced by intramolecular NH...F hydrogen bonds.

In an additional publication study a few years earlier by the same group, the influence of a fluorine side-group substitution on the crystal structure formation from a polar solvent was investigated.<sup>105</sup> The structure of 1,3,5-tris(2-fluoro-2-methylpropionylamino)benzene was solved by solid-state NMR spectroscopy, XRD methods and computer simulations, and it

showed a lamellar arrangement of molecules. Here one of the carbonyl groups is tilted to a different direction than the other two with respect to the benzene ring in every single molecule, but the fluorine atoms only contribute to intramolecular interactions.

**1,3,5-Cyclohexanetrismides:** 1,3,5-Cyclohexanetrismides (CTAs) have a different self-assembly behavior and solid-state arrangement compared to the molecules based on a benzene core. The acyclic cores result in a different packing of the molecules. Fan et al.'s investigations show that the amide groups in a *cis,cis*-cyclohexanetricarboxamide bearing three picoline substituents can rotate freely because they are not hindered by conjugation.<sup>106</sup> Therefore, all amide groups point in the same direction and they form nearly linear hydrogen bonds, which makes a helical assembly unnecessary.<sup>71,106</sup> The intermolecular distance of the CTAs in a supramolecular column is larger than for BTAs due to linearly arranged hydrogen bonds.<sup>89</sup> CTAs with branched side chains were investigated to be packed more compact than the ones with linear substituents due to a less equally distribution around the acyclic core.<sup>107</sup>

A systematic comparison of the thermal properties, phase behavior and mesophase structures of BTAs and CTAs was made by Timme et al.<sup>45,108</sup> The study compared BTAs and CTAs with linear and branched alkyls substituents to obtain a deeper understanding of the structure-property relationships. With the help of POM, XRD, differential scanning calorimetry (DSC), and infrared spectroscopy (IR), it was possible to identify a large variety of columnar mesophases for the different BTA and CTA molecules. He found that linear-substituted BTAs showed a broader liquid crystalline phase with increasing chain length. Transition temperatures of CTAs were higher than those of BTAs. Branched substituents showed higher transition temperatures than linear analogs. He observed a columnar nematic phase (N<sub>c</sub>) for molecules with cyclohexane core. This was the first time that such a mesophase was found for a single-component system. Another interesting result was accomplished. Small columnar BTA aggregates were still present above the clearing temperature, making a differentiation into optical isotropic phase and molecular isotropic phase necessary.

Based on the three topics briefly addressed in this introduction, fluorine containing organic molecules, columnar mesophases and self-assembly to supramolecular structures, this thesis addresses for the first-time supramolecular systems based on trismides with linear perfluorinated side chains.



## 2. Objectives of the thesis

The thesis is structured into the following three chapters (see figure 7): (1) thermal properties, mesophase behavior and structure property relations of two series of 1,3,5-benzenetrisamides (BTAs) with linear perfluorinated side chains, (2) melt electrospinning of trisamides with linear perfluorinated side chains, and (3) self-assembly and co-self-assembly studies of 1,3,5-benzenetrisamides from solution.

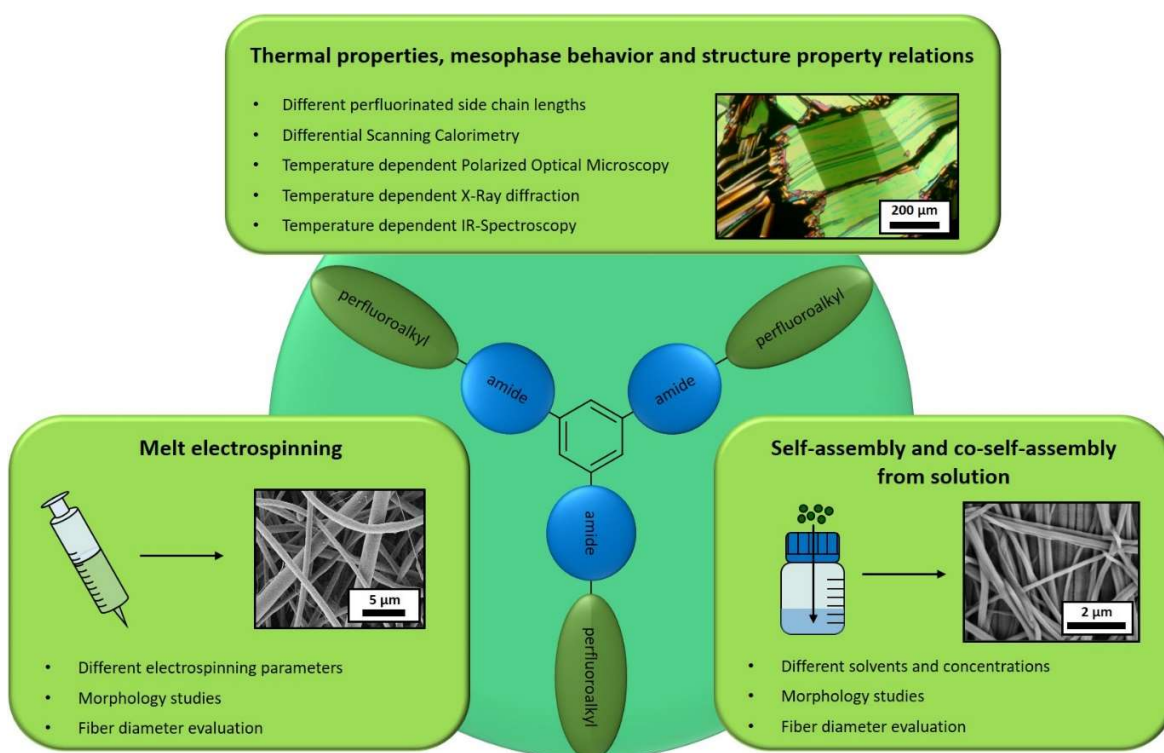


Figure 7: Objectives of the thesis: studies on the thermal properties, the mesophase behavior and structure property relations of 1,3,5-benzenetrisamides with linear perfluorinated side chains as well as the processing to supramolecular fibers by melt electrospinning and by self-assembly and co-self-assembly studies from solution.

### 1: Thermal properties, mesophase behavior and structure property relations of two series of 1,3,5-benzenetrisamides with linear perfluorinated side chains

Different BTAs with linear perfluorinated side chains varying in the length of the linear perfluorinated side chains of three up to eight carbon atoms, and in the connectivity of the amide linkage, are characterized with respect to their thermal properties, mesophase behavior, and structure property relations. Measurement techniques are Differential

Scanning Calorimetry (DSC), Polarized Optical Microscopy (POM), as well as temperature dependent X-Ray Diffraction (XRD) and Infrared Spectroscopy (IR). Special focus is on the mesophase behavior with respect to the formation of liquid crystalline phases. One 1,3,5-cyclohexanetrissamide (CTA) with linear perfluorinated side chains is characterized for comparison. Similar BTAs and CTAs without fluorination but the same molecular architecture were already studied by Timme et al.<sup>45,89,108</sup>. The results of the trisamides with the linear perfluorinated side chains should be compared with their non-fluorinated analogs.

### ***2: Melt electrospinning of trisamides with linear perfluorinated side chains***

Selected BTAs with different linear perfluorinated side chain length including the CTA derivative should be processed to thin supramolecular fibers by melt electrospinning. By variation of the melt electrospinning parameters, an optimal parameter set for different BTAs should be found regarding the supramolecular fiber quality as determined by fiber size, size distributions and fiber shape. The results should be compared to BTAs of the same architecture bearing alkyl side chains. Additionally, conditions for melt electrospinning with the aim to process rather thick fibers in the range of about 5 to 15  $\mu\text{m}$  should be found. These thick fibers are required in a collaboration with the chair of Physical Chemistry II at the University of Bayreuth for direct force measurement experiments. Supramolecular fiber mats made of BTAs with linear perfluorinated and alkylated side chains should be investigated by wettability measurements and compared to each other.

### ***3: Self-assembly of 1,3,5-benzenetrissamides with perfluorinated side chains and co-self-assembly of structurally related 1,3,5-benzenetrissamides from solution***

In a bottom-up self-assembly approach, selected BTAs with linear perfluorinated side chains are self-assembled into supramolecular fibers from solution. Therefore, suitable solvents for dissolution of the molecules as well as for fiber formation upon cooling or evaporation should be identified. In case of successful preparation of supramolecular fibers, characterization methods to evaluate the fiber size and size distribution and to investigate the fiber shape should be employed. Additionally, in a new co-self-assembly approach, the objective was to simultaneously self-assemble two BTAs from solution. These experiments were carried out in a woven as support scaffold. Two structurally related BTAs, one with linear perfluorinated side chains as well as one BTA with alkyl side chains were selected. In pre-experiments, the most suitable solvent or solvent mixture should be identified. The type of self-assembly, with respect to the arrangement of the two BTA molecules within the self-assembled fibers, should be determined by means of the molecular composition of the single fibers in the self-assembled morphologies.

### 3. Thermal properties, mesophase behavior and structure property relations of two series of 1,3,5-benzenetrisamides with linear perfluorinated side chains

The objective of this chapter is the characterization of a series of 1,3,5-benzenetrisamides (BTAs), varying in the connectivity of the amide linkage and the length of the linear perfluorinated side chains from three up to eight carbon atoms. In addition, for comparison, one 1,3,5-cyclohexanetrisamide (CTA) was investigated. The applied characterization methods are Differential Scanning Calorimetry (DSC), Optical Polarization Light Microscopy (POM), temperature dependent X-Ray Diffraction (XRD) and Infrared Spectroscopy (IR) for the investigation of the phase behavior and Thermogravimetric Analysis (TGA) for the thermal stability. Structurally analog BTAs with alkyl side chains and the same molecular architecture were already studied in detail at the chair of Macromolecular Chemistry I by Andreas Timme et al.<sup>45,108</sup> The results of the non-fluorinated 1,3,5-benzenetrisamides and 1,3,5-cyclohexanetrisamides are compared with the perfluorinated BTAs and CTA of this thesis at the end of this chapter.

#### 3.1 Molecular structure of the trisamides

Table 2 shows the molecular structures of the investigated two series of BTAs and the numbering of the compounds used throughout this thesis. The first series (**1a-1f**) is based on 1,3,5-triaminobenzene as core and the second series (**2a-2f**) on 1,3,5-benzenetricarboxylic acid. It must be mentioned that for the same number of carbon atoms in the side chain, the BTA series based on 1,3,5-triaminobenzene (**1a-f**) contains two additional fluorine atoms. In the case for the BTAs based on trimesic acid (**2a-f**), the group directly connected to the amide group is a CH<sub>2</sub> group. This is due to the commercial availability of the starting materials.

For the purpose of comparison, a CTA based on (1*s*,3*s*,5*s*)-cyclohexane-1,3,5-tricarboxylic acid with a perfluorinated side chain length of seven carbon atoms was also investigated. In analogy to the work by Timme<sup>45,108</sup>. It could be expected that this CTA with long side chain length may show a nematic phase. This nematic phase is of fundamental interest, also in view of the processing to fibers by melt electrospinning.

Table 2: Chemical structures and numbering of the BTAs based on 1,3,5-triaminobenzene (**1a-1f**), trimesic acid (**2a-2f**) and (1s,3s,5s)-cyclohexane-1,3,5-tricarboxylic acid (**3a**) with linear perfluorinated side chains.

<p><b>R:</b></p> <p>Perfluorinated side chains</p>	<p style="text-align: center;"><b>R:</b> -(CF<sub>2</sub>)<sub>5</sub>-CF<sub>3</sub></p>		
<p>-(CF<sub>2</sub>)<sub>2</sub>-CF<sub>3</sub></p> <p>-(CF<sub>2</sub>)<sub>2</sub>-CF<sub>3</sub></p> <p>-(CF<sub>2</sub>)<sub>3</sub>-CF<sub>3</sub></p> <p>-(CF<sub>2</sub>)<sub>4</sub>-CF<sub>3</sub></p> <p>-(CF<sub>2</sub>)<sub>5</sub>-CF<sub>3</sub></p> <p>-(CF<sub>2</sub>)<sub>6</sub>-CF<sub>3</sub></p>	<p><b>1a</b></p> <p><b>1b</b></p> <p><b>1c</b></p> <p><b>1d</b></p> <p><b>1e</b></p> <p><b>1f</b></p>	<p><b>2a</b></p> <p><b>2b</b></p> <p><b>2c</b></p> <p><b>2d</b></p> <p><b>2e</b></p> <p><b>2f</b></p>	<p><b>3a</b></p>

### 3.2 Characterization methods

For determination of the phase behavior and mesophases of the trisamides, different characterization methods were used. Each method gives certain conclusions about the thermal properties and phase behavior of the materials, but only the combination reveals the entire phase behavior.

#### **Thermogravimetric Analysis (TGA)**

In a Thermogravimetric Analysis (TGA) experiment, the sample is placed in crucibles under inert gas atmosphere. The sample is heated with a continuous rate (here 10 K/min) to temperatures above the expected decomposition temperature. During the measurement, the weight of the sample is determined. The resulting data are plotted in a weight-loss versus temperature diagram. The emerging curve progression allows to make conclusions about the dryness, the evaporation behavior, and the thermal stability of the material. In the first region, the slope of the curve should be zero, indicating that the material is thermally stable,

no decomposition takes place and no residual solvent is present. In the second region the function and the initial weight slowly begins to decrease which means that the material begins to sublime or evaporate. This is in particular the case for small molecules. A very fast and complete loss of weight indicates that the material sublimates or evaporates. A non-uniform decrease is a sign that the material first changes into a molten state and then decomposes at higher temperatures.

The TGA experiments of the BTAs based on 1,3,5-triaminobenzene (**1a–1f**) are shown in figure 8.

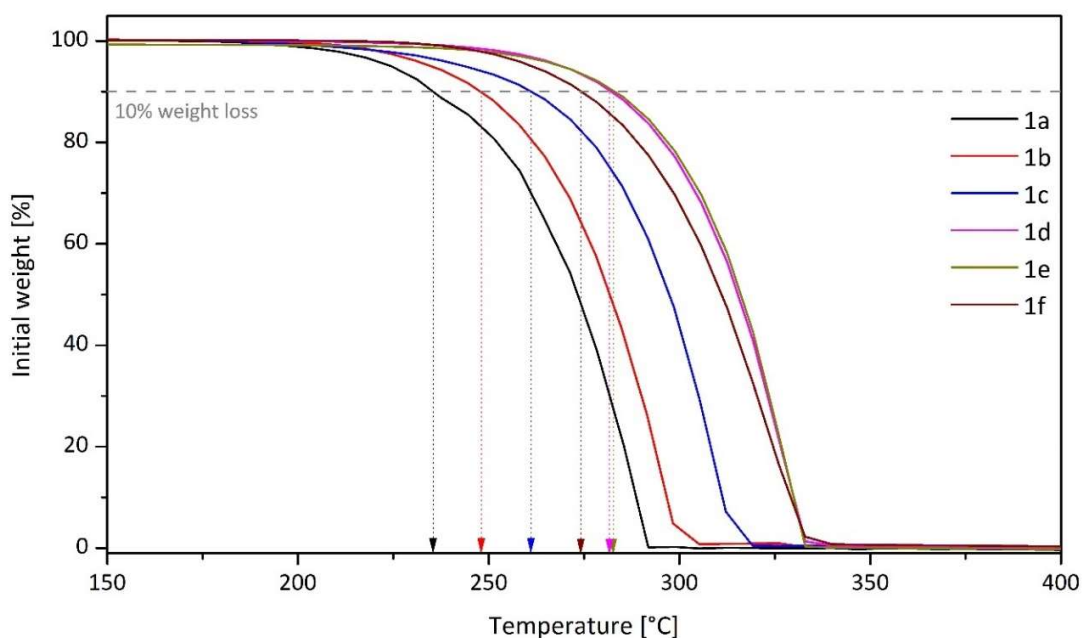


Figure 8: Thermogravimetric Analysis (heating rate: 10 k/min, N<sub>2</sub> atmosphere) curves of 1,3,5-benzenetrisamides **1a–f** based on 1,3,5-triaminobenzene with linear perfluorinated side chains. The arrows point to the temperature of 10 % initial weight loss.

To compare the weight loss, the grey dashed line indicates the 10 % weight loss and the colored arrows point to the corresponding temperature. All materials show a similar curve progression and the materials evaporate to 100 % of the initial weight. With respect to the different side chain lengths, the thermal stability increases with increasing chain length. A 10 % weight loss at 242°C is observed for the BTA with the shortest side chains **1a**. The 10 % weight loss increases systematically with longer side chains.

In figure 9 the TGA curves of the BTAs based on trimesic acid **2a-f** and CTA **3a** are shown. The same conditions were used as before (figure 8). The weight loss behavior is the same for the BTAs **2a-f**, which can be seen by similar curve progressions. The temperatures of 10 % initial weight loss are increasing with increasing side chain length from a temperature of 297 °C for **2a** to 347 °C for **2f**. Compound **3a** is thermally very stable and reaches the 10 % initial weight loss at a temperature of 344 °C. It can also be examined that the weight loss is very fast indicating a sublimation. The thermal stability of the CTA is most comparable to the BTA based on trimesic acid with the longest linear perfluorinated side chains **2f**. In this series, also a final 100 % weight loss was observed.

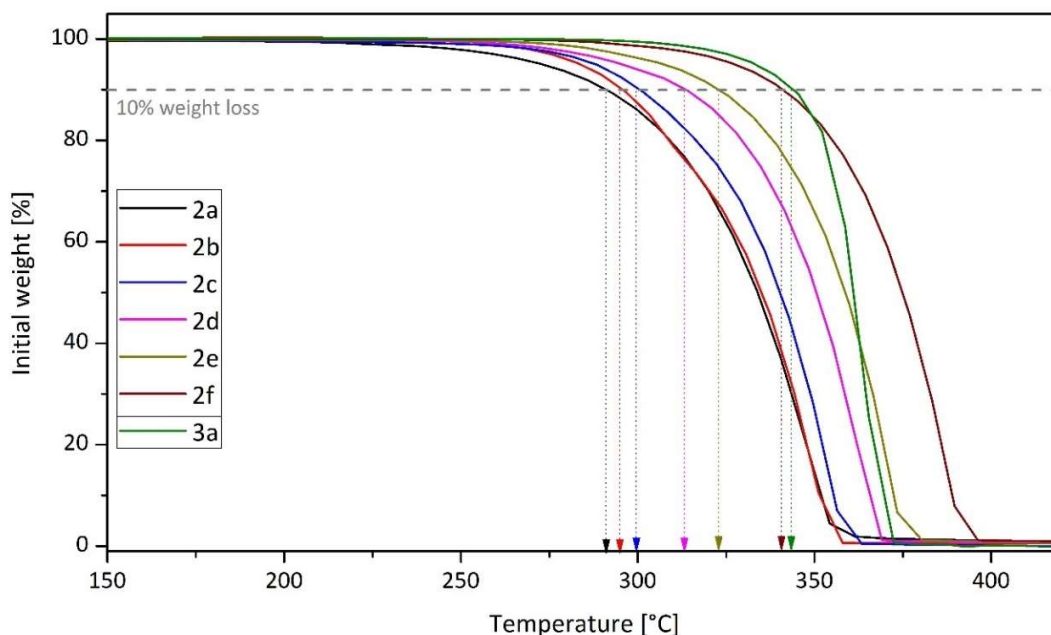


Figure 9: Thermogravimetric Analysis (heating rate: 10 k/min,  $N_2$  atmosphere) curves of the 1,3,5-benzenetrisamides **2a-f** based on trimesic acid with different length of linear perfluorinated side chains. In addition, the Thermogravimetric Analysis curve of the (1s,3s,5s)-cyclohexane-1,3,5-tricarboxylic acid based trisamide **3a** is shown (green curve). The arrows point to the temperature of 10 % initial weight loss.

### Differential Scanning Calorimetry (DSC)

The Differential Scanning Calorimetry (DSC) is a method to study the thermal transitions of a material by determination of the enthalpy change at the phase transitions. The sample in a crucible is placed in a chamber and heated or cooled with a constant heating or cooling ratio. When upon heating a transition from one into another phase occurs, the material needs more

energy. In a second chamber, a reference is heated the same way. During the measurement, both chambers are kept at the same temperature. When a transition is reached, the DSC compensates the energy to keep both chambers at the same temperature. This energy is recorded and can be displayed graphically by the measured heat flow versus the temperature. By using this method, it is possible to determine the temperatures of phase transitions upon heating and cooling. Generally, and also within this thesis, the peak maxima or minima are reported as transition temperatures.

### ***Polarized Optical Microscopy (POM)***

Polarized Optical Microscopy (POM) is based on an optical microscope in combination with two crossed polarizers. The purpose is that for a material in the isotropic phase, no light passes while for an anisotropic material different textures can be observed. A thin film of material between glass slides is placed in a hot stage and adjusted to the desired temperature. The optical appearance of mesophases shows typical textures, which often allows a determination of the type of mesophase. For example, columnar hexagonal mesophases ( $\text{Col}_h$ ) often show a dendritic or spherulitic texture (figure 10 left) while a nematic phase (N) is characterized by a typical *schlieren* texture (figure 10 right). Some phases are difficult to differentiate, such as crystalline or plastic crystalline mesophases. It is possible to observe the behavior under shear which gives conclusions about the strength of the textures and if the material is still viscous or completely solidified.

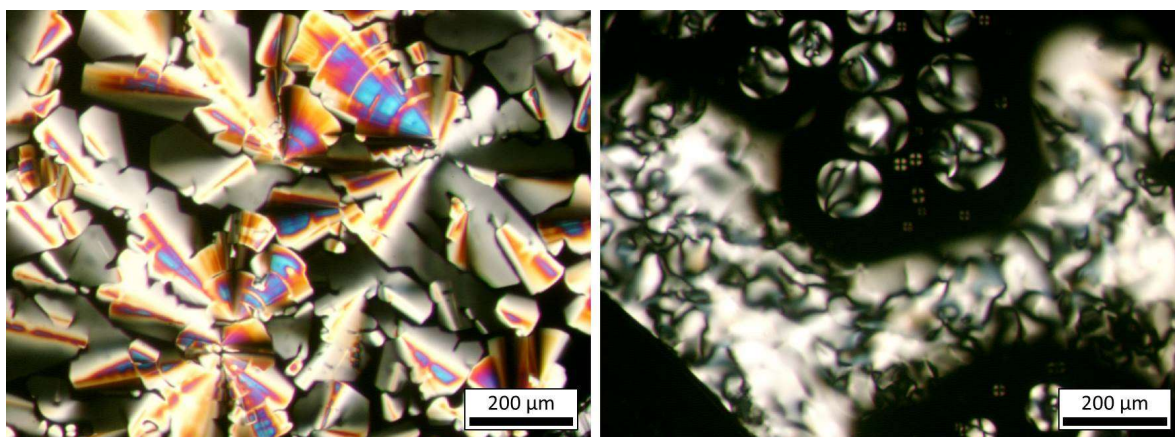


Figure 10: Polarized Optical Microscopy pictures of examples for a typical dendritic mesophase texture of 1,3,5-benzenetrisamide **2c** at 304 °C (left) and a schlieren texture of the nematic phase of 1,3,5-cyclohexanetrisamide **3a** at 325 °C (right).

### ***X-Ray Diffraction (XRD)***

The X-Ray Diffraction (XRD) technique is a method to determine one, two and three-dimensional molecular arrangements of a material and the distance between the molecules in the crystalline state but also in a mesophase. Although the order in a mesophase is not as high as in the crystalline state, it is still possible to detect significant signals. For example, in a Col<sub>h</sub> phase, there are still signals for the distances between the single molecules within the columns and the column-to-column distance itself.

The theory of the XRD method bases on diffractions in a lattice and was described by *Bragg*. The lattice distance  $d$  stands for the distance between two adjacent lattice layers. It originates from the assumption that in a perfect crystalline state, the crystal is built up by layers, which are again consisting of highly ordered atoms. These layers are called lattice planes. Because of the periodical arrangement of the atoms, there exist several lattice planes parallel to each other. If an X-ray beam strikes a crystal, it is not completely reflected but the beam penetrates through several lattice planes. All the scattered rays can interfere. Constructive interference occurs when the wavelength is an integer number  $n$  multiple of the wavelength of the light  $\lambda$ . Hence, if it is a different value, rays extinguish each other resulting in destructive interference. Constructive interference leads to signals in an X-ray diffractogram while destructive interference results in no significant signals.

By further geometrical considerations for the diffraction, *Braggs Law* applies:

$$n \lambda = 2 d_{hkl} \sin \theta$$

with  $\lambda$  as the wavelength,  $d$  the lattice distance with  $h, k, l$  as the *Miller Indices* and  $\theta$  as the *Bragg* angle describing the angle of the incident beam to the lattice plain when constructive interference is occurring. The following paragraphs are assumed from the theory chapter of the work done by Axel Eisenmann at the chair of Macromolecular Chemistry I.<sup>109</sup>

For a two-dimensional Col<sub>h</sub> phase, the lattice parameters are given with  $a = b$  and  $\gamma = 120^\circ$ . Using these parameters, the lattice distance can be calculated by the following equation:

$$\frac{1}{d_{hk0}} = \frac{1}{a} \cdot \sqrt{\frac{4}{3}(h^2 + k^2 + hk)}$$

with  $a$  as the column distance. To determine the column distance, the equation has to be changed to

$$a = d_{hk0} \cdot \sqrt{\frac{4}{3}(h^2 + k^2 + hk)}$$

which leads to the following relations for the different lattice distances of the parallel lattice plains:

$$d_{100} : d_{110} : d_{200} : d_{210} : d_{300} \dots = 1 : \frac{1}{\sqrt{3}} : \frac{1}{2} : \frac{1}{\sqrt{7}} : \frac{1}{3} \dots$$

and for the *Bragg* angles, the following relations can be used:

$$\theta_{100} : \theta_{110} : \theta_{200} : \theta_{210} : \theta_{300} \dots \approx 1 : \sqrt{3} : 2 : \sqrt{7} : 3 \dots$$

The higher the values of the *Miller Indices* the smaller is the signal intensity. This means that for a  $\text{Col}_h$  mesophase the signals for [100], [110] and [200] should be the strongest while signals of higher order are often too small to detect. In case of a columnar phase, the [100] signal describes the distance between the single columns. Sometimes it is also possible to find the [001] signal standing for the distance between the molecules within the columns, which is found at high scattering angles. If this signal is very precise, the single molecules in the column are highly ordered. On the other hand, if this signal cannot be found or is very diffuse, this means that the molecules can move and rotate in their position and are not strongly fixed. Figure 11 displays an example of the XRD measurements of the different phases of **1b** upon cooling from 250 °C to room temperature (RT). When the material is in the isotropic phase, distinct signals are not present because no long-range molecular order exists. The signals are broad and diffuse and originate from the unordered molecules. This is shown in figure 11 at a temperature of 250 °C. At 210 °C, a liquid crystalline mesophase is present. The liquid crystalline mesophase shows a few distinct signals which can be assigned. In case of compound **1b**, a  $\text{Col}_h$  phase is present. There are additional signals indicating that the phase is more ordered than a normal  $\text{Col}_h$  phase. The additional signals are mixed signals ( $h, k, l \neq 0$ ) and may originate from a three-dimensional arrangement. This leads to the conclusion that the phase is a plastic crystalline columnar hexagonal mesophase ( $\text{Col}_{hp}$ ).<sup>40,42,110</sup> The pattern at 100 °C shows more additional signals indicating that the material is in the crystalline state. The crystalline state is the most ordered state. Since this thesis concentrates on liquid crystalline phases, we did not attempt to resolve the crystal structure of the solid state.

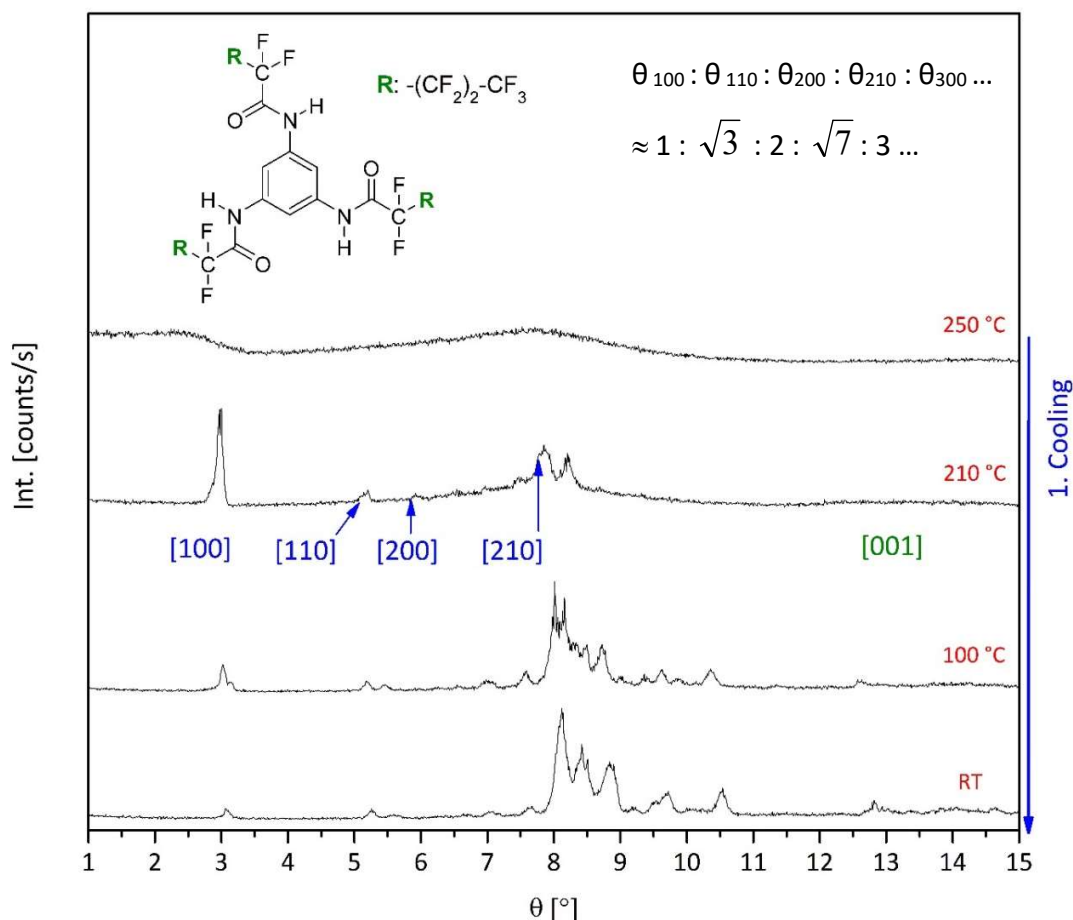


Figure 11: X-Ray Diffraction patterns of **1b** upon cooling from 250 °C to room temperature. The blue and green numerics in parenthesis stand for the signals indicating a columnar hexagonal pattern: Blue = signal found, green = signal not found.  $\theta$  = Bragg angle.

### Infrared Spectroscopy (IR)

During an Infrared Spectroscopy (IR) measurement, the sample is exposed to IR radiation over a range of different wave numbers, i.e. different energy levels. The chemical bonds within a molecule are of different strength. Depending on their strength, energy is absorbed and can stimulate the bonds to vibrate. Detecting the absorbed energy over a measurement range results in absorption spectra where the wave numbers of the absorption bands are proportional to the energy of specific bonds.<sup>111</sup>

For trisamides, the most interesting IR-bands originate from the hydrogen bonds of the amide groups. The presence of these signals at specific wave numbers proves the presence of intramolecular hydrogen bonds between the molecules. When the material changes into the isotropic phase, the hydrogen bonds break and the C=O and N-H bonds of the amide groups

can vibrate more freely. This can be observed by IR spectroscopy as the bands appear at different wave numbers. The most interesting absorption bands are:<sup>93,111,112</sup>

- *Amid A*: Valence vibration  $\nu(\text{N-H})$  at 3400 to 3300  $\text{cm}^{-1}$  in the non-hydrogen bonded form. In the hydrogen bonded form, a band appears in the range of 3300 to 3200  $\text{cm}^{-1}$ .
- *Amide-I-band*: Combination vibration with the most part of the valence vibration of  $\nu(\text{C=O})$  at 1680 to 1630  $\text{cm}^{-1}$  in the non-hydrogen bonded form. Appears at lower wave numbers in the hydrogen bonded form.
- *Amide-II-band*: Combination vibration with the most part of the deformation vibration  $\delta(\text{N-H})$  at 1550 to 1520  $\text{cm}^{-1}$  in the non-hydrogen bonded form. Appears at higher wave numbers at about 1560  $\text{cm}^{-1}$  in the hydrogen bonded form.
- A band for the vibration of the C-F-bonds  $\nu(\text{C-F})$  appear at around 1365 to 1120  $\text{cm}^{-1}$ .

As an example, figure 12 shows the IR spectrum of **1e** in the solid state at 30 °C.

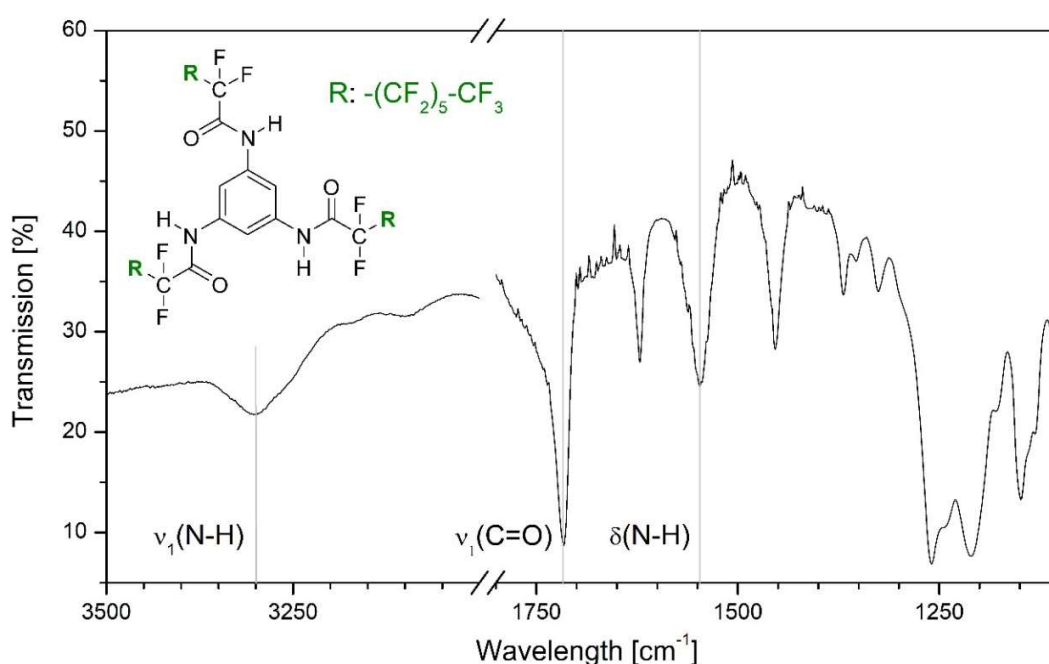


Figure 12: Infrared Spectroscopy spectrum of **1e** in the solid state at 30 °C; vertical grey lines: band positioning of the specific signals.

Here the trisamide is in a hydrogen bonded state and the most characteristic absorption bands are present. The valence vibration band  $\nu(\text{N-H})$  can be found in the region of high wavelengths at 3300  $\text{cm}^{-1}$ , while the amide-I-band, as well as the amide-II-band, are at lower

wave numbers of 1716 and 1547  $\text{cm}^{-1}$ , respectively. The amide-I-band can be found at higher wave numbers as it would be expected in the hydrogen bonded state due to the influence of the highly electronegative fluorine atoms at the  $\text{CF}_2$  group directly connected to the  $\text{C}=\text{O}$  group. Many bands can be found below 1500  $\text{cm}^{-1}$  in the fingerprint region. These bands originate mainly from all manner of bending vibrations within the molecules also from vibrations of groups with heavy atoms such as fluorine. The high amount of different vibration bands in this region causes an overlapping of the different bands, which makes it difficult to identify the single bands. The vibration of the C-F-bonds can be found in figure 12 between 1300 and 1200  $\text{cm}^{-1}$ .

Temperature dependent IR measurements were carried out for all compounds to investigate changes of the state of the hydrogen bonding at different temperatures. The IR spectra of **1e**, **2e** and **3a** will be shown and discussed in the specific subchapters as selected examples because the results are similar for all other perfluorinated BTAs. The IR spectra of the other compounds can be found in the appendix (7.2 Appendix II: Additional data).

In figure 13 the appearing and disappearing of the valence vibrations in the hydrogen bonded and non-hydrogen bonded form of  $\nu(\text{N-H})$  and  $\nu(\text{C}=\text{O})$  are shown for compound **1e** as an example. The band of the vibrational signals from the hydrogen bonded form ( $\nu_1(\text{N-H})$  and  $\nu_1(\text{C}=\text{O})$ ) are disappearing with increasing temperature which can be explained by breaking of the hydrogen bonds. The bands appear in the non-hydrogen bonded form at higher values for ( $\nu_2(\text{N-H})$  and  $\nu_2(\text{C}=\text{O})$ ).

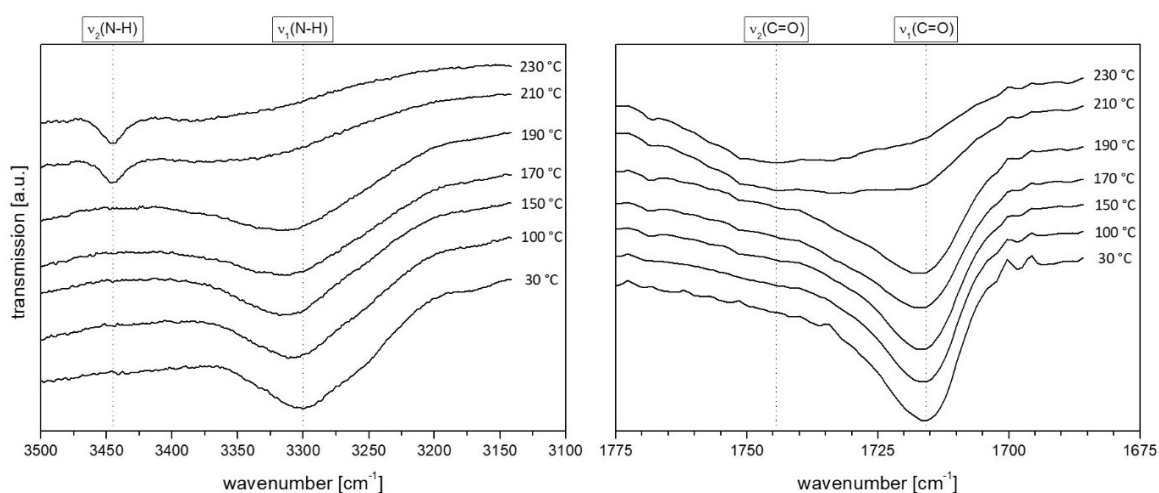
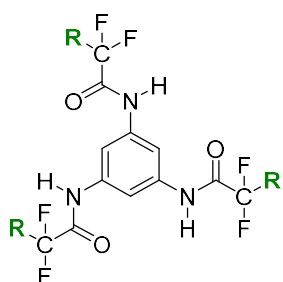


Figure 13: Infrared Spectroscopy spectra of **1e** as a function of the temperature upon heating with the  $\nu(\text{N-H})$  vibration (left) and the  $\nu(\text{C}=\text{O})$  vibration (right). Vertical dashed lines mark the absorption in the solid state ( $\nu_1$ : hydrogen bonded form), and in the isotropic phase ( $\nu_2$ : non-hydrogen bonded form)

### 3.3 Phase behavior of 1,3,5-benzenetrisamides with linear perfluorinated side chains based on 1,3,5-triaminobenzene

First, the BTAs with linear perfluorinated side chains based on 1,3,5-triaminobenzene will be discussed in detail.

#### 3.3.1 BTA based on 1,3,5-triaminobenzene with heptafluoropropyl side chains (1a)



N,N',N''-1,3,5-benzenetriyl-tris[2,2,3,3,4,4,4-heptafluorobutanamide]

R:  $-\text{CF}_2\text{-CF}_3$

**DSC:** The DSC measurements were performed with trisamide powder directly after synthesis without further thermal treatment. The measurement included three heating and cooling cycles. The first and second heating as well as the first and second cooling scans are shown in figure 14. The transition temperatures of the first heating scan may not be meaningful because a rearrangement of the molecules within the first heating after synthesis is possible. The trisamide sample was heated up in the first heating scan to a temperature of 275 °C with a heating rate of 10 K/min. After this temperature was reached, the sample was cooled down to 50 °C with a cooling rate of 10 K/min before the second heating was performed again up to 275 °C, followed by the second cooling down to 50 °C. The third heating and cooling scans were performed to ensure the results of the second heating and cooling. They are not shown here because they resulted in the same curves as the second scans. For the final comparison of the transition temperatures, the second heating transitions will be used throughout the thesis.

The second heating of the BTA based on 1,3,5-triaminobenzene with heptafluoropropyl side chains (**1a**) shows two transitions, one with low enthalpy at 152 °C (5 kJ/mol) and one with high enthalpy at 246 °C (34 kJ/mol) which can be seen in figure 14. The low enthalpy value of the first transition at 152 °C indicates only a small change in the molecular arrangement while the high enthalpy value of the second transition temperature at 246 °C could be the transition into the isotropic phase (clearing temperature  $T_c$ ).

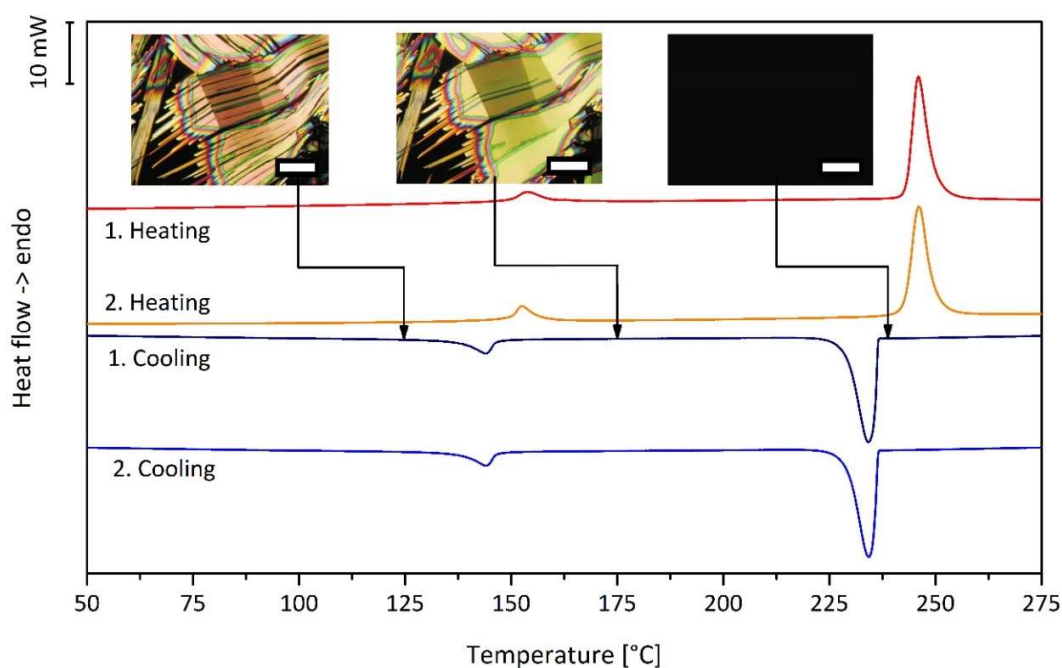


Figure 14: Differential Scanning Calorimetry heating and cooling scans of **1a** (heating and cooling rate: 10 K/min,  $N_2$  atmosphere), scale of the Polarized Optical Microscopy pictures: 200  $\mu m$ . The mesophase textures of the Polarized Optical Microscopy pictures were taken at the marked temperatures within the first cooling scan.

**POM:** Above the clearing temperature at about 250 °C, the material is in the isotropic phase, indicated that no light passes the crossed polarizers of the microscope. The molecules have no long-range order. Cooling below the first transition temperature causes the material to form birefringent platelet textures. Deformation of the material (figure 15 right) results in a bending and folding of the band-like textures demonstrating that the material is at this temperature not crystalline but liquid crystalline or plastic crystalline. Completely crystalline structures break and split under shearing force.<sup>45</sup> Further cooling below 140 °C causes crack development within the platelet structure. Deformation below this temperature causes breaking, indicating the crystalline state. This means that the transition at 144 °C (upon cooling) is a transition from the liquid crystalline or plastic crystalline mesophase into the crystalline state.

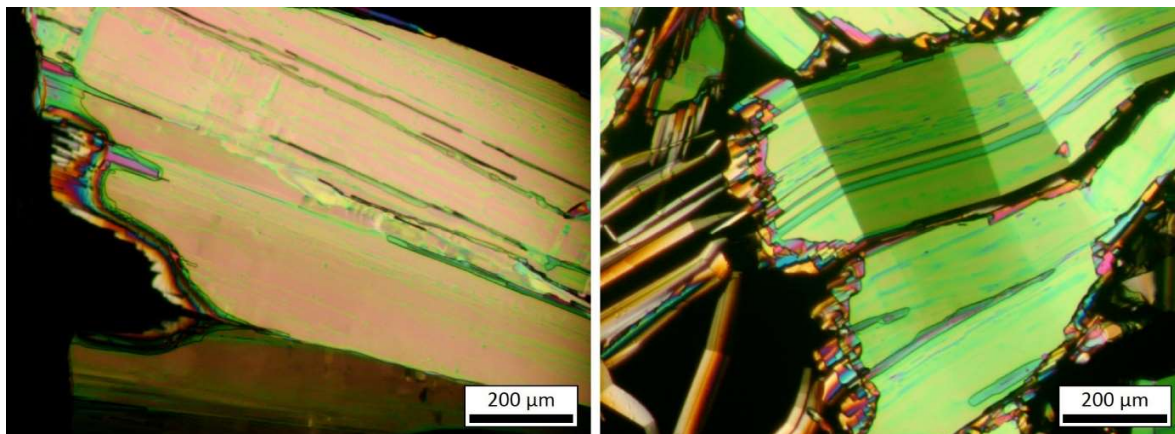


Figure 15: Polarized Optical Microscopy pictures of **1a**, taken at 235 °C before (left) and after (right) the deformation process.

**XRD:** The patterns for the heating scans at RT, 100 °C, 200 °C and 250 °C are shown in figure 16. The patterns of the scans at RT and 100 °C, where the material should be in the solid state relating to the DSC curve at first heating, comprise many signals indicating a crystalline state. The signal positions and intensities are slightly different which can be caused by reorganization of the molecules at first heating of the material directly after synthesis. However, the overall patterns are still the same. The pattern at 200 °C, where the material resides in the mesophase, is different to the ones at RT and 100 °C. There are still a lot of signals present, which indicate a structured molecular arrangement, but the intensities and positions of the signals changed compared to the crystalline pattern. This can be explained by the presence of a plastic crystalline mesophase. For the identification as a  $\text{Col}_h$  phase, the required signal positions are marked in figure 16 with green and blue numerics in parenthesis in the pattern at 200 °C. For a  $\text{Col}_h$  phase, at least the signals for [100] and [110] are required but the signal for [110] is missing. It is also not possible to identify the [001] signal which stands for the molecular distance in a columnar arrangement. The [100] signal can be calculated to a column-to-column distance of 1.37 nm for **1a**. The pattern at 250 °C is a typical pattern for a liquid material showing no distinct signals because the molecules can move freely within the melt.

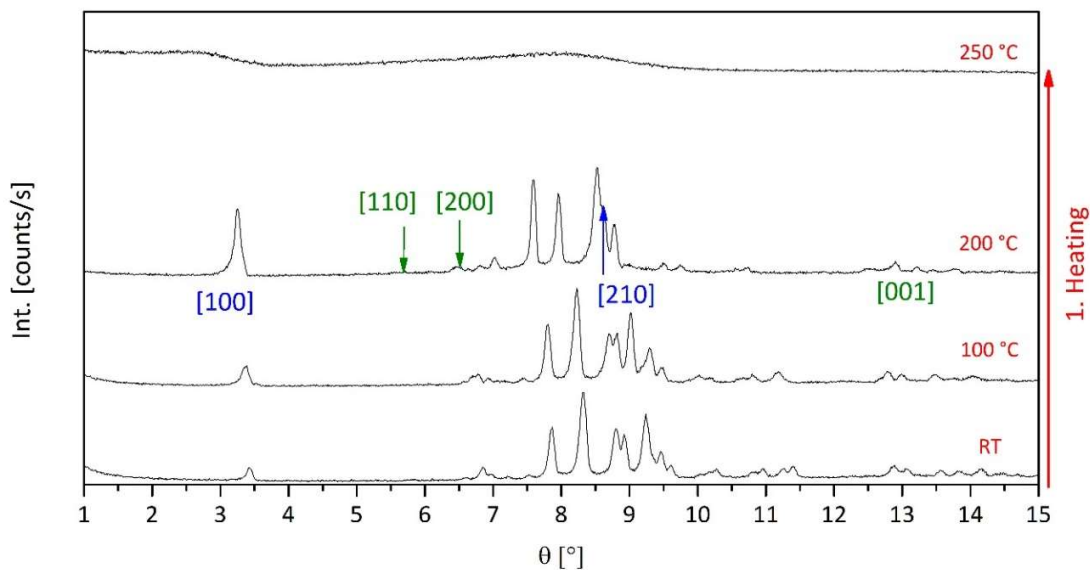
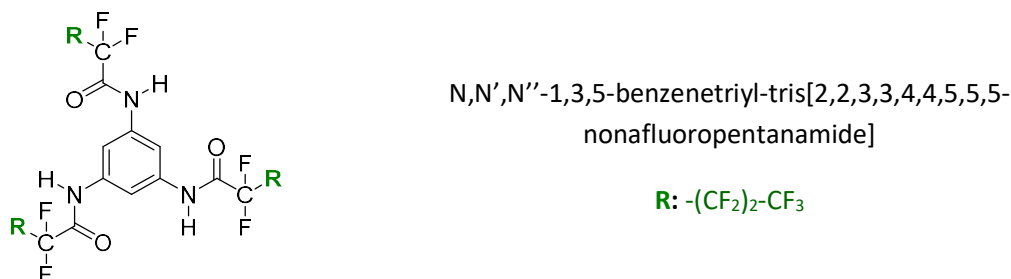


Figure 16: X-Ray Diffraction patterns of the different phases of **1a** at different temperatures upon heating. The blue and green numerics in parenthesis stand for the signals indicating a columnar hexagonal pattern: Blue = signal found, green = signal not found.  $\theta$  = Bragg angle.

The combination of the results of DSC, POM and XRD lead to the following phase characteristics of **1a** (second heating):

Cr 152 °C (5 kJ/mol) M<sub>p</sub> 246 °C (34 kJ/mol) I

### 3.3.2 BTA based on 1,3,5-triaminobenzene with nonafluorobutyl side chains (**1b**)



**DSC:** The DSC measurements were carried out by performing three heating and cooling cycles from 50 °C to 275 °C. Within the second heating curve of the BTA based on 1,3,5-triaminobenzene with nonafluorobutyl side chains (**1b**) in figure 17, two transitions can be found. The first at 177 °C with low enthalpy (5 kJ/mol) indicating the transition into a mesophase with small changes in the molecular order. The second at 228 °C with high enthalpy (22 kJ/mol) can stand for the clearing transition from the meso- into the isotropic phase.

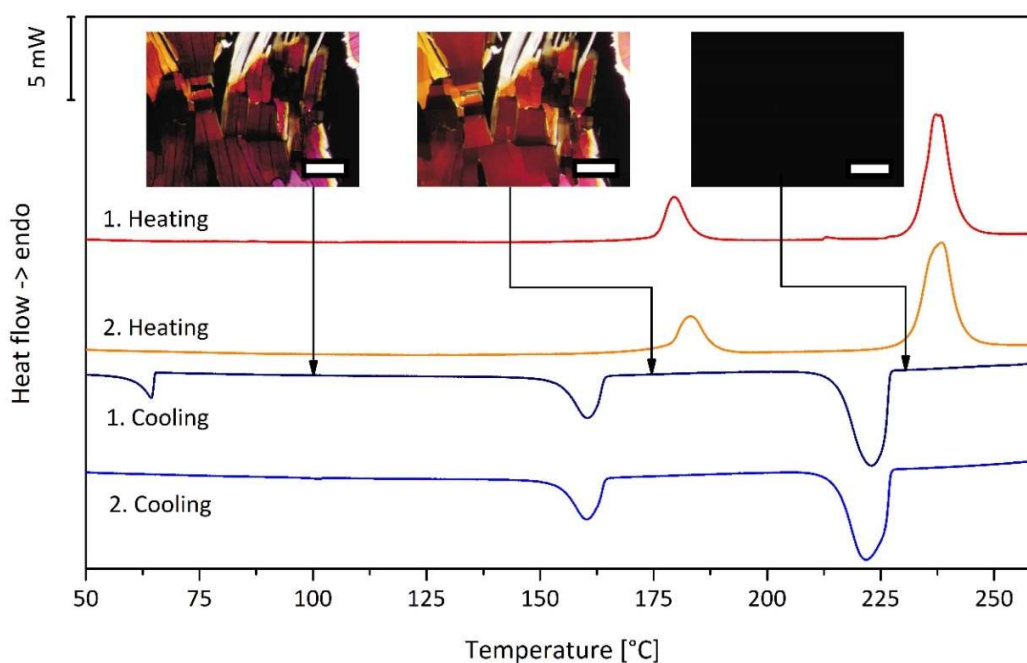


Figure 17: Differential Scanning Calorimetry heating and cooling scans of **1b** (heating and cooling rate: 10 K/min,  $\text{N}_2$  atmosphere), scale of the Polarized Optical Microscopy pictures: 200  $\mu\text{m}$ . The mesophase textures of Polarized Optical Microscopy pictures were taken at the marked temperatures within the first cooling scan.

**POM:** Cooling down from the isotropic phase at about 240 °C to the mesophase, the material rapidly forms birefringent band-like textures. Shearing at 225 °C causes the bands to bend and fold (see figure 18 right) which is a typical sign for a liquid or plastic crystalline mesophase. After cooling down below the second transition temperature at about 160 °C, shearing of the material causes breaking of the band-like textures. In conclusion, the material resides in a crystalline state at RT, changes into a liquid or plastic crystalline mesophase at the melting temperature, and changes again into the isotropic phase at the clearing temperature.

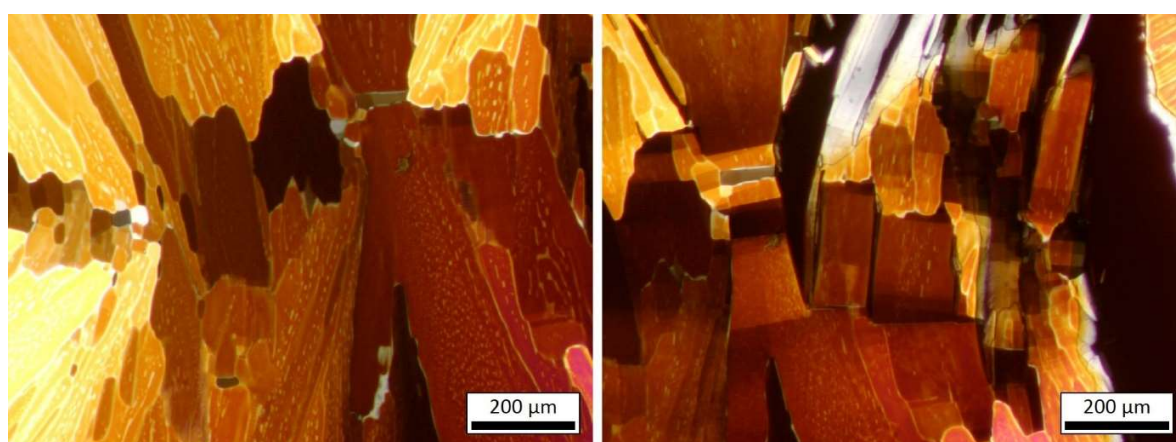


Figure 18: Polarized Optical Microscopy pictures of **1b**, taken at 225 °C before (left) and after (right) the deformation process.

**XRD:** The XRD patterns of **1b** (figure 19) at RT and 100 °C indicate a crystalline state due to the number of signals over the whole measurement range. The XRD measurement in the mesophase at 210 °C shows a diffuse halo with additional precise signals. In the case of columnar supramolecular materials, this halo can be related to a typical short-range order for liquids. In contrary to a crystalline state, the liquid crystalline phase has a lower grade of order due to the disorder in the side chains.<sup>40,42,93,110,113–116</sup> A closer look at the specific signals shows that the [100], [110], [200] and [210] signals are present which identifies a columnar hexagonal order. The additional signals are mixed signals ( $h, k, l \neq 0$ ) and originate from a three-dimensional arrangement indicating that the mesophase is a columnar hexagonal plastic crystalline mesophase (Col<sub>hp</sub>). The pattern in the isotropic phase at 250 °C is typical for liquids with a diffuse halo showing that there is no long-range order between the single molecules. The signal for [100] can be calculated to a column-to-column distance of 1.47 nm but it is not possible to clearly identify the [001] signal for the molecular distance within the columns.

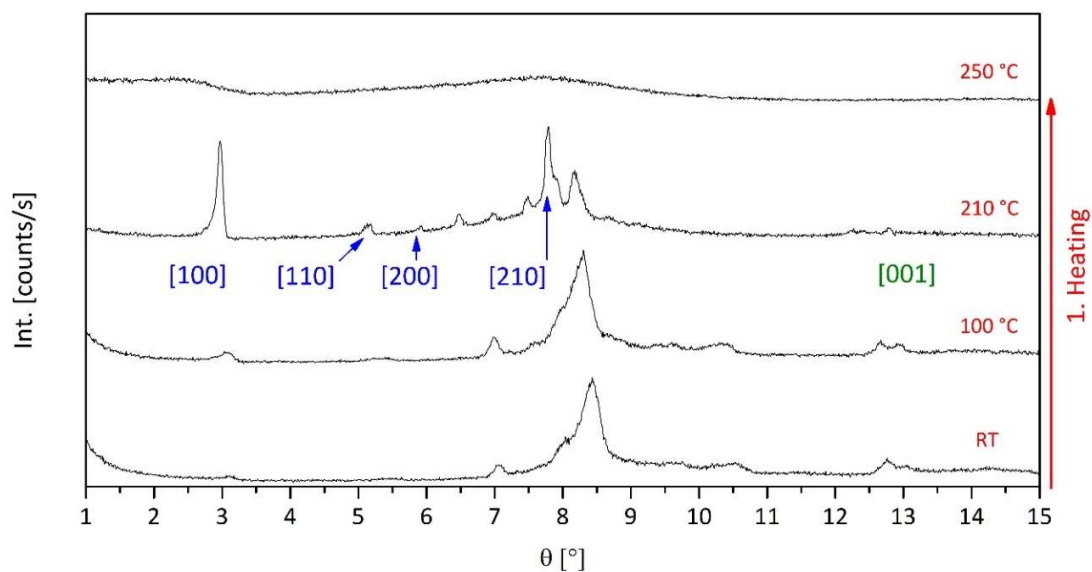
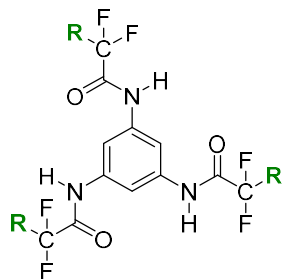


Figure 19: X-Ray Diffraction patterns of the different phases of **1b** at different temperatures upon heating. The blue and green numerics in parenthesis stand for the signals indicating a columnar hexagonal pattern: Blue = signal found, green = signal not found.  $\theta$  = Bragg angle.

The combination of the results of DSC, POM and XRD leads to the following phase characteristics of **1b** (second heating):

Cr 177 °C (5 kJ/mol) Col<sub>hp</sub> 229 °C (22 kJ/mol) I

### 3.3.3 BTA based on 1,3,5-triaminobenzene with undecafluoropentyl side chains (1c)



N,N',N''-1,3,5-benzenetriyl-tris[2,2,3,3,4,4,5,5,6,6,6-undecafluorohexanamide]



**DSC:** The DSC measurements were carried out by performing three heating and cooling cycles between temperatures of 50 °C and 240 °C. The second heating curve (see figure 20) of the BTA based 1,3,5-triaminobenzene with undecafluoropentyl side chains **1c** shows two transitions at 158 °C and 216 °C. The first at 158 °C has a medium transition enthalpy (11 kJ/mol) which may be explained by a phase transition from a crystalline state into a liquid crystalline mesophase. The enthalpy for this transition is higher than for compounds **1a** and **1b** indicating that there may not be a plastic crystalline mesophase but a liquid crystalline phase. The second transition at 216 °C has an enthalpy of 23 kJ/mol and may stand for the transition from the mesophase into the isotropic phase.

**POM:** Above the transition with higher enthalpy at 216 °C, no light passes the crossed polarizers indicating that the material is in the isotropic phase. After cooling below 200 °C, the material develops a dendritic texture, which is typical for a  $\text{Col}_h$  phase. This proves that the transition with higher enthalpy is the clearing temperature of the material. The dendritic texture can be sheared at 195 °C as it can be seen in figure 21 and causes smearing. It is possible to deform the material upon cooling down to a temperature of 135 °C. Deformation of the material below this temperature causes crystalline breaking of the textures. This indicates that the lower transition is the transition from the mesophase into the crystalline state.

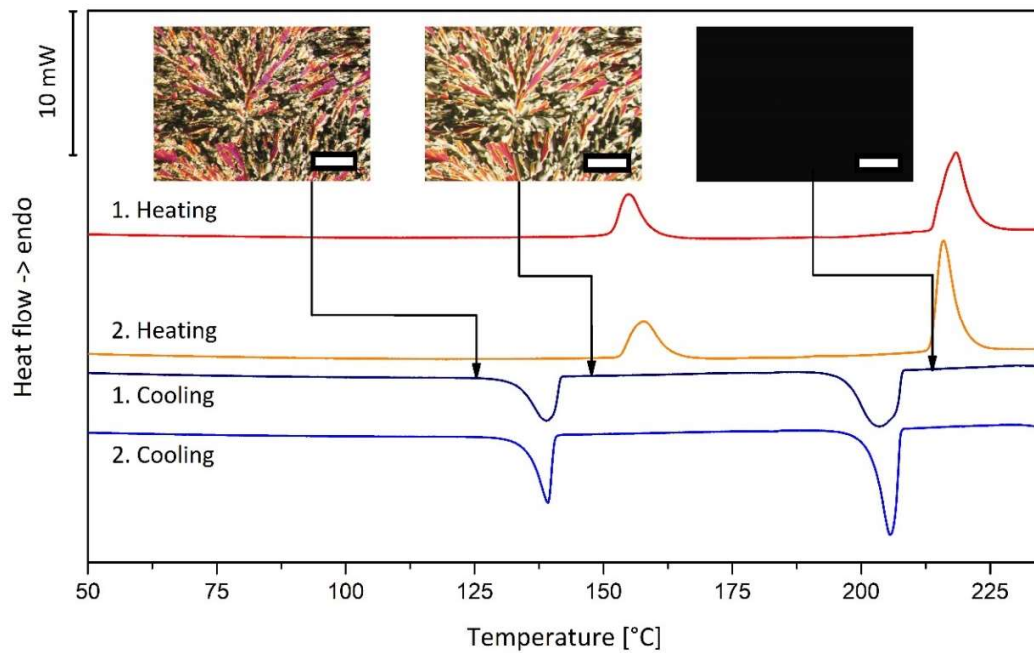


Figure 20: Differential Scanning Calorimetry heating and cooling scans of **1c** (heating and cooling rate: 10 K/min, N<sub>2</sub> atmosphere), scale of the Polarized Optical Microscopy pictures: 200  $\mu$ m. The mesophase textures of the Polarized Optical Microscopy pictures were taken at the marked temperatures within the first cooling scan.

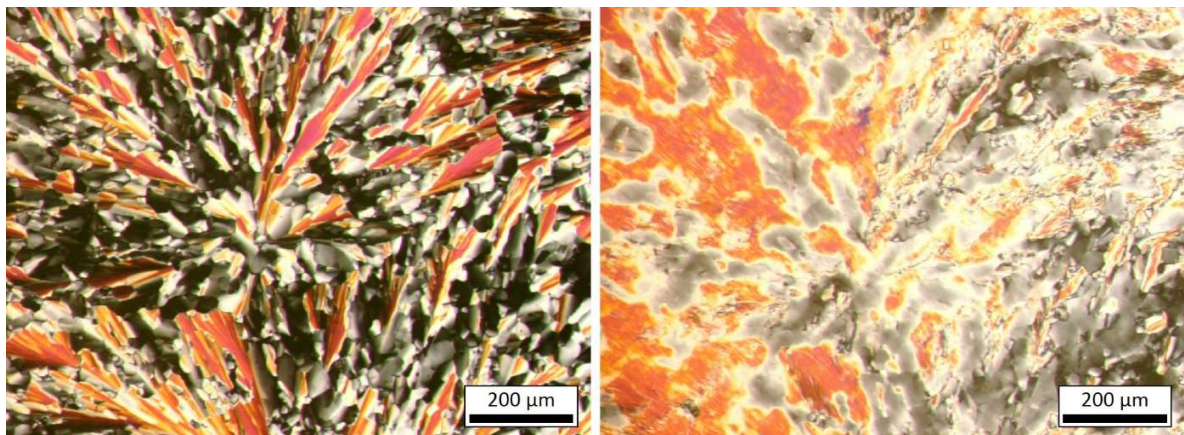


Figure 21: Polarized Optical Microscopy pictures of **1c**, taken at 195 °C before (left) and after (right) the deformation process.

**XRD:** The patterns at RT and 100 °C in figure 22 show the same signals upon heating as it could be expected after the DSC results. At 185 °C, the pattern shows three distinct signals beside the typical diffuse halo for non-ordered side chains. The distance of the signals to each other indicate the presence of a  $\text{Col}_h$  phase with the most important signals [100], [110] and the additional signal for [210]. The [200] signal cannot be clearly identified. Nevertheless, the mesophase can be identified as a  $\text{Col}_h$  phase but because of the lack of the [001] signal it is determined as a columnar hexagonal disordered ( $\text{Col}_{hd}$ ) mesophase. The signal for [100] at 185 °C can be calculated to a column-to-column distance of 1.61 nm. At 230 °C and above, the material is in the isotropic phase.

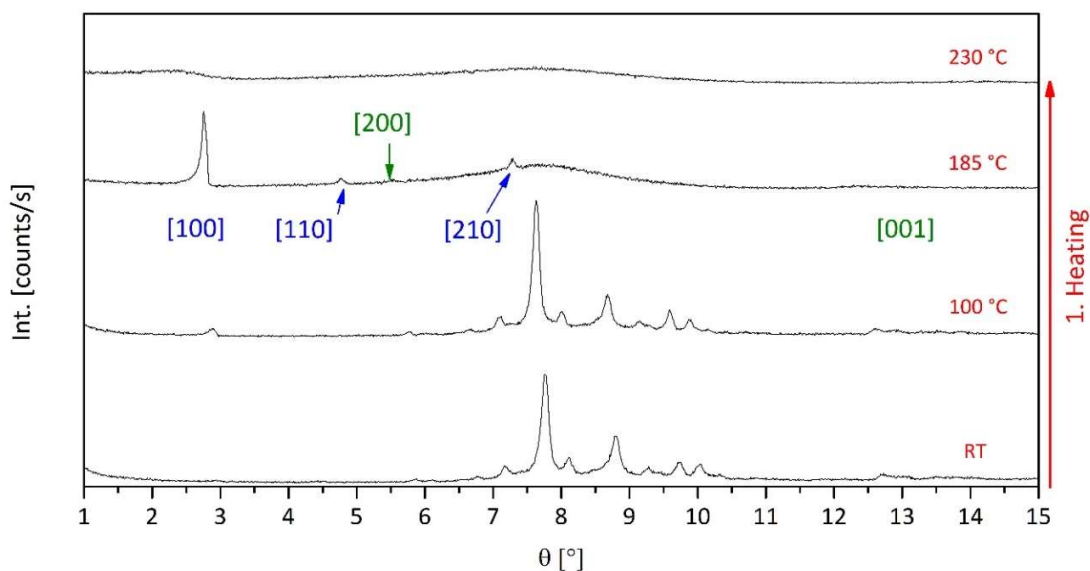
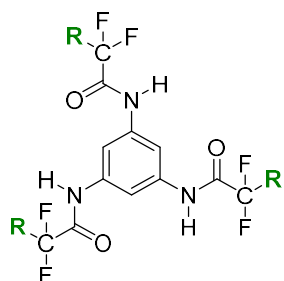


Figure 22: X-Ray Diffraction patterns of the different phases of **1c** at different temperatures upon heating. The blue and green numerics in parenthesis stand for the signals indicating a columnar hexagonal pattern. Blue = signal found, green = signal not found.  $\theta$  = Bragg angle.

The combination of the results of DSC, POM and XRD lead to the following phase characteristics of **1c** (second heating):

Cr 158 °C (11 kJ/mol)  $\text{Col}_{hd}$  216 °C (23 kJ/mol) I

### 3.3.4 BTA based on 1,3,5-triaminobenzene with tridecafluorohexyl side chains (1d)



$N,N',N''$ -1,3,5-benzenetriyl-tris[2,2,3,3,4,4,5,5,6,6,7,7,7-tridecafluoroheptanamide]

**R:**  $-(CF_2)_4-CF_3$

**DSC:** The DSC measurements were carried out by performing three heating and cooling cycles between temperatures of 50 °C and 230 °C. The second heating curve of the BTA based on 1,3,5-triaminobenzene with tridecafluorohexyl side chains (**1d**) in figure 23 shows two transitions. One is at 148 °C with a medium enthalpy (16 kJ/mol), which may be identified as the melting temperature, and another at 211 °C with a medium transition enthalpy (20 kJ/mol), which may stand for the clearing temperature. The difference in enthalpy of the two transition temperatures is not very high which can indicate that the molecular order in the different phases is not comparable to each other.

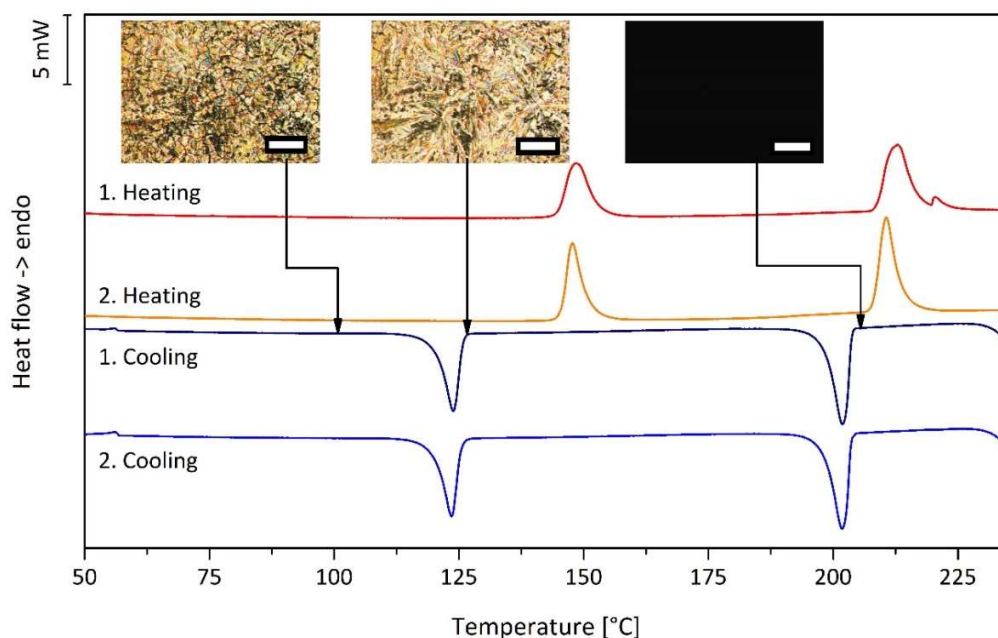


Figure 23: Differential Scanning Calorimetry heating and cooling scans of **1d** (heating and cooling rate: 10 K/min,  $N_2$  atmosphere), scale of the Polarized Optical Microscopy pictures: 200  $\mu m$ . The mesophase textures of the Polarized Optical Microscopy pictures were taken at the marked temperatures within the first cooling scan.

**POM:** Above 213 °C, the material resides in the isotropic phase. Below 200 °C upon cooling, the material forms a bilateral mixture of a dendritic and spherulitic texture indicating a Col<sub>h</sub> phase. The material can be sheared at 195 °C in the mesophase, which causes smearing of the texture. Figure 24 shows the mesophase textures before (left) and after (right) deformation at 195 °C upon cooling. Below a temperature of 124 °C, the material reaches a solid state where shearing causes crystalline breaking.

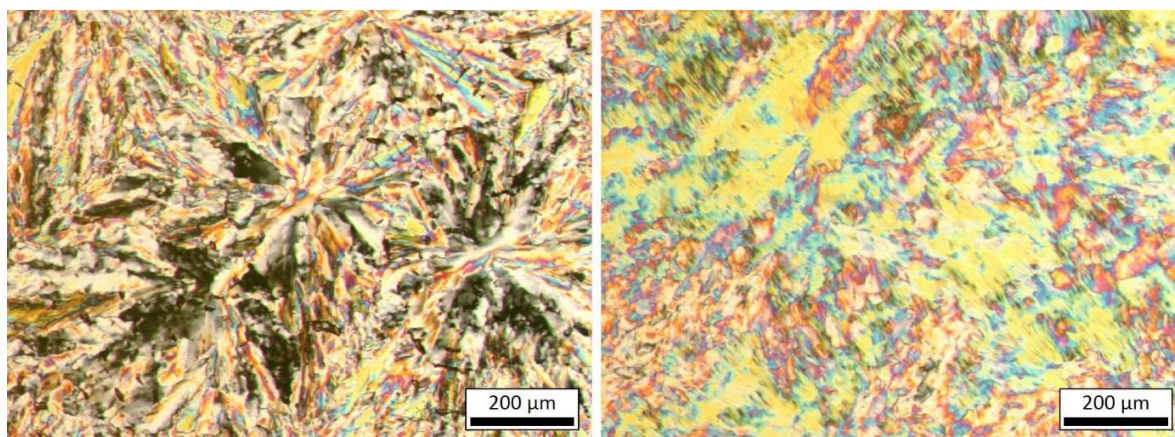


Figure 24: Polarized Optical Microscopy pictures of **1d**, taken at 195 °C before (left) and after (right) the deformation process.

**XRD:** The XRD patterns of material **1d** in figure 25 show a crystalline state pattern at RT and 100 °C with only small differences due to the rearrangement of the molecules within the first heating directly after synthesis. The pattern of the XRD scan in the mesophase at 185 °C exhibits two distinct signals which can be identified as the [100] and [110] signals. The [001] signal cannot be identified which results in a determination of the mesophase as a Col<sub>hd</sub> phase. The signal for [100] can be calculated to a column-to-column distance of 1.71 nm. The pattern at 230 °C shows a typical pattern for a liquid material, which is the same results as it was found in the DSC measurements.

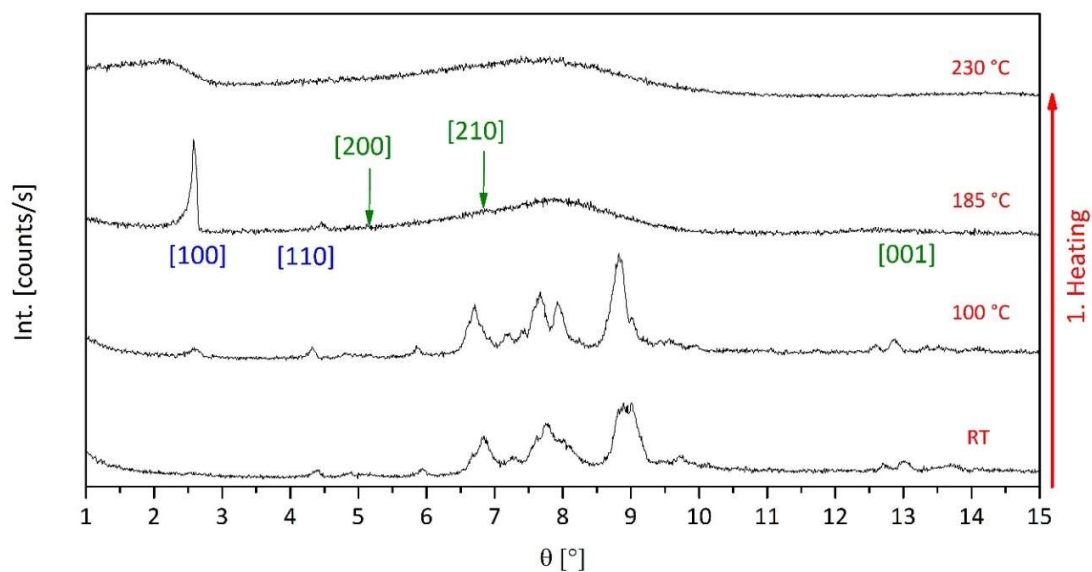
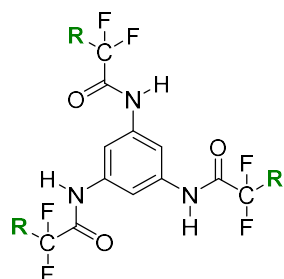


Figure 25: X-Ray Diffraction patterns of the different phases of **1d** at different temperatures upon heating. The blue and green numerics in parenthesis stand for the signals indicating a columnar hexagonal pattern: Blue = signal found, green = signal not found.  $\theta$  = Bragg angle.

The combination of the results of DSC, POM and XRD lead to the following phase characteristics of **1d** (second heating):

Cr 148 °C (16 kJ/mol) Col<sub>hd</sub> 211 °C (20 kJ/mol) I

### 3.3.5 BTA based on 1,3,5-triaminobenzene with pentadecafluoroheptyl side chains (1e)



N,N',N''-1,3,5-benzenetriyl-tris[2,2,3,3,4,4,5,5,6,6,7,7,8,8,8-pentadecafluorooctanamide]

R:  $-(\text{CF}_2)_5\text{-CF}_3$

**DSC:** The DSC measurements were carried out by performing three heating and cooling cycles between temperatures of 50 °C and 230 °C. The thermal characterization of the BTA based on 1,3,5-triaminobenzene with pentadecafluoroheptyl side chains (**1e**) in figure 26 shows two transitions within the second heating curve. One additional transition can be found in the first heating at 146 °C with an enthalpy of 5 kJ/mol but it disappears in the second heating. The two reversible transitions at 158 °C with a medium transition enthalpy of 17 kJ/mol and at 207 °C with 16 kJ/mol may stand for the melting and clearing temperature of the compound.

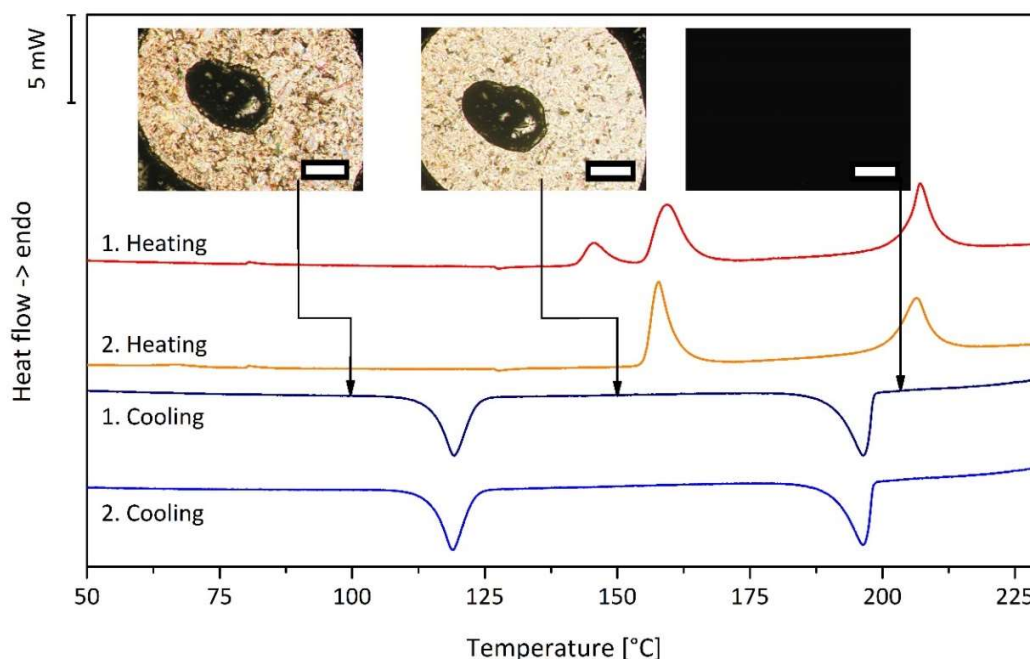


Figure 26: Differential Scanning Calorimetry heating and cooling scans of **1e** (heating and cooling rate: 10 K/min,  $\text{N}_2$  atmosphere), scale of the Polarized Optical Microscopy pictures: 200  $\mu\text{m}$ . The mesophase textures of the Polarized Optical Microscopy pictures were taken at the marked temperatures within the first cooling scan.

**POM:** At first heating the textures of the material brightens between 150 to 160 °C, which indicates the transition into a mesophase. Passing 200 °C, the material changes into the isotropic phase indicated by a black picture. Upon cooling, a spherulitic texture appears at 198 °C, which indicates a Col<sub>h</sub> phase. Deformation at 190 °C causes smearing (figure 27 right) which is possible until a temperature of 121 °C is reached. Below, shearing causes crystalline breaking of the texture.

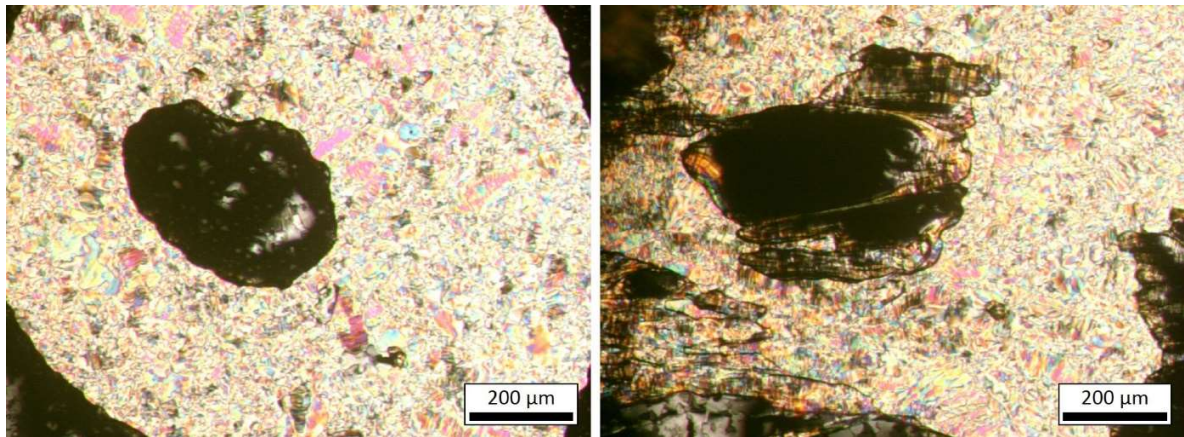


Figure 27: Polarized Optical Microscopy pictures of **1e**, taken at 190 °C before (left) and after (right) the deformation process.

**XRD:** The XRD patterns for **1e** displayed in figure 28 show a pattern of a crystalline state at RT and 100 °C, an isotropic phase at 225 °C and a Col<sub>hd</sub> phase at 185 °C. In the mesophase at 185 °C the signals for [100] and [110] can be found which allows the identification of a Col<sub>h</sub> phase but the lack of the [001] signal denotes that the order within the columns is low and the phase can be determined as a Col<sub>hd</sub> phase. The signal for [100] can be calculated to a column-to-column distance of 1.82 nm.

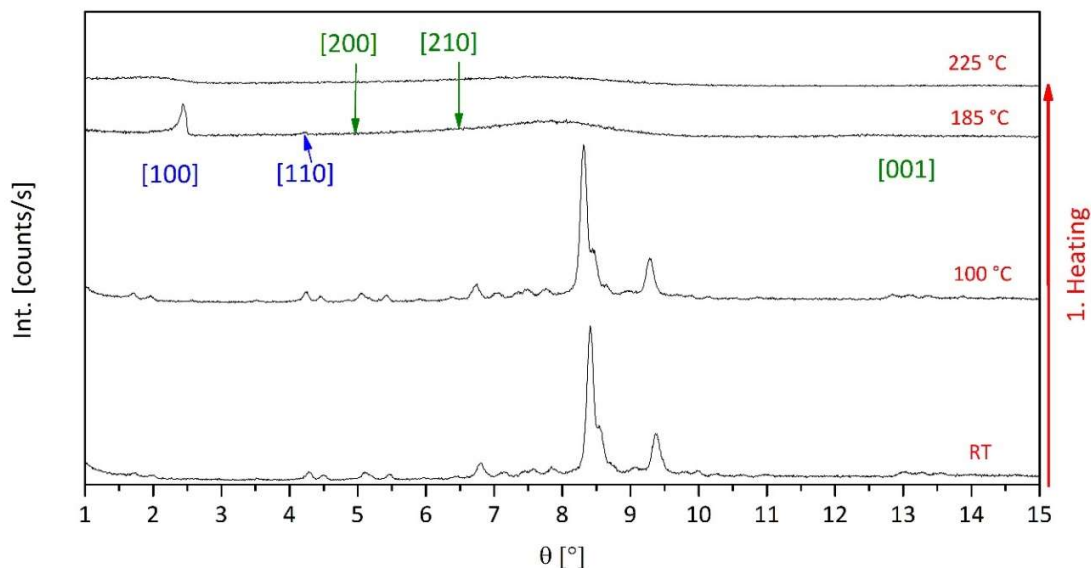


Figure 28: X-Ray Diffraction patterns of the different phases of **1e** at different temperatures upon heating. The blue and green numerics in parenthesis stand for the signals indicating a columnar hexagonal pattern. Blue = signal found, green = signal not found.  $\theta$  = Bragg angle.

The combination of the results of DSC, POM and XRD lead to the following phase characteristics of **1e** (second heating):

Cr 158 °C (17 kJ/mol) Col<sub>hd</sub> 207 °C (16 kJ/mol) I

**Temperature dependent IR-spectroscopy:** IR spectra of **1e** were taken at different temperatures from 30 °C, where the material is in the solid state, up to 230 °C in the isotropic phase. The spectra are shown in figure 29. The most important vibration bands  $\nu_1(\text{N-H})$  at 3301  $\text{cm}^{-1}$  (a),  $\nu_1(\text{C=O})$  at 1716  $\text{cm}^{-1}$  (c) and the combination vibration with the most part of the deformation vibration  $\delta(\text{N-H})$  at 1594  $\text{cm}^{-1}$  are marked with grey vertical lines. The vibrational signal  $\nu(\text{C-F})$  can also be found as a broad band between 1270 and 1170  $\text{cm}^{-1}$ . Above 200 °C, the vibrational bands of the hydrogen bonded form  $\nu_1(\text{N-H})$  and  $\nu_1(\text{C=O})$  are disappearing and the bands for the non-hydrogen bonded form  $\nu_2(\text{N-H})$  at 3444  $\text{cm}^{-1}$  (b) and  $\nu_2(\text{C=O})$  at 1744  $\text{cm}^{-1}$  (d) are appearing.

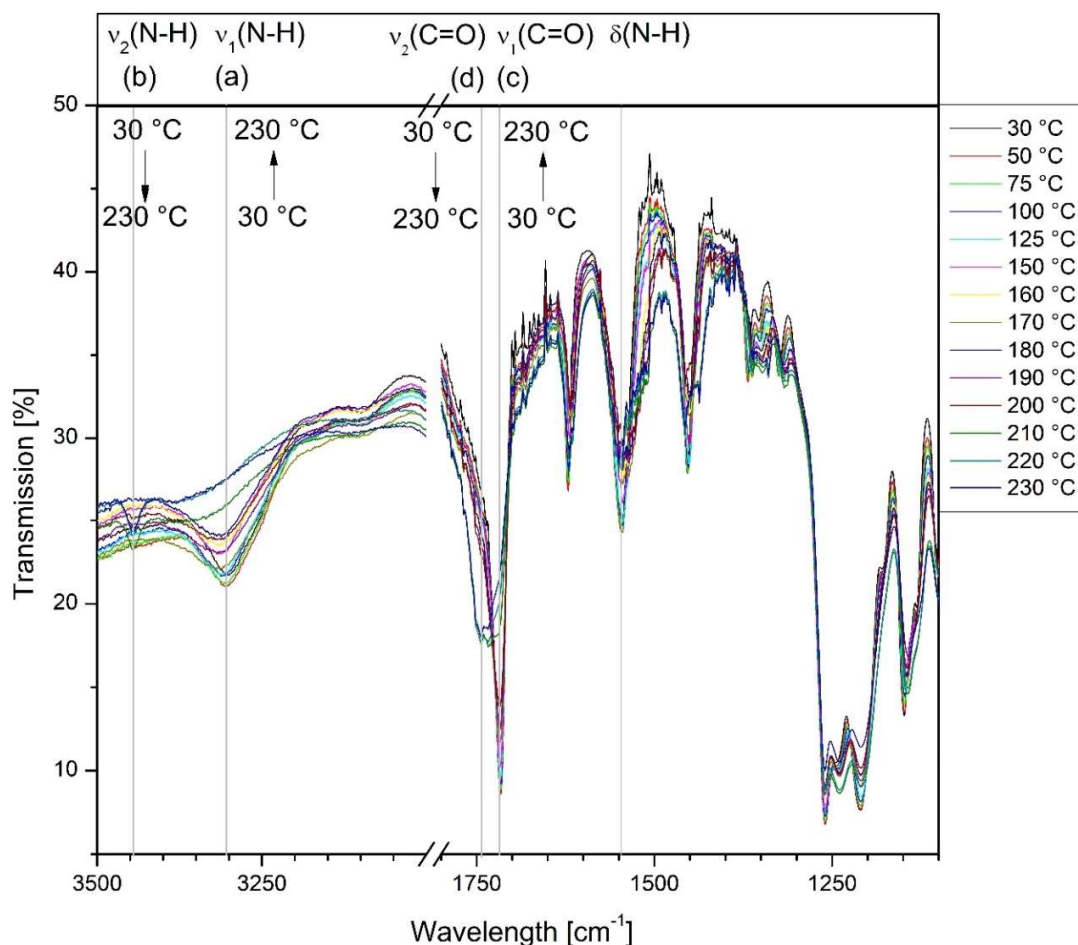


Figure 29: Infrared Spectroscopy spectra of **1e** at different temperatures upon heating; vertical grey lines: band maximum of the specific vibrational and/or deformational signals at 30 °C.

For a closer look at the change of the bands with increasing temperature, their absorbance was calculated using the baseline technique and plotted as a function of the temperature (figure 30). The baseline technique is a mathematical calculation to get a quantitative analysis of the IR spectroscopy by using the *Lambert-Beer Law*.<sup>111</sup> According to the *Lambert-Beer Law* the extinction  $E$  can be calculated by

$$E = \lg (I_0/I)$$

with  $I_0$  and  $I$  as the intensity (transmittance) of the radiation before and after passing the sample. For the exact determination of the absorption, the baseline technique must be used because there is no baseline reference. An arbitrary straight line is used as a tangent for the selected absorption band and the transmission value of the new tangent baseline at the IR spectra band maximum is used as  $I_0$ , which allows calculating the extinction. Application of

this technique on the IR spectra and plotting the calculated extinction as a function of the temperature gives conclusions about the change of the IR bands at specific wave numbers. In this thesis the vibrational bands of (C=O) and (N-H) were investigated with this technique because they represent the existence and strength of the hydrogen bonds between the BTA and CTA columns. The results for **1e** are shown in figure 30.

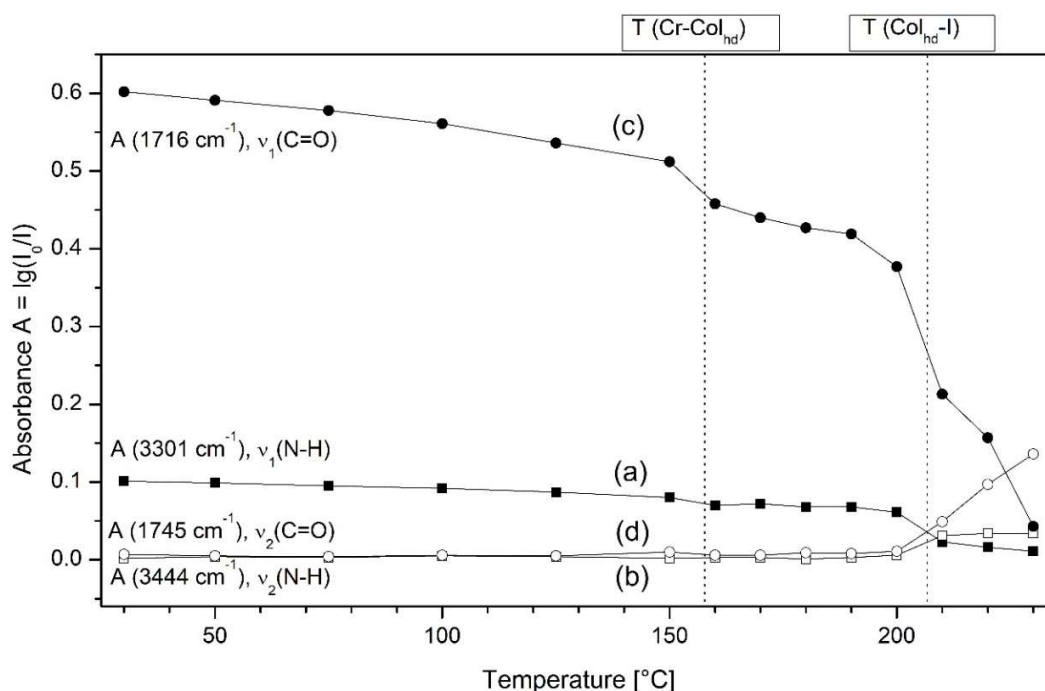
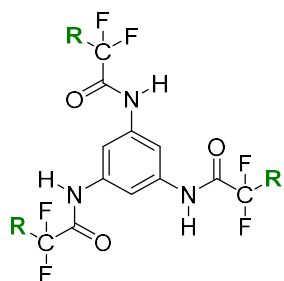


Figure 30: Infrared Spectroscopy absorbance of **1e** as a function of the temperature; circles:  $\nu(\text{C}=\text{O})$ , square:  $\nu(\text{N}-\text{H})$ , filled symbols: hydrogen bonded form  $\nu_1$ , unfilled symbols: non-hydrogen bonded form  $\nu_2$ ; vertical dashed lines: transition temperatures (second heating of DSC).

Regarding figure 30, the curves for the absorbance of the strongly hydrogen bonded form  $\nu_1(\text{N}-\text{H})$  and  $\nu_1(\text{C}=\text{O})$  are first decreasing slowly and show a shoulder at the first transition from the crystalline state into the  $\text{Col}_{\text{hd}}$  phase at about 160 °C which indicates a change in the molecular order. At about 205 °C, the absorbance decreases strongly at the transition from the mesophase into the isotropic phase due to breaking of the hydrogen bonds. At the same temperature, the signal for the non-hydrogen bonded form  $\nu_2(\text{N}-\text{H})$  and  $\nu_2(\text{C}=\text{O})$  is increasing, proving the presence of non-hydrogen bonded BTAs.

### 3.3.6 BTA based on 1,3,5-triaminobenzene with heptafluorooctyl side chains (**1f**)



N,N',N''-1,3,5-benzenetriyl-tris[2,2,3,3,4,4,5,5,6,6,7,7,8,8,9,9,9-heptafluorooctanamide]

R:  $-(CF_2)_6-CF_3$

**DSC:** The DSC measurements were carried out by performing three heating and cooling cycles between temperatures of 50 °C and 230 °C. The BTA based on 1,3,5-triaminobenzene with heptafluorooctyl side chains **1f** shows two reversible transitions upon second heating in the DSC curves displayed in figure 31. One transition can be found at 166 °C with high transition enthalpy of 23 kJ/mol, which may indicate the transition from the crystalline state into a mesophase, and another at 206 °C with medium transition enthalpy of 14 kJ/mol, which may stand for the transition from the meso- into the isotropic phase.

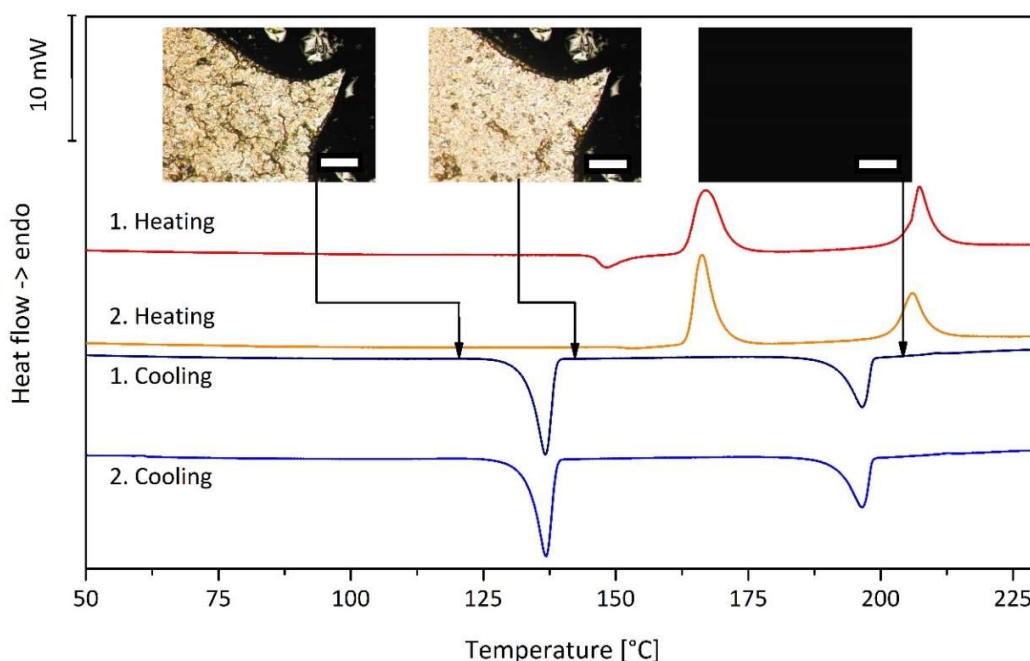


Figure 31: Differential Scanning Calorimetry heating and cooling scans of **1f** (heating and cooling rate: 10 K/min,  $N_2$  atmosphere), scale of the Polarized Optical Microscopy pictures: 200  $\mu m$ . The mesophase textures of the Polarized Optical Microscopy pictures were taken at the marked temperatures within the first cooling scan.

**POM:** Upon first heating, between 160 to 170 °C, the compound under the crossed polarizers begins to brighten which indicates the transition into a mesophase. At 196 to 200 °C the image turns black due to the transition into the isotropic phase. Upon first cooling, a fractionary spherulitic texture appears at 196 °C and the compound can be sheared indicating a liquid crystalline phase. Combined with the spherulitic texture, the mesophase can be identified as a Col<sub>h</sub> phase. Shearing of the material, as it is shown in figure 32 at 185 °C, is possible until a temperature of 136 °C is reached. Below, deformation causes crystalline breaking of the texture and thermal cracks occur with decreasing temperature. The POM results indicate that the transition at 167 °C is the melting temperature and the transition at 207 °C is the clearing temperature.

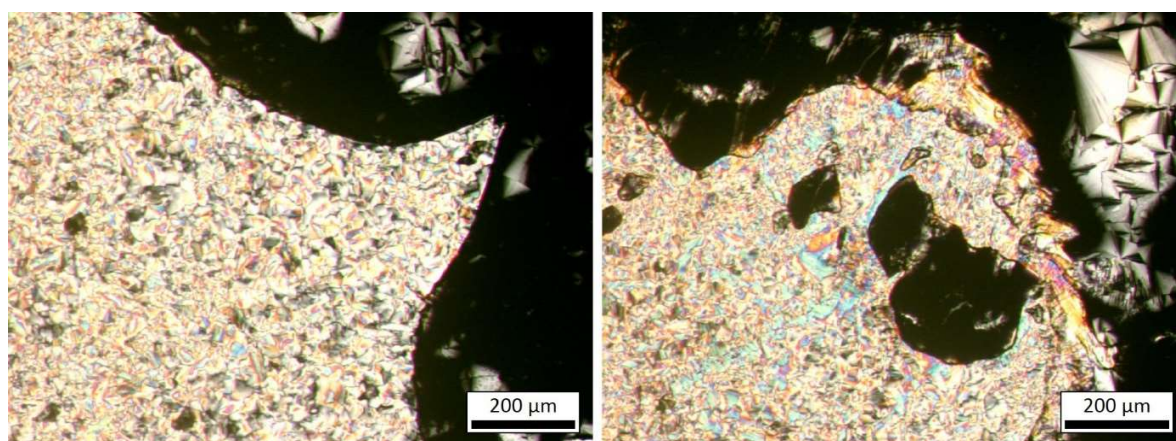


Figure 32: Polarized Optical Microscopy pictures of **1f**, taken at 185 °C before (left) and after (right) the deformation process.

**XRD:** The patterns at RT and 100 °C upon heating cannot be clearly identified as patterns standing for a crystalline state because they show no distinct signals (patterns not shown here). It is possible that the material resides in a glass-like state after synthesis, which would result in very diffuse signals. The patterns upon cooling shown in figure 33 include signals that are more distinct since the material had enough time to rearrange and build an ordered crystalline structure, which goes with the results from the POM and DSC measurements. At 185 °C, two distinct signals can be found with the distance ratio for a Col<sub>h</sub> phase, but the [001] signal cannot be found, indicating the presence of a Col<sub>hd</sub> mesophase. The signal for [100] can be calculated to a column-to-column distance of 1.90 nm. The pattern at 225 °C shows a typical isotropic phase appearance.

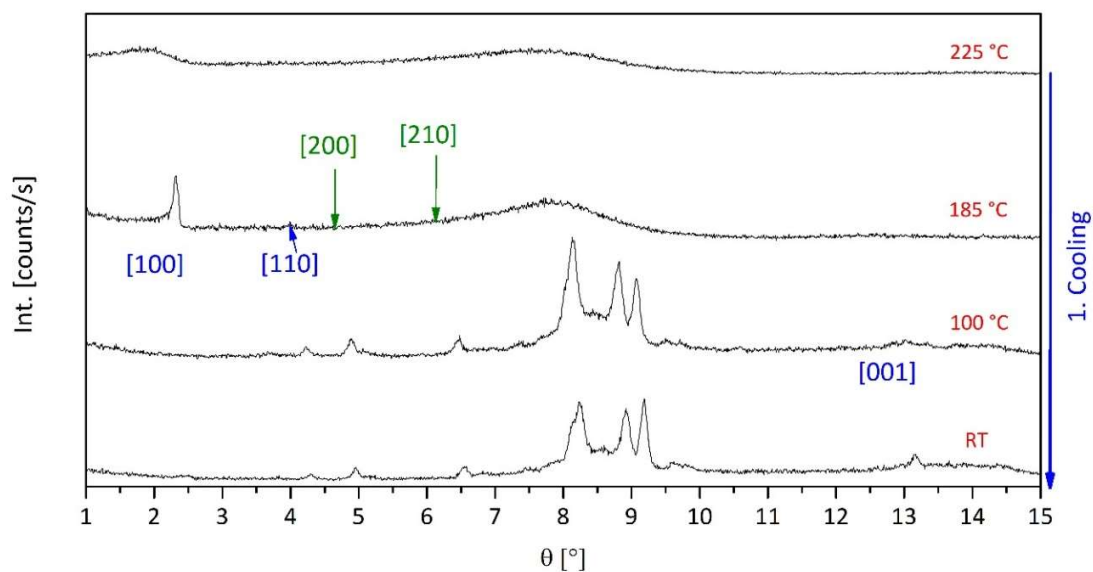


Figure 33: X-Ray Diffraction patterns of the different phases of **1f** at different temperatures upon cooling. The blue and green numerics in parenthesis stand for the signals indicating a columnar hexagonal pattern: Blue = signal found, green = signal not found.  $\theta$  = Bragg angle.

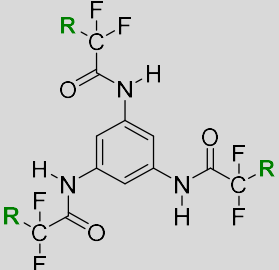
The combination of the results of DSC, POM and XRD lead to the following phase characteristics of **1f** (second heating):

Cr 166 °C (23 kJ/mol) Col<sub>hd</sub> 206 °C (14 kJ/mol) I

### 3.3.7 Comparison within this series

In the following, the results of the BTA series based on 1,3,5-triaminobenzene with linear perfluorinated side chains will be compared in terms of mesophase behavior, column-to-column distance, transition temperatures, and mesophase range. The transition temperatures were taken from the DSC curves of the second heating, and are summarized with their corresponding transition enthalpy in table 3.

Table 3: Phase behavior of 1,3,5-benzenetrisamides based on 1,3,5-triaminobenzene with linear perfluorinated side chains (**1a-f**).

 <b>R:</b>	Transition temperatures and enthalpy values, DSC, second heating (10 k/min)	
-CF <sub>2</sub> -CF <sub>3</sub>	<b>1a</b>	Cr 152 °C (5 kJ/mol) M <sub>p</sub> 246 °C (34 kJ/mol) I
-(CF <sub>2</sub> ) <sub>2</sub> -CF <sub>3</sub>	<b>1b</b>	Cr 177 °C (5 kJ/mol) Col <sub>hp</sub> 229 °C (22 kJ/mol) I
-(CF <sub>2</sub> ) <sub>3</sub> -CF <sub>3</sub>	<b>1c</b>	Cr 158 °C (11 kJ/mol) Col <sub>hd</sub> 216 °C (23 kJ/mol) I
-(CF <sub>2</sub> ) <sub>4</sub> -CF <sub>3</sub>	<b>1d</b>	Cr 149 °C (16 kJ/mol) Col <sub>hd</sub> 213 °C (20 kJ/mol) I
-(CF <sub>2</sub> ) <sub>5</sub> -CF <sub>3</sub>	<b>1e</b>	Cr 158 °C (17 kJ/mol) Col <sub>hd</sub> 207 °C (16 kJ/mol) I
-(CF <sub>2</sub> ) <sub>6</sub> -CF <sub>3</sub>	<b>1f</b>	Cr 166 °C (23 kJ/mol) Col <sub>hd</sub> 206 °C (14 kJ/mol) I

Cr: crystalline state, Col: columnar mesophase, M: unidentified mesophase, I: isotropic phase, d: disordered liquid crystalline, h: hexagonal, p: plastic crystalline.

Trisamides **1a** and **1b** show *plastic crystalline mesophases* between the crystalline state and the isotropic phase. The plastic crystalline mesophase of **1a** cannot be identified as a columnar phase because the required signals in the XRD measurement were not detected.

The XRD scans of **1b** show the typical signals for a Col<sub>h</sub> phase. The trisamides **1c**, **1d**, **1e** and **1f** with longer side chains show *liquid crystalline phases* in form of a Col<sub>hd</sub> phase. POM investigations upon cooling show the development of dendritic or partially spherulitic textures, which can be sheared, proving the liquid crystalline character. All mesophases were identified as hexagonal disordered phases because the required [001] signal, pointing to a regular molecular distance in the columns, was not detected by XRD.

The XRD patterns contain signals, which originate from distances between scattering points of the molecular order. The distances can be calculated from the scattering angles. For a columnar phase, the distance of the [100] signal represents the *distance between the columns*. Figure 34 summarizes the calculated distances from the [100] signals of the BTAs based on the 1,3,5-triaminobenzene core. The distance between the columns increases with the side chain length. The distance is increasing linearly with each additional CF<sub>2</sub> group by a value of about 0.1 nm. For **1a** the calculated distance of the [100] signal fits perfectly to the linear increase of the column distances of the whole BTA series indicating that this material also exhibits a columnar phase.

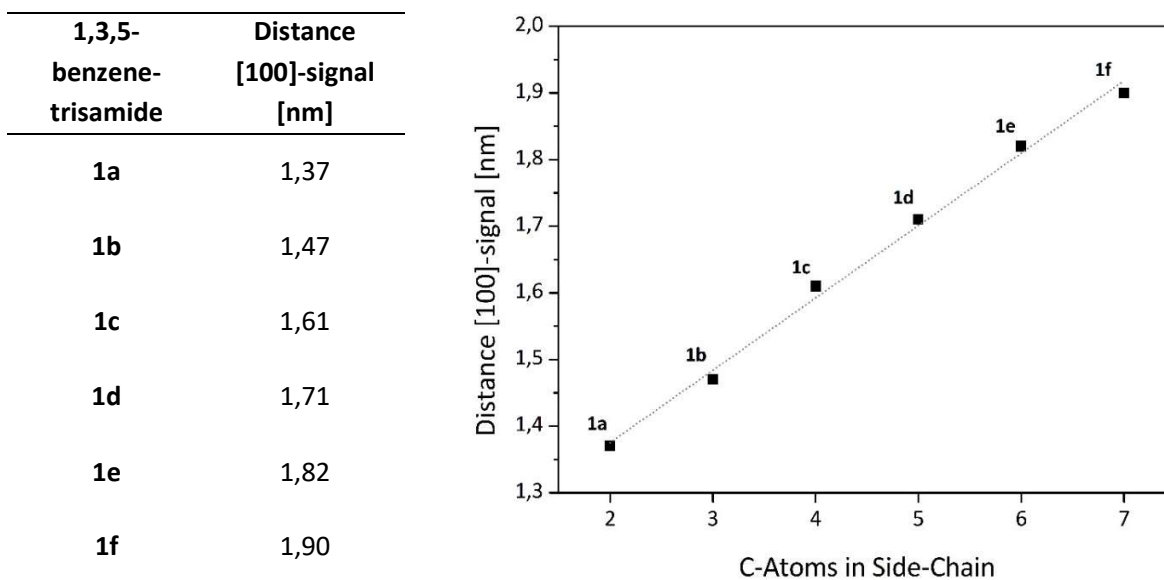


Figure 34: Distances from the [100] signal of the X-Ray Diffraction patterns at 200 °C (**1a**), 210 °C (**1b**) and 185 °C (**1c** to **1f**), which stands for the column-to-column distance in a columnar mesophase, dependent on the side chain length.

The *phase transition temperatures* dependent on the linear perfluorinated side chain length can be seen in figure 35. The clearing temperatures are decreasing with increasing side chain length from 250 °C for **1a** down to 225 °C for **1f**. Compounds **1a** and **1b**, which showed plastic crystalline mesophases, have 20 to 30 degrees higher clearing temperatures than the other BTAs with liquid crystalline phases. The clearing temperature change of the compounds **1c**, **1d**, **1e** and **1f** is only about 9 degrees. With respect to the melting temperatures, a clear tendency cannot be found. All melting temperatures are in the range from 149 to 177 °C.

With a temperature range of 94 degrees, **1a** has the broadest *mesophase range*. For compound **1b**, the range is 62 degrees. For the compounds **1c** and **1d**, it is nearly constant with 58 degrees and 64 degrees, respectively. For **1e**, it decreases to 49 degrees and for **1f**, the mesophase range is only 40 degrees.

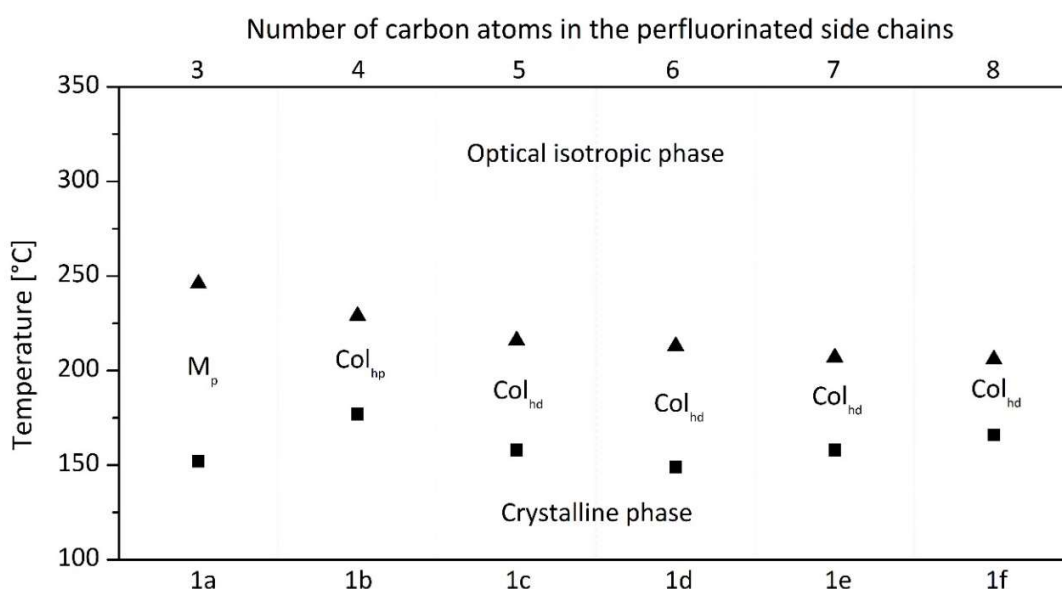


Figure 35: Phase transition temperatures (Differential Scanning Calorimetry, second heating) of 1,3,5-benzenetrisamides **1a-f** based on 1,3,5-triaminobenzene with linear perfluorinated side chains dependent on the side chain length. ▲: clearing temperature, ■: melting temperature, Col: columnar mesophase, M: unidentified mesophase, p: plastic crystalline, d: disordered liquid crystalline, h: hexagonal.

Figure 36 compares the transition enthalpy values of the second heating curves of the DSC as function of the perfluorinated side chain length. Both trisamides **1a** and **1b** show low *transition enthalpy* for the melting transition and high values for the clearing transition. This supports the mesophase identification as plastic crystalline mesophases with a higher ordered phase. Compound **1c** with a  $Col_{hd}$  mesophase has a transition enthalpy of 11 kJ/mol

for the melting transition and 23 kJ/mol for the clearing transition. Compared to **1c** the transition enthalpy value difference for **1d** between the melting and the clearing temperature is decreasing from 12 kJ/mol to 4 kJ/mol. For **1e**, both values are nearly the same. For the 1,3,5-benzenetrisamide with the longest side chains **1f**, the enthalpy value of the clearing transitions is higher than that of the melting transition. With increasing perfluorinated side chain length the molecular order in the mesophase decreases proven by the decreasing enthalpies of the clearing temperature and the increasing enthalpies of the melting temperature.

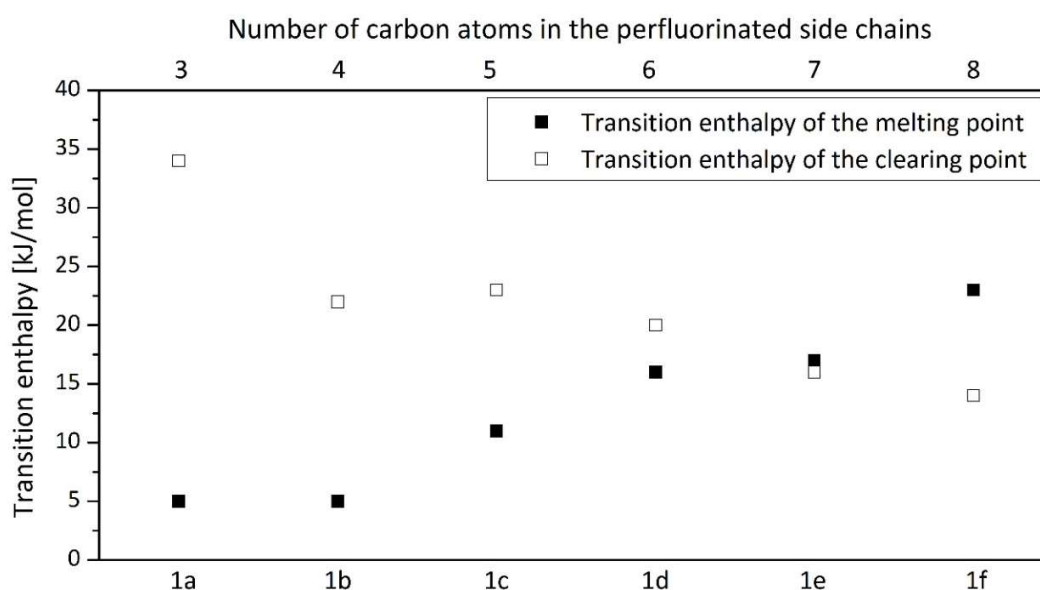
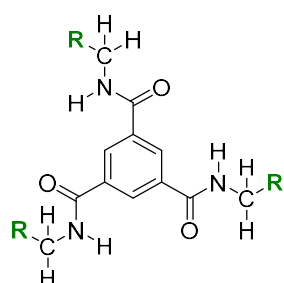


Figure 36: Comparison of the transition enthalpy values of 1,3,5-benzenetrisamides based on 1,3,5-triaminobenzene with linear perfluorinated side chains dependent on the side chain length (Differential Scanning Calorimetry, second heating).

### 3.4 Phase behavior of 1,3,5-benzenetrisamides with linear perfluorinated side chains based on trimesic acid

After discussion of the BTAs based on 1,3,5-triaminobenzene, the BTAs based on trimesic acid with linear perfluorinated side chains **2a-f** will be considered. The XRD measurements for the BTAs based on trimesic acid could only be performed up to a temperature of 250 °C because of the temperature limitation of the equipment. Therefore, the compounds never passed the clearing temperature within the XRD measurement and did not reach the isotropic state.

#### 3.4.1 BTA based on trimesic acid with pentafluoropropyl side chains (**2a**)



N,N',N''-tris[2,2,3,3,3-pentafluoropropyl]-  
1,3,5-benzenetricarboxamide

R: -CF<sub>2</sub>-CF<sub>3</sub>

**DSC:** The DSC measurements were carried out by performing three heating and cooling cycles between temperatures of 50 °C and 315 °C. The DSC curve of the BTA based on trimesic acid with pentafluoropropyl side chains (**2a**) displayed in figure 37 shows one transition at 294 °C with a high transition enthalpy of 38 kJ/mol at second heating. Closer examination reveals another transition at 247 °C with very low enthalpy 0.3 kJ/mol, which can also be found in the first cooling scan at 216 °C. It can be expected that the transition with higher enthalpy stands for the transition into the isotropic phase.

**POM:** Upon first heating, no change of the texture can be observed until the compound reaches the temperature for the isotropic phase between 288 to 292 °C. Upon cooling, **1a** slowly develops band-like textures which first appear at 280 °C. Figure 38 shows a band-like texture. Shearing at 250 °C causes bending and folding indicating a plastic crystalline mesophase. At 150 °C upon cooling, the texture changes in color and has a crystalline appearance which can be seen in the POM picture in figure 37. Deformation at this temperature causes breaking of the band texture, pointing to a crystalline state.

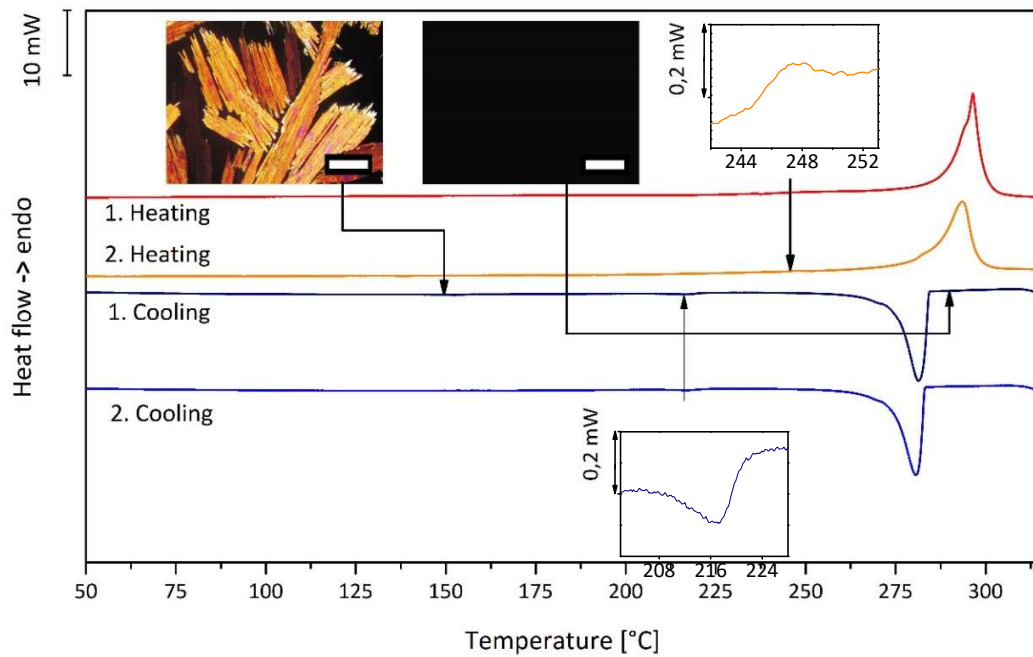


Figure 37: Differential Scanning Calorimetry heating and cooling scans of **2a** (heating and cooling rate: 10 K/min,  $N_2$  atmosphere), scale of the Polarized Optical Microscopy pictures: 200  $\mu m$ . The mesophase textures of the Polarized Optical Microscopy pictures were taken at the marked temperatures within the first cooling scan.

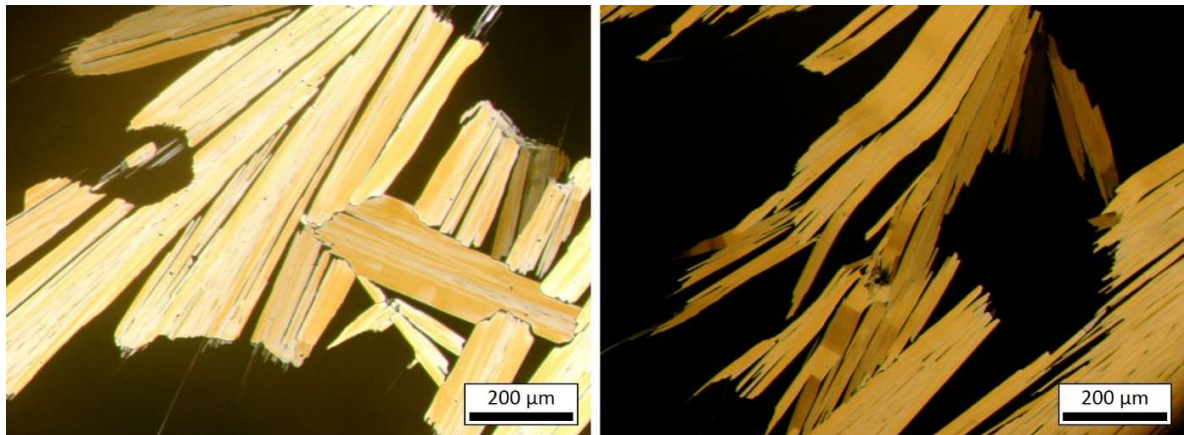


Figure 38: Polarized Optical Microscopy pictures of **2a**, taken at 280 °C before (left) and at 250 °C after (right) the deformation process.

**XRD:** The XRD scans of **1a** upon heating and cooling can be seen in figure 39 and they show different patterns.

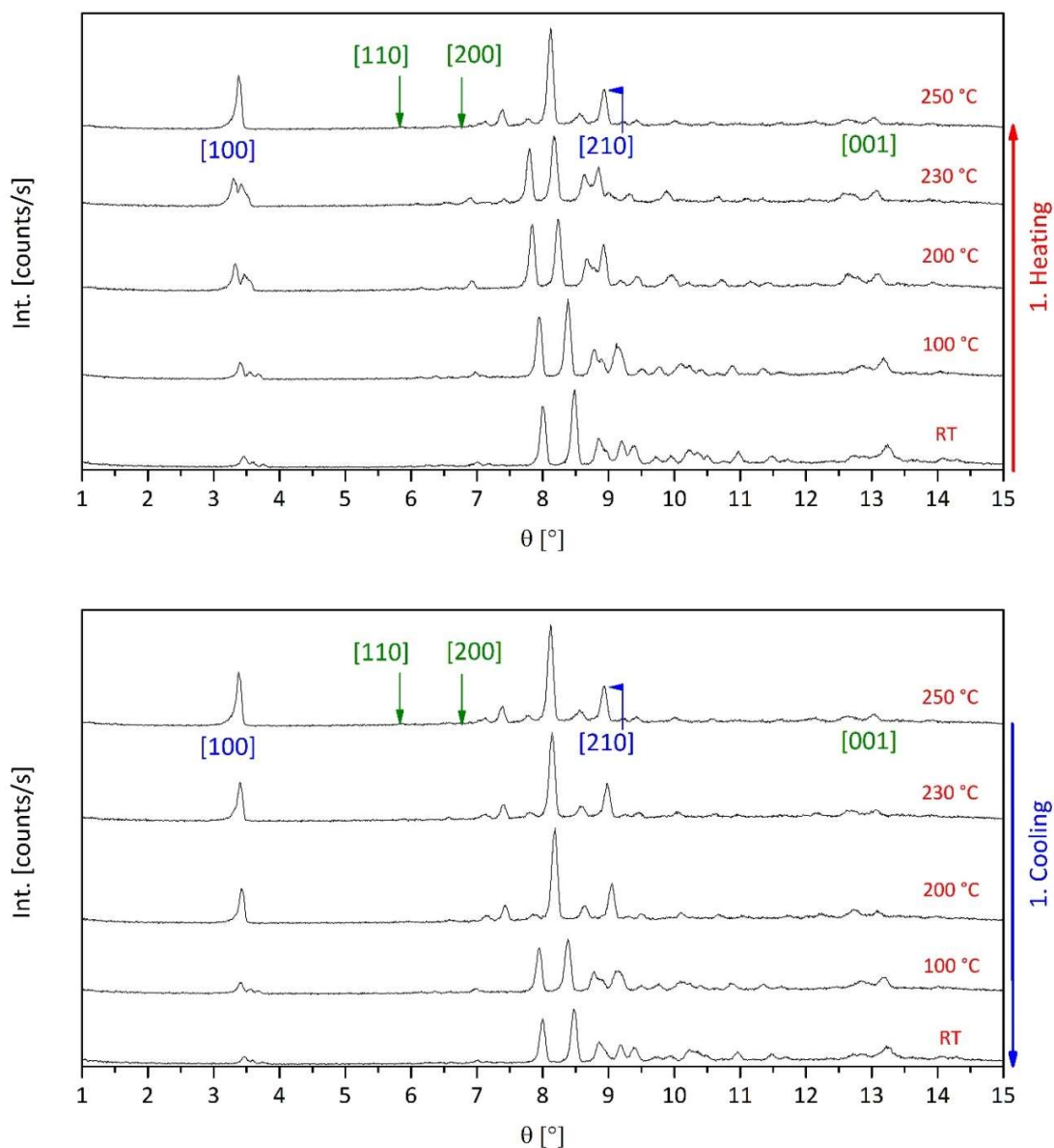


Figure 39: X-Ray Diffraction patterns of the different phases of **2a** at different temperatures upon heating and cooling. The blue and green numerics in parenthesis stand for the signals indicating a columnar hexagonal pattern: Blue = signal found, green = signal not found.  $\theta$  = Bragg angle.

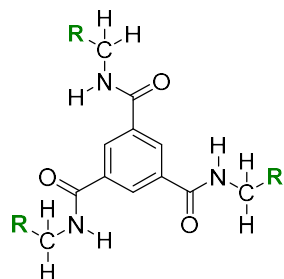
Beginning with the pattern at RT of the heating procedure, a lot of signals can be found indicating a crystalline state. Upon heating, the patterns at 100, 200 and 230 °C show only

slight differences due to slow reorganization processes of the material within first heating after synthesis. The pattern at 250 °C, a liquid or plastic crystalline mesophase identified from the DSC and POM characterizations, is different but still a few similar signals to the patterns at lower temperatures can be found indicating that the molecular order of the crystalline state and the mesophase are not very different which indicates the presence of a plastic crystalline mesophase. This can also explain the very low enthalpy value of the transition temperature at about 247 °C. In the mesophase at 250 °C, only the [100] and the [210] signals can be identified which do not allow a clear determination of a Col<sub>h</sub> phase. The signal for [100] can be calculated to a column-to-column distance of 1.31 nm. It is also not possible to clearly identify the [001] signal and therefore the molecular distance. The scans upon cooling show that the pattern of the XRD measurement within the mesophase stays the same until the temperature falls below 200 °C. At a temperature of 100 °C, the pattern looks similar to the one at RT but different to the patterns measured at higher temperature. In the DSC scan at first cooling, the transition could be found at 216 °C but the XRD pattern at 200 °C still shows the same signals as in the mesophase. This may be explained by a very slow transition.

*The combination of the results of DSC, POM and XRD lead to the following phase characteristics of **2a** (second heating):*

Cr 247 °C (0.3 kJ/mol) M<sub>p</sub> 294 °C (38 kJ/mol) I

### 3.4.2 BTA based on trimesic acid with heptafluorobutyl side chains (**2b**)



N,N',N''-tris[2,2,3,3,4,4,4-heptafluorobutyl]-  
1,3,5-benzenetricarboxamide



**DSC:** The DSC measurements were carried out by performing three heating and cooling cycles between temperatures of 50 °C and 340 °C. The DSC curves of the BTA based on trimesic acid with heptafluorobutyl side chains (**2b**) are displayed in figure 40. The second heating curve shows one transition at 318 °C with a high transition enthalpy of 53 kJ/mol. It can be expected that it is the transition from a highly ordered phase or the crystalline state into the isotropic phase.

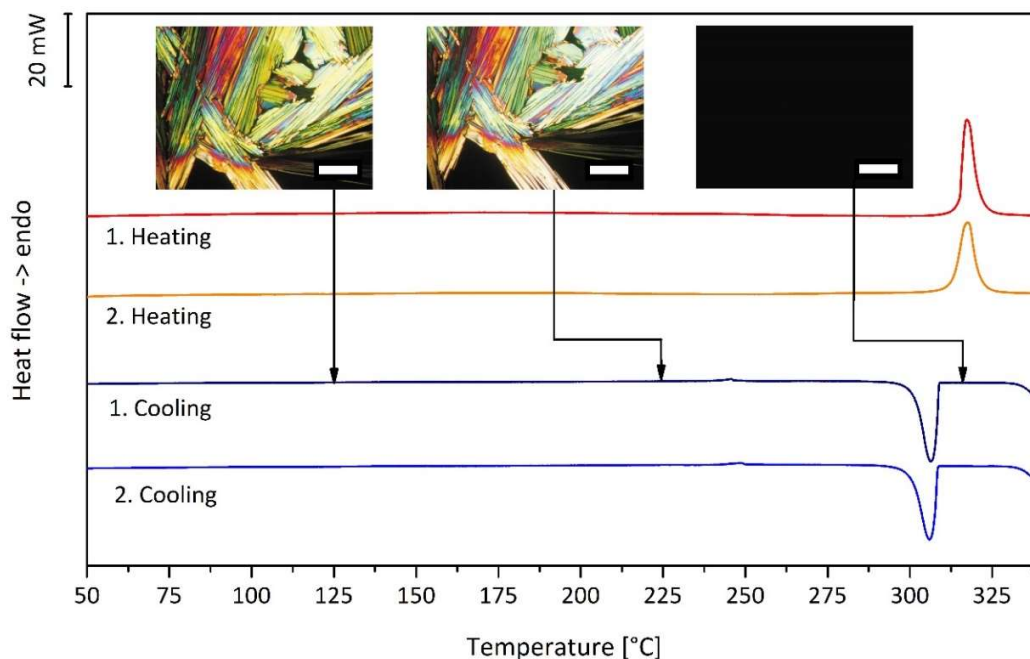


Figure 40: Differential Scanning Calorimetry heating and cooling scans of **2b** (heating and cooling rate: 10 K/min,  $\text{N}_2$  atmosphere), scale of the Polarized Optical Microscopy pictures: 200  $\mu\text{m}$ . The mesophase textures of the Polarized Optical Microscopy pictures were taken at the marked temperatures within the first cooling scan.

**POM:** Upon first heating, no change in the texture of the trisamide powder can be observed until about 310 to 320 °C, where the compound changes into the isotropic phase. Upon cooling, fast development of a band-like texture at 304 °C can be observed which is not bendable as it can be seen in figure 41. Deformation of the band texture at this temperature causes smearing indicating a liquid crystalline mesophase. Below 150 °C, deformation causes breaking of the textures pointing to a crystalline state.

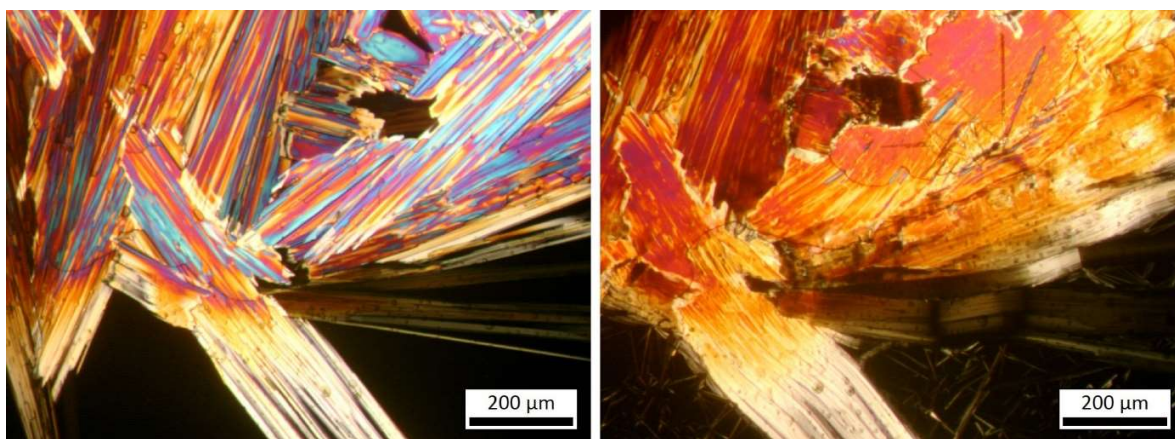


Figure 41: Polarized Optical Microscopy pictures of **2b**, taken at 304 °C before (left) and after (right) the deformation process.

**XRD:** The XRD patterns for **2b**, displayed in figure 42, upon heating show slightly different signal positions and intensities at RT, 100 °C and 150 °C which can be explained by recrystallization and reorganization processes. The pattern at 200 °C is different. A few signals can still be found at the same position than in the pattern at 150 °C but they are smaller which can be due to a very slow change of the molecular order. The pattern at 250 °C shows again a different pattern than at 150 °C, 100 °C and RT. It is similar to the pattern at 200 °C but some signals increased while others decreased in intensity. This is another proof for a very slow transition. There are still a lot of small signals left at 250 °C, which is typical for a highly ordered phase. At this temperature, the isotropic phase is not yet reached which means that a different phase than the one at RT must be present. The patterns at cooling give the same conclusions. All patterns are slightly different. The same signal positions can be found in different patterns but with different intensities. The greatest difference can be found between 200 °C and 150 °C indicating that the transition from one into another phase should be located between these temperatures. It is not possible to identify a Col<sub>h</sub> phase because important signals such as the [110] signal cannot be found. If the signal located at about 3

degrees is assumed to be the [100] signal, it can be calculated to a column-to-column distance of 1.45 nm.

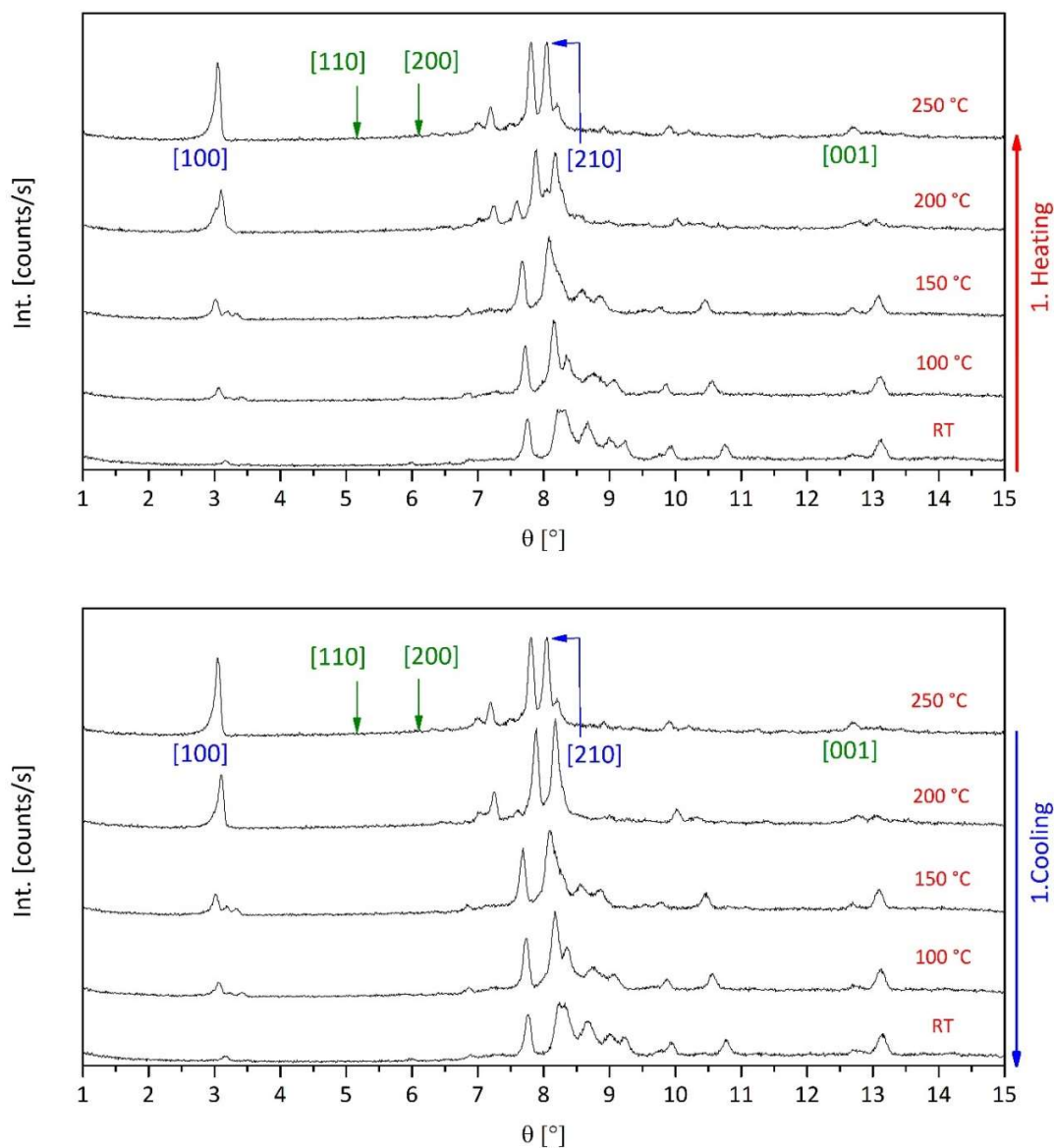


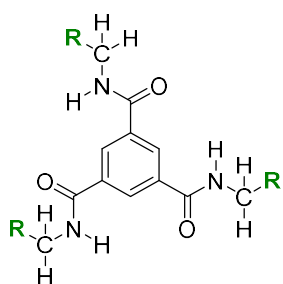
Figure 42: X-Ray Diffraction patterns of the different phases of **2b** at different temperatures upon heating and cooling. The blue and green numerics in parenthesis stand for the signals indicating a columnar hexagonal pattern: Blue = signal found, green = signal not found.  $\theta$  = Bragg angle.

The mesophase of **2b** cannot be identified precisely. Therefore it is denoted as an unidentified liquid crystalline mesophase  $M_{LC}$ .

The combination of the results of DSC, POM and XRD lead to the following phase characteristics of **2b** (second heating):

Cr 150-200 °C (detected by POM) M<sub>LC</sub> 318 °C (53 kJ/mol) I

### 3.4.3 BTA based on trimesic acid with nonafluoropentyl side chains (**2c**)



N,N',N''-tris[2,2,3,3,4,4,5,5,5-nonafluoropentyl]-  
1,3,5-benzenetricarboxamide

R:  $-(CF_2)_3-CF_3$

**DSC:** The DSC measurements were carried out by performing three heating and cooling cycles between temperatures of 50 °C and 340 °C. In figure 43, the DSC curves of the BTA based on trimesic acid with nonafluoropentyl side chains (**2c**) are displayed. The first heating shows three transitions but the one at lowest temperature disappears within the following heating cycles. The two reversible transitions at 277 °C with low enthalpy of 3 kJ/mol and at 312 °C with higher enthalpy of 45 kJ/mol may stand for the melting and clearing temperatures.

**POM:** Upon first heating, the texture brightens between 275 to 281 °C which indicates the presence of a mesophase. At 298 to 306 °C the isotropic phase is reached. Cooling to 304 °C causes a development of a partly dendritic and spherulitic texture indicating a liquid crystalline Col<sub>h</sub> phase. Shearing of the texture at 304 °C causes shifting of the texture and a change in color (figure 44). Between 275 to 250 °C, the textures change from a yellowish color to a dark purple and the compound is solidified. Further cooling causes thermal crack development typical for a material in the crystalline state.

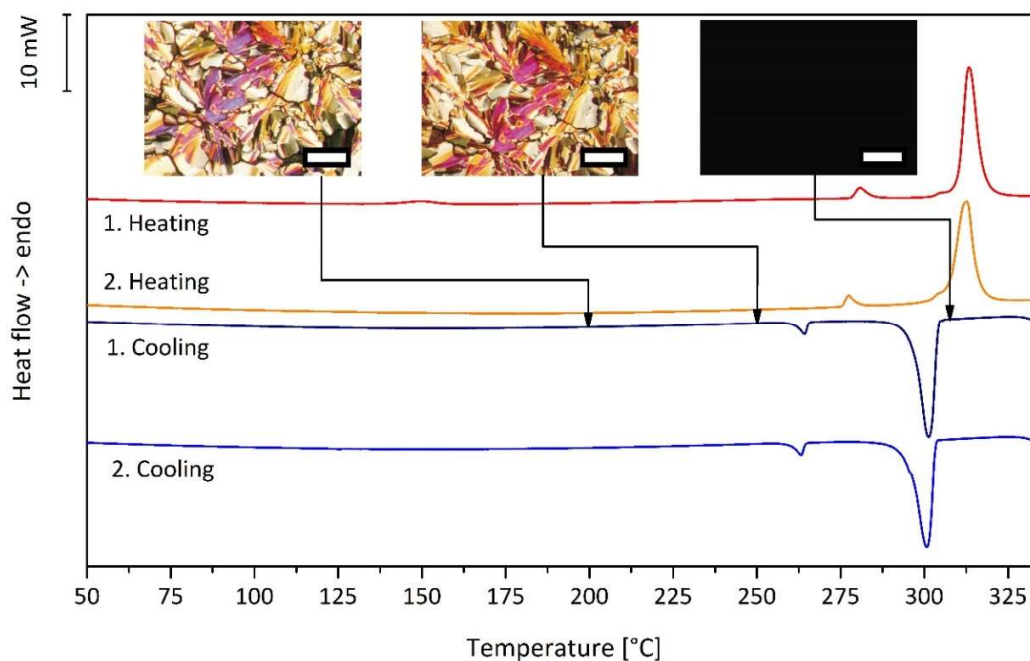


Figure 43: Differential Scanning Calorimetry heating and cooling scans of **2c** (heating and cooling rate: 10 K/min,  $N_2$  atmosphere), scale of the Polarized Optical Microscopy pictures: 200  $\mu m$ . The mesophase textures of the Polarized Optical Microscopy pictures were taken at the marked temperatures within the first cooling scan.

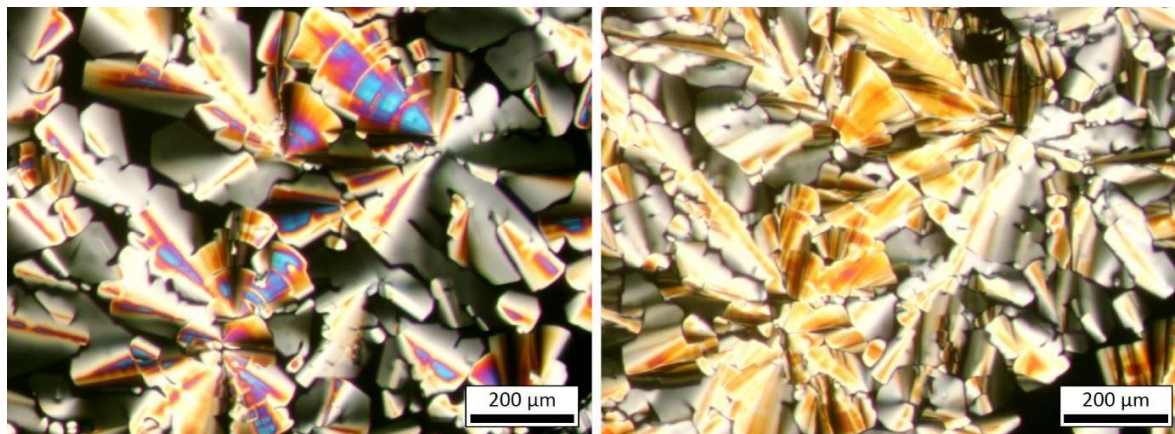


Figure 44: Polarized Optical Microscopy pictures of **2c**, taken at 304 °C before (left) and after (right) the deformation process.

**XRD:** The XRD patterns of material **2c** upon heating are shown in figure 45. It is not possible to make any conclusions about the mesophase because the DSC results revealed that it can be found between 279 to 314 °C at heating and 305 to 263 °C at cooling, which is above the

temperature limit of the XRD apparatus. The patterns are taken in the phases below the melting temperature which could be identified by POM as a solid state. Less distinct signals can be found which is not typical for a crystalline state. A small change in the signal patterns from RT to 250 °C can be observed and the [100] signal is present which appears at 100 °C, intensifying with increasing temperature and it can be calculated to a column-to-column distance of 1.58 nm. This may indicate that a columnar phase is developed with increasing temperature, but the lack of additional signals does not allow the identification of a Col<sub>h</sub> phase. It is possible to identify the [001] signal which stands for the molecular distance and it can be calculated to value of 0.35 nm.

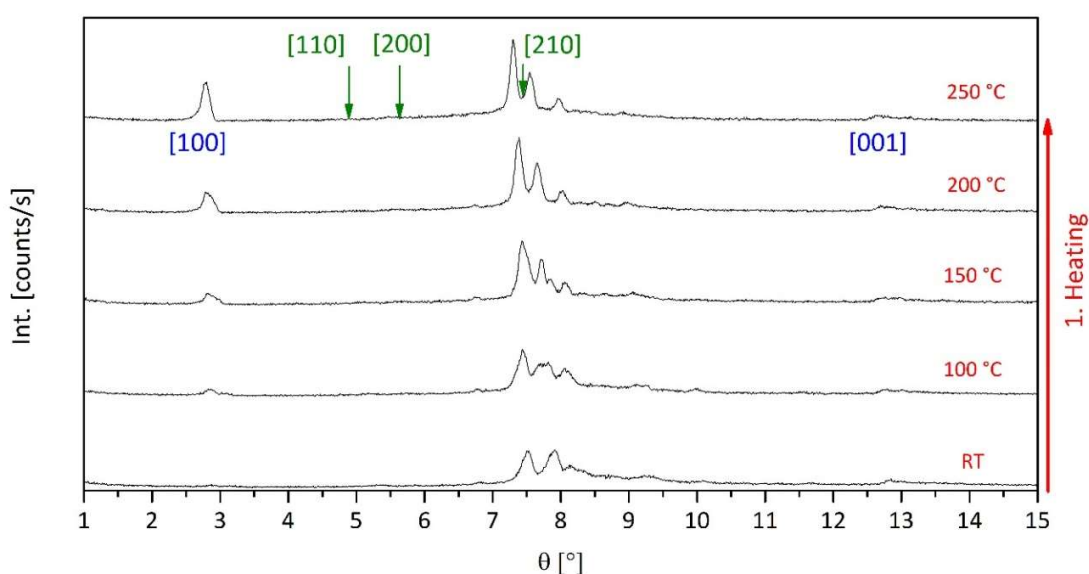


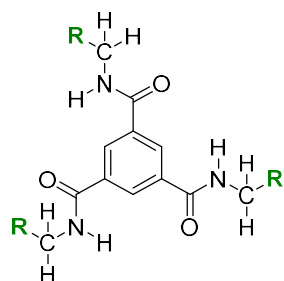
Figure 45: X-Ray Diffraction patterns of the different phases of **2c** at different temperatures upon heating. The blue and green numerics in parenthesis stand for the signals indicating a columnar hexagonal pattern: Blue = signal found, green = signal not found.  $\theta$  = Bragg angle.

The mesophase of **2c** cannot be identified precisely. Therefore it is denoted as an unidentified liquid crystalline mesophase M<sub>LC</sub>.

The combination of the results of DSC, POM and XRD lead to the following phase characteristics of **2c** (second heating):

$$\text{Cr } 277 \text{ }^\circ\text{C (3 kJ/mol)} \text{ M}_{\text{LC}} \text{ } 312 \text{ }^\circ\text{C (45 kJ/mol)} \text{ I}$$

### 3.4.4 BTA based on trimesic acid with undecafluorohexyl side chains (**2d**)



N,N',N''-tris[2,2,3,3,4,4,5,5,6,6,6-undecafluorohexyl]-  
1,3,5-benzenetricarboxamide

R:  $-(CF_2)_4-CF_3$

**DSC:** The DSC measurements were carried out by performing three heating and cooling cycles between temperatures of 50 °C and 340 °C. The DSC curves of the BTA based on trimesic acid with undecafluorohexyl side chains (**2d**) are shown in figure 46. Upon first heating, two transitions with very low enthalpy at 98 °C (1 kJ/mol) and 223 °C (1 kJ/mol), one transition with low enthalpy at 195 °C (5 kJ/mol) and one transition with the highest enthalpy at 308 °C (44 kJ/mol) can be found. Upon second heating, the transition at 98 °C disappears while the temperatures of the other transitions shift to smaller values. Compound **2d** has three reversible transitions: one transition at 182 °C with an enthalpy of 4 kJ/mol, a second at 216 °C with an enthalpy of 1 kJ/mol, and a third at 305 °C with an enthalpy of 40 kJ/mol.

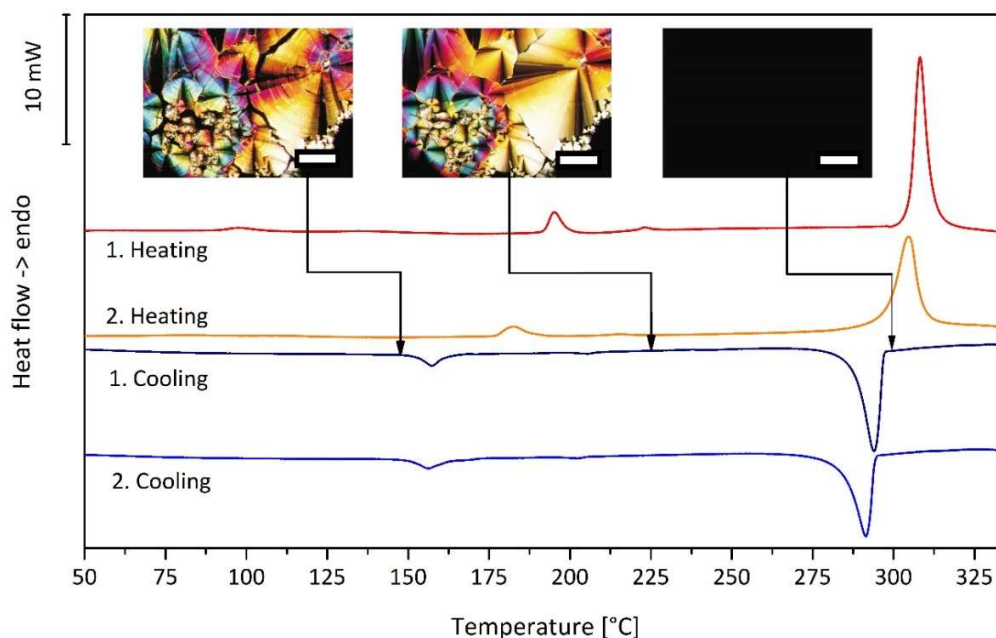


Figure 46: Differential Scanning Calorimetry heating and cooling scans of **2d** (heating and cooling rate: 10 K/min,  $N_2$  atmosphere), scale of the Polarized Optical Microscopy pictures: 200  $\mu m$ . The mesophase textures of the Polarized Optical Microscopy pictures were taken at the marked temperatures within the first cooling scan.

**POM:** Upon first heating, observation by POM shows a brightening of the material between 200 to 220 °C, which indicates the presence of a mesophase. Between 295 to 300 °C, the compound changes into the isotropic phase. Upon cooling at 291 °C, a spherulitic texture develops. The spherulitic texture, indicating a Col<sub>h</sub> phase, is surrounded by isotropic liquid, which slowly forms the texture upon further cooling. Deformation at 275 °C causes a change of the textures color as well as shifting of the texture as it can be seen in figure 47. At 180 °C, deformation causes crystalline breaking of the textures. Combination of the DSC and POM results lead to one transition temperature at 302 °C with high enthalpy, which can be identified as the clearing temperature and the transition at 180 °C with low enthalpy as the melting temperature. It is not possible to get a clear identification for the third transition at 216 °C but the deformation indicates a liquid crystalline mesophase.

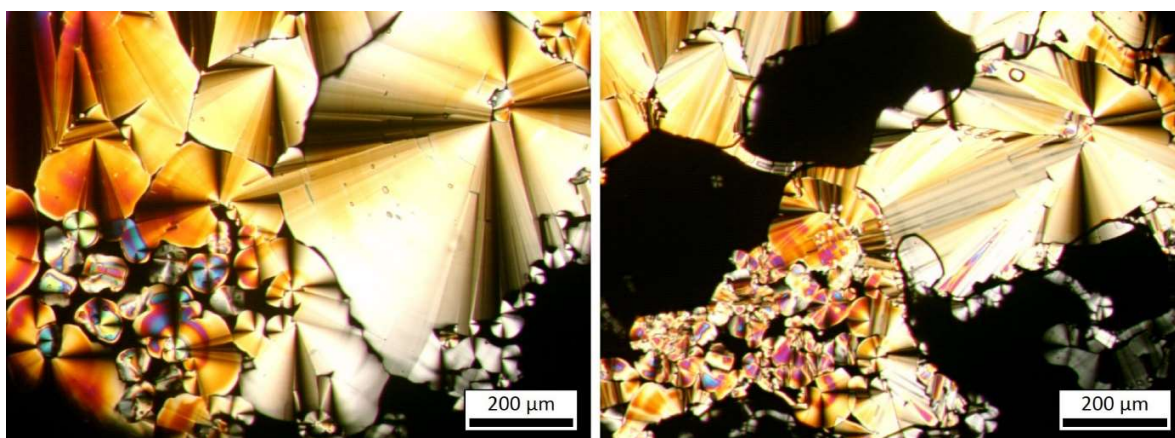


Figure 47: Polarized Optical Microscopy pictures of **2d**, taken at 275 °C before (left) and after (right) the deformation process.

**XRD:** The XRD patterns of **2d** shown in figure 48 indicate a crystalline state at RT up to at least 150 °C, although the signals of the patterns are different. This may be due to thermal rearrangements of the molecules within the trisamide powder after synthesis. Between temperatures of 150 °C and 210 °C, the pattern changes from a crystalline state into a different pattern. Most of the signals disappear and the [100] signal appears with highest intensity. A few small signals can be found in the diffuse halo region at 210 °C, which can be explained by the presence of a mixture of mesophase and crystalline state. At 250 °C, the small signals disappear and only one distinct signal can be found, which fits into the signal distance ratio of a Col<sub>h</sub> phase as the [210] signal. It is still not sure if the phase is a Col<sub>h</sub> phase because beside the [100] signal, the other most important [110] signal cannot be found. There are also not enough signals present for the identification of a plastic crystalline mesophase.

It is possible to find the [001] signal at 250 °C and it can be calculated to a molecular distance of 0.35 nm while the signal for [100] can be calculated to a column-to-column distance of 1.72 nm.

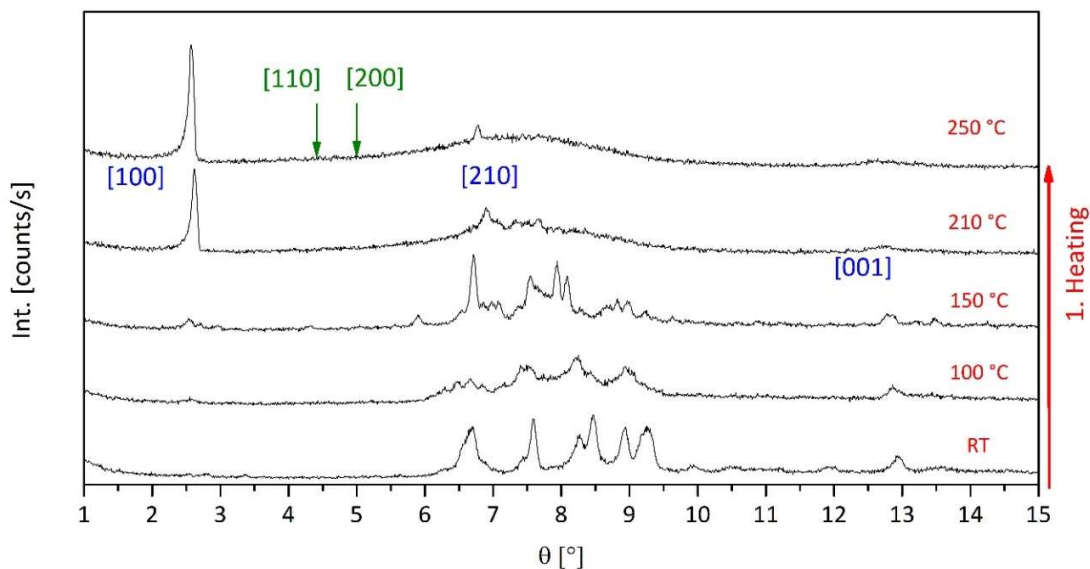
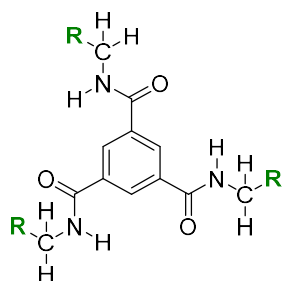


Figure 48: X-Ray Diffraction patterns of the different phases of **2d** at different temperatures upon heating. The blue and green numerics in parenthesis stand for the signals indicating a columnar hexagonal pattern: Blue = signal found, green = signal not found.  $\theta$  = Bragg angle.

The mesophases of **2d** cannot be identified precisely. Therefore they are denoted as unidentified liquid crystalline mesophase  $M_{LC1}$  and  $M_{LC2}$ .

The combination of the results of DSC, POM and XRD lead to the following phase characteristics of **2d** (second heating):

Cr 182 °C (4 kJ/mol)  $M_{LC1}$  216 °C (1 kJ/mol)  $M_{LC2}$  305 °C (40 kJ/mol) I

3.4.5 BTA based on trimesic acid with tridecafluoroheptyl side chains (**2e**)

N,N',N''-tris[2,2,3,3,4,4,5,5,6,6,7,7,7-tridecafluoroheptyl]-  
1,3,5-benzenetricarboxamide

R:  $-(CF_2)_5-CF_3$

**DSC:** The DSC measurements were carried out by performing three heating and cooling cycles between temperatures of 50 °C and 340 °C. The first heating curve of the BTA based on trimesic acid with tridecafluoroheptyl side chains (**2e**) shown in figure 49 reveals two transitions with low enthalpy at 172 °C (5 kJ/mol) and 190 °C (3 kJ/mol) and one transition with very high enthalpy at 304 °C (42 kJ/mol). Upon second heating, the two lower transitions combine to one medium transition at 166 °C (9 kJ/mol), while the transition with higher enthalpy shifts to a lower temperature (299 °C) and has a lower enthalpy value (38 kJ/mol). It can be assumed that **2e** has a melting temperature at 165 °C and a clearing temperature at 302 °C with a mesophase in between.

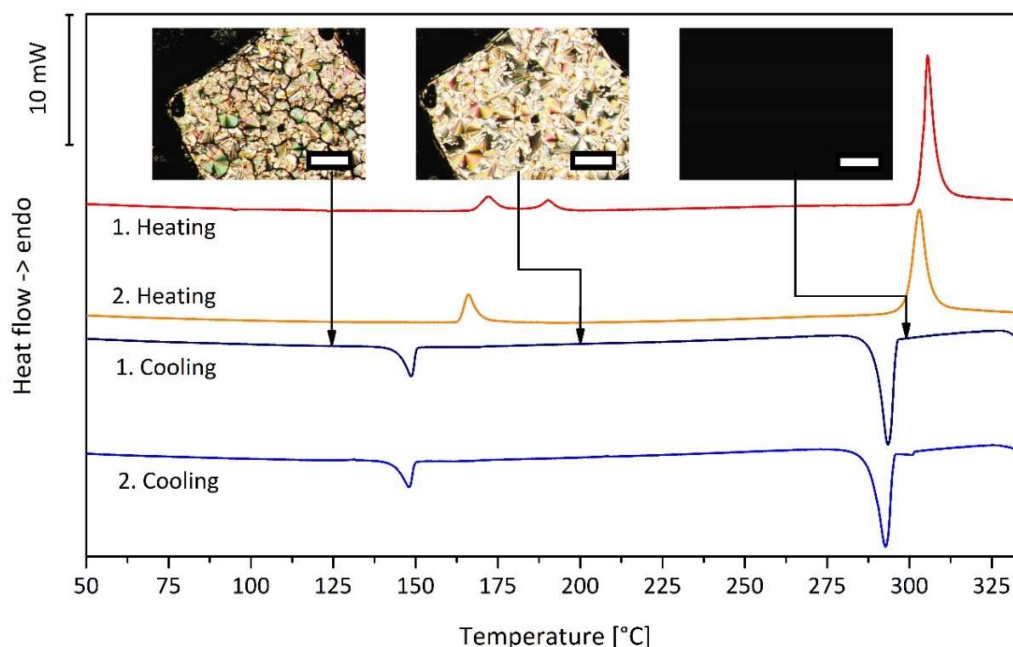
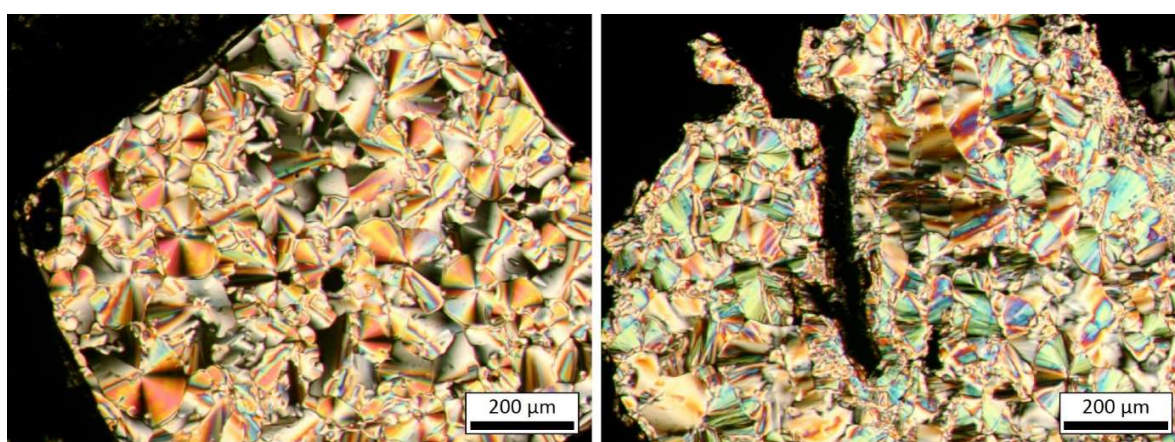


Figure 49: Differential Scanning Calorimetry heating and cooling scans of **2e** (heating and cooling rate: 10 K/min), scale of the Polarized Optical Microscopy pictures: 200  $\mu\text{m}$ . The mesophase textures of the Polarized Optical Microscopy pictures were taken at the marked temperatures within the first cooling scan.

**POM:** The POM investigation shows a brightening of the material between 176 to 205 °C and a transition into the isotropic phase between 293 to 296 °C upon first heating. Cooling of the material causes development of a spherulitic texture at about 284 °C, which can be sheared at 275 °C (figure 50) and indicates a liquid crystalline Col<sub>h</sub> phase. As it was the case for **2d**, the spherulitic texture of **2e** is surrounded by isotropic liquid, which slowly develops spherulites upon cooling. After cooling below 150 °C, the material is solid and breaks after deformation. The POM results support the DSC analysis with the clearing temperature at 302 °C and the melting temperature at 165 °C.



*Figure 50: Polarized Optical Microscopy pictures of **2e**, taken at 275 °C before (left) and after (right) the deformation process.*

**XRD:** The XRD patterns of **2e**, displayed in figure 51, give no conclusion about the molecular order in the mesophase because only the [100] signal can be clearly identified from the pattern at 250 °C. The patterns at RT and 100 °C show no typical crystalline structure but the patterns are different from that at 250 °C also upon cooling, which excludes the possibility that the material just froze into a glass-like structure. The [001] signal can be calculated to a value of 0.35 nm and the signal for [100] to a column-to-column distance of 1.83 nm

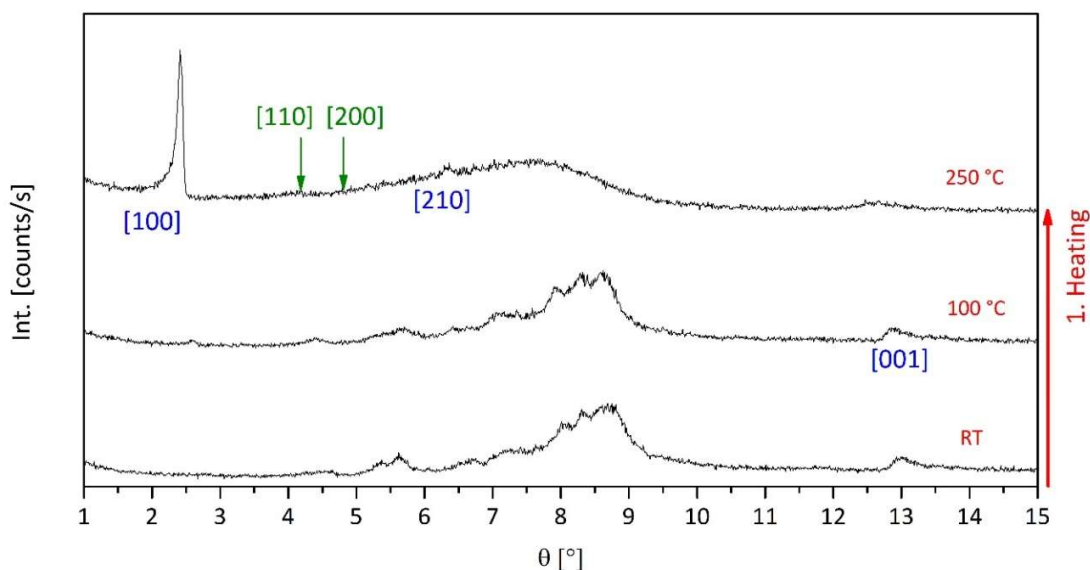


Figure 51: X-Ray Diffraction patterns of the different phases of **2e** at different temperatures upon heating. The blue and green numerics in parenthesis stand for the signals indicating a columnar hexagonal pattern: Blue = signal found, green = signal not found.  $\theta$  = Bragg angle.

The mesophase of **2e** cannot be identified precisely. Therefore it is denoted as unidentified liquid crystalline mesophase  $M_{LC}$ .

The combination of the results of DSC, POM and XRD lead to the following phase characteristics of **2e** (second heating):

$$\text{Cr } 166 \text{ }^\circ\text{C} \text{ (9 kJ/mol)} \text{ } M_{LC} \text{ } 299 \text{ }^\circ\text{C} \text{ (38 kJ/mol)} \text{ I}$$

**Temperature dependent IR-spectroscopy:** IR spectra of **2e** were taken at different temperatures from the solid state at 30 °C up the isotropic phase at 320 °C. The spectra are shown in figure 52 and the most important vibration bands  $\nu_1(\text{N-H})$  at 3252  $\text{cm}^{-1}$  (a) and  $\nu_1(\text{C=O})$  at 1662  $\text{cm}^{-1}$  (c) and the combination vibration with the most part of the deformation vibration  $\delta(\text{N-H})$  at 1571  $\text{cm}^{-1}$  are marked with grey vertical lines. The vibrational signal  $\nu(\text{C-F})$  can be found as a broad band in the range of 1270 to 1170  $\text{cm}^{-1}$ . The vibrational bands  $\nu_1(\text{N-H})$  and  $\nu_1(\text{C=O})$  of the hydrogen bonded form disappear with increasing temperature and the non-hydrogen bonded form  $\nu_2(\text{N-H})$  at 3394  $\text{cm}^{-1}$  (b) and  $\nu_2(\text{C=O})$  at 1734  $\text{cm}^{-1}$  (d) appear.

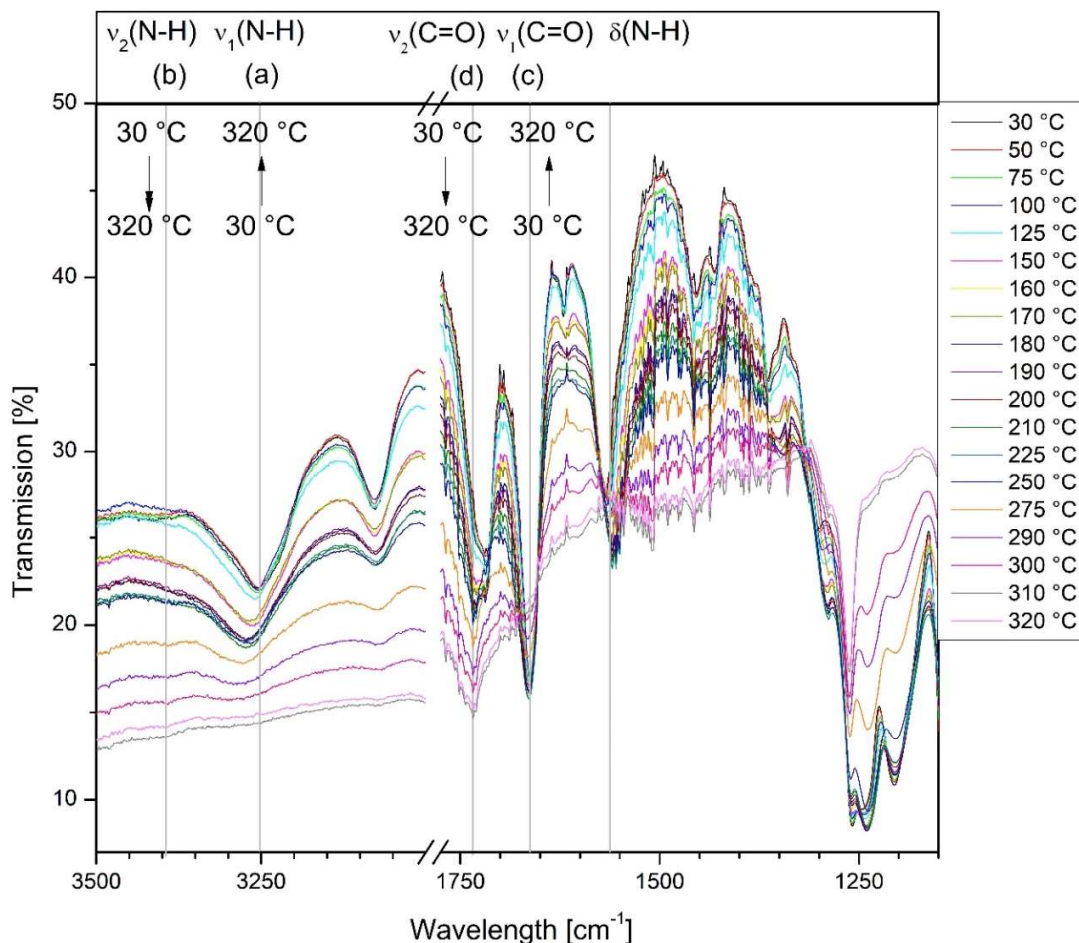


Figure 52: Infrared Spectroscopy spectra of **2e** at different temperatures upon heating; vertical grey lines: band maximum of the specific vibrational and/or deformational signals at 30 °C.

The absorbance of the vibrational bands  $\nu_1(\text{N-H})$  and  $\nu_1(\text{C=O})$  was calculated and plotted as function of the temperature, shown in figure 53. The absorbance of the hydrogen bonded form is decreasing slowly with increasing temperature, and above 250 °C, the decrease intensifies until the transition from the mesophase into the isotropic phase is passed. The absorbance for the band of the non-hydrogen bonded form reaches its maximum above 300 °C, meaning that the hydrogen bonds are broken in the isotropic phase. The IR spectra and the absorbance diagram prove the existence of hydrogen bonds between the single perfluorinated BTAs based on trimesic acid at room temperature and until the isotropic phase.

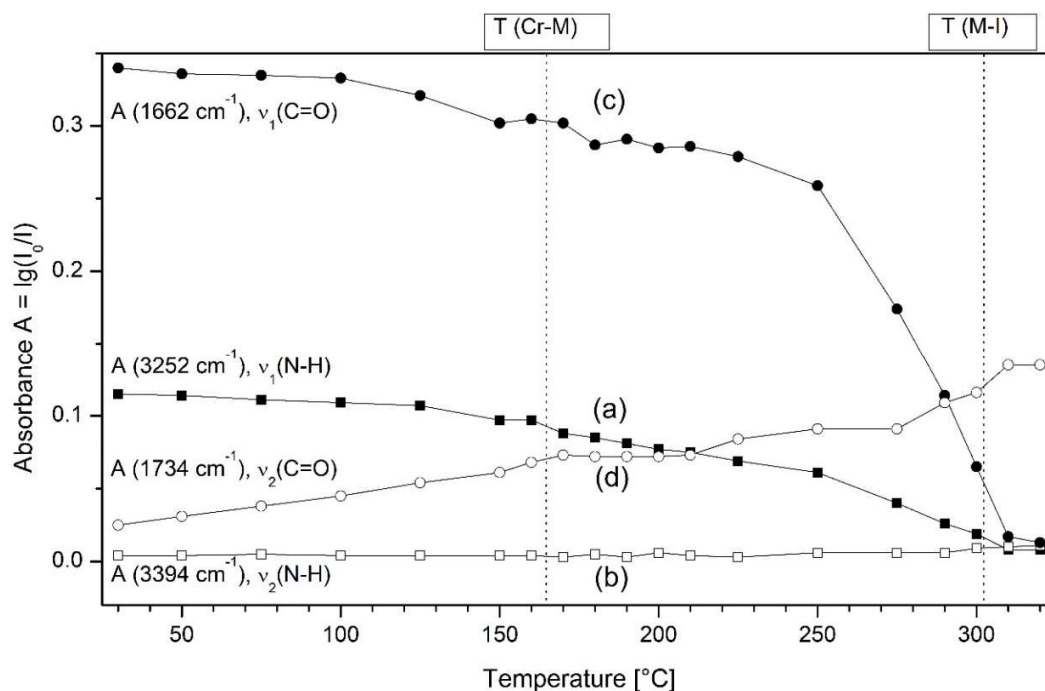
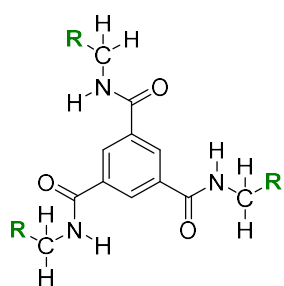


Figure 53: Infrared Spectroscopy absorbance of **2e** as a function of the temperature; circles:  $\nu(\text{C}=\text{O})$ , square:  $\nu(\text{N}-\text{H})$ , filled symbols: hydrogen bonded form  $\nu_1$ , unfilled symbols: non-hydrogen bonded form  $\nu_2$ ; vertical dashed lines: transition temperatures (second heating of DSC).

### 3.4.6 BTA based on trimesic acid with pentadecafluorooctyl side chains (**2f**)



N,N',N''-tris[2,2,3,3,4,4,5,5,6,6,7,7,8,8,8-pentadecafluorooctyl]-1,3,5-benzenetricarboxamide



**DSC:** The DSC measurements were carried out by performing three heating and cooling cycles between temperatures of 50 °C and 315 °C. Upon first heating of the BTA based on trimesic acid with pentadecafluorooctyl side chains (**2f**), three transitions can be found as displayed in figure 54. One with very low enthalpy at 186 °C (2 kJ/mol), one with medium enthalpy at 208 °C (12 kJ/mol) and one with high enthalpy at 303 °C (32 kJ/mol). Upon second heating, the three transitions are still present and can be found at 190 °C (0.7 kJ/mol), 207 °C (14 kJ/mol) and 303 °C (27 kJ/mol), respectively. The transitions at 207 °C and 303 °C can also

be found upon cooling, their temperature values are shifted to lower values because of an undercooling effect. The transition at 190 °C can also be found in the cooling scan but the transition region has broadened.

**POM:** The first heating of **2f** reveals a brightening of the material between 200 to 210 °C indicating the presence of a mesophase, and a change into the isotropic phase at about 296 °C to 298 °C. Upon cooling a slow development of a spherulitic texture, beginning at 290 °C, which denotes a liquid crystalline Col<sub>h</sub> phase, can be observed. Deformation of the material at 225 °C causes a liquid crystalline smearing of the material as it is shown in figure 55. Further cooling causes solidification of the material between 170 to 165 °C, which can be proven by breaking of the material after shearing.

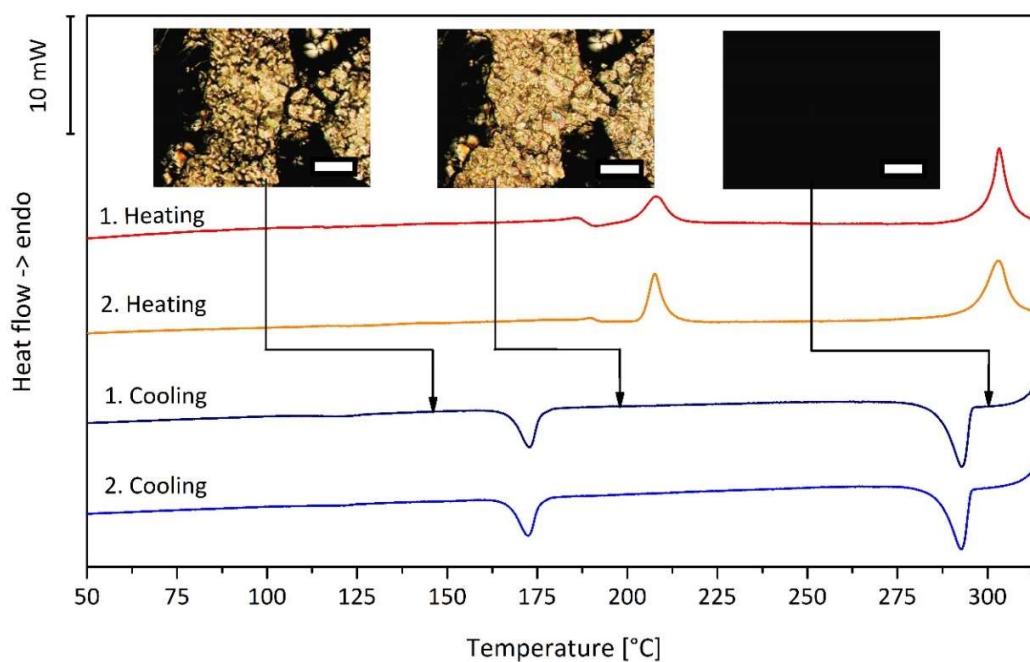


Figure 54: Differential Scanning Calorimetry heating and cooling scans of **2f** (heating and cooling rate: 10 K/min, N<sub>2</sub> atmosphere), scale of the Polarized Optical Microscopy pictures: 200 μm. The mesophase textures of the Polarized Optical Microscopy pictures were taken at the marked temperatures within the first cooling scan.

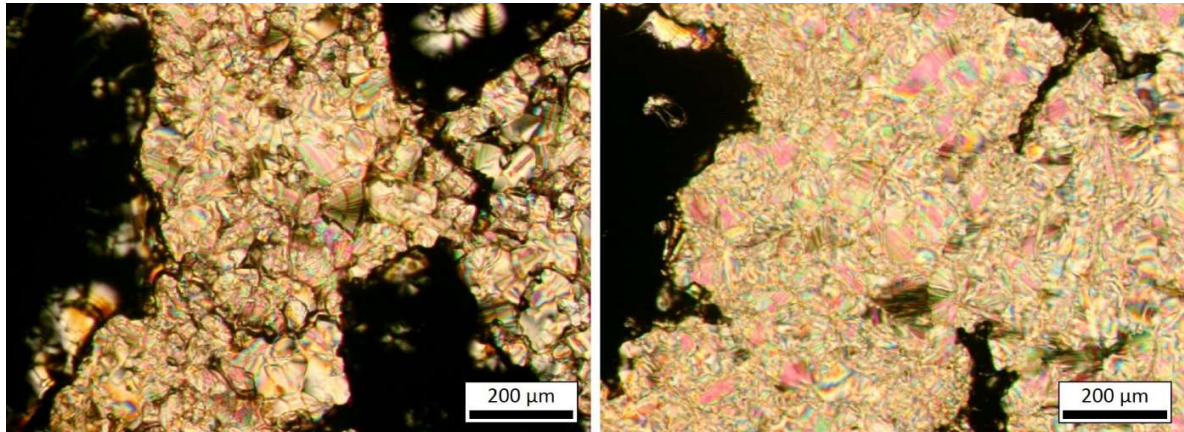


Figure 55: Polarized Optical Microscopy pictures of **2f**, taken at 225 °C before (left) and after (right) the deformation process.

**XRD:** The XRD patterns of **2f** are displayed in figure 56. At RT and 100 °C, the patterns show no typical crystalline signal arrangement. The signal [001] can be found which gets more diffuse with increasing temperature. The pattern at 190 °C upon heating still contains some signals, which can also be found at lower temperatures.

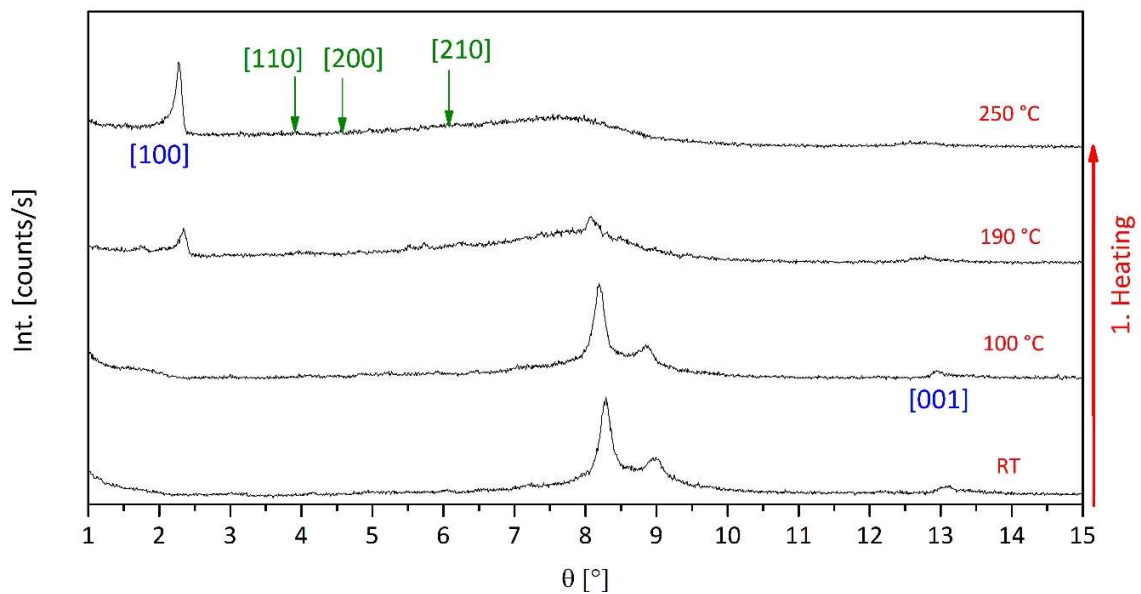


Figure 56: X-Ray Diffraction patterns of the different phases of **2f** at different temperatures upon heating. The blue and green numerics in parenthesis stand for the signals indicating a columnar hexagonal pattern: Blue = signal found, green = signal not found.  $\theta$  = Bragg angle.

This may be explained by a very slow transition. The signal [100] appears at 190 °C and intensifies at 250 °C but no additional signals can be found to determine the mesophase as a Col<sub>h</sub> phase. As it was the case for **2d** and **2e**, the [001] signal can be clearly identified at lower temperatures and can be calculated to a molecular distance of 0.34 nm. The signal for [100] can be calculated to a column-to-column distance of 1.94 nm at 250 °C.

The mesophase of **2f** cannot be identified precisely. Therefore it is denoted as unidentified liquid crystalline mesophase M<sub>LC</sub>.

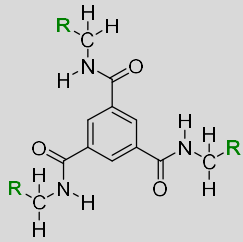
*The combination of the results of DSC, POM and XRD lead to the following phase characteristics of **2f** (second heating):*

Cr<sub>1</sub> 190 °C (0.7 kJ/mol) Cr<sub>2</sub> 207 °C (14 kJ/mol) M<sub>LC</sub> 303 °C (27 kJ/mol) I

### 3.4.7 Comparison within this series

The characterization results of the BTAs based on trimesic acid with linear perfluorinated side chains are summarized in table 4 with the transition temperatures and their corresponding transition enthalpy values, both taken from the second heating curves of the DSC.

Table 4: Phase behavior of 1,3,5-benzenetrisamides based on trimesic acid with linear perfluorinated side chains (**2a-f**).

 <b>R:</b>	<p style="text-align: center;"><b>Transition temperatures and enthalpy values, DSC, second heating (10 k/min)</b></p>
-CF <sub>2</sub> -CF <sub>3</sub>	<b>2a</b> Cr 247 °C (0.3 kJ/mol) M <sub>p</sub> 294 °C (38 kJ/mol) I
-(CF <sub>2</sub> ) <sub>2</sub> -CF <sub>3</sub>	<b>2b</b> Cr 150-200 °C (a) M <sub>LC</sub> 318 °C (53 kJ/mol) I
-(CF <sub>2</sub> ) <sub>3</sub> -CF <sub>3</sub>	<b>2c</b> Cr 277 °C (3 kJ/mol) M <sub>LC</sub> 312 °C (45 kJ/mol) I
-(CF <sub>2</sub> ) <sub>4</sub> -CF <sub>3</sub>	<b>2d</b> Cr 182 °C (4 kJ/mol) M <sub>LC1</sub> 216 °C (1 kJ/mol) M <sub>LC2</sub> 305 °C (40 kJ/mol) I
-(CF <sub>2</sub> ) <sub>5</sub> -CF <sub>3</sub>	<b>2e</b> Cr 166 °C (9 kJ/mol) M <sub>LC</sub> 299 °C (38 kJ/mol) I
-(CF <sub>2</sub> ) <sub>6</sub> -CF <sub>3</sub>	<b>2f</b> Cr <sub>1</sub> 190 °C (0.7 kJ/mol) Cr <sub>2</sub> 207 °C (14 kJ/mol) M <sub>LC</sub> 303 °C (27 kJ/mol) I

Col: columnar mesophase, M: unidentified mesophase, I: isotropic phase, p: plastic crystalline; (a) Not detected by DSC, detected by a change in the pattern of the XRD measurements

The BTA with the shortest side chains **2a** showed a *plastic crystalline mesophase* with a low transition enthalpy from the crystalline state. The transition enthalpy is much lower than the enthalpy from the mesophase into the isotropic phase at 294 °C. This can be explained by the higher molecular order of the plastic crystalline mesophase, which varies only slightly from the crystalline state. This can also be seen in the XRD patterns of the mesophase because there are still many signals present. The DSC investigation for **2b** shows only one transition with high enthalpy representing the clearing transition but with consideration of the XRD patterns, there is another transition between 150 °C and 200 °C. This transition cannot be found in the DSC, which means that the transition enthalpy is very small indicating a plastic

mesophase with high molecular order. The deformation experiments with POM showed no bending or folding of the band-like texture. The compounds with longer side chains revealed two (**2c** and **2e**) or three (**2d** and **2f**) transitions while always the one at highest temperature had also the highest transition enthalpy. This indicates that the mesophases of the BTAs based on trimesic acid may have a high order.

The results of the XRD patterns of the BTAs based on trimesic acid allow no clear identification of a  $\text{Col}_h$  phase but the [100] signal was always present. In figure 57 (left), the *columnar distances* calculated from the [100] signals are shown, and on the right, these values are plotted as a function of the linear perfluorinated side chain length. The calculated distances from the [100] signal of the BTAs based on trimesic acid increase linearly with linear perfluorinated side chain length, with about 0.1 nm per additional  $\text{CF}_2$  group. Although, no clear  $\text{Col}_h$  phase could be found, the similar distance increase of the BTAs based on 1,3,5-triaminobenzene indicate the presence of columnar phases here, too.

1,3,5-benzene-trisamide	Distance [100]-signal [nm]
<b>2a</b>	1,31
<b>2b</b>	1,45
<b>2c</b>	1,58
<b>2d</b>	1,72
<b>2e</b>	1,83
<b>2f</b>	1,94

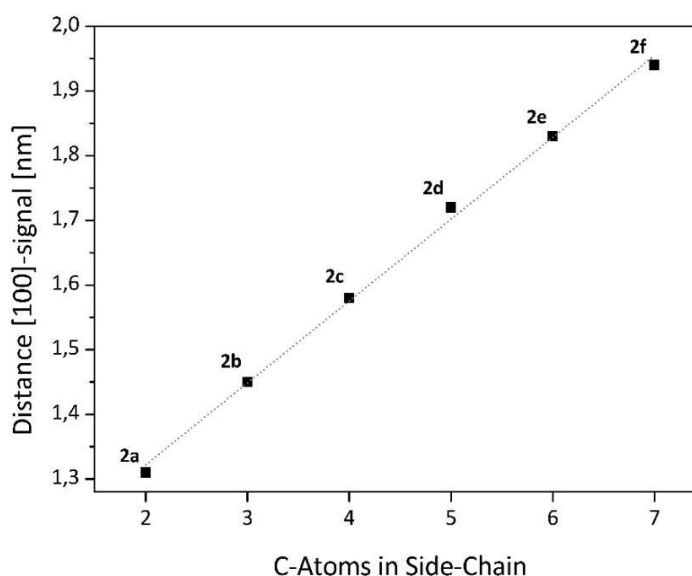


Figure 57: Distances calculated from the [100] signal of the X-Ray Diffraction patterns at 250 °C, which stands for the column-to-column distance in a columnar mesophase, dependent on the side chain length.

Another argument for the presence of  $\text{Col}_h$  phases is that for all BTAs based on trimesic acid, the [001] signal was found, and it showed similar intermolecular distances of 0.34 nm or 0.35 nm. Typically, this signal is found in highly ordered columnar mesophases.<sup>45</sup>

The *phase transition temperatures* dependent on the linear perfluorinated side chain length is shown in figure 58. It is not possible to find a clear tendency for the melting temperatures as well as for the clearing temperatures with increasing linear perfluorinated side chain length. The clearing temperatures are in a temperature range of 24 degrees, with a value of 294 °C for **2a** as the lowest, and 318 °C for **2b** as the highest temperature. For **2a**, the melting temperature is at a high value of 247 °C. The melting temperature of **2b** cannot be clearly identified but it has to be between temperatures of 150 °C and 200 °C. For **2c**, the melting temperature can be found at 277 °C while for **2d** it falls back down to 182 °C. Compounds **2e** and **2f** showed melting temperatures at 166 °C and 190 °C, respectively. The compounds **2d** and **2f** also revealed a mesophase-to-mesophase transition, which could be detected at 216 °C for **2d** and at 207 °C for **2f**.

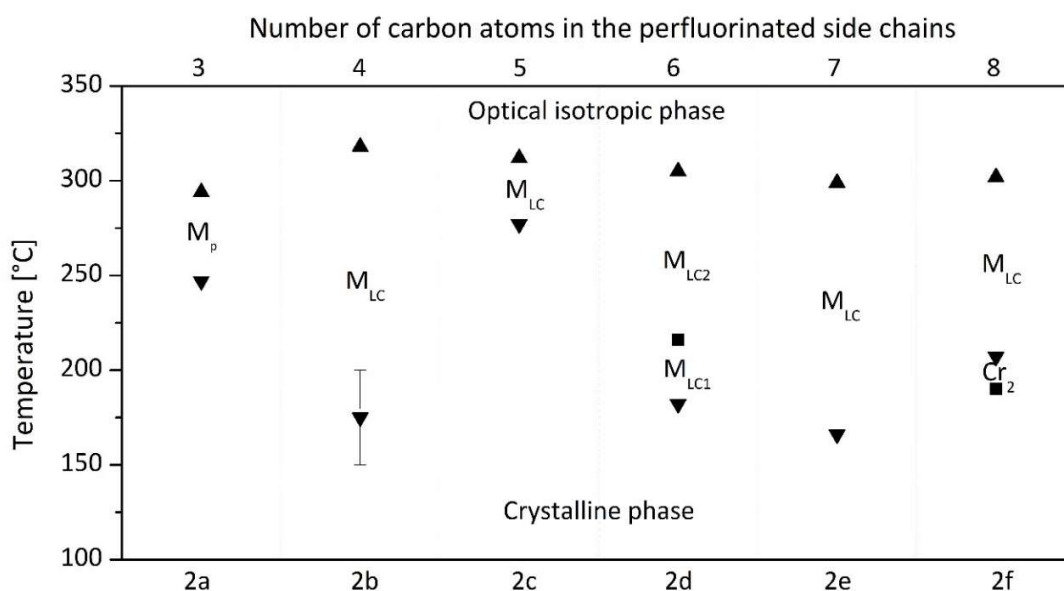


Figure 58: Phase transition temperatures of 1,3,5-benzenetrisamides based on trimesic acid and linear perfluorinated side chains dependent on the side chain length (Differential Scanning Calorimetry, second Heating). ▲: clearing temperature, ▼: melting temperature, ■: mesophase-to-mesophase or solid state to solid state transition, Cr: crystalline state, M: unidentified mesophase, p: plastic crystalline, LC: liquid crystalline.

Figure 59 shows the *transition enthalpy* values of the BTAs based on trimesic acid with linear perfluorinated side chains as a function of the side chain length from the DSC curves at second heating. The enthalpy values for the melting transitions show the tendency to increase with side chain length (0.3 kJ/mol for **2a** to 14 kJ/mol for **2f**). The transition enthalpy of the clearing temperatures is decreasing (53 kJ/mol for **2b** to 27 kJ/mol for **2f**) except for **2a** where the transition enthalpy of the clearing temperature is lower than that for **2b**.

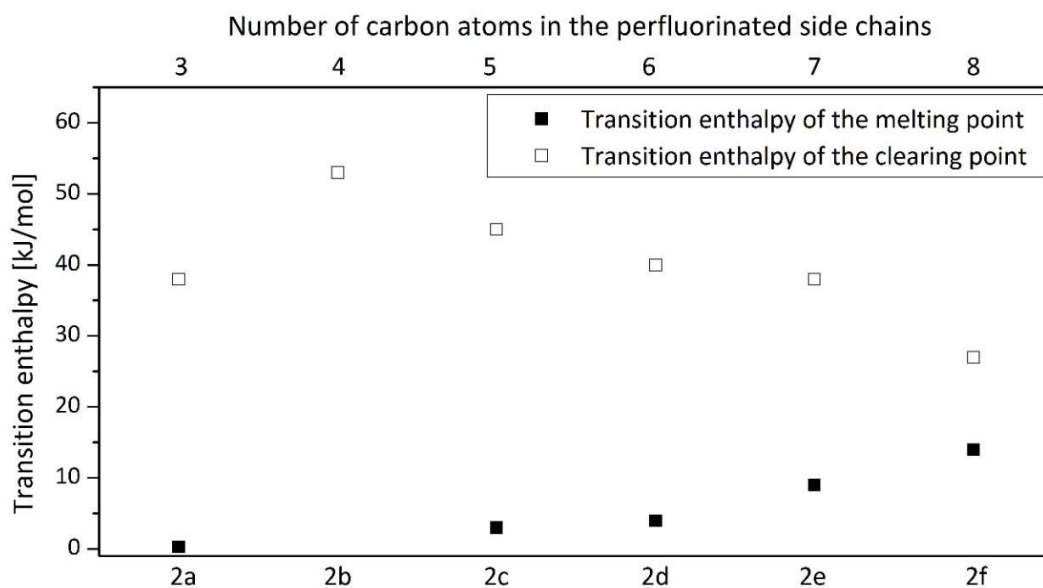
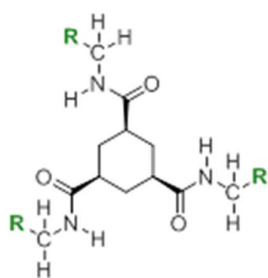


Figure 59: Comparison of the transition enthalpy values of 1,3,5-benzenetrisamides based on trimesic acid with linear perfluorinated side chains dependent on the side chain length (Differential Scanning Calorimetry, second heating).

### 3.5 Phase behavior of a 1,3,5-cyclohexanetrissamide with linear perfluorinated side chains

In addition to BTAs **1** and **2**, a 1,3,5-cyclohexanetrissamide (CTA) **3** with tridecafluoroheptyl side chains based on (1s,3s,5s)-cyclohexanetricarboxylic acid was investigated and the characterization is shown in the following.



(1s,3s,5s)-N<sup>1</sup>,N<sup>3</sup>,N<sup>5</sup>- tris(2,2,3,3,4,4,5,5,6,6,7,7,7-tridecafluoroheptyl)cyclohexane-1,3,5-tricarboxamide



**DSC:** In the DSC measurements, three heating and cooling cycles between temperatures of 50 °C and 355 °C were carried out. In figure 60, the DSC curves of the CTA **3a** are shown for the first three heating and two cooling scans.

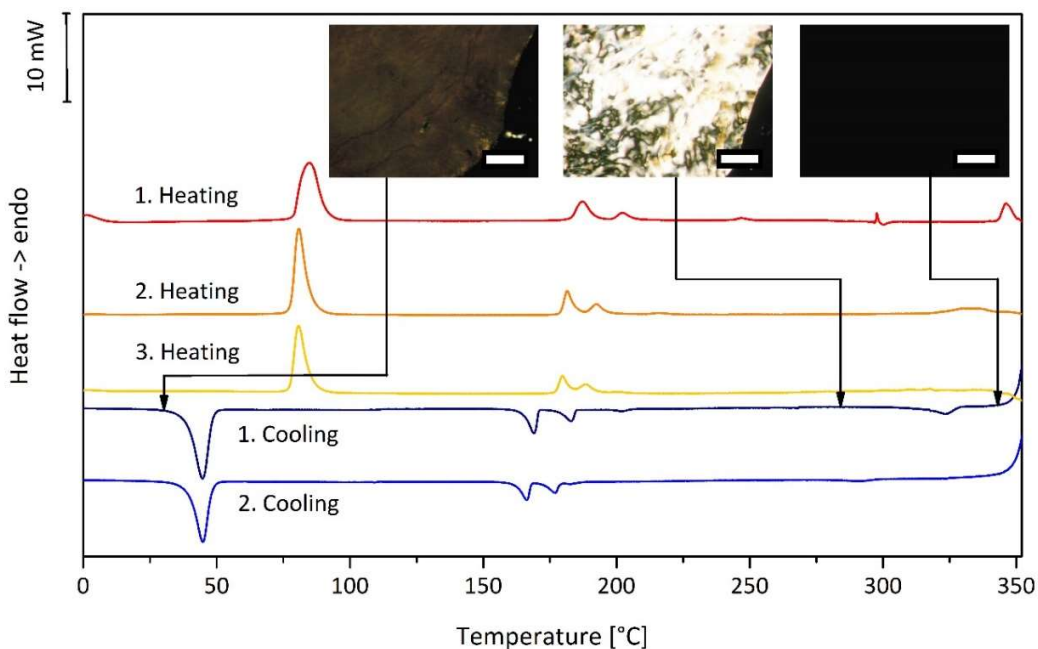


Figure 60: Differential Scanning Calorimetry heating and cooling scans of **3a** (heating and cooling rate: 10 K/min, N<sub>2</sub> atmosphere), scale of the Polarized Optical Microscopy pictures: 200 μm. The mesophase textures of the Polarized Optical Microscopy pictures were taken at the marked temperatures within the first cooling scan.

The first heating exhibits one transition with high enthalpy at 85 °C (46 kJ/mol), three transitions with lower enthalpy at 187 °C (10 kJ/mol), 202 °C (7 kJ/mol) and 346 °C (6 kJ/mol) and one transition with very low enthalpy at 246 °C (0.7 kJ/mol). The second heating reveals only four transitions, one with high enthalpy at 81 °C (34 kJ/mol), two with low enthalpy at 182 °C (6 kJ/mol) and 189 °C (3 kJ/mol), and one very broad transition between 328 to 338 °C (3 kJ/mol). The third heating shows only the first three transitions. The transition at 346 °C, found upon first heating, broadens and disappears with increasing exposure to temperature. This can be explained by a degradation of the compound above the temperature of the highest transition, considering that **3a** already reaches a weight loss of 10 % at 351 °C.

**POM:** Upon first heating, **3a** shows a brightening between 78 to 85 °C indicating a transition into a mesophase. Another transition can be observed between 175 to 196 °C where the powder changes to a *schlieren* texture, which is typical for a nematic phase. At 340 °C, the *schlieren* texture disappears and the material changes into the isotropic phase. At this temperature, the material already begins to evaporate and decompose. Subsequent cooling causes development of the nematic *schlieren* texture between 325 to 320 °C. Deformation of the nematic mesophase at 250 °C (figure 61 top right and left) causes smearing of the texture which is another proof for a nematic liquid crystalline mesophase. The liquid-like deformation is possible until a temperature of 160 °C is reached. The texture quickly changes into a solid-state texture and shearing causes crack formation (figure 61 bottom left). At 48 °C, the texture changes again to a uniformly dark brown colored texture, which remains constant until RT (figure 61 bottom right).

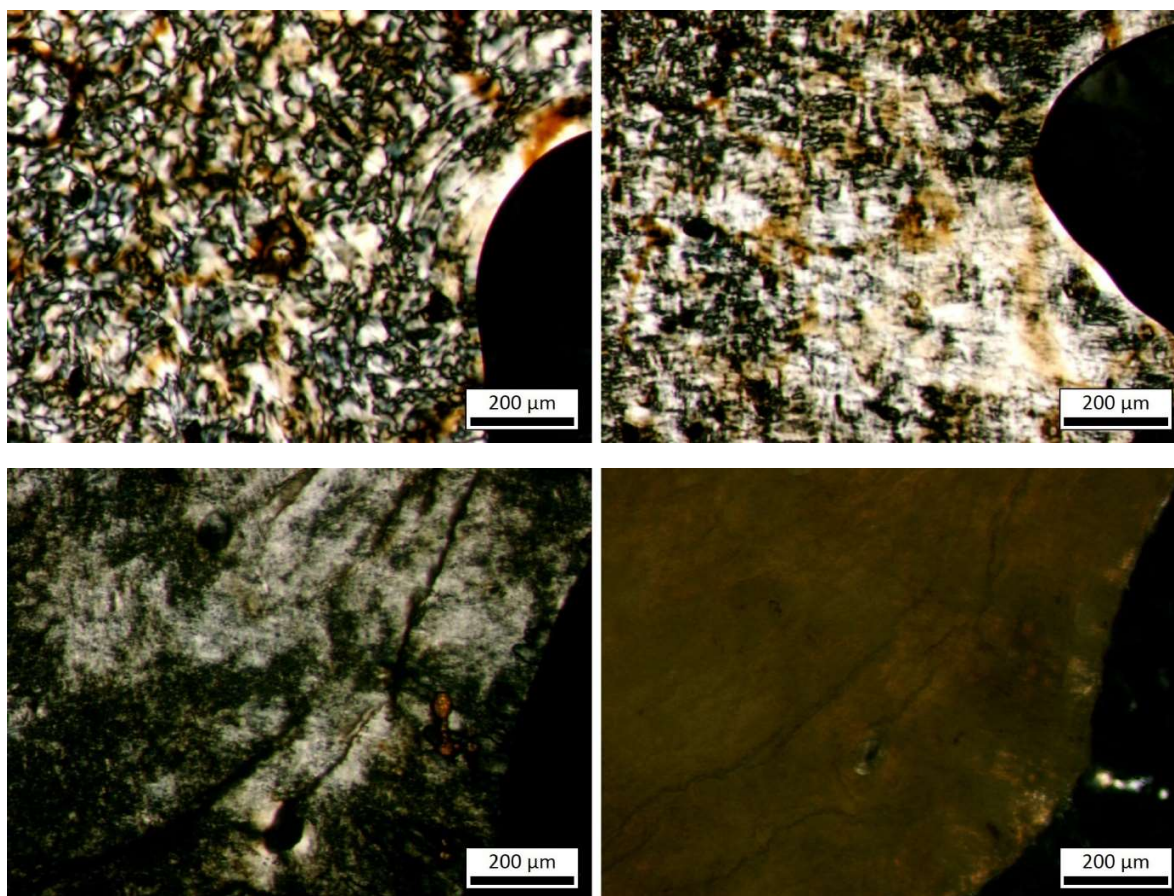


Figure 61: Polarized Optical Microscopy pictures of **3a**, taken at 250 °C before (top left) and after (top right) shearing. The crystalline state at 150 °C after deformation (bottom left) and at 30 °C (bottom right) are shown.

The transition around 340 °C stands for the clearing temperature of the material. It can be assumed that the melting temperature is one of the transitions at 175 °C or 196 °C.

Compared to the 1,3,5-benzenetrisamides, **3a** is the only material which shows a nematic phase. This means that the existence of the cyclohexane core is important for the development of a nematic phase. This can be explained by the molecular structure. It was already shown that derivatives with cyclohexane cores have a different conformation in which the amide groups in the assembled supramolecular column are pointing vertical to the core plain.<sup>71,106</sup> This is the conformation for the development of hydrogen bonds in an ecliptic arrangement of the side chains instead of a helical structure as it is the case for BTAs. Because of the aromatic nature of the benzene core of BTAs, the amide groups are partially conjugated to the core and this causes a non-vertical alignment with respect to the core plain.

**XRD:** The XRD pattern of **3a** at RT, shown in figure 62, exhibit a typical crystalline pattern with many signals over the entire scattering angle range. The pattern at 140 °C, already above the first transition examined by DSC and POM, also contains signals, which are not fitting to a Col<sub>h</sub> pattern. This indicates that the transition at 81 °C is a transition from one into another crystalline state. At 190 °C, the pattern includes one strong and diffuse halo as it is typical for a liquid crystalline phase. One specific but small signal at around 4 degrees and another diffuse signal at 9 to 10 degrees are visible. A columnar phase can also not be identified here. The patterns at 220 °C and 250 °C show the same progressions only the signal at 4 degrees gets smaller at 220 °C and disappears at 250 °C. The nematic phase is a mesophase with low molecular order. The patterns from 190 °C, 220 °C and 250 °C indicate that the material resides in a nematic phase. Within the mesophase at 190 °C, only the [100] signal, which can be calculated to a distance of 1.20 nm, and the [200] signal can be found. Also the [001] signal is present and can be calculated to a molecular distance of 0.47 nm which is a typical value for CTA materials.<sup>45</sup>

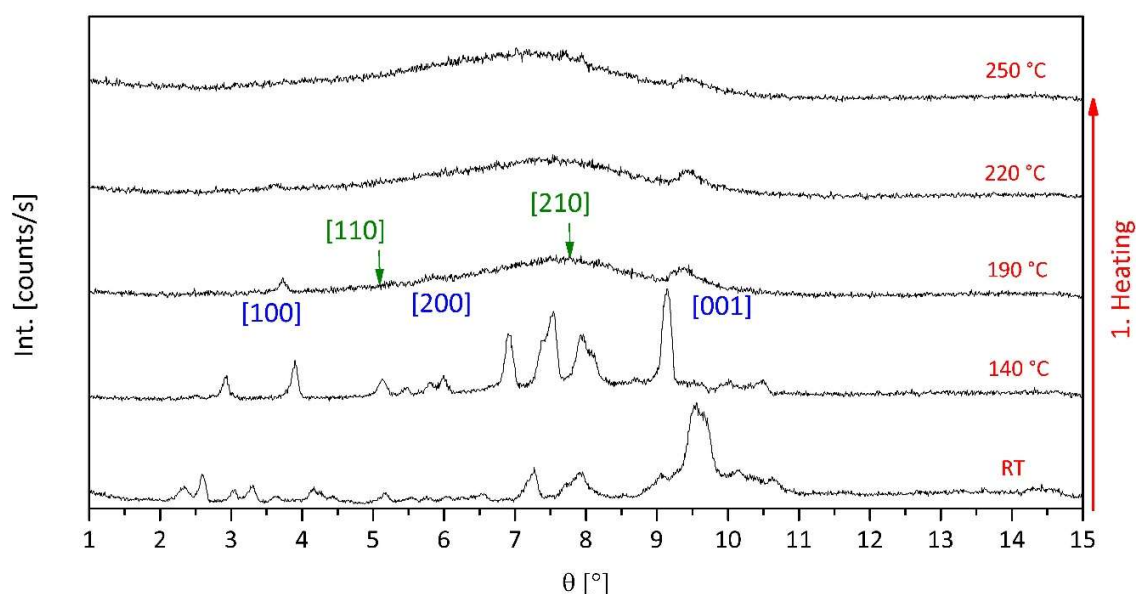


Figure 62: X-Ray Diffraction patterns of the different phases of **3a** at different temperatures upon heating. The blue and green numerics in parenthesis stand for the signals indicating a columnar hexagonal pattern: Blue = signal found, green = signal not found.  $\theta$  = Bragg angle.

In a columnar nematic phase N<sub>C</sub>, the molecules are ordered in columns where a typical intermolecular distance as well as a diffuse signal for the column-to-column distance are present. In a discotic nematic phase N<sub>D</sub> the columnar as well as the intermolecular distance

signals are not present. The patterns of the nematic mesophase in figure 62 at 220 °C and 250 °C include a sharp signal for the intermolecular distance [001] and at 220 °C a small signal for an intercolumnar distance. Therefore, the nematic phase at 220 °C can be identified as a  $N_C$  phase. Although the signal for the intercolumnar distance disappears at 250 °C, the intermolecular distance signal is still present indicating a slow loss of order with increasing temperature.

The mesophase between 182 °C and 189 °C cannot be identified and is denoted as unidentified liquid crystalline mesophase  $M_{LC}$ .

*The combination of the results of DSC, POM and XRD lead to the following phase characteristics of 3a (DSC, second heating):*

$Cr_1$  81 °C (34 kJ/mol)  $Cr_2$  182 °C (6 kJ/mol)  $M_{LC}$  189 °C (3 kJ/mol)  $N_C$  346 °C (first heating; 6 kJ/mol) I

**Temperature dependent IR-spectroscopy:** The IR spectra of **3a** from 30 °C in the solid state up to 350 °C where the material is in the isotropic phase are displayed in figure 63. The most important bands for the presence of hydrogen bonded trisamides at 30 °C,  $\nu_1(N-H)$  at 3247  $cm^{-1}$  (a) and  $\nu_1(C=O)$  at 1661  $cm^{-1}$  (c) as well as the combination vibration with the most part of the deformation vibration  $\delta(N-H)$  at 1556  $cm^{-1}$  are marked with vertical grey lines. A broad band at 1270  $cm^{-1}$  to 1170  $cm^{-1}$  stands for the  $\nu(C-F)$  signals of the linear perfluorinated side chains.

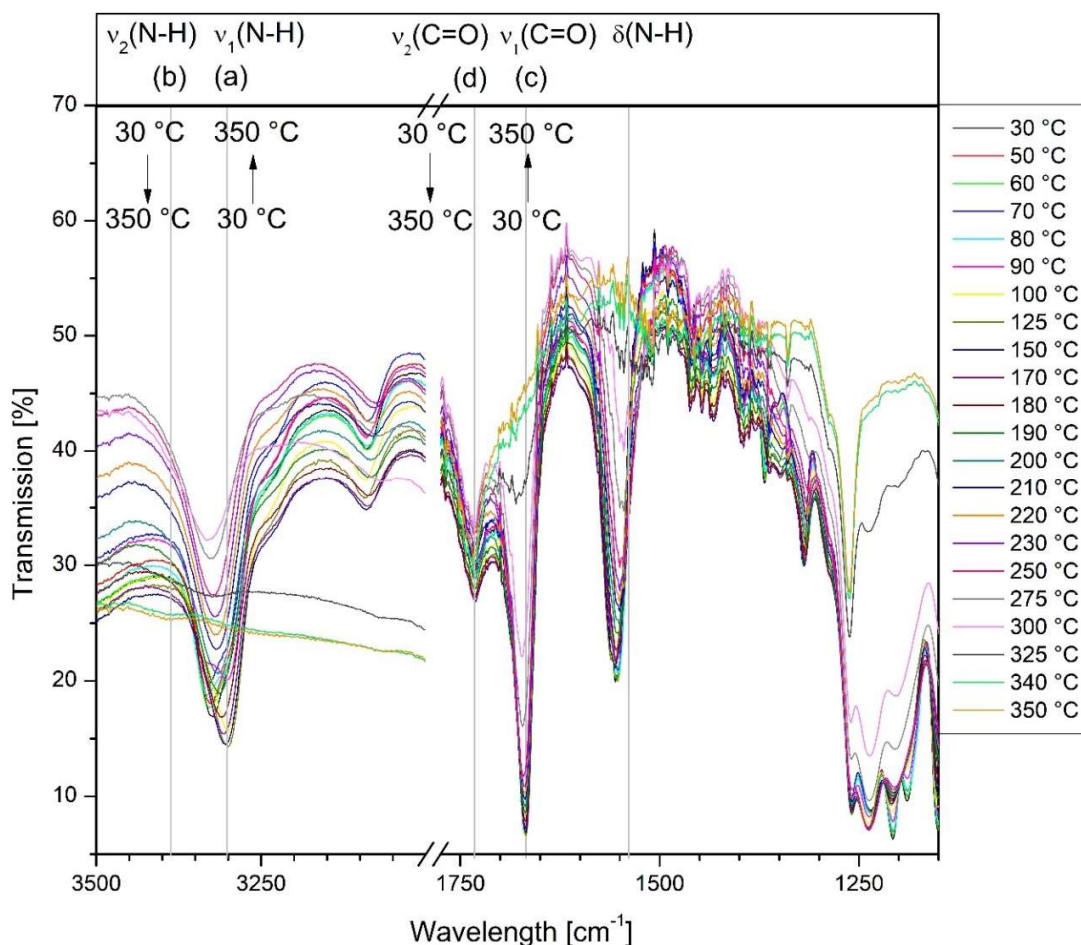


Figure 63: Infrared Spectroscopy spectra of **3a** at different temperatures upon heating; vertical grey lines: band maximum of the specific vibrational and/or deformational signals at 30 °C.

Examination of the IR scans at different temperatures reveals that the bands indicating the hydrogen bonded form  $\nu_1(\text{N-H})$  (a) and  $\nu_1(\text{C=O})$  (c) disappear with increasing temperature and appear at 340 °C with wave numbers of 3391  $\text{cm}^{-1}$  for  $\nu_2(\text{N-H})$  (b) and 1733  $\text{cm}^{-1}$  for  $\nu_2(\text{C=O})$  (d). In figure 64, the calculated absorbance values for the hydrogen bonded and non-hydrogen bonded forms are plotted as function of the temperature. A slow decrease in absorbance of the hydrogen bonded form can be observed until the transition temperature from the unidentified mesophase to the nematic phase is reached. Then the decrease intensifies while the absorbance for the non-hydrogen bonded form is increasing in the temperature range from 275 °C to 350 °C.

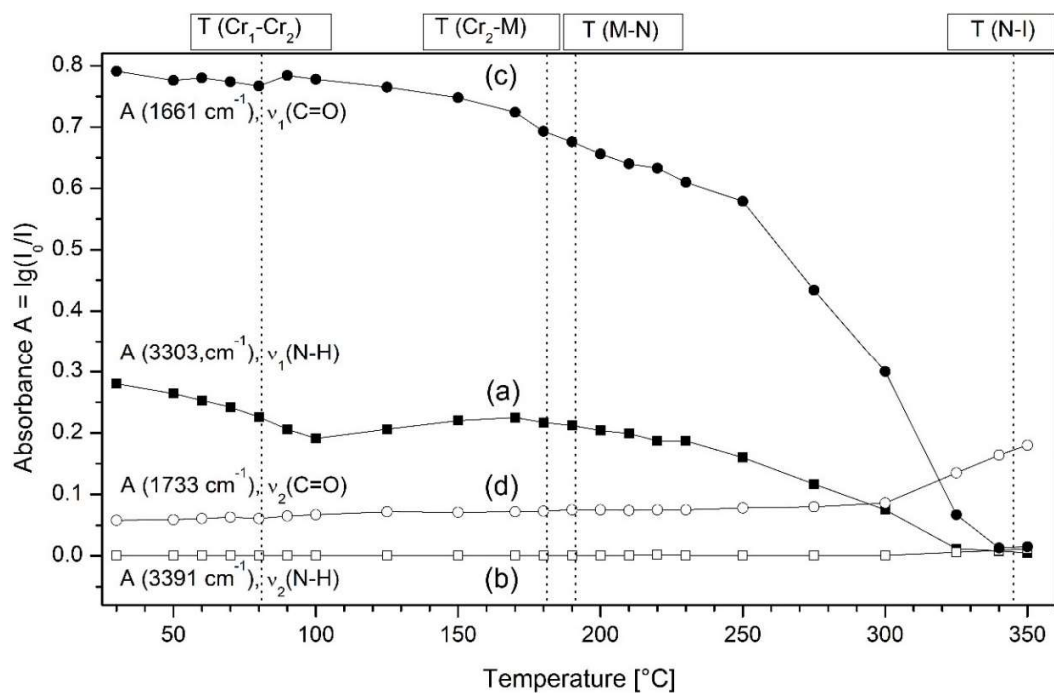


Figure 64: Infrared Spectroscopy absorbance of **3a** as a function of the temperature; circles:  $\nu(\text{C=O})$ , square:  $\nu(\text{N-H})$ , filled symbols: hydrogen bonded form  $\nu_1$ , unfilled symbols: non-hydrogen bonded form  $\nu_2$ ; vertical dashed lines: transition temperatures (second heating of Differential Scanning Calorimetry with 10 K/min).

### 3.6 Summary

In this chapter the thermal properties, mesophase behavior, and structure property relations of 1,3,5-benzenetrisamides (BTAs) with linear perfluorinated side chains were investigated. Two different BTA series bearing linear perfluorinated side chains of different lengths from three up to eight carbon atoms, one based on 1,3,5-triaminobenzene core and the other based on trimesic acid core were characterized. In addition, one 1,3,5-cyclohexanetrisamide (CTA) with a perfluorinated side chain length of seven carbon atoms based on (1*s*,3*s*,5*s*)-cyclohexane-1,3,5-tricarboxylic acid was investigated.

#### *Comparison of BTAs with different cores*

Regarding the *transition temperatures*, the BTAs based on 1,3,5-triaminobenzene have much lower clearing temperatures. The clearing temperature of the BTA with perfluorinated side chains of three carbon atoms based on 1,3,5-triaminobenzene **1a** is with 246 °C the highest clearing temperature of all investigated BTAs based on 1,3,5-triaminobenzene. In comparison to the BTAs based on trimesic acid, **2a** with a clearing temperature of 294 °C, this is still 48 degrees lower than the clearing temperature of the BTA with the same perfluorinated side chain length. Compound **2a** has the lowest clearing temperature of the BTAs based on trimesic acid. The same tendency can be found for the melting temperatures, but the difference is smaller. The mesophase range decreases with increasing linear perfluorinated side chain length for the BTAs based on 1,3,5-triaminobenzene. In this contrast, the BTAs based on trimesic acid show no tendency with increasing linear perfluorinated side chain length. The mesophase range differs from a small range of 35 degrees for the BTA with side chain length of five carbon atoms **2c**, to a broad range of 137 degrees for the BTA with side chain length of seven carbon atoms **2e**.

The *transition enthalpies* show the same tendency for both BTA series. The enthalpy of the melting temperature increases while the enthalpy for the clearing temperature decreases with increasing linear perfluorinated side chain length. In the case of the BTA series based on 1,3,5-triaminobenzene, the enthalpy of the clearing temperature falls below the enthalpy of the melting temperature for the BTAs with the longest linear perfluorinated side chains of seven (**1e**) and eight (**1f**) carbon atoms. This is not the case for the BTAs based on trimesic acid.

The difference in transition temperatures and enthalpies between the two BTA series can be explained by a different molecular structure. Albuquerque et al. showed that the amide groups of BTAs based on 1,3,5-triaminobenzenes are more planarized with the central benzene core and weaker hydrogen bonds are formed,<sup>91</sup> thus leading to a decrease in the

physical bonding strength of the BTA molecules. Therefore, lower energies are needed to break the hydrogen bonds resulting in lower clearing temperatures and enthalpies.

With regard to the *mesophase behavior*, columnar hexagonal ordered phases ( $\text{Col}_h$ ) were identified for all mesophases for the BTAs based on 1,3,5-triaminobenzene. The patterns of the BTAs based on trimesic acid allow no clear identification for columnar ordered phases. However, both BTA series show a linear increase of the column-to-column distance of 0.1 nm for every additional  $\text{CF}_2$  group in the linear perfluorinated side chains. This indicates that the BTAs based on trimesic acid also develop  $\text{Col}_h$  phases. This was additionally proven by shearing of the compounds in the mesophase under crossed polarizers with POM. Plastic crystalline mesophases were found for BTAs with shorter linear perfluorinated side chains of three carbon atoms (**1a**, **2a**) and four carbon atoms (**1b**) which is an indication that the compounds form higher ordered mesophases. With increasing linear perfluorinated side chain length, the molecular order in the mesophase decreases.

#### ***Comparison between BTAs and CTAs with linear perfluorinated and alkyl side chains***

The results of the phase behavior of the BTA and CTA compounds with linear perfluorinated side chains are compared to the results of the BTA and CTA compounds with the same molecular architecture, bearing linear alkyl side chains, as investigated by Timme et al.<sup>45,108</sup>

For BTAs with alkyl side chains, Timme found highly ordered or plastic crystalline columnar mesophases for BTAs based on trimesic acid bearing linear alkyl side chains. The higher ordered columnar hexagonal plastic crystalline ( $\text{Col}_{hp}$ ) mesophase was found for the BTAs with side chains up to six carbon atoms. Longer side chains result in the development of lesser-ordered columnar hexagonal ordered ( $\text{Col}_{ho}$ ) phases. The decrease in the molecular order in the mesophase could also be found for the BTAs bearing linear perfluorinated side chains.

Another similarity is the linear increase of the *intercolumnar distance* of about 0.1 nm per additional  $\text{CH}_2$  or  $\text{CF}_2$  group. The intercolumnar distance of a BTA based on trimesic acid with a linear perfluorinated side chain length of five carbon atoms has a value of 1.57 nm with linear alkyl and 1.58 nm with linear perfluorinated side chains in the mesophase. The intermolecular distance for the BTA with linear alkyl side chains is 0.35 nm, which is the same value found for the same BTA with linear perfluorinated side chains. This indicates that the mesophase structure of the investigated BTAs based on trimesic acid with linear alkyl or linear perfluorinated side chains is similar.

The most significant difference between the two BTA species are the values of the *clearing temperatures*. The BTAs bearing linear perfluorinated side chains show higher clearing

temperatures of about 300 °C, while the BTAs with linear alkyl side chains have clearing temperatures between 207 °C and 243 °C. This is a difference of more than 50 degrees. A significant difference can be found for the BTAs based on 1,3,5-triaminobenzene core. The BTAs with linear alkyl side chains of six and eight carbon atoms show no mesophases. Only the compound with ten carbon atoms in the side chains passes through a highly ordered unidentified plastic crystalline mesophase. In contrast, the BTAs with linear perfluorinated side chains of three up to eight carbon atoms based on 1,3,5-triaminobenzene core show mesophases between the solid state and the isotropic melt.

The *cyclohexane-based trisamide (CTA)* with linear perfluorinated side chains of seven carbon atoms is the only compound, which develops a columnar nematic mesophase ( $N_c$ ). Timme found a columnar nematic mesophase also for the CTA with linear alkyl side chains of the same length. The intermolecular distance is 0.47 nm for both CTA species. This same value indicates that the columns of the different CTA species are build up in the same way of stacking. With regard to the clearing temperature, the CTA with linear perfluorinated side chains has a value of about 30 degrees higher than the same CTA bearing linear alkyl side chains. The mesophase temperature range for the alkylated species is only about 30 degrees while for the CTA with linear perfluorinated side chains the range is much broader with 150 degrees.

## 4. Melt electrospinning of trisamides with linear perfluorinated side chains\*

Electrospinning is a technique for fiber fabrication by elongation of a jet through an electric field.<sup>117–122</sup> An electric field is applied to overcome the surface tension and to develop a jet of a desired material from solution, suspension, or melt.<sup>122,123</sup>

The largest area of *electrospinning is spinning from solution*.<sup>120,121</sup> The viscosity of the solution can be adjusted and the jet is additionally cooled by the solvent evaporation. The polymer chains are entangled in solution reducing the chance that the electrospun jet disrupts into droplets and electrospinning occurs. In the past years, many materials were fabricated to fibers by solution electrospinning. Examples are biopolymers such as peptides<sup>124–126</sup>, biodegradable polymers such as polycaprolactone<sup>127</sup>, commercial polymers such as PAN<sup>123</sup> and PMMA<sup>128</sup>, or high performance polyimides<sup>118,121</sup>.

In 2006, Long et al. showed that electrospinning to homogeneous fibers from solution with low molecular weight lecithin molecules is possible. He observed that it is necessary to have sufficient intermolecular interactions between the molecules which are acting quasi similar to chain entanglements in polymeric systems.<sup>129</sup> In the following years a lot of research in the field of electrospinning of supramolecular materials such as the fabrication of fibers from pillararenes<sup>130</sup>, heteroditopic monomers<sup>131</sup> or the incorporation of supramolecular compounds for modification of polymers after the electrospinning process<sup>132–134</sup> were reported. Also, a combination of a commercial polymer with a supramolecular material is possible. In a core-shell electrospinning approach where a PS core fiber was processed, which was seeded with trisamides as shell, Burgard et al. created a fiber morphology with off-standing branches, which showed unique properties in air filtration studies.<sup>135</sup>

When it comes to electrospinning of fluorinated materials, electrospinning of fluoropolymers was patented in 2018 by the Honeywell International Inc. which shows that the fabrication of materials and fibers containing fluorine is still a matter of interest.<sup>136</sup> Fluorinated polymers or polymers with perfluorinated substituents were used to process fiber mats<sup>137–140</sup> and membranes<sup>141–143</sup> with superhydrophobic surfaces or bioceramics for biomedical applications<sup>144</sup> by electrospinning. For example Govinna et al. produced membranes of electrospun blends with poly(vinylidene fluoride) and a random fluorinated copolymer for oil-water separation.<sup>145</sup> Nanofibrous materials of fluor-containing polymers and incorporated ZnO particles were prepared by electrospinning which showed antibacterial activity against a pathogenic microorganism.<sup>146</sup>

*\*part of the chapter is published in "Neugirg B.R.; Helfricht N.; Czich S.; Schmidt, H.-W.; Papastavrou G.; Fery A. Polymer* **2016**, 363–371, Long-range interaction forces between melt-electrospun 1,3,5-cyclohexanetrissamide fibers in crossed-cylinder geometry."

Beside solution electrospinning, *electrospinning from melt* is also a method to produce fibers, however mostly in the range of micrometer diameters. This field and its state of the art was recently reviewed in a chapter of a book from 2017 by Wunner et al.<sup>147</sup> As he describes, published work in this field is much less common than studies based on solution electrospinning. This can be explained by the fact that the fabrication of well-designed melt-based electrospinning devices is technically more demanding than assembling a laboratory-scaled bench top solution electrospinning machine. Nevertheless, if controlled appropriately, the produced fiber can be directed to the collector without instabilities, which, in combination with 3D moving stages, makes this technique a new 3D printing technique. A positive aspect from a process point of view is that no solvent is involved which eliminates toxicity.

In 2012, Singer et al. from our research group at the chair of Macromolecular Chemistry I at the University of Bayreuth reported for the first time melt electrospinning of 1,3,5-cyclohexane- (CTA) and 1,3,5-benzenetrisamides (BTA) into fibers.<sup>83</sup> One cyclohexane-1,3,5- and two types of 1,3,5-benzenetrisamides were selected differing in direction of the linkage of the amide groups to the core and in the core structure itself. It was possible to melt electrospin fibers from the isotropic phase of the BTA derivatives and from the nematic phase of the CTA derivative. The average fiber diameters varied around 0.5  $\mu\text{m}$  up to 12  $\mu\text{m}$  depending on the molecular structure and the electrospinning parameters. In a further publication, structure-property relations with respect to melt spinnability and fiber morphology were investigated in detail for over thirty different small molecules with self-assembly potential based on trisamides, bisamides and even tertiary 1,3,5-benzenetrisamides.<sup>148</sup> Several trisamide species formed reproducible fibers. Linear substituents facilitated the formation of uniform supramolecular nanofibers. Melt electrospun BTA fibers also proved to be mechanically robust.<sup>149,150</sup> In a publication of Kluge et al. in collaboration with our research group from 2012, the influence of the molecular structure on the mechanical properties of self-assembled 1,3,5-benzenetrisamide nanofibers was investigated. They found that the variation of the molecular structure allows the changing of the morphology of the fiber resulting in the possibility to tune the stiffness over a wide range.<sup>149</sup> In another study they compared the mechanical properties of electrospun fibers with fibers formed by self-assembly with the result, that fibers with comparable stiffness and modulus can be processed.<sup>150</sup>

In this thesis, melt electrospinning was used to form supramolecular fibers of BTAs with perfluorinated side chains. A schematic illustration of the instrumental setup as well as the fiber formation via melt electrospinning is shown in figure 65.

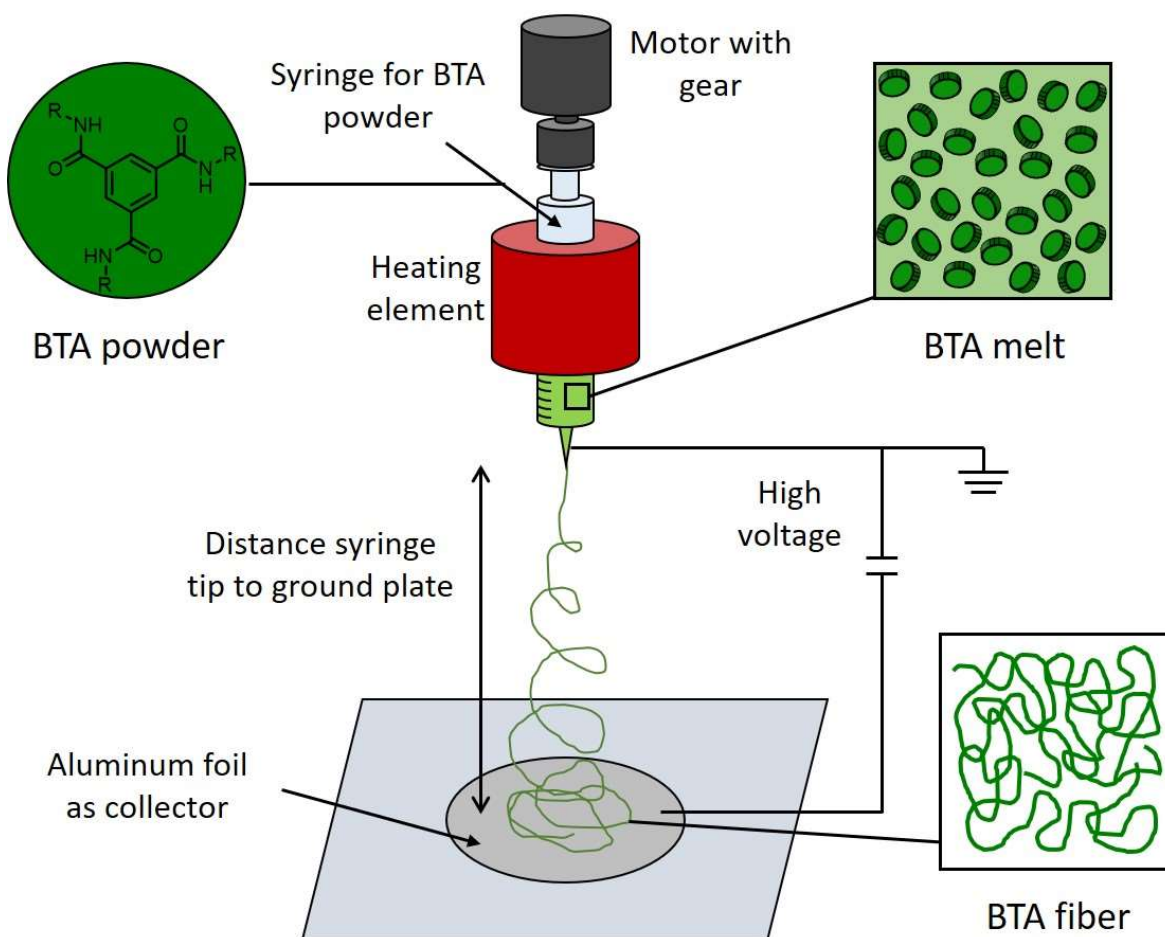


Figure 65: Schematic illustration of the instrumental setup and to produce supramolecular BTA fibers by the melt electrospinning technique. BTA powder is melted in a syringe with a surrounding heating element and extruded to supramolecular fibers with the aid of an electrical field. The diameter of the resulting fiber can be varied by different electrospinning parameters.

The BTA powder is transferred into a glass syringe and heated up into a low viscous melt such as the isotropic phase where the single molecules are randomly distributed and have no order. The spinning temperature is different for every material and it is important to find the right temperature to obtain fibers with good quality. The spinning temperature has to be selected with respect to the transition into the isotropic phase and decomposition onset.<sup>148</sup> After the melt reached the desired temperature, a gear motor, which is located at the

backside of the syringe, is started and the flow rate can be adjusted. The flow rate influences the fiber morphology and thickness directly.<sup>100</sup> The BTA melt is pumped through the needle tip, the inner spinneret diameter is around 0.5 mm, into an electric field region. In this region, the high voltage is applied and the syringe tip, as well as the collector at the bottom of the electric field region, is used as electrode. The working distance is the distance between the syringe tip and the collector. In combination with the applied high voltage, the distance determines the strength of the electric field. The electric field strength is usually between 100 kV/m and 500 kV/m. The required voltage mostly in the range of 7 kV to 50 kV can either be applied at the syringe tip or at the collector.<sup>100</sup> For example if a negative voltage is applied at the syringe tip, the melt is negatively charged and accelerated towards the collector, which is then either grounded or oppositely charged. It is possible to reverse the direction of the electric field which can be interesting for different electrical charge behavior of the melt.<sup>120,121,151,152</sup> In our equipment the distance between the syringe tip to the collector can be varied between 3 cm up to 25 cm.<sup>100</sup> It is important that the distance is long enough because the jet can be solidified before it reaches the collector to avoid the collection of coalesced fibers. The melt forms a pendant drop at the tip of the spinneret and begins to deform to a Taylor cone when the drop gets electrically charged in the presence of the electric field. A single fluidic jet is formed when the electrostatic charges overcome the surface tension and the viscoelastic properties of the melt, and the jet is then accelerated towards the collector. Internal stress caused by charge repulsion result in an alignment of the polymer chains along the fiber axis and a thinning of the jet can be observed. After a certain distance the jet begins to coil and buckle because of occurring instabilities which can be axisymmetric (Rayleigh instability or bending) or non-axisymmetric (whipping). The Rayleigh instability occurs when the applied electric field or the viscosity of the material is low. Bending and whipping instabilities arise from the charge-charge repulsion of the excess charges present in the jet. The instabilities result in a jet thinning and the thinning rate decreases when the temperature of the melt comes close to the melting temperature of the material.<sup>100,118</sup>

The objective of this chapter of the thesis is the processing of BTAs and one CTA with linear perfluorinated side chains to thin fibers with uniform surface by melt electrospinning. Therefore, the best parameters for different perfluorinated compounds, varying in their side chain length and core architecture, had to be found and optimized, meaning the *spinning temperature*  $T_{\text{Spin}}$ , the applied *electric voltage*  $U$ , and the *working distance*  $D$ . If the electrospinning process was successful, the quality of the resulting fibers should be evaluated with respect to the fiber size distribution and by SEM. Additionally, comparably thick fibers in the range of 5  $\mu\text{m}$  to 15  $\mu\text{m}$  in diameter should be produced for direct force measurements.

### 4.1 Experimental procedure

The experiments were performed in a custom designed electrospinning equipment (see 7.1 Appendix I: Analytical equipment and procedures) as follows: the BTA was placed into a glass syringe bearing a metal tip before it was placed in the heating element and connected to the gear motor. After the spinning temperature was reached, the system was equilibrated for at least 5 min to ensure that all material was melted. In the next step, the flow rate was adjusted before the high voltage was applied. Every experiment was finished after 5 to 10 seconds. The fibers were collected on an aluminum foil and later carefully transferred onto a SEM holder.

Several experiments were performed for every compound under different electrospinning parameters. The spinning temperature was varied between three different temperatures. The BTAs were always heated up to twenty degrees above their melting temperature ( $T_{Spin1}$ ), cooled down ten degrees ( $T_{Spin2}$ ), and another ten degrees ( $T_{Spin3}$ ). At every  $T_{Spin}$ , the applied voltage was varied between -15, -20, -30, -40 and -50 kV and for every voltage value, the working distance was also varied between 4, 6 and 9 cm, resulting in field strength values of 2.2 kV/cm up to 10 kV/cm. As it was the case that fibers could only be achieved in a field strength range of 3.3 kV/cm to 7.5 kV/cm, only results within this range are shown and discussed in the following. In our equipment, the high voltage is applied to the collector and positively charged at the needle tip. This means that the collector is negatively charged which results in a field direction from tip to ground plate. To express this field direction, negative voltages are given. The flow rate was always held constant at 200  $\mu$ L/h.

### 4.2 Characterization methods

#### *Scanning Electron Microscopy (SEM)*

The best possibility to get an insight and to take images of the resulting morphologies of the produced fibers is the observation by Scanning Electron Microscopy (SEM). When the beam hits and penetrates the sample, the energy exchange results in the reflection of high-energy electrons by elastic scattering, emission of secondary electrons by inelastic scattering and the emission of electromagnetic radiation. The samples are sputtered with a thin platinum layer of about 2 nm prior to SEM imaging. In this thesis the most common standard detection mode, the Secondary Electrons (SE) detection mode was used to get images. SEM images of the electrospun fibers were taken to determine the fiber quality with respect to the fiber shape, surface morphology, and to evaluate the fiber diameter and fiber size distribution.



### 4.3 Selected trisamides

Three different trisamides with linear perfluorinated side chains, two BTAs and one CTA, were selected for the melt electrospinning experiments. Figure 67 shows the chemical structures.

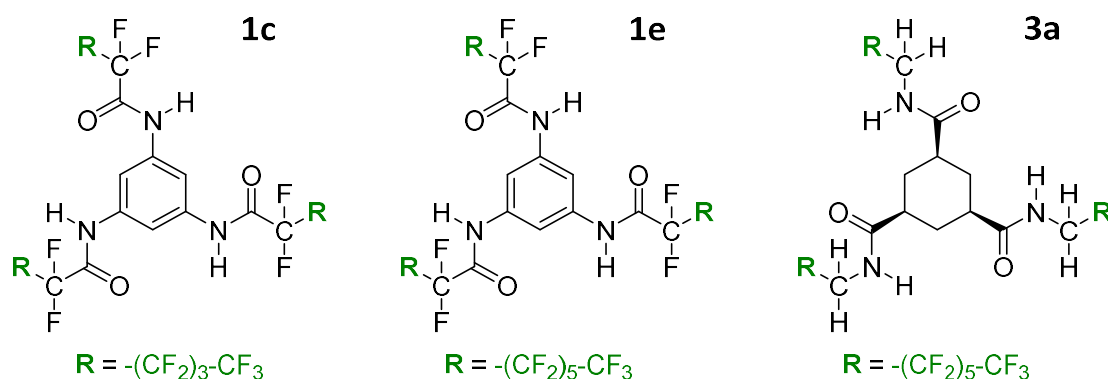


Figure 67: Chemical structures of the benzene trisamides **1c** and **1e**, and the cyclohexane trisamide **3a** selected for the melt electrospinning studies.

The two BTA compounds are based on 1,3,5-triaminobenzene bearing linear perfluorinated side chains of five (**1c**) and seven (**1e**) carbon atoms. Both form a columnar mesophase between the crystalline state and the isotropic phase. The CTA **3a** is based on (1*s*,3*s*,5*s*)-cyclohexane-1,3,5-tricarboxylic acid with linear perfluorinated side chains of seven carbon atoms and forms a nematic phase before the transition into the isotropic phase upon heating. The nematic phase with its low viscosity is very similar to the isotropic phase. Therefore, it should be possible to process fibers from the nematic mesophase by melt electrospinning. In the following, only the results of **1c** and **3a** will be discussed in more detail, while the results of **1e** can be found in the appendix (7.2 Appendix II: Additional data).

### 4.4 Melt electrospinning experiments with the aim to obtain thin fibers

Before the electrospinning results of the BTAs **1c** and CTA **3a** are presented, the phase behavior and weight loss (TGA) will be discussed. Both are important for the selection of the electrospinning temperatures. Subsequently, the resulting fibers imaged by SEM and the corresponding fiber size distributions are discussed. For every different *electrospinning temperature*  $T_{spin}$  and *working distance*  $D$ , a different figure with varying applied voltage and corresponding electric field strength will be shown to directly compare the change of fiber quality produced at different applied voltages. The fiber diameter results of all electrospinning experiments are always summarized in tables at the end of the subchapters of every compound.

#### 4.4.1 Electrospinning of the BTA with undecafluoropentyl side chains (**1c**)

The phase behavior of **1c** was already discussed in chapter 3 and is summarized in figure 68 by the results from the first heating and cooling curve from DSC analysis. Included is also the temperature at 10 % initial weight loss ( $T_{-10\text{wt}\%}$ ) from TGA. The three selected electrospinning temperatures  $T_{\text{Spin}1}$ ,  $T_{\text{Spin}2}$  and  $T_{\text{Spin}3}$  are marked in green. In the publication by Singer et al., a spinning temperatures of twenty degrees above  $T_C$  were found to be the best for electrospinning of structurally related BTAs without perfluorinated side chains<sup>100</sup>. Therefore,  $T_{\text{Spin}1}$  was selected at 236 °C for **1c**.  $T_{\text{Spin}2}$  was selected ten degrees below at 226 °C, after it was equilibrated at 236 °C. Upon cooling, **1c** shows an undercooling effect of 13 degrees at the transition from the isotropic to the mesophase. Therefore, it is possible to select  $T_{\text{Spin}3}$  at 216 °C because **1c** is then still in the isotropic phase.

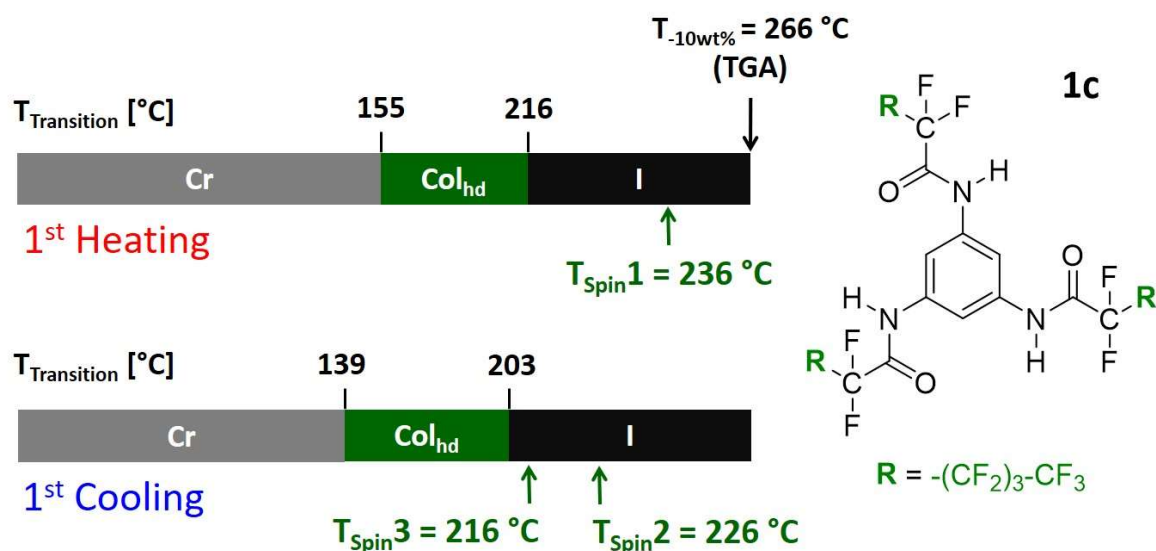


Figure 68: Trisamide **1c** with phase transition temperatures at first heating and cooling (Differential Scanning Calorimetry, heating and cooling rate 10 K/min), type of mesophase (Cr: crystalline, Col: columnar mesophase, h: hexagonal, d: disordered, I: isotropic), temperature of 10 % weight loss, and the selected spinning temperatures  $T_{\text{Spin}1}$ ,  $T_{\text{Spin}2}$  and  $T_{\text{Spin}3}$  in green.

### Electrospinning results of **1c** at a spinning temperature of 236 °C

For different *working distances* of 4 cm (figure 69), 6 cm (figure 70), and 9 cm (figure 71), the electrospinning results of **1c** obtained at a spinning temperature of 236 °C at different applied voltages are shown. In addition, the histograms of the average fiber diameter and fiber size distributions are shown.

At a *working distance* of 4 cm (figure 69), fibers at applied voltages of -15, -20, and -30 kV were obtained corresponding to electrical field strengths of 3.8, 5.0 and 7.5 kV/cm, respectively.

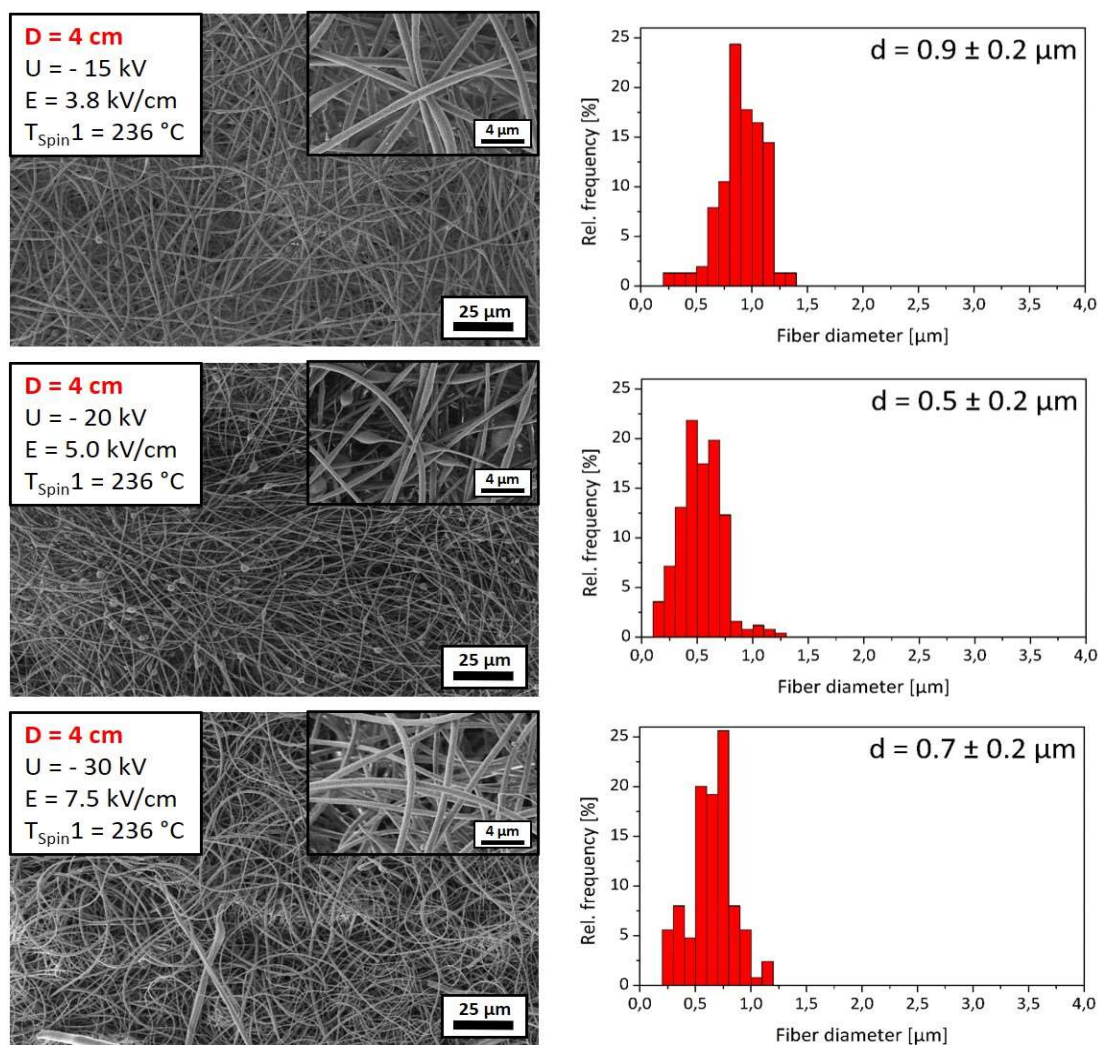


Figure 69: Scanning Electron Microscopy images (left) of electrospun fibers of **1c** produced at  $T_{\text{Spin}1}$  of 236 °C, **working distance D of 4 cm** and an electrospinning applied voltage  $U$  of -15 (top), -20 (middle), and -30 kV (bottom). Bar diagrams (right) show the fiber diameter dependent on the relative frequency of an evaluation of  $n = 150$  fiber diameters and the average value including standard deviation.

The image at -15 kV show fibers with a uniform surface and good thickness homogeneity but also a few beads can be found. The average fiber diameter is  $0.9 \pm 0.2 \mu\text{m}$ . At an applied voltage of -20 kV, additional beads are present, but the fibers have also a good quality. The average fiber diameter without beads is  $0.5 \pm 0.2 \mu\text{m}$ . The fibers obtained from an applied voltage of -30 kV show no beads, have therefore the best fiber quality with uniform surface, and are also thin with an average fiber diameter of  $0.7 \pm 0.2 \mu\text{m}$ .

Regarding the images of the samples produced at a longer *working distance of 6 cm* (figure 70), fibers were formed at applied voltages of -20, -30 and -40 kV corresponding to electrical field strengths of 3.3, 5.0 and 6.7 kV/cm, respectively.

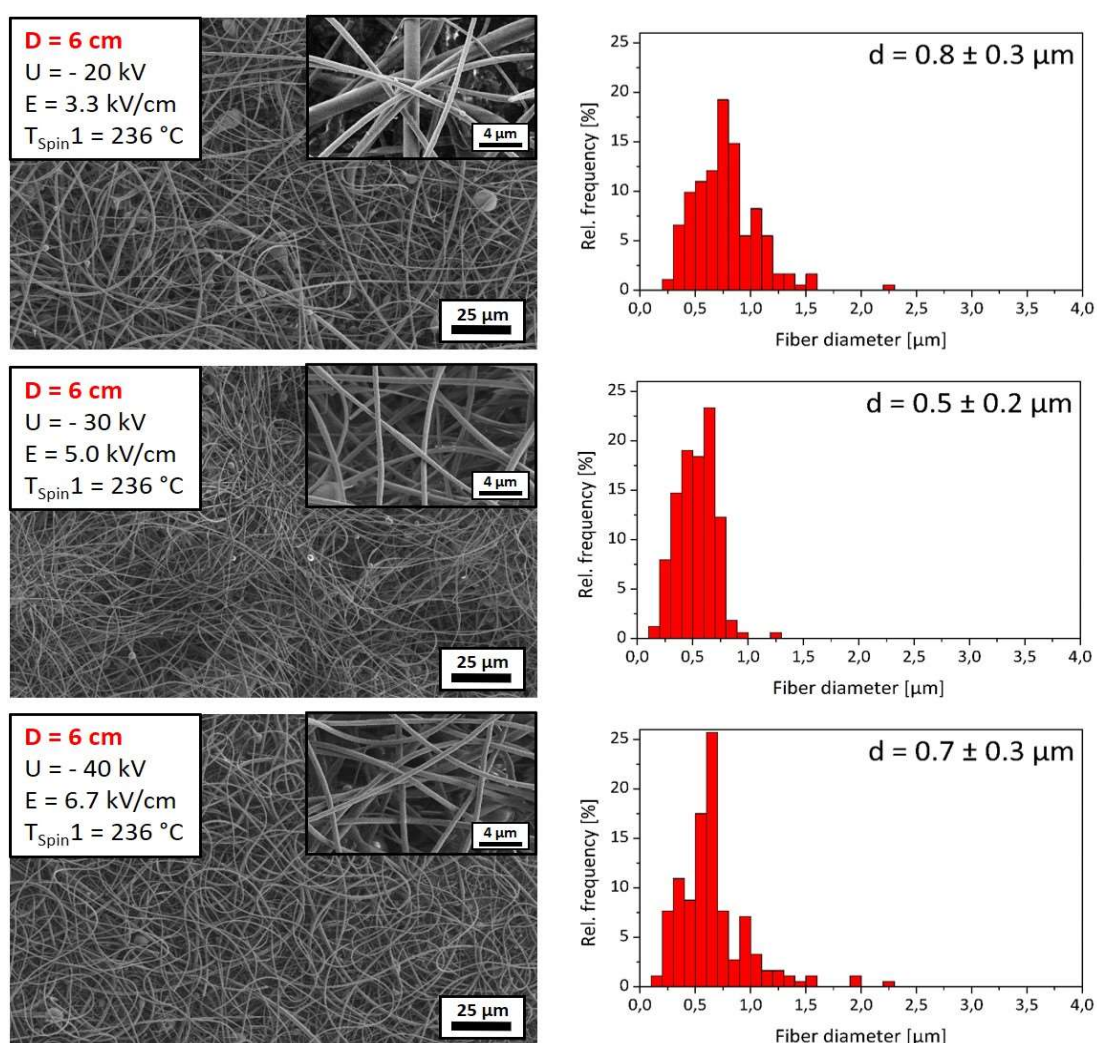


Figure 70: Scanning Electron Microscopy images (left) of electrospun fibers of **1c** produced at  $T_{Spin1}$  of 236 °C, **working distance D of 6 cm** and an electrospinning applied voltage  $U$  of -20 (top), -30 (middle), and -40 kV (bottom). Bar diagrams (right) show the fiber diameter dependent on the relative frequency of an evaluation of  $n = 150$  fiber diameters and the average value including standard deviation.

Fibers obtained at an applied voltage of -20 kV have beads, but show a uniform surface and also good thickness homogeneity with an average fiber diameter of  $0.8 \pm 0.3 \mu\text{m}$ . Thinner fibers are obtained with the best quality processed at an applied voltage of -30 kV and average fiber diameter of  $0.5 \pm 0.2 \mu\text{m}$ . At -40 kV, the average fiber diameter of the obtained fibers is  $0.7 \pm 0.3 \mu\text{m}$  with uniform surface, but also a few thicker fibers with about over  $2 \mu\text{m}$  in diameter.

At a *working distance of 9 cm*, (figure 71) fibers could be formed at applied voltages of -30, -40, and -50 kV corresponding to electrical field strengths of 3.3, 4.4 and 5.6 kV/cm, respectively.

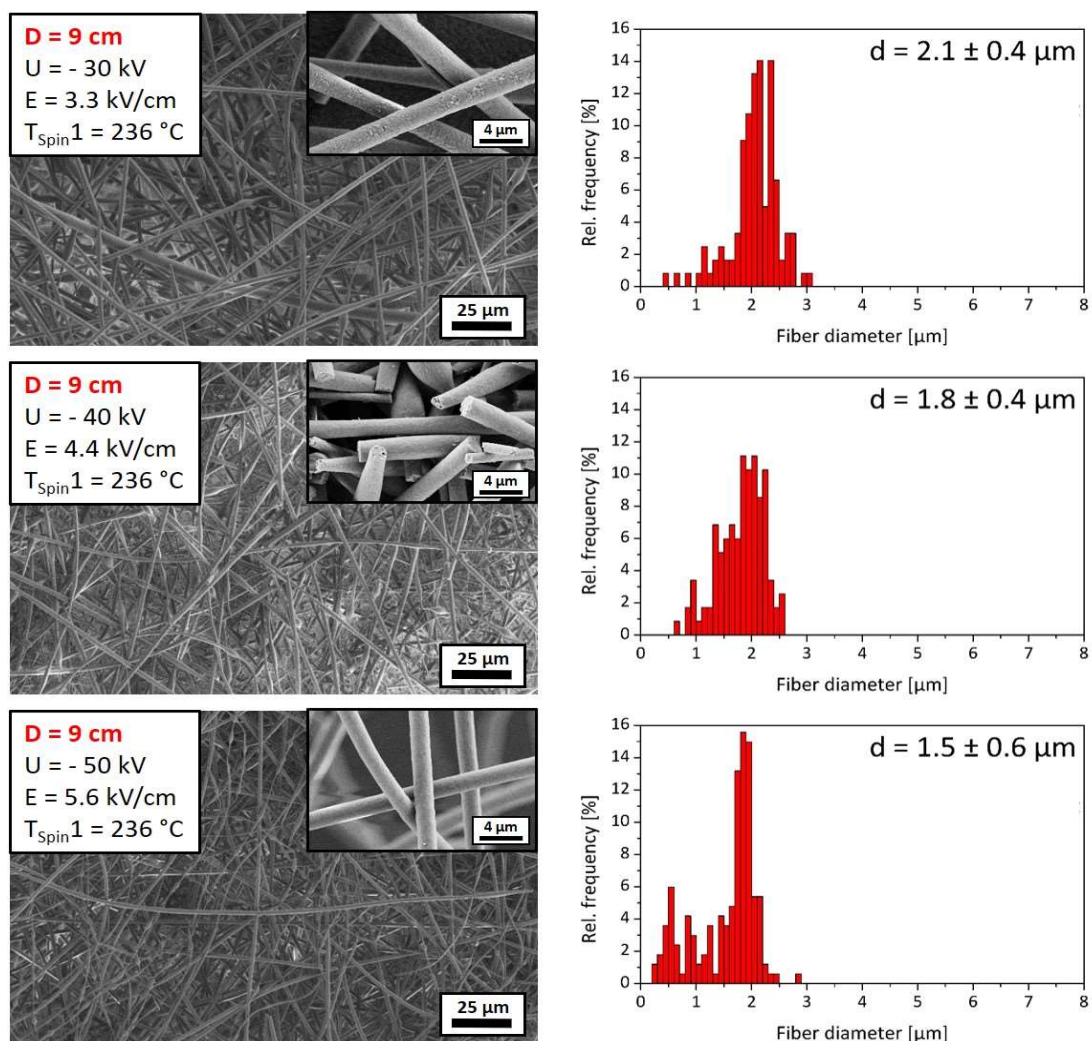


Figure 71: Scanning Electron Microscopy images (left) of electrospun fibers of **1c** produced at  $T_{Spin1}$  of 236 °C, **working distance D of 9 cm** and an electrospinning applied voltage  $U$  of -30 (top), -40 (middle), and -50 kV (bottom). Bar diagrams (right) show the fiber diameter dependent on the relative frequency of an evaluation of  $n = 150$  fiber diameters and the average value including standard deviation.

All the fibers in figure 71 have a uniform surface and the average fiber diameters are at least twice as thick as the fibers obtained at lower working distances. The average fiber diameters are in the range of  $2.1 \pm 0.4 \mu\text{m}$  ( $U = -30 \text{ kV}$ ),  $1.8 \pm 0.4 \mu\text{m}$  ( $U = -40 \text{ kV}$ ), and  $1.5 \pm 0.6 \mu\text{m}$  ( $U = -50 \text{ kV}$ ), respectively, with low standard deviation indicating good thickness homogeneity.

### **Electrospinning results of 1c at a spinning temperature of 226 °C**

For different *working distances* of 4 cm (figure 72), 6 cm (figure 73), and 9 cm (figure 74), the electrospinning results of **1c** obtained at a spinning temperature of 226 °C at different applied voltages are shown. In addition, the histograms of the average fiber size and fiber size distributions are shown.

Electrospinning at a *working distance* of 4 cm (figure 72) was successful at applied voltages of -20 and -30 kV corresponding to electrical field strengths of 5.0 and 7.5 kV/cm, respectively. At lower voltage, the material dropped from the syringe tip and at higher voltage a flashover occurred. The picture of the sample produced at -20 kV shows many beads indicating that the viscosity of the melt is too high. The resulted fibers have an average fiber diameter of  $0.8 \pm 0.3 \mu\text{m}$ . At higher applied voltage of -30 kV, only a few beads can be found. The fibers have a uniform surface with homogeneous thickness of  $1.0 \pm 0.4 \mu\text{m}$  in diameter.

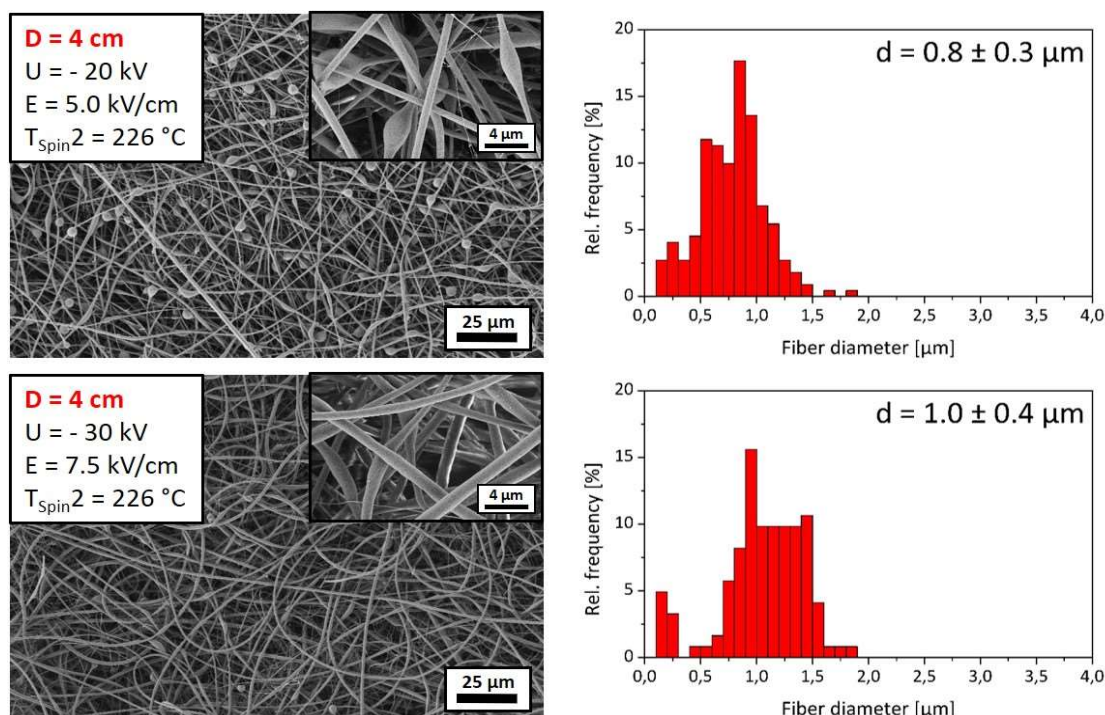


Figure 72: Scanning Electron Microscopy images (left) of electrospun fibers of **1c** produced at  $T_{\text{Spin}2}$  of 226 °C, **working distance D of 4 cm** and an electrospinning applied voltage  $U$  of -20 (top) and -30 kV (bottom). The bar diagrams (right) show the fiber diameter dependent on the relative frequency of an evaluation of  $n = 150$  fiber diameters and the average value including standard deviation.

At a higher *working distance* of 6 cm, (figure 73) fibers were processed at applied voltages of -20, -30 and -40 kV corresponding to electrical field strengths of 3.3, 5.0 and 6.7 kV/cm, respectively. A low average fiber diameter of 0.5  $\mu\text{m}$  was found for the fibers processed at the lowest applied voltage, but also a high standard deviation of 0.3  $\mu\text{m}$  was found. The best fiber quality was achieved at -30 kV with an average fiber diameter of 0.8  $\mu\text{m}$  and a low standard deviation of 0.2  $\mu\text{m}$ . This can also be seen by the presence of only homogeneous fibers with uniform surface by investigation of the SEM images. Thicker fibers were obtained at -40 kV but the standard deviation is high ( $0.8 \pm 0.5 \mu\text{m}$ ).

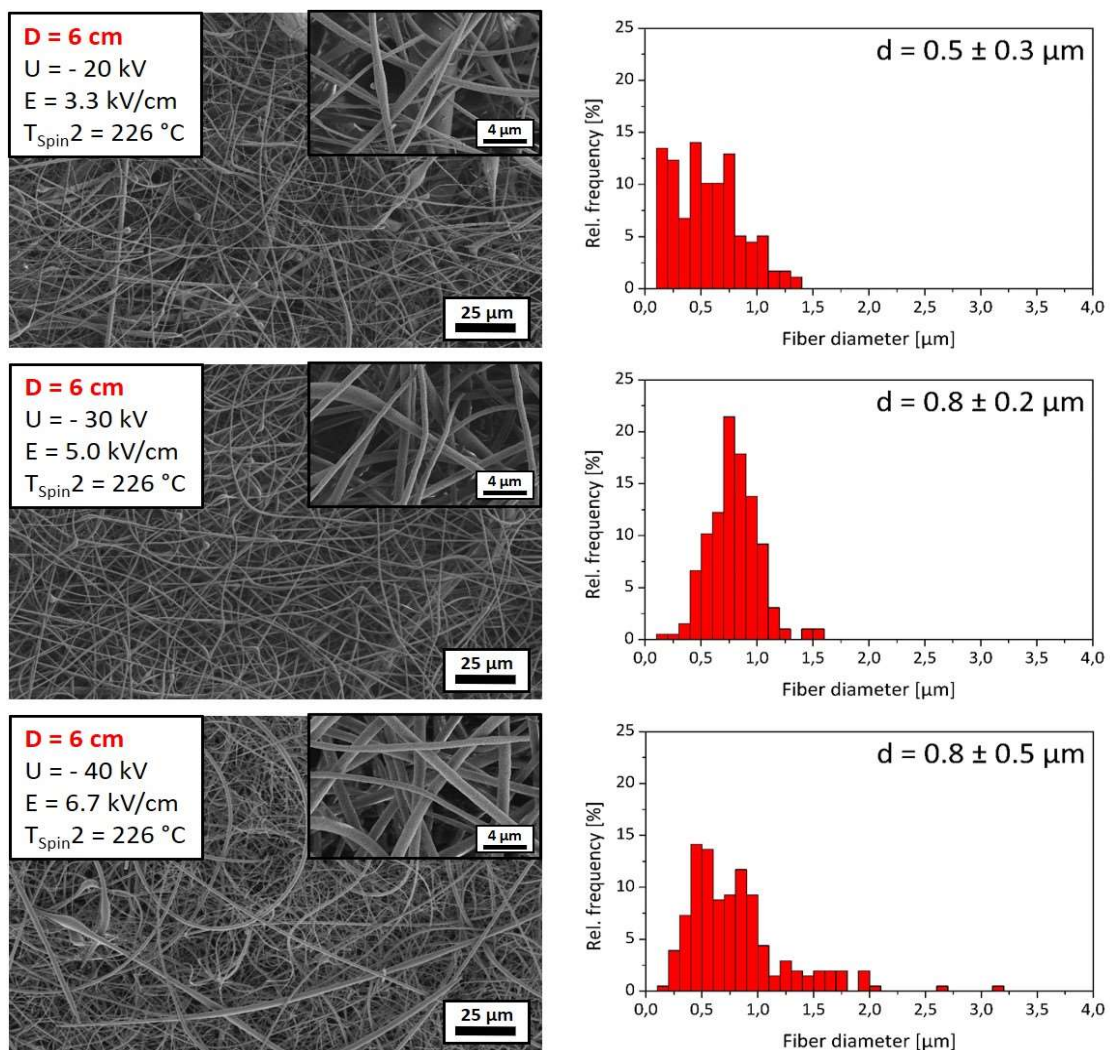


Figure 73: Scanning Electron Microscopy images (left) of electrospun fibers of **1c** produced at  $T_{\text{Spin}2}$  of 226 °C, **working distance D** of 6 cm and an electrospinning applied voltage  $U$  of -20 (top), -30 (middle), and -40 kV (bottom). Bar diagrams (right) show the fiber diameter dependent on the relative frequency of an evaluation of  $n = 150$  fiber diameters and the average value including standard deviation.

The electrospinning at a *working distance of 9 cm* (figure 74) was possible at applied voltages of -30, -40 and -50 kV corresponding to electrical field strengths of 3.3, 4.4 and 5.6 kV/cm, respectively. The best fiber quality can be found for the fibers processed at -30 kV, but with a comparably high average fiber diameter of  $2.6 \pm 0.6 \mu\text{m}$  with regard to the other fiber samples. With a low standard deviation, the thickness homogeneity is in a very good range. Processed at -40 kV, a few beads can be found while the average fiber diameter of the fibers is in the range of  $1.7 \mu\text{m}$  with a standard deviation of  $0.8 \mu\text{m}$ . Processed at the highest applied voltage of -50 kV, the fibers have many beads resulting in a low fiber quality. The fiber diameter remains in the range of  $1.7 \mu\text{m}$  as it is also the case for fibers processed at -40 kV, and the standard deviation is still high with  $0.9 \mu\text{m}$ .

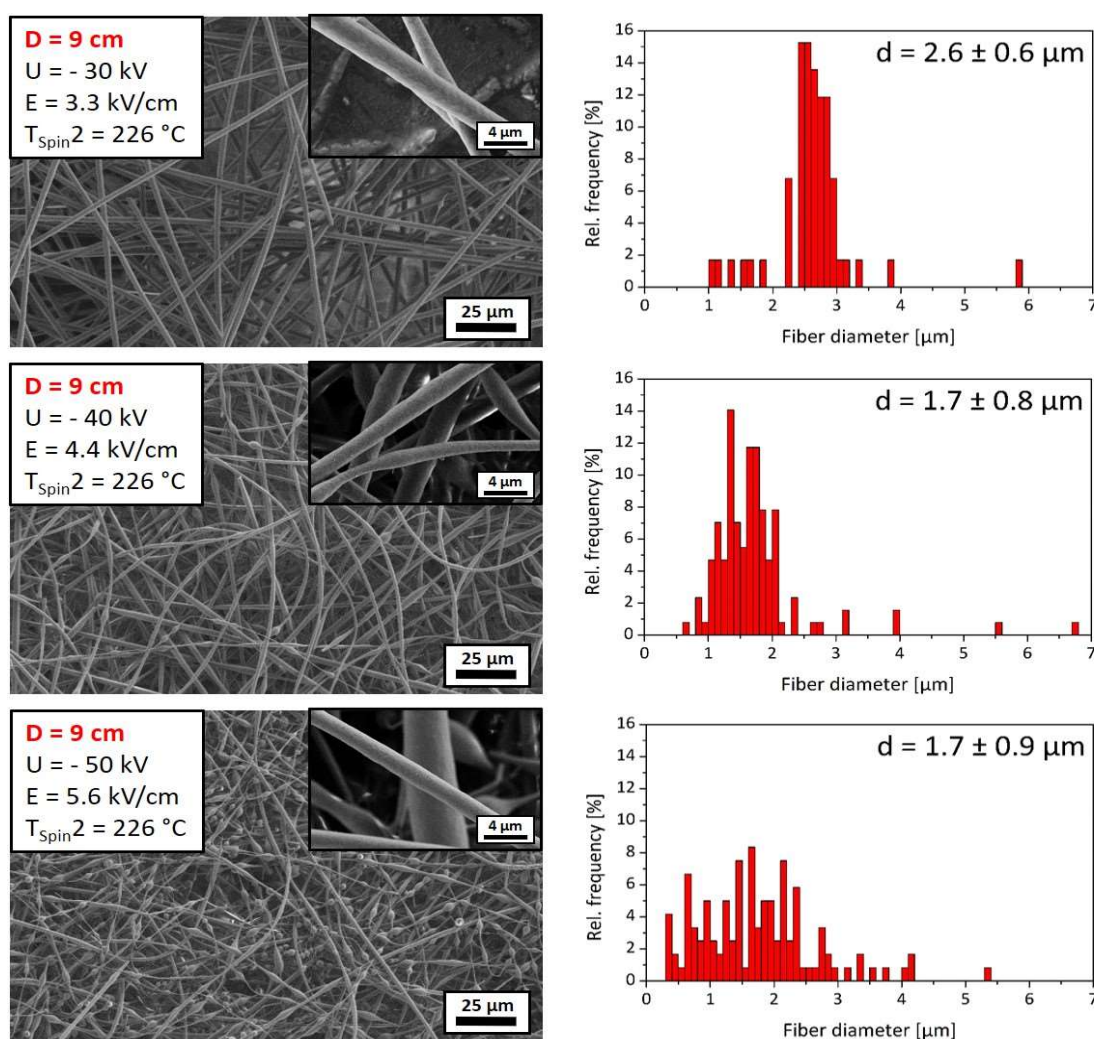


Figure 74: Scanning Electron Microscopy images (left) of electrospun fibers of **1c** produced at  $T_{\text{Spin}2}$  of  $226 \text{ }^\circ\text{C}$ , **working distance D of 9 cm** and an electrospinning applied voltage  $U$  of -30 (top), -40 (middle), and -50 kV (bottom). Bar diagrams (right) show the fiber diameter dependent on the relative frequency of an evaluation of  $n = 150$  fiber diameters and the average value including standard deviation.

### Electrospinning results of **1c** at a spinning temperature of 216 °C

The next three figures show the electrospinning results of **1c** at the three different *working distances* of 4 cm (figure 75), 6 cm (figure 76), and 9 cm (figure 77), obtained from the melt electrospinning at a spinning temperature of 216 °C. In addition, the histograms of the average fiber size and fiber size distributions are shown.

At a *working distance* of 4 cm (figure 75), it was possible to electrospin fibers at applied voltages of -20, -30 kV corresponding to electrical field strengths of 5.0 and 7.5 kV/cm, respectively. Fibers with uniform surface and good qualities were obtained proven by a high homogeneity of the fiber diameters. The average fiber diameters are  $1.1 \pm 0.3 \mu\text{m}$  processed at -20 kV and  $1.4 \pm 0.4 \mu\text{m}$  at -30 kV.

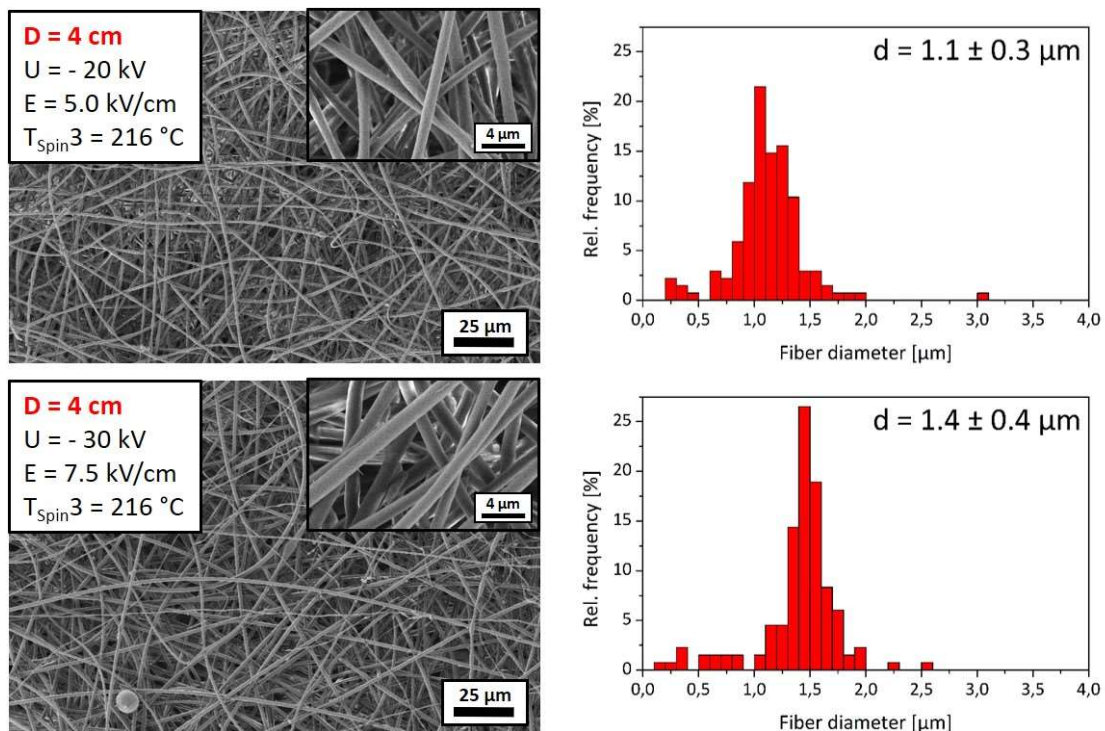


Figure 75: Scanning Electron Microscopy images (left) of electrospun fibers of **1c** produced at  $T_{\text{Spin}3}$  of 216 °C, **working distance D of 4 cm** and an electrospinning applied voltage  $U$  of -20 (top) and -30 kV (bottom). The bar diagrams (right) show the fiber diameter dependent on the relative frequency of an evaluation of  $n = 150$  fiber diameters and the average value including standard deviation.

The results of fibers processed at a *working distance of 6 cm* can be seen in figure 76. Fibers were obtained at applied voltages of -30 and -40 kV corresponding to electrical field strengths of 5.0 and 6.7 kV/cm, respectively. The average fiber diameter of the fibers obtained at the lower applied voltage is also lower with  $0.8 \pm 0.3 \mu\text{m}$  than the average diameter of the fibers processed at higher applied voltage with  $1.2 \pm 0.3 \mu\text{m}$ . The good fiber quality is proven by the low standard deviation and the fiber morphologies as it can be seen in the SEM images. The fibers are roundly shaped with homogeneous thickness fabricated at both applied voltages, only a few beads can be found.

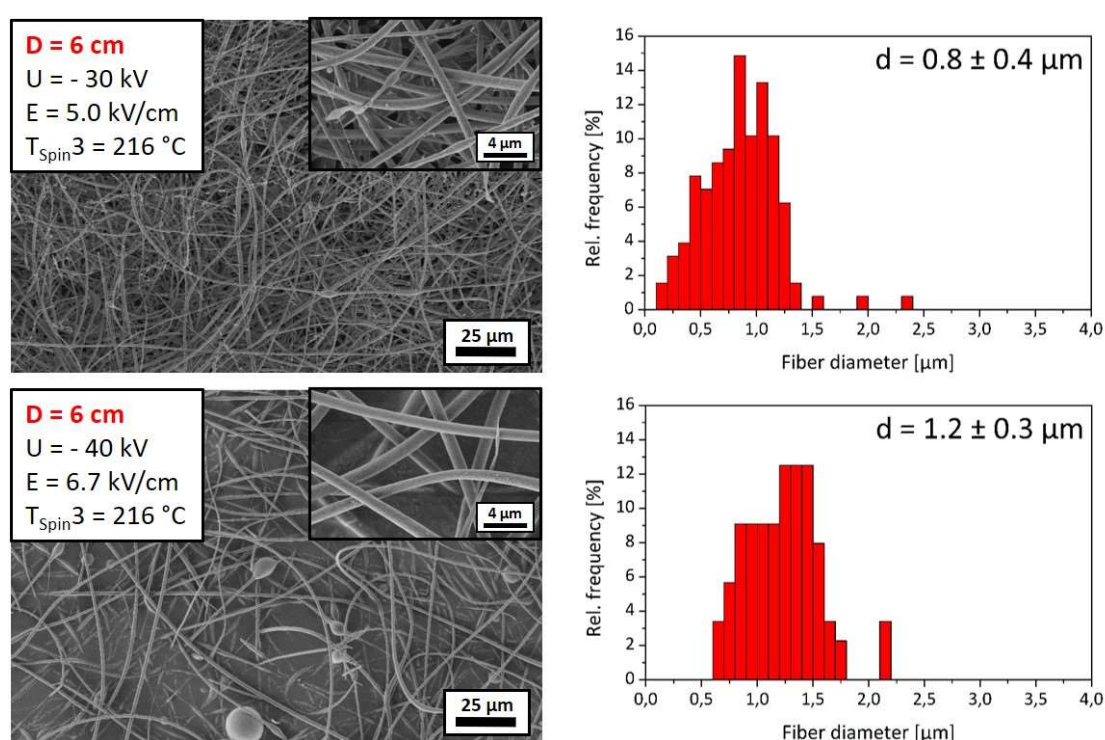


Figure 76: Scanning Electron Microscopy images (left) of electrospun fibers of **1c** produced at  $T_{\text{Spin}3}$  of  $216 \text{ }^\circ\text{C}$ , **working distance D of 6 cm** and an electrospinning applied voltage  $U$  of -30 (top) and -40 kV (bottom). The bar diagrams (right) show the fiber diameter dependent on the relative frequency of an evaluation of  $n = 150$  fiber diameters and the average value including standard deviation.

Processing at a longer *working distance of 9 cm* (figure 77), it was possible to obtain fibers at applied voltage of -30, -40 and -50 kV corresponding to electrical field strengths of 3.3, 4.4 and 5.6 kV/cm, respectively. Observation of the SEM images of the fibers processed at -30 kV reveals fibers with uniform surface and homogeneously average fiber diameter of  $1.7 \pm 0.4 \mu\text{m}$ . The fiber quality decreases with increasing applied voltage but the standard deviation is still around half of the average fiber diameter. Many thin fibers are present on

both fiber samples processed at -40 and -50 kV with an average fiber diameter of about  $0.6 \pm 0.2 \mu\text{m}$  and  $0.6 \pm 0.4 \mu\text{m}$ , respectively. The higher standard deviation of the fiber sample processed at -50 kV is due to a few fibers with much higher diameter values of more than  $2.5 \mu\text{m}$ .

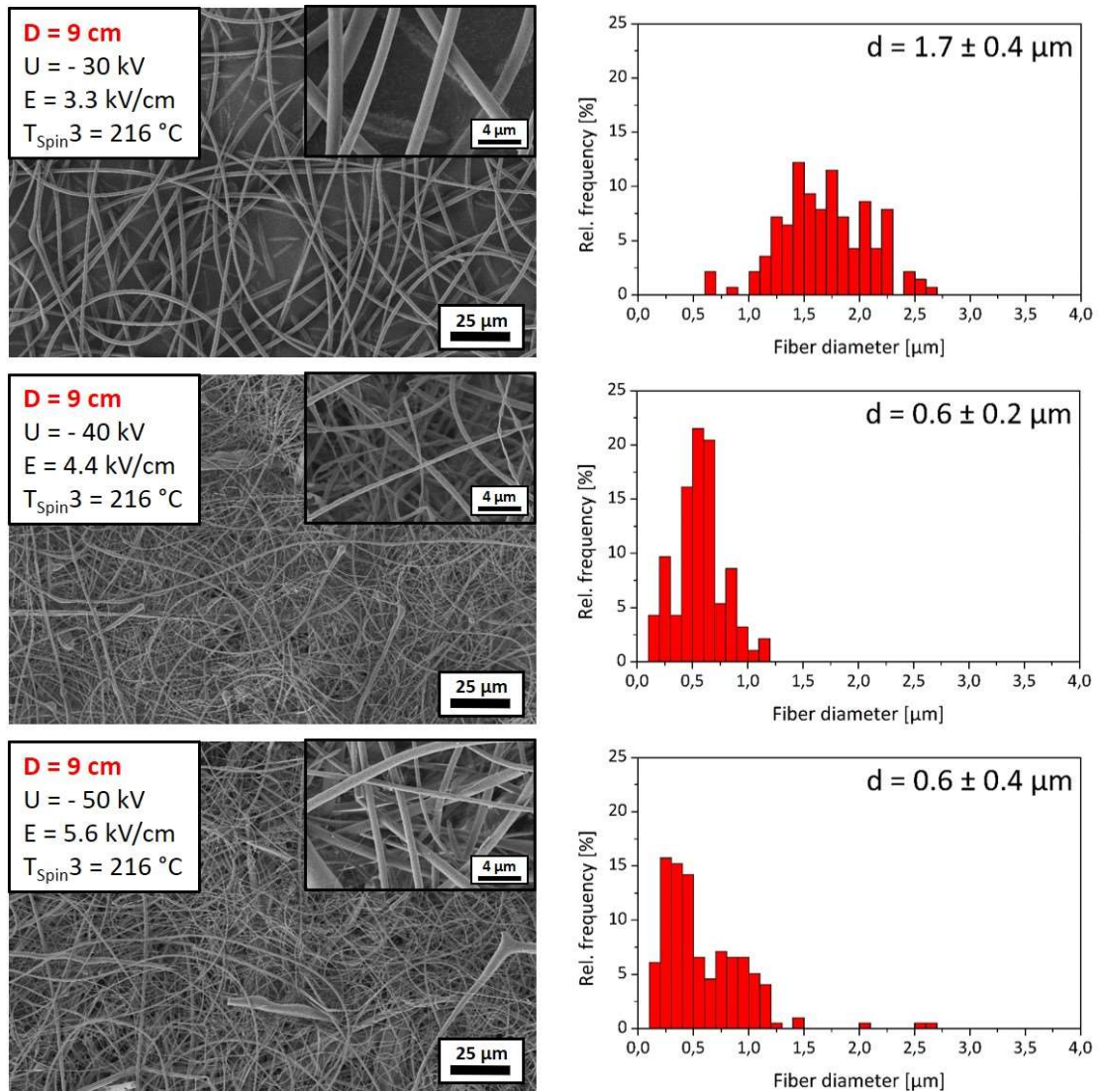


Figure 77: Scanning Electron Microscopy images (left) of electrospun fibers of **1c** produced at  $T_{\text{Spin}3}$  of  $216 \text{ }^\circ\text{C}$ , **working distance D of 9 cm** and an electrospinning applied voltage  $U$  of -30 (top), -40 (middle), and -50 kV (bottom). Bar diagrams (right) show the fiber diameter dependent on the relative frequency of an evaluation of  $n = 150$  fiber diameters and the average value including standard deviation.

The results of all electrospinning experiments with **1c** are summarized in table 5. Compound **1c** could be processed by melt electrospinning to fibers with average fiber diameters ranging between 0.5 to 2.6  $\mu\text{m}$  depending on the electrospinning parameters. The thinnest fibers with the best fiber quality of  $0.5 \pm 0.2 \mu\text{m}$  were produced at a spinning temperature of 236  $^{\circ}\text{C}$ , 6 cm working distance and applied voltage of  $U = -30 \text{ kV}$  ( $E = 5.0 \text{ kV/cm}$ ). Second best results with average fiber diameter of  $0.7 \pm 0.3 \mu\text{m}$  were obtained at the same spinning temperature and working distance but an applied voltage of  $U = -40 \text{ kV}$  ( $E = 6.7 \text{ kV/cm}$ ). For other parameter sets, thinner average fiber diameters than  $0.7 \mu\text{m}$  could be obtained, but their fiber quality is not as good in terms of bead formation or uniformity. This indicates that the highest electrospinning temperature as well as a working distance of 6 cm, resulting in electric field strengths of  $E = 5.0 \text{ kV/cm}$  and  $6.7 \text{ kV/cm}$ , are the best parameters to achieve good fiber qualities for this compound.

Table 5: Average fiber diameters including standard deviations of the electrospinning results of **1c** dependent on the electrospinning temperature  $T_{\text{Spin}}$  and the applied electric field strength  $E$  (with the corresponding parameter combination of working distance  $D$  and applied high voltage  $U$ ). The best results are shown in green.

$T_{\text{Spin}}$ ( $^{\circ}\text{C}$ ) $E$ (kV/cm)		$T_{\text{Spin}1} = 236$	$T_{\text{Spin}2} = 226$	$T_{\text{Spin}3} = 216$
		<b>3.3</b> D = 6 cm; U = -20 kV	$0.8 \pm 0.3 \mu\text{m}^*$	$0.5 \pm 0.3 \mu\text{m}^*$
<b>3.3</b> D = 9 cm; U = -30 kV	$2.1 \pm 0.4 \mu\text{m}$	$2.6 \pm 0.6 \mu\text{m}$	$1.7 \pm 0.4 \mu\text{m}$	
<b>3.8</b> D = 4 cm; U = -15 kV	$0.9 \pm 0.2 \mu\text{m}$	droplet formation	droplet formation	
<b>4.4</b> D = 9 cm; U = -40 kV	$1.8 \pm 0.4 \mu\text{m}$	$1.7 \pm 0.8 \mu\text{m}^*$	$0.6 \pm 0.2 \mu\text{m}^*$	
<b>5.0</b> D = 4 cm; U = -20 kV	$0.5 \pm 0.2 \mu\text{m}^*$	$0.8 \pm 0.3 \mu\text{m}^*$	$1.1 \pm 0.3 \mu\text{m}$	
	D = 6 cm; U = -30 kV	<b><math>0.5 \pm 0.2 \mu\text{m}</math></b>	$0.8 \pm 0.2 \mu\text{m}^*$	$0.8 \pm 0.4 \mu\text{m}^*$
<b>5.6</b> D = 9 cm; U = -50 kV	$1.5 \pm 0.6 \mu\text{m}$	$1.7 \pm 0.9 \mu\text{m}^*$	$0.6 \pm 0.4 \mu\text{m}^*$	
<b>6.7</b> D = 6 cm; U = -40 kV	<b><math>0.7 \pm 0.3 \mu\text{m}</math></b>	$0.8 \pm 0.5 \mu\text{m}$	$1.2 \pm 0.3 \mu\text{m}^*$	
<b>7.5</b> D = 4 cm; U = -30 kV	$0.7 \pm 0.2 \mu\text{m}^*$	$1.0 \pm 0.4 \mu\text{m}^*$	$1.4 \pm 0.4 \mu\text{m}$	

\*fibers of this sample have beads or show high thickness inhomogeneity alongside the fiber direction

Overall, no other clear tendencies for increasing or decreasing electrospinning temperature, working distance and applied electric field on the average fiber diameters can be found. For example, at a low electric field of  $E = 3.3$  kV/cm, the fiber diameter results for different parameter combinations differ strongly, which is not the case at an electric field of 5.0 kV/cm. This shows that not only the applied electric field itself, but also the single parameters of working distance and applied voltage play a certain role for the resulting fiber diameters. A possible explanation for the different results at the different parameter combinations can be the nature of the highly fluorinated compound and its phase behavior. Because of the very low surface tension of highly fluorinated substances<sup>3</sup>, it is possible that a proper Taylor cone cannot be developed and the melt simply wets the syringe tip in an uncontrolled manner, influencing the whole electrospinning procedure. Another reason can be the low sublimation temperature compared to completely alkylated counterparts. It is possible that some of the material, which resides in the melt, leaving the syringe tip is directly sublimating and is then no longer part of the electrospinning process. This uncontrollable sublimation would also cause undetermined changes in the fiber formation, for example resulting thickness deviations.

The same experiments as they were performed with BTA **1c**, were done with *N,N',N''-1,3,5-benzenetriyl-tris[2,2,3,3,4,4,5,5,6,6,7,7,8,8,8-pentadecafluorooctanamide]* (**1e**). The detailed results can be found in the appendix (7.2 Appendix II: Additional data). In summary, the electrospinning of **1e** was successfully performed resulting in fibers with uniform surface and average fiber diameters in the range of 0.4  $\mu\text{m}$  up to 1.8  $\mu\text{m}$ . Only for a few experiments, the standard deviations remain below half of the actual average fiber diameter caused by the lack of thicker fibers. In these cases, fibers with good fiber quality were obtained. The fibers with best overall quality were obtained at an electrospinning temperature of 207 °C, a working distance of 6 cm and an applied voltage of -40 kV ( $E = 6.7$  kV/cm) resulting in an average fiber diameter of  $0.4 \pm 0.2$   $\mu\text{m}$ . Second best results were obtained at electrospinning temperature of 227 °C at the same working distance and applied voltage with average fiber diameter of  $0.6 \pm 0.5$   $\mu\text{m}$ .

#### 4.4.3 Electrospinning of the CTA with tridecafluoroheptyl side chains (**3a**)

The feature of this cyclohexane based trisamide is that it forms a nematic phase. Compound **3a** was electrospun at three different electrospinning temperatures  $T_{\text{Spin}1} = 350\text{ }^{\circ}\text{C}$ ,  $T_{\text{Spin}2} = 325\text{ }^{\circ}\text{C}$ , and  $T_{\text{Spin}3} = 290\text{ }^{\circ}\text{C}$ . In figure 78, the transition temperatures of the first heating curve of the DSC are shown. The temperature of 10 % initial weight loss determined by TGA is also given. The three electrospinning temperatures are marked in green.

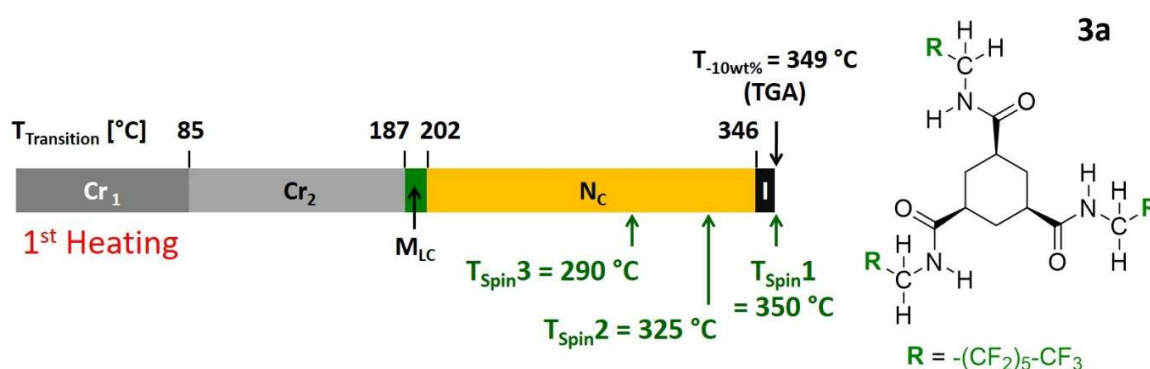


Figure 78: Trisamide **3a** with phase transition temperatures at first heating and cooling (Differential Scanning Calorimetry, heating and cooling rate 10 K/min), type of mesophase (Cr: crystalline, M: unidentified mesophase, LC: liquid crystalline, N: nematic mesophase, C: columnar, I: isotropic), temperature of 10 % weight loss, and the selected spinning temperatures  $T_{\text{Spin}1}$ ,  $T_{\text{Spin}2}$  and  $T_{\text{Spin}3}$  in green.

$T_{\text{Spin}1}$  was selected above the clearing temperature ( $T_c$ ), where the material resides in the isotropic phase, while  $T_{\text{Spin}2}$  and  $T_{\text{Spin}3}$  were selected below  $T_c$  in the nematic mesophase. The electrospinning experiments of **3a** were carried out by directly heating up to  $T_{\text{Spin}2}$  and  $T_{\text{Spin}3}$  without equilibration of the compound in the isotropic phase first. The reason is the thermal stability. As it can be seen in figure 78, **3a** has already reached the 10 % initial weight loss at a temperature of 349 °C. Therefore,  $T_{\text{Spin}1}$  was selected slightly above  $T_c$ . Another difference to the experiments with the BTAs is that only a working distance of 6 cm was used.

### **Electrospinning results of 3a at a spinning temperature of 350 °C in the isotropic phase**

In figure 79, the results of the electrospinning from the isotropic phase at a *spinning temperature of 350 °C* at different applied voltages are shown. In addition, the histograms of the average fiber size and fiber size distributions are shown.

The SEM images reveal a broad fiber distribution. It was possible to process fibers at applied voltage of -30 and -40 kV corresponding to electrical field strengths of 5.0 and 6.7 kV/cm, respectively. At -30 kV, mostly fibers in the range of 0.5  $\mu\text{m}$  up to 4.0  $\mu\text{m}$  were obtained while at -40 kV most of the fibers are in the range of 0.1  $\mu\text{m}$  and 2.5  $\mu\text{m}$ . Nevertheless, thicker fibers were obtained in both cases, which causes much higher average fiber diameters of  $2.2 \pm 1.4 \mu\text{m}$  at -30 kV and  $1.7 \pm 1.8 \mu\text{m}$  at -40 kV.

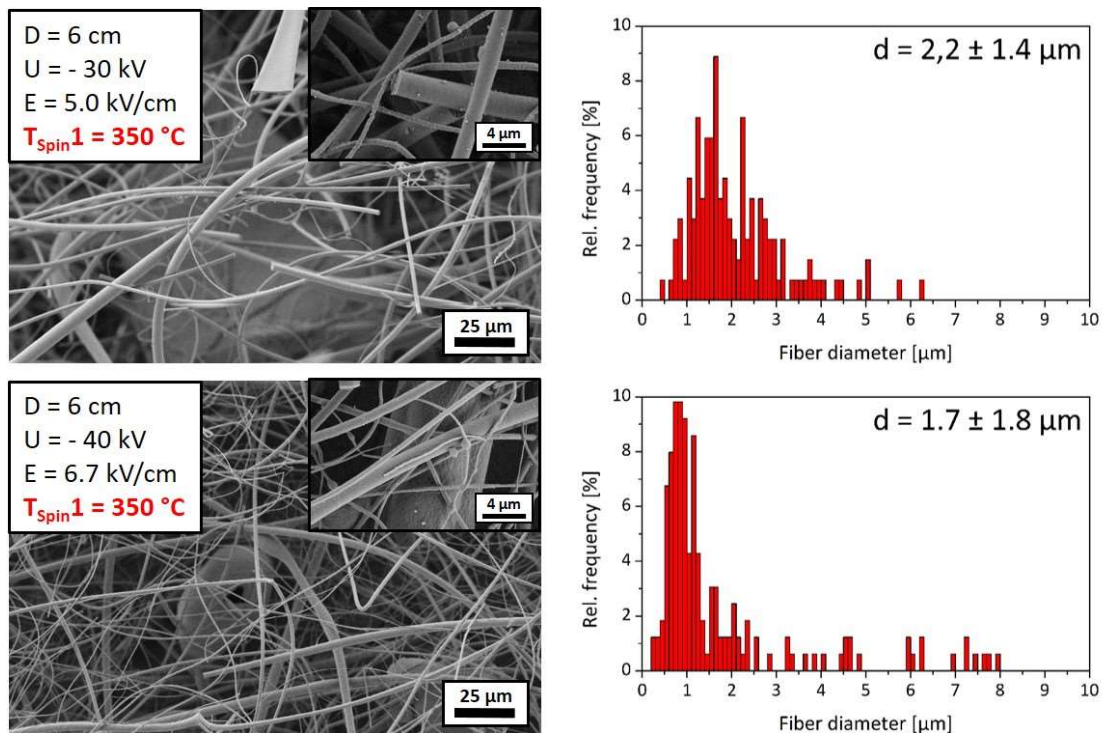
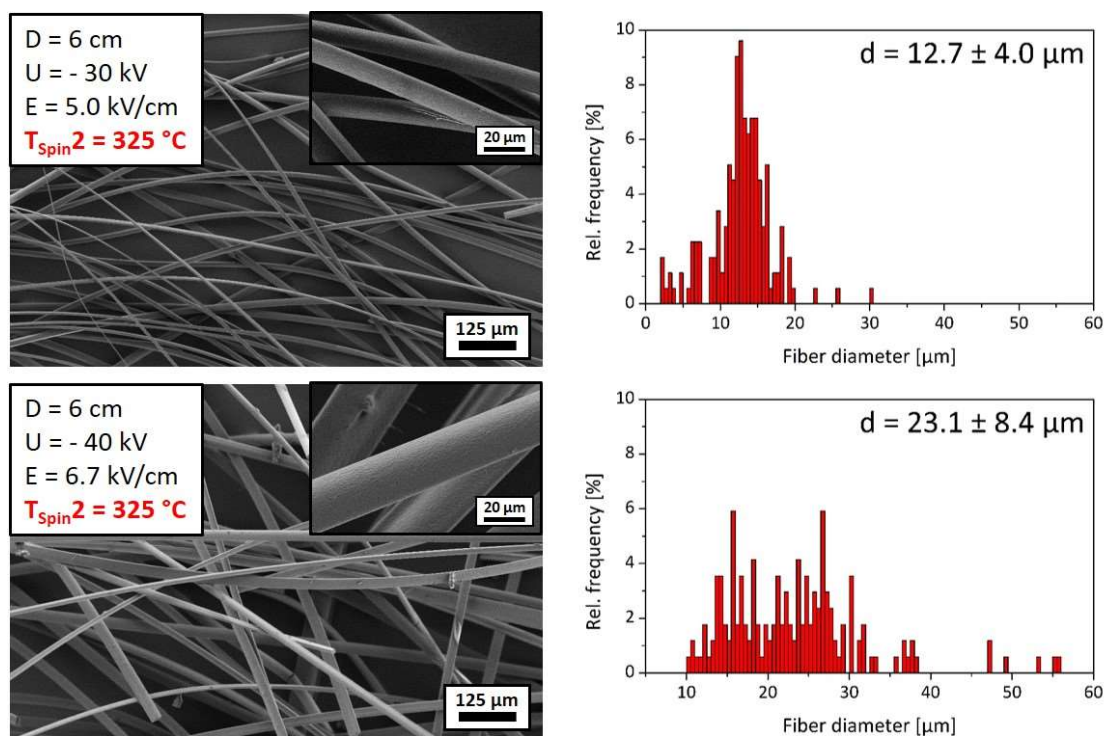


Figure 79: Scanning Electron Microscopy images (left) of electrospun fibers of **3a** produced at  $T_{\text{Spin}1}$  of **350 °C**, working distance  $D$  of 6 cm and an electrospinning applied voltage  $U$  of -30 (top) and -40 kV (bottom). The bar diagrams (right) show the fiber diameter dependent on the relative frequency of an evaluation of  $n = 150$  fiber diameters and the average value including standard deviation.

### ***Electrospinning of 3a at a spinning temperature of 325 °C in the nematic phase***

Figure 80 shows the electrospinning of **3a** at a *spinning temperature of 325 °C* from the nematic mesophase at different applied voltages. In addition, the histograms of the average fiber size and fiber size distributions are shown.

The SEM images prove that much thicker fibers with a uniform surface and homogeneous thickness along the fiber direction were formed. The electrospinning was possible at applied voltages of -30 kV and -40 kV corresponding to electrical field strengths of 5.0 and 6.7 kV/cm, respectively. Processed at -30 kV, a fiber size distribution with low standard deviation is obtained and the average fiber diameter is  $12.7 \pm 4.0 \mu\text{m}$ . At an applied voltage of -40 kV, the fiber diameter increases up to an average fiber diameter of  $23.1 \pm 8.4 \mu\text{m}$  but the fiber size distribution is broader and some fibers with diameters up to more than 55  $\mu\text{m}$  are formed.



**Figure 80:** Scanning Electron Microscopy images (left) of electrospun fibers of **3a** produced at  $T_{\text{Spin}2}$  of **325 °C**, working distance  $D$  of 6 cm and an electrospinning applied voltage  $U$  of -30 (top) and -40 kV (bottom). The bar diagrams (right) show the fiber diameter dependent on the relative frequency of an evaluation of  $n = 150$  fiber diameters and the average value including standard deviation.

### ***Electrospinning of 3a at a spinning temperature of 290 °C in the nematic phase***

Figure 81 shows the electrospinning results of **3a** at an *electrospinning temperature of 290 °C* from the nematic phase at different applied voltages. In addition, the histograms of the average fiber size and fiber size distributions are shown.

The SEM images show that in both cases fibers with uniform surface and good fiber quality were obtained. It was possible to obtain fibers at applied voltages of -20 kV and -30 kV corresponding to electrical field strengths of 3.3 kV/cm and 5.0 kV/cm, respectively. At the lower applied voltage, the fibers result in an average fiber diameter of  $4.2 \pm 1.5 \mu\text{m}$  but the fiber size distribution includes fibers with diameters in the range of one up to nearly nine micrometers in a broad distribution. Processed at -30 kV, the fibers are thinner with an average fiber diameter of  $1.7 \pm 0.4 \mu\text{m}$  and the fiber size distribution ranges only up to about four micrometers.

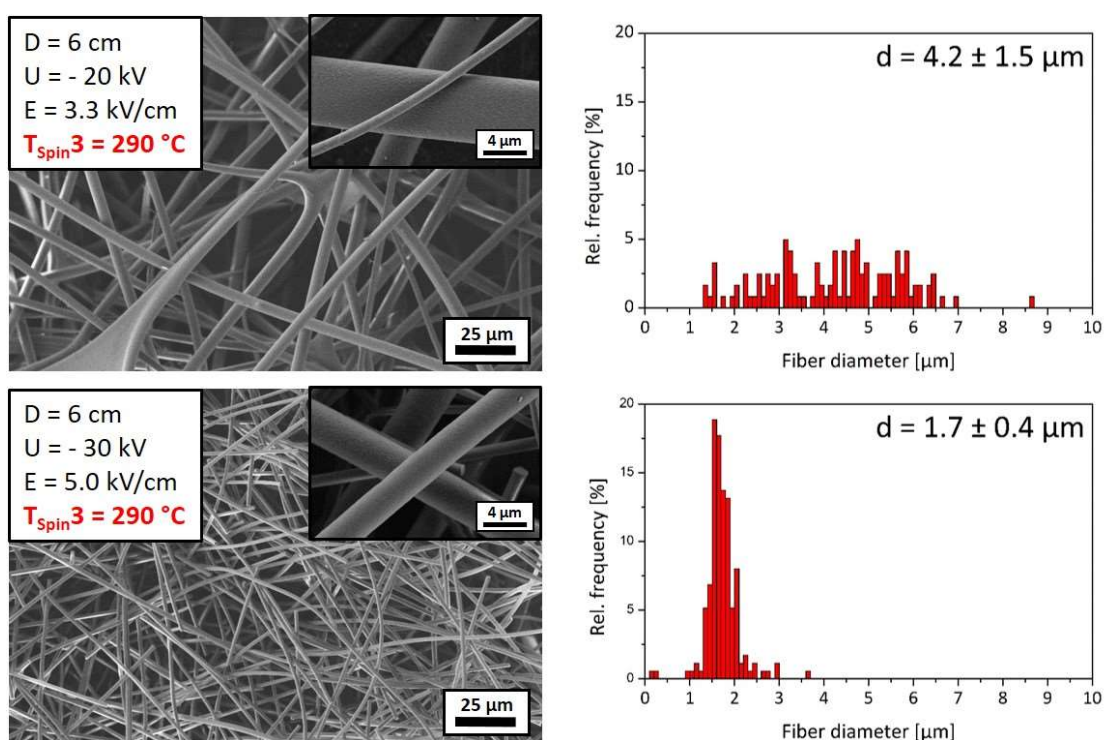


Figure 81: Scanning Electron Microscopy images (left) of electrospun fibers of **3a** produced at  $T_{\text{Spin}3}$  of **290 °C**, working distance  $D$  of 6 cm and an electrospinning applied voltage  $U$  of -20 (top) and -30 kV (bottom). The bar diagrams (right) show the fiber diameter dependent on the relative frequency of an evaluation of  $n = 150$  fiber diameters and the average value including standard deviation.

Compound **3a** was successfully processed to fibers by electrospinning from the isotropic phase and the nematic mesophase. The resulting average fiber diameters including the standard deviation of the samples are summarized in table 6.

Strongly dependent on the electrospinning temperature, fibers with average fiber diameters of  $1.7 \pm 0.4 \mu\text{m}$  up to  $23.1 \pm 8.4 \mu\text{m}$  were obtained. At an electrospinning temperature of  $350 \text{ }^\circ\text{C}$ , processed from the *isotropic phase*, the formed fibers have average fiber diameters of about two micrometers. Though, the fiber size distribution is broad which can be explained by an instability due to partial sublimation of the compound already in the syringe and directly after leaving the syringe tip. Another possible explanation can be the very low surface tension of highly fluorinated compounds, which can cause the melt to wet the syringe tip instead of developing a proper Taylor cone.

At a spinning temperature of  $325 \text{ }^\circ\text{C}$  slightly below the clearing temperature, the compound is in the *nematic mesophase*, electrospinning results in the formation of thick fibers of about  $12.7 \pm 4.0 \mu\text{m}$  at an applied voltage of  $-30 \text{ kV}$  ( $E = 5.0 \text{ kV/cm}$ ) up to  $23.1 \pm 8.4 \mu\text{m}$  at  $-40 \text{ kV}$  ( $E = 6.7 \text{ kV/cm}$ ). It is possible that the compound already sublimated in the syringe, which can cause an internal pressure, which could lead to a faster and uncontrolled increase of the flow rate and the broad fiber size distribution. At last, electrospinning at a temperature of  $290 \text{ }^\circ\text{C}$ , still from the nematic mesophase but at a temperature where **3a** is thermally completely stable, was performed. In this case the average fiber diameters are  $4.2 \pm 1.5 \mu\text{m}$  at an applied voltage of  $-20 \text{ kV}$  ( $E = 3.3 \text{ kV/cm}$ ) and  $1.7 \pm 0.4 \mu\text{m}$  at  $-30 \text{ kV}$  ( $E = 5.0 \text{ kV/cm}$ ). The experiment at  $-30 \text{ kV}$  resulted in the thinnest fibers with the best fiber quality and a low fiber size distribution. Compared to the fibers processed at  $325 \text{ }^\circ\text{C}$ , also from the nematic phase, the fibers are thinner, and it was possible to electrospin at lower electric field strength.

Table 6: Average fiber diameters including standard deviations of the electrospinning results of **3a** dependent on the electrospinning temperature  $T_{\text{Spin}}$  and the applied electric field strength  $E$  (with the corresponding parameter combination of working distance  $D$  and applied high voltage  $U$ ). The best result is shown in green.

$T_{\text{Spin}}$ ( $^\circ\text{C}$ )		$T_{\text{Spin}1} = 350$ (isotropic phase)	$T_{\text{Spin}2} = 325$ (nematic phase)	$T_{\text{Spin}3} = 290$ (nematic phase)
$E$ (kV/cm)				
<b>3.3</b>	$D = 6 \text{ cm};$ $U = -20 \text{ kV}$	droplet formation	droplet formation	$4.2 \pm 1.5 \mu\text{m}^*$
<b>5.0</b>	$D = 6 \text{ cm};$ $U = -30 \text{ kV}$	$2.2 \pm 1.4 \mu\text{m}^*$	$12.7 \pm 4.0 \mu\text{m}$	<b><math>1.7 \pm 0.4 \mu\text{m}</math></b>
<b>6.7</b>	$D = 6 \text{ cm};$ $U = -40 \text{ kV}$	$1.7 \pm 1.8 \mu\text{m}^*$	$23.1 \pm 8.4 \mu\text{m}$	flashover

\*fibers of this sample have beads or show high thickness inhomogeneity alongside the fiber direction

#### 4.5 Melt electrospinning experiments with the aim to obtain thick fibers

In this chapter, the melt electrospinning of nine different BTAs and CTAs to comparably thick fibers for the determination of the long-range interaction forces by direct force measurements is described. Direct force measurement is a technique by using atomic force microscopy (AFM) to probe the interactions of an AFM tip with a sample.<sup>153</sup> The objective here was the production of fibers with at least 5  $\mu\text{m}$  up to 15  $\mu\text{m}$  in diameter. The fiber thickness should be suitable for the performance of the direct force measurements between two cylindrical fibers in crossed-cylinder geometry.<sup>154</sup> These measurements were carried out within the chair of Physical Chemistry II (Prof. Dr. Andreas Fery).

##### 4.5.1 Experimental procedure

Before the electrospinning experiments were performed, the phase behavior of the compounds was determined. Therefore, DSC and TGA was used to investigate the thermal stability, identify mesophases and their corresponding transition temperatures. Observation of the thermal phase behavior by POM was used to get further information on the different phases. The results of the trisamides not already described in chapter 3 can be found in the appendix (7.2 Appendix II: Additional data).

After the phase behavior of the materials was determined, the electrospinning parameters had to be chosen. It was necessary to find parameter combinations where it was possible to spin fibers with uniform surface and the required thickness. Some parameter dependencies had to be considered. The electrospinning temperature ( $T_{\text{Spin}}$ ) had to be as low as possible to prevent sublimation and get a lower viscosity<sup>83</sup> of the material, but also high enough to carry out a proper spinning process. Therefore, the material was always heated up to about 20 °C to 30 °C above  $T_c$  but still in the range of limited weight loss. In the case of compounds with a nematic phase, a temperature in the nematic mesophase was chosen for  $T_{\text{Spin}}$ . The applied voltage was chosen to be as low as possible to hold the acceleration of the jet in the electric field also as low as possible, but also high enough to prevent bead formation. Voltage and working distance were applied that the electric field strength was in the range of 2.5 kV/cm and 5.0 kV/cm. Finally, the flow rate was varied between 500, 1k, 2.5k, 5k and 10k  $\mu\text{L}/\text{h}$ . A higher flow rate should result in a thicker jet. In combination with a low acceleration, the melt electrospinning should result in fibers with the discussed diameters of 5  $\mu\text{m}$  up to 15  $\mu\text{m}$ .

Because it was only necessary to get a few fibers of the desired fiber diameter, no fiber size distribution was evaluated. SEM images of the samples were taken to make sure that fibers in the desired diameter range could be found on the sample, and the diameter of one up to four fibers was measured.

### 4.5.2 Selected materials

Nine different trisamides, three 1,3,5-cyclohexanetrissamides, four BTAs based on trimesic acid core, and two 1,3,5-triaminobenzene based BTAs, were investigated with respect to melt electrospinning to thick fibers. In figure 82, the chemical structures of the compounds can be seen.

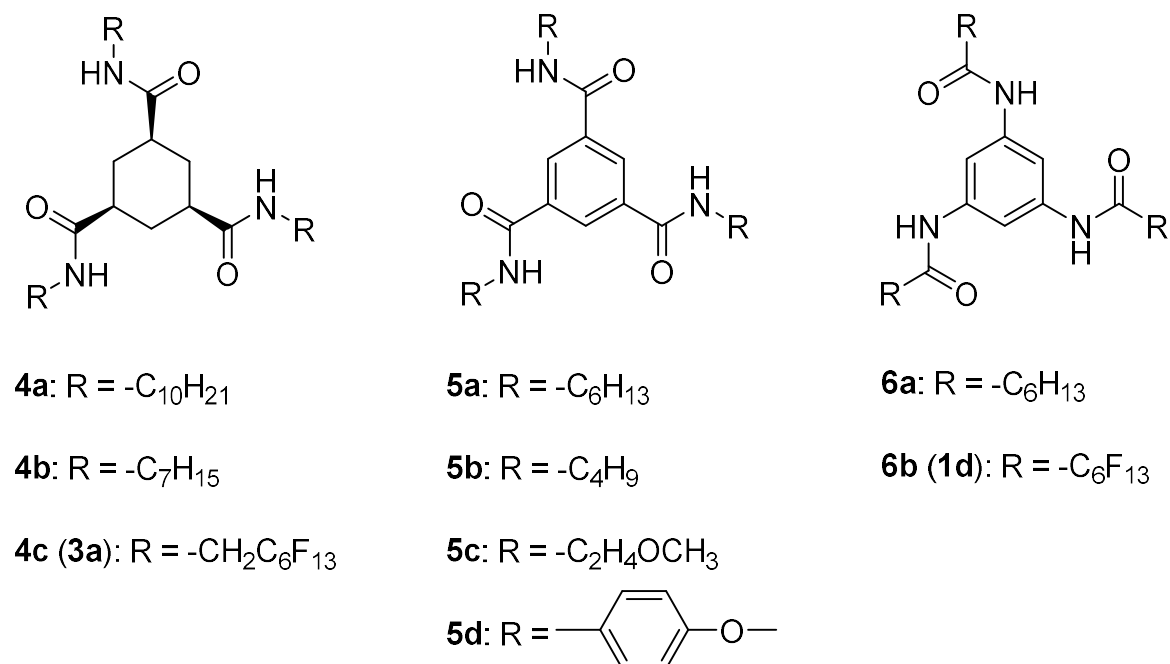


Figure 82: Chemical structures of the trisamides used for melt electrospinning to prepare thick fibers. Left: 1,3,5-cyclohexanetrissamides **4a** and **4b** with alkyl side chains, and **4c** with perfluorinated side chains. Middle: 1,3,5-benzenetrissamides based on trimesic acid **5a**, **5b**, **5c** and **5d** with different side chains. Right: 1,3,5-benzenetrissamides based on 1,3,5-triaminobenzene **6a** with alkyl side chains and **6b** with perfluorinated side chains. (Trisamide **4c** is also denoted as **3a** in the previous chapter, trisamide **6b** is denoted as **1d**).

Compounds **4a**, **4b**, **5a** and **5b** were already characterized by Timme et al.<sup>108</sup> as well as **6a**<sup>45</sup>. These compounds were already electrospun by Singer et al.<sup>148</sup> which resulted in average fiber diameters of  $7.7 \pm 3.0 \mu\text{m}$  at  $300^\circ\text{C}$  and  $1.2 \pm 0.7 \mu\text{m}$  at  $330^\circ\text{C}$  for **4a**, and  $2.8 \pm 0.8 \mu\text{m}$  at  $310^\circ\text{C}$  and  $1.9 \pm 0.6 \mu\text{m}$  at  $340^\circ\text{C}$  for **4b**. The melt electrospinning at four different temperatures between  $240^\circ\text{C}$  and  $300^\circ\text{C}$  of **5a** resulted in fibers with average fiber diameters between  $0.5 \pm 0.3 \mu\text{m}$  and  $0.5 \pm 0.2 \mu\text{m}$ . **6a** was electrospun to fibers with average fiber diameters of  $0.7 \pm 0.3 \mu\text{m}$  at a temperature of  $200^\circ\text{C}$ . In all cases, except the fibers formed by **4a**, the achieved average fiber diameters were too thin for the purpose of the direct force measurements.

### 4.5.3 Results of the melt electrospinning to thick fibers

#### *Results of the CTAs based on (1s,3s,5s)-cyclohexane-1,3,5-tricarboxylic acid*

The three CTAs are based on (1s,3s,5s)-cyclohexane-1,3,5-tricarboxylic acid only differing in their side chain length and alkyl or perfluorinated side chains. **4a** is bearing three alkyl decyl side chains, **4b** three alkyl heptyl side chains, and **4c** three perfluorinated heptyl side chains. Trisamide **4c** is the same compound, which was designated as **3a** in chapter 3, and its melt electrospinning results are shown earlier within this chapter. In the first heating of the DSC analysis, **4a** and **4b** show a nematic mesophase between 246 °C and 307 °C for **4a**, and between 280 °C and 308 °C for **4b**. **4c** has a nematic mesophase between 202 °C and 346 °C.

All CTA compounds were electrospun from the nematic phase at a  $T_{\text{spin}}$  of 300 °C. The images in figure 83 show the chemical structure, phase behavior, and  $T_{\text{spin}}$  in green (left), and SEM images of the fiber samples (right). For **4a** (figure 83 top) electrospinning parameters of a flow rate of 500  $\mu\text{l}/\text{h}$ , applied voltage of -30 kV and working distance of 6 cm ( $E = 5.0 \text{ kV}/\text{cm}$ ) were applied to obtain fibers of about 6.4  $\mu\text{m}$  in diameter. For **4b** (figure 83 middle) a flow rate of 5k  $\mu\text{l}/\text{h}$  at an applied voltage of -15 kV and working distance of 4 cm ( $E = 3.8 \text{ kV}/\text{cm}$ ) was used to obtain fibers of about 8.7  $\mu\text{m}$  in diameter. CTA **4c** (figure 83 bottom) was processed with identical parameter set than **4a** to produce fibers with a diameter of 11.4  $\mu\text{m}$ .

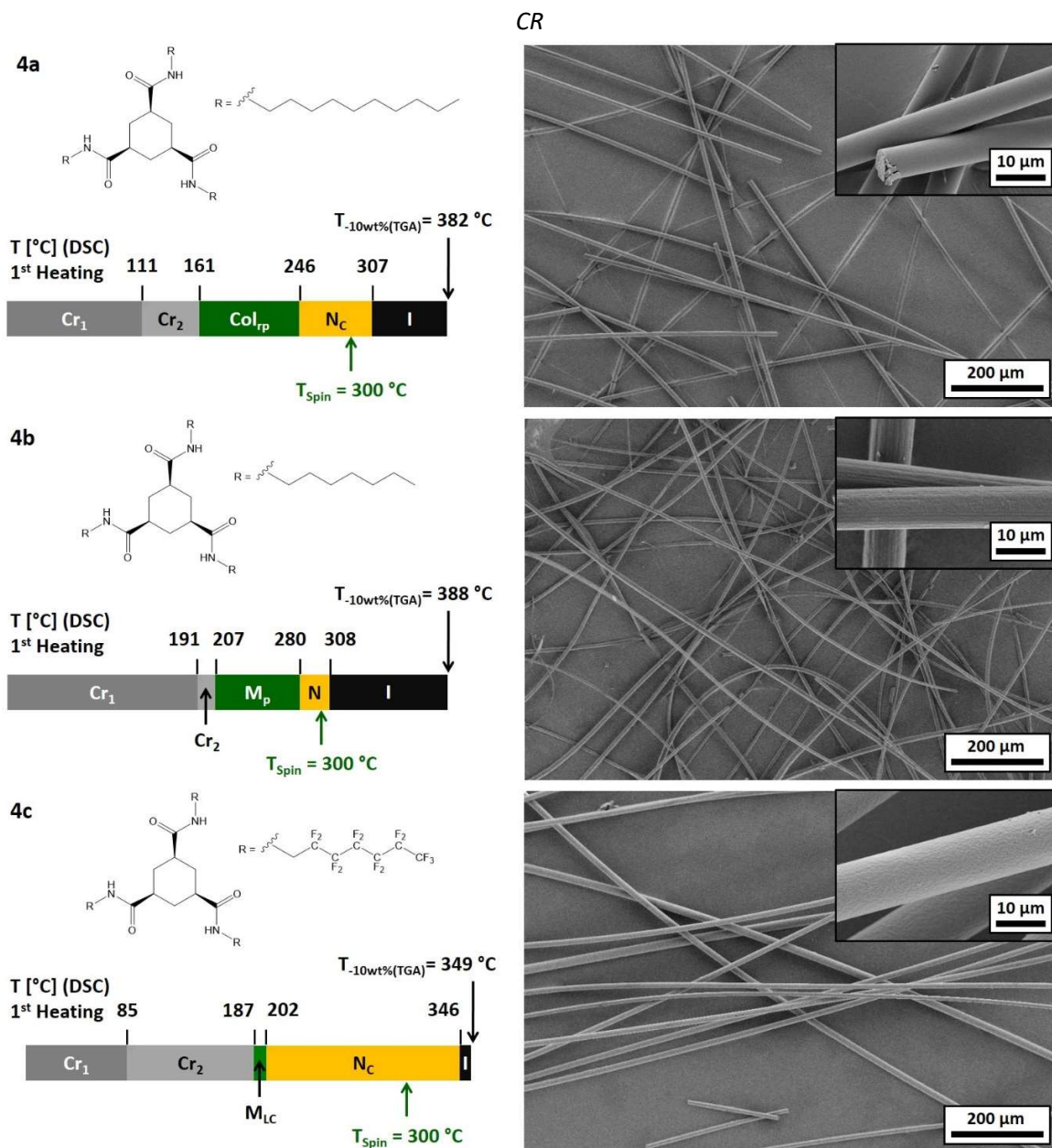


Figure 83: Chemical structure, phase behavior (Cr: crystalline, M: unidentified mesophase, N: nematic mesophase, N<sub>c</sub>: columnar nematic mesophase, Col: columnar mesophase, r: rectangular, p: plastic, I: isotropic), and Scanning Electron Microscopy images of the electrospun fibers. All electrospinning experiments were carried out at  $T_{\text{Spin}}$  of 300 °C under the following conditions: **4a** (working distance of 6 cm, applied voltage of -30 kV ( $E = 5.0$  kV/cm), flow rate of 500  $\mu\text{l/h}$ ), **4b** (working distance of 4 cm, applied voltage of -15 kV ( $E = 3.8$  kV/cm), flow rate of 5k  $\mu\text{l/h}$ ), and **4c** (working distance of 6 cm, applied voltage of -30 kV ( $E = 5.0$  kV/cm) flow rate of 500  $\mu\text{l/h}$ ).

**Results of the BTAs based on trimesic acid**

The BTA series designated with **5** is based on trimesic acid and all phase transition are taken from the first heating curve of the DSC analysis. **5a** is a BTA bearing three alkyl hexyl side chains and shows a Col<sub>hp</sub> phase, followed by a Col<sub>h</sub> phase and transition into the isotropic phase at 207 °C upon heating. **5b** bears three alkyl butyl side chains and passes an undefined plastic mesophase before it changes into the isotropic phase at 236 °C upon heating. **5c** bears three 2-methoxyethyl groups and directly changes from the crystalline state into the isotropic phase at 149 °C without passing a mesophase. **5d** bears three 4-methoxyphenyl side chains, shows no mesophase and changes into the isotropic phase at 275 °C.

The BTAs based on trimesic acid were electrospun to thick fibers at different parameter sets. Figure 84 shows the chemical structure, phase behavior, electrospinning temperature ( $T_{Spin}$ ) in green (left), and SEM images of the fiber samples (right). Both BTAs with linear alkyl side chains **5a** and **5b** were processed at a working distance of 4 cm. For **5a** (figure 84 top) a flow rate of 5k  $\mu$ l/h, an electrospinning temperature of 210 °C after equilibration and cooling down from 230 °C, and an applied voltage of -20 kV ( $E = 5.0$  kV/cm) resulted in fiber diameters of about 5.0  $\mu$ m. For **5b** (figure 84 second from top) the flow rate was 10k  $\mu$ l/h, the electrospinning temperature 250 °C after equilibration and cooling down from 260 °C, and the applied voltage -15 kV ( $E = 3.8$  kV/cm). Fibers of about 0.9  $\mu$ m up to the desired range of about 5.9  $\mu$ m in diameter could be processed. At the same working distance and applied voltage, but only a flow rate of 5k  $\mu$ l/h and an electrospinning temperature of 151°C after equilibration and cooling down from 161 °C, **5c** (figure 84 third from top) bearing 2-methoxyethyl chains formed fibers in the range of about 2.7  $\mu$ m up to 7.1  $\mu$ m in diameter. The BTA bearing 4-methoxyphenyl side chains **5d** (figure 84 bottom) was processed at an electrospinning temperature of 300 °C, an applied voltage of -15 kV ( $E = 3.8$  kV/cm), a flow rate of 5k  $\mu$ l/h, and a working distance of 4 cm. The obtained fibers have a diameter of about 7.8  $\mu$ m.

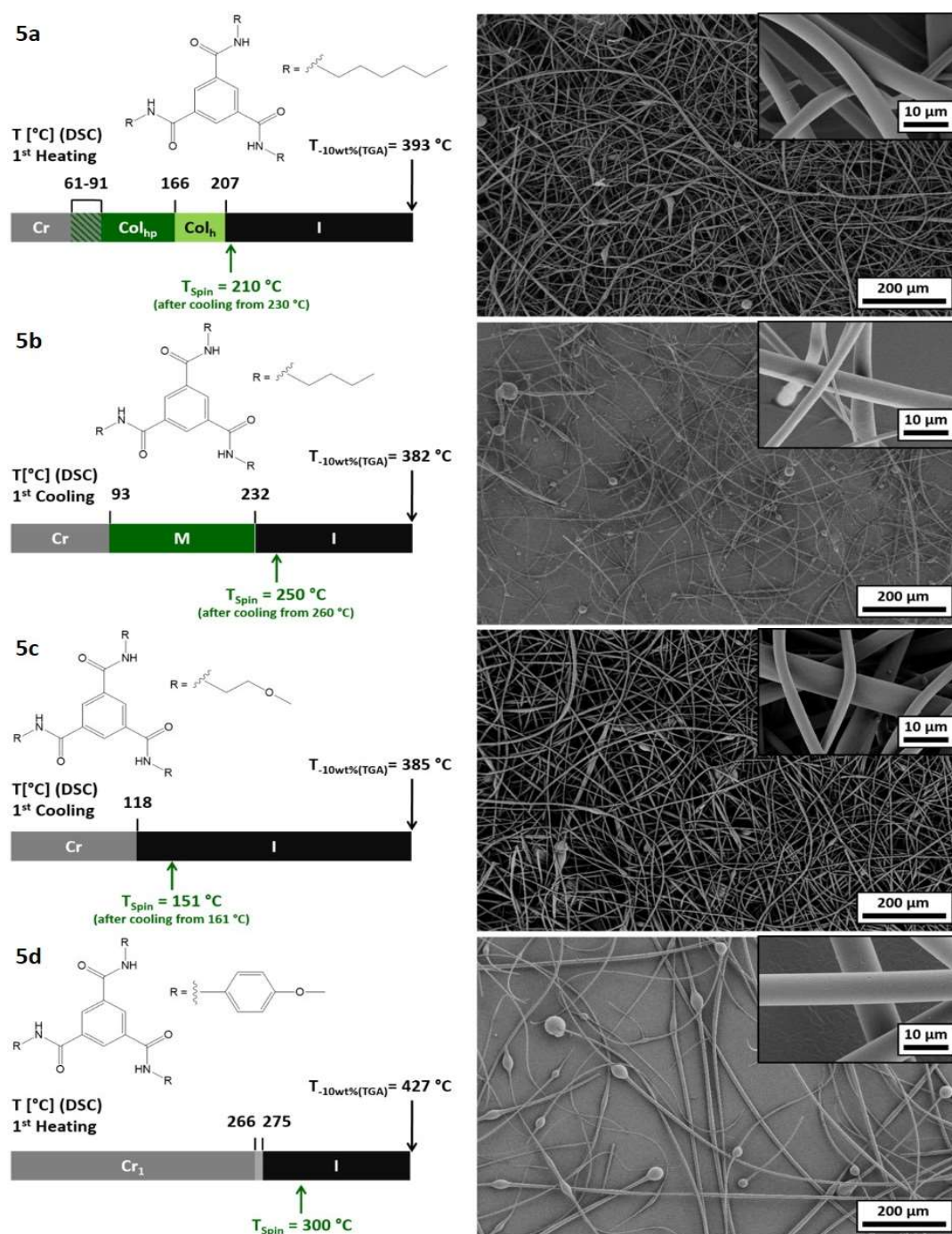


Figure 84: Chemical structure, phase behavior (Cr: crystalline, Col: columnar mesophase, M: unidentified mesophase, h: hexagonal, p: plastic, I: isotropic), and Scanning Electron Microscopy images of electrospun fibers. The electrospinning conditions were as follows: **5a** ( $T_{\text{Spin}}$  of 210 °C, working distance of 4 cm, applied voltage of -20 kV ( $E = 5.0$  kV/cm), flow rate of 5k  $\mu\text{l/h}$ ), **5b** ( $T_{\text{Spin}}$  of 250 °C, working distance of 4 cm, applied voltage of -15 kV ( $E = 3.8$  kV/cm), flow rate of 10k  $\mu\text{l/h}$ ), **5c** ( $T_{\text{Spin}}$  of 151 °C, working distance of 4 cm, applied voltage of -15 kV ( $E = 3.8$  kV/cm), flow rate of 5k  $\mu\text{l/h}$ ), and **5d** ( $T_{\text{Spin}}$  of 300 °C, working distance of 4 cm, applied voltage of -15 kV ( $E = 3.8$  kV/cm), flow rate of 5k  $\mu\text{l/h}$ ).

### Results of the BTAs based on 1,3,5-triaminobenzene

BTAs **6a** and **6b** are based on 1,3,5-triaminobenzene. The phase transitions are taken from the first heating curve of the DSC analysis. BTA **6a** bearing three alkyl hexyl chains, directly changes from the crystalline state into the isotropic phase at 166 °C upon heating. BTA **6b** with three perfluorinated hexyl chains shows a Col<sub>hd</sub> phase before it changes into the isotropic phase at 211 °C.

Figure 85 shows the chemical structure, phase behavior, electrospinning temperature ( $T_{Spin}$ ) in green (left), and SEM images of the fiber samples (right). The BTAs based on 1,3,5-triaminobenzene were both processed with a flow rate of 5k  $\mu$ l/h and applied voltage of -15 kV. BTA **6a** (figure 85 top) bearing alkyl side chains formed fibers at an electrospinning temperature of 190 °C and a working distance of 6 cm ( $E = 2.5$  kV/cm) of about 3.5  $\mu$ m up to 7.0  $\mu$ m in diameter. The BTA **6b** (figure 85 bottom) bearing perfluorinated side chains could be processed at an electrospinning temperature of 210 °C, after cooling down from 230 °C, and a working distance of 4 cm ( $E = 3.8$  kV/cm) to fibers with diameters of about 7.0  $\mu$ m.

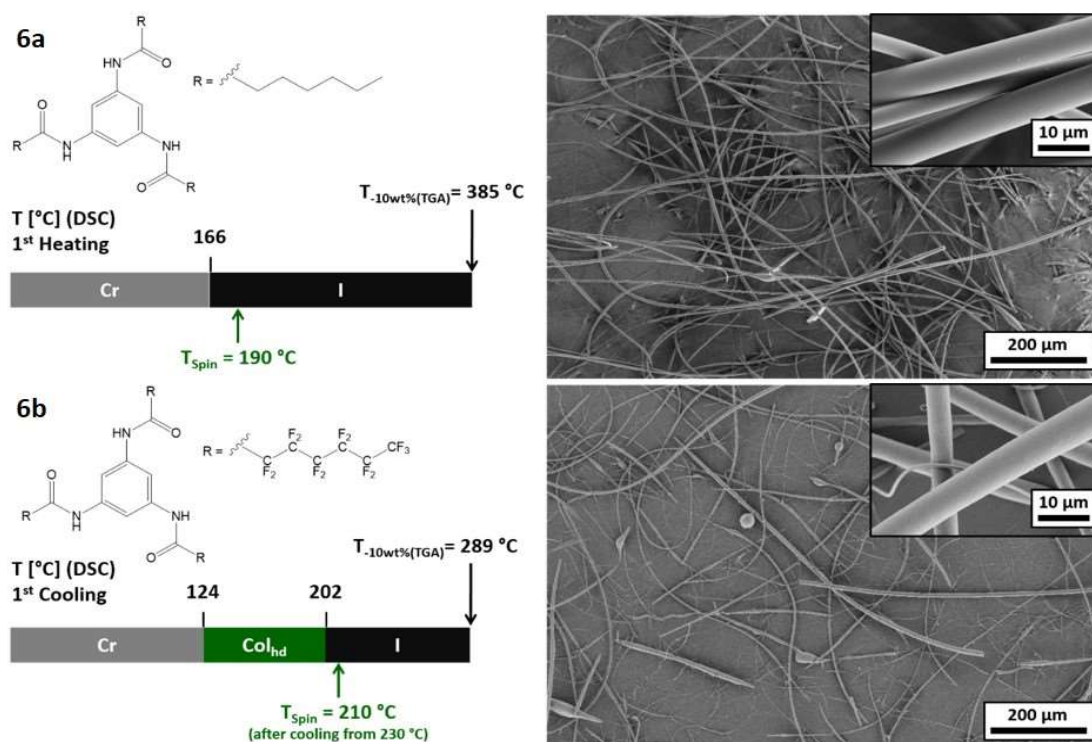
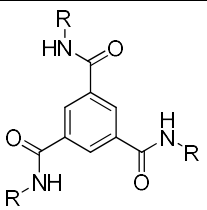
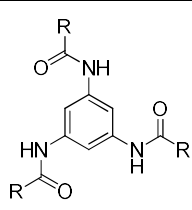


Figure 85: Chemical structure, phase behavior (Cr: crystalline, Col: columnar mesophase, h: hexagonal, d: disordered, I: isotropic), and Scanning Electron Microscopy images of electrospun fibers of **6a** ( $T_{Spin}$  of 190 °C, a working distance of 6 cm, applied voltage of -15 kV ( $E = 2.5$  kV/cm), flow rate of 5k  $\mu$ l/h) and **6b** ( $T_{Spin}$  of 210 °C, working distance of 4 cm, applied voltage of -15 kV ( $E = 3.8$  kV/cm), flow rate of 5k  $\mu$ l/h.)

#### 4.5.4 Summary

It was possible to electrospin all nine different trisamides to fibers of a suitable thickness for the direct force measurements by variation of the electric field strength in a range of 2.5 kV/cm up to 5.0 kV/cm. The best electrospinning parameter set had to be found, meaning the electrospinning temperature, applied voltage, working distance, and flow rate, to obtain fibers of desired thickness. In table 7, the chemical structures of the trisamides, the resulting fiber diameters and the applied parameters are summarized. The three CTA compounds could be processed from a nematic mesophases at flow rates of 500  $\mu\text{l/h}$ , except the CTA bearing three alkyl heptyl side chains. For the BTAs, it was necessary to increase the flow rate up to 10k  $\mu\text{l/h}$  to get fibers in the desired diameter range.

Table 7: Melt electrospinning of 1,3,5-cyclohexane- and 1,3,5-benzenetrisamides to thick fibers. The chemical structures and designation (in bracket the designation from chapter 3), the electrospinning parameters and the resulting fiber diameters measured from Scanning Electron Microscopy images of one up to four fibers can be seen.  $T_{\text{Spin}}$  = electrospinning temperature,  $E$  = electric field strength,  $D$  = working distance,  $U$  = applied voltage.

Designation	Chemical structure	Electrospinning parameters	Fiber diameter [ $\mu\text{m}$ ]
<b>4a</b>	Core 1; R = $-\text{C}_{10}\text{H}_{21}$	$T_{\text{Spin}} = 300\text{ }^{\circ}\text{C}$ ; $E = 5.0\text{ kV/cm}$ ; $D = 6\text{ cm}$ ; $U = -30\text{ kV}$ ; flow rate = 500 $\mu\text{l/h}$	6.4
<b>4b</b>	Core 1; R = $-\text{C}_7\text{H}_{15}$	$T_{\text{Spin}} = 300\text{ }^{\circ}\text{C}$ ; $E = 3.8\text{ kV/cm}$ ; $D = 4\text{ cm}$ ; $U = -15\text{ kV}$ ; flow rate = 5k $\mu\text{l/h}$	8.7
<b>4c (3a)</b>	Core 1; R = $-\text{CH}_2\text{C}_6\text{F}_{13}$	$T_{\text{Spin}} = 300\text{ }^{\circ}\text{C}$ ; $E = 5.0\text{ kV/cm}$ ; $D = 6\text{ cm}$ ; $U = -30\text{ kV}$ ; flow rate = 500 $\mu\text{l/h}$	11.4
<b>5a</b>	Core 2; R = $-\text{C}_6\text{H}_{13}$	$T_{\text{Spin}} = 210\text{ }^{\circ}\text{C}$ ; $E = 5.0\text{ kV/cm}$ ; $D = 4\text{ cm}$ ; $U = -20\text{ kV}$ ; flow rate = 5k $\mu\text{l/h}$	5.0
<b>5b</b>	Core 2; R = $-\text{C}_4\text{H}_9$	$T_{\text{Spin}} = 250\text{ }^{\circ}\text{C}$ ; $E = 3.8\text{ kV/cm}$ ; $D = 4\text{ cm}$ ; $U = -15\text{ kV}$ ; flow rate = 10k $\mu\text{l/h}$	0.9 up to 5.9
<b>5c</b>	Core 2; R = $-\text{C}_2\text{H}_4\text{OCH}_3$	$T_{\text{Spin}} = 151\text{ }^{\circ}\text{C}$ ; $E = 3.8\text{ kV/cm}$ ; $D = 4\text{ cm}$ ; $U = -15\text{ kV}$ ; flow rate = 5k $\mu\text{l/h}$	2.7 up to 7.1
<b>5d</b>	Core 2; R = $-(\text{phenyl})-\text{O}-\text{CH}_3$	$T_{\text{Spin}} = 300\text{ }^{\circ}\text{C}$ ; $E = 3.8\text{ kV/cm}$ ; $D = 4\text{ cm}$ ; $U = -15\text{ kV}$ ; flow rate = 5k $\mu\text{l/h}$	7.8
<b>6a</b>	Core 3; R = $-\text{C}_6\text{H}_{13}$	$T_{\text{Spin}} = 190\text{ }^{\circ}\text{C}$ ; $E = 2.5\text{ kV/cm}$ ; $D = 6\text{ cm}$ ; $U = -15\text{ kV}$ ; flow rate = 5k $\mu\text{l/h}$	3.5 up to 7.0
<b>6b (1d)</b>	Core 3; R = $-\text{C}_6\text{F}_{13}$	$T_{\text{Spin}} = 210\text{ }^{\circ}\text{C}$ ; $E = 3.8\text{ kV/cm}$ ; $D = 4\text{ cm}$ ; $U = -15\text{ kV}$ ; flow rate = 5k $\mu\text{l/h}$	7.0
 <p>Core 1</p>		 <p>Core 2</p>	
 <p>Core 3</p>			

#### 4.5.5 Determination of the surface properties by wettability measurements

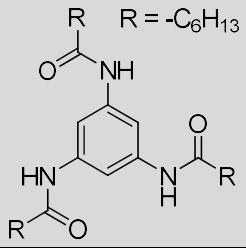
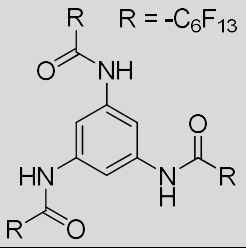
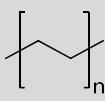
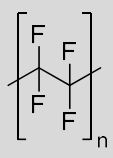
A common method to determine the surface properties of a material is the determination of the contact angle of a droplet of a liquid material. The contact angle quantifies the wettability of a solid surface by a specific liquid and is dependent on the free surface energy of the different materials. It reflects the relative strength of the liquid, solid and vapor molecular interactions. When a small amount of liquid is placed on a surface, it can develop a droplet or simply wet the surface. When the interactions of the liquid and solid phase are small, a droplet will be developed while, when the interaction is high, the liquid is driven to expand on the surface. This can be investigated by measurement of the contact angle at the triple point of the solid, liquid and vapor phase of the contact area. When the interactions are low, a high contact angle will be found resulting in a low wettability of the surface with the specific liquid.

Solid perfluorocarbon surfaces such as poly(tetrafluoroethylene) (PTFE) have high contact angles of 108 degrees in contact with water due to a very low surface tension of 18.5 dyn/cm. This is also the reason for the anti-stick and low-friction properties.<sup>3,155</sup> This low surface tension and high contact angle can only be found for a surface which is densely covered by fluorine atoms.<sup>3</sup> A surface of low density polyethylene (LDPE) shows a contact angle of 94 degrees and a higher surface tension of 31 dyn/cm.<sup>155</sup>

In this subchapter, investigations on the surface properties of fiber mats of two BTAs based on 1,3,5-triaminobenzene **6a** bearing linear alkyl hexyl side chains and **6b** bearing linear perfluorinated hexyl side chains (for chemical structures see figure 82) are described. The fibers mats were processed with the same electrospinning parameter set as it was described in chapter 4.5. The wettability measurements were performed to determine the surface properties of the electrospun fibers. For the determination of the contact angle of the electrospun fiber mats, they were transferred onto a neat glass slide. As testing liquids, two materials with strongly different polarity were chosen to investigate the interactions of the fluorinated and alkylated fiber surface with polar and nonpolar liquids: demineralized water with a polarity  $E_T^N$  of 1.0, and diiodomethane with a polarity  $E_T^N$  of 0.179.<sup>156</sup>  $E_T^N$  stands for the normalized empirical parameter of solvent polarity, which is described in more detail later in chapter 5.1.3. Droplets of 18  $\mu$ l demineralized water or 6  $\mu$ l diiodomethane were given on the fiber mats. The contact angle was measured at five different droplet spots on the sample. At every spot, the analyzing software measured the contact angle over a time period of 30 seconds and five measurement values were taken to get an average contact angle at the specific measurement point.

The resulting contact angles of the wettability measurements of fiber mats formed by **6a** and **6b** with demineralized water and diiodomethane are summarized in table 8 compared to the values found with demineralized water for PTFE and LDPE surfaces in the literature.<sup>155</sup> The BTA with alkylated side chains **6a** shows an average contact angle of  $122.8 \pm 5.0$  degrees to demineralized water and a lower average contact angle of  $42.5 \pm 18.2$  degrees to the nearly nonpolar diiodomethane. The fiber mat made of the BTA with perfluorinated side chains **6b** shows with  $142.2 \pm 8.9$  degrees an about 20 degrees higher average contact angle than BTA **6a** to demineralized water, and with  $113.4 \pm 8.3$  degrees to diiodomethane still a much higher value than it is the case for BTA **6a**. The high contact angles to the fiber mat formed by the BTA with linear perfluorinated side chains **6b** to both polar and nonpolar liquids indicate a surface densely covered by fluorine with the property of very high hydrophobicity. The hydrophobicity is still higher than for PTFE and also for LDPE, but it has to be hold in mind that the sample surface of the fiber mat is not completely flat which makes the comparison to the LDPE and PTFE values difficult.

*Table 8: Contact angles determined by wettability measurements of fiber mats made of **6a** and **6b** by using demineralized water and diiodomethane as liquid materials, including the values found with demineralized water for polytetrafluoroethylene and low-density polyethylene surfaces for comparison.<sup>155</sup>*

	<b>6a</b> 	<b>6b (1d)</b> 	LDPE 	PTFE 
Demineralized Water	$122.8 \pm 5.0^\circ$	$142.2 \pm 8.9^\circ$	$94^\circ$	$108^\circ$
Diiodomethane	$42.5 \pm 18.2^\circ$	$113.4 \pm 8.3^\circ$	n. a.	n. a.

#### 4.7 Summary

In this chapter, the melt electrospinning of two BTAs and one CTA with linear perfluorinated side chains *with the aim to produce thin fibers* is described. Two BTAs based on 1,3,5-triaminobenzene with perfluorinated side chains of five and seven carbon atoms, as well as a CTA based on (1*s*,3*s*,5*s*)-cyclohexane-1,3,5-tricarboxylic acid with perfluorinated side chains of seven carbon atoms were employed. The electrospinning parameters, electrospinning temperature, working distance and applied voltage (electric field) were varied to optimize their influence on the resulting fiber diameters, shape and quality.

Thin fibers with average fiber diameters in the range of 0.5  $\mu\text{m}$  up to 3.8  $\mu\text{m}$  were fabricated with the BTA bearing side chains of five carbon atoms. The best result with the thinnest fibers and best fiber quality was obtained from an experiment with an electric field strength of 5.0 kV/cm. They showed an average diameter of  $0.5 \pm 0.2 \mu\text{m}$ . Second best results had a diameter of  $0.7 \pm 0.3 \mu\text{m}$  from an experiment with an electric field strength of 6.7 kV/cm. In the case of the BTA bearing side chains of seven carbon atoms, the average fiber diameters ranged between 0.4  $\mu\text{m}$  up to 2.1  $\mu\text{m}$ . The fibers with best overall quality were obtained from experiments with an electric field strength of 6.7 kV/cm. The thinnest fibers had an average fiber diameter of  $0.4 \pm 0.2 \mu\text{m}$ , second best results showed an average fiber diameter of  $0.6 \pm 0.5 \mu\text{m}$ . The CTA was electrospun from the isotropic phase as well as from the nematic phase, but the experiments resulted in fibers with good quality only from the nematic phase. The thinnest fibers with best quality had an average fiber diameter of  $1.7 \pm 0.4 \mu\text{m}$  and were obtained from an experiment at an electric field strength of 5.0 kV. Although, it was possible to process thin fibers with a good fiber quality from trisamides with linear perfluorinated side chains, no clear parameter dependency on the fiber quality and thickness could be found as it is the case for BTAs with linear alkyl side chains<sup>100</sup>.

Nine different trisamides, three CTAs and six BTAs, were successfully melt electrospun *with the aim to produce thick fibers* in a desired diameter range of 5  $\mu\text{m}$  up to 15  $\mu\text{m}$  for direct force measurements. This was achieved by varying the electric field strength in a range of 2.5 kV/cm to 5.0 kV/cm, the working distance between 4 cm and 6 cm, the applied voltage between -15, -20 or -30 kV, and the flow rate between 500 up to 10k  $\mu\text{l/h}$ . Two of them were already used for direct force measurements and the results were published in 2016.<sup>154</sup>

*Wettability measurements* with fiber mats of BTAs bearing linear alkyl and perfluorinated side chains showed that the fluorinated trisamide has a higher hydrophobic surface with a contact angle to demineralized water of  $142.2 \pm 8.9$  degrees and also the contact angle to a nonpolar liquid was higher than that of the trisamide with alkylated side chains.

In conclusion, it is possible to get thin and thick fibers with uniform surface by electrospinning of BTAs and CTAs with linear perfluorinated side chains, but it is very important to find the right parameter combinations, because the highly fluorinated materials show a high sublimation tendency.



## 5. Self-assembly of 1,3,5-benzenetrisamides with perfluorinated side chains and co-self-assembly of structurally related 1,3,5-benzenetrisamides from solution

In supramolecular systems, the substitution of hydrogen by fluorine atoms can cause a significant change in self-assembly. Alameddine et al. reported on a mesomorphic hexabenzocoronene (HBC) as a disc-like core with fluorinated side chains and the ability to self-assemble in well-defined architectures.<sup>51</sup> They showed that the substitution of CH<sub>2</sub> groups with CF<sub>2</sub> groups in the side chains increases the melting temperature in contrast to the corresponding alkyl derivatives. Another group found a change in the self-assembly behavior of HBCs substituted with fluorine atoms compared to the non-substituted derivative.<sup>157</sup> When substituted with fluorine, non-tubular aggregates were formed while the non-substituted HBC formed nanotubular structures. Soler et al. showed that highly fluorinated 15-membered macrocycles favor the formation of smectic mesophases with wide temperature ranges in comparison to hydrocarbon analogs.<sup>158</sup> The results of increasing phase transition temperatures of disc-like molecules by introducing fluorinated or perfluorinated chains was also observed with substituted triphenylene derivatives.<sup>47,48,159</sup> This is explained by an increase of rigidity of the molecule by introducing fluorine atoms.<sup>160</sup> Zhou et al. synthesized discotic self-assembling liquid crystalline porphyrin with partial chain fluorination. They found that compared to the non-fluorinated side chains, the fluorinated derivative enhances the tendency towards uniform alignment and self-assembly.<sup>56</sup> Dupuy et al. used a partially fluorinated substituent to build a surfactant with a hydrophilic ethylene oxide moiety as polar head group, and a fluorinated hydrophobic and oleophobic moiety, both responsible for self-assembly into micelles.<sup>161</sup>

Interesting research is also reported for the formation of *supramolecular nanofibers*. Krieg et al. used a perylene diimide amphiphile with an attached perfluorooctyl chain to dramatically enhance supramolecular assembly in aqueous environments.<sup>162</sup> Supramolecular nanofibers formed by these molecules were two orders of magnitude longer than in the case of non-fluorinated analogs under the same conditions. Aebischer et al. used hexa-*peri*-hexabenzocoronene with side chains consisting of an alkyl and a perfluorinated section to prepare nanofibers from benzotrifluoride solution at different concentrations. Fiber bundle cross sections of typically 500 x 200 nm of laterally aggregated columns were shown for high concentrations. The average length was about 20 μm at low concentrations. Isolated fibers with an apparent diameter of 25 nm and a typical length of 3 μm were found. Subtracting 15 nm for a platinum coating, which was used for the cryo-SEM investigations, indicated monocolumnar fibers.<sup>163</sup> Typically it is possible to control the supramolecular fiber diameter

by a suitable bottom-up self-assembly approach, but it is not easy to tailor the fiber length. Most recently in 2019, Steinlein et al. achieved to control the fiber length by ultrasonification at different sonication times and viscosity of the dispersion medium, making it possible to tailor the aspect ratio of benzenetrisamides.<sup>164</sup>

Considering *1,3,5-benzenetrisamides with halogenated substituents*, the use of fluorinated or perfluorinated side chains is of current interest. Van Houtem et al. reported on the self-assembly of a  $C_3$ -symmetrical 3,3'-bis(acrylamino)-2,2'-bipyridine discotic possessing three peripheral partial fluorinated 3,4,5-trialkoxyphenyl moiety units and co-assembled them with non-fluorinated derivatives in fluorinated solvents.<sup>165</sup> Stals et al. used achiral BTAs with two alkyl and one partially fluorinated side chain to cause a symmetry breaking in self-assembly, which was not observed in systems that are racemic or achiral.<sup>98</sup> The role of fluorine in BTAs was also shown by Rajput et al., reporting the influence of solvents in the crystallization of tris(*p*-halogen-phenyl) substituted BTAs.<sup>80</sup> The BTA with fluorine substituted *p*-phenyl side group was the only one showing no solvent influence on the resulting crystal structure, while substituted with iodine, chlorine and bromine, the BTA crystallizes in different crystal structures from different solvents.

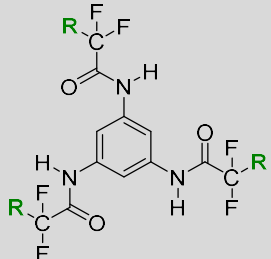
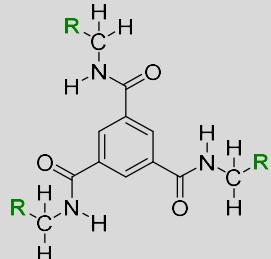
This chapter of the thesis reports on a systematic self-assembly study of BTA molecules with linear perfluorinated side chains from different solvents. Additionally, the last subchapter reports on the co-self-assembly of structurally related BTAs, one compound with perfluorinated side chains and one with alkyl side chains.

### 5.1 Self-assembly of BTAs with linear perfluorinated side chains

BTAs with linear perfluorinated side chains with lengths of three, five and seven carbon atoms based on 1,3,5-triaminobenzene **1a**, **1c** and **1e**, and BTAs based on trimesic acid **2a**, **2c** and **2e** were selected for the self-assembly experiments. Table 9 shows the selected BTAs with their chemical structure and the same numbering used in the previous chapter. The self-assembly experiments were carried out from common organic solvents with different polarities.

There are three different routes reported to self-assemble BTAs into supramolecular fibers via the bottom-up approach.<sup>166</sup> These three routes (**A**, **B** and **C**) are schematically shown in figure 86. In all cases, the BTAs have to be completely soluble at the selected concentration. In route **A**, the BTA is completely soluble at room temperature (a) and the self-assembly is driven by the increase in concentration during evaporation of the solvent. In route **B**, the BTA is dissolved at elevated temperature (b) and the self-assembly occurs upon cooling to RT at a constant concentration. In route **C**, the BTA is completely dissolved at elevated temperature (c) and the self-assembly is carried out upon cooling and simultaneous solvent evaporation.

Table 9: 1,3,5-Benzenetrisamides based on 1,3,5-triaminobenzene (**1a**, **1c** and **1e**) and on trimesic acid (**2a**, **2c** and **2e**) with linear perfluorinated side chains selected for the self-assembly studies from solution.

R: Perfluorinated side chains		
-CF <sub>2</sub> -CF <sub>3</sub>	<b>1a</b>	<b>2a</b>
-(CF <sub>2</sub> ) <sub>3</sub> -CF <sub>3</sub>	<b>1c</b>	<b>2c</b>
-(CF <sub>2</sub> ) <sub>5</sub> -CF <sub>3</sub>	<b>1e</b>	<b>2e</b>

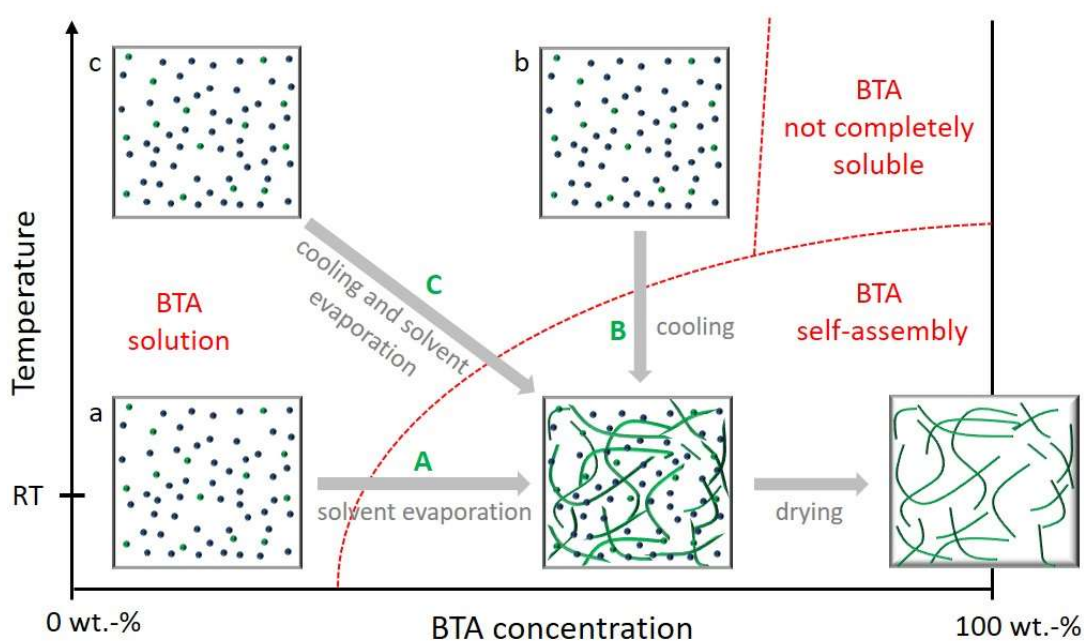
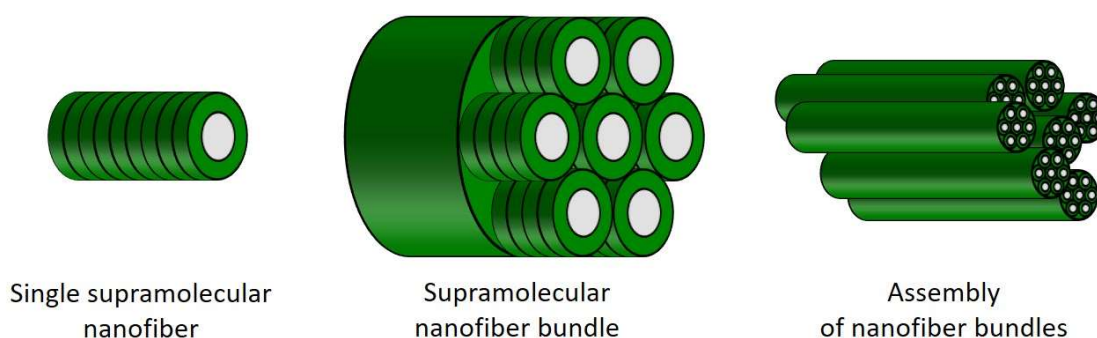


Figure 86: Different routes for the 1,3,5-benzenetrisamides to self-assemble into supramolecular fibers via bottom-up approach. **A**: 1,3,5-Benzenetrisamides are dissolved at RT (a) and fibers form during solvent evaporation; **B**: 1,3,5-Benzenetrisamides are dissolved at elevated temperature (b) and fibers form upon cooling at given constant concentration; **C**: 1,3,5-Benzenetrisamides are dissolved at elevated temperature (c) and fibers form upon cooling and during solvent evaporation. Figure modified from reference<sup>167</sup>.

The schematic illustration in figure 87 depicts possible fiber morphologies of supramolecular BTA fibers. When BTAs self-assemble, they can build up *single supramolecular nanofibers* made of only one column with a diameter of 1-2 nm. The second and most common possibility is the formation of *supramolecular nanofiber bundles*. Supramolecular nanofiber bundles can aggregate to form *assemblies of nanofiber bundles*. In all cases, the perfluorinated peripheral side chains of the BTAs always cause a fiber surface densely filled with fluorine atoms. This is illustrated by the green colored areas in figure 87.



*Figure 87: Schematic illustration of possible supramolecular fibers. Left: Single supramolecular nanofibers consist of a single columnar stack of 1,3,5-benzenetrisamides. Middle: A bundle of single supramolecular nanofibers is formed. Right: The supramolecular nanofiber bundles can build up aggregates of supramolecular nanofiber bundles. All fluorinated trisamide assemblies exhibit a fluorinated surface, indicated in green.*

### 5.1.1 Experimental procedures

Dispersions of BTA and solvent mixtures with concentrations of 0.01, 0.025 and 0.1 wt.% were prepared and stirred for 15 min at RT. If the BTA was not completely dissolved, which was checked by observation of solid material scattering the beam of a green laser pointer, the mixtures were heated in five degree steps until the boiling temperature. After each heating step, 15 min time was allowed to equilibrate the sample. When the BTA was dissolved completely, the solution was cooled down to RT. A few drops of the dispersions were transferred into an aluminum DSC pan cap fixed on a SEM stub. Subsequently, the solvent was allowed to evaporate at RT for at least 48 h before the sample was investigated by SEM.

### 5.1.2 Characterization methods

#### *Scanning Electron Microscopy (SEM)*

The best possibility to get an insight and to take images of the resulting morphologies of the self-assembled BTAs is the observation by Scanning Electron Microscopy (SEM). By using different magnifications, it is possible to investigate supramolecular nanofiber bundles and assemblies of supramolecular nanofiber bundles. Therefore, SEM was used to characterize the fiber morphologies of the self-assembled BTAs.

#### *Fiber diameter evaluation*

The fiber diameter evaluation was carried out as it was already described in chapter 4.2 with the difference, that for the calculation of the fiber size distribution 200 instead of 150 diameter values were used. The fiber quality was determined by the optical observation of the fibers especially the fiber morphology and thickness homogeneity along the fibers, as well as the calculated standard deviation of the average fiber diameters. A high quality was determined by a standard deviation as low as possible but necessarily lower than half of the actual average fiber diameter. In most cases, the average fiber diameter and the standard deviation are written with one position after decimal point. When the average fiber diameter is below 0.2  $\mu\text{m}$ , the result is written with two positions after decimal point.

### 5.1.3 Selected solvents

A number of 14 common organic solvents with different polarity were used for the self-assembly experiments to find the best solvents for a specific BTA resulting in a good fiber quality. Table 10 summarizes the solvents used in this thesis ordered by their normalized empirical parameters of solvent polarity  $E_T^N$ .<sup>156,168</sup> Solvent-dependent absorptions of compounds have been studied as potential reference process for establishing empirical scales of solvent polarity. The  $E_T^N$  value stands for the normalized  $E_T(30)$  value which is based on the transition energy for the longest-wavelength solvatochromic absorption band of the pyridinium N-phenolate betaine dye measured by Dimroth and Reichhardt.<sup>169</sup> It is simply defined as the transition energy of the dissolved betaine dye measured in kcal/mol.

Table 10: Solvents used for the self-assembly experiments of 1,3,5-benzenetrisamides with linear perfluorinated side chains ordered by their normalized empirical parameters of solvent polarity  $E_T^N$ <sup>156</sup>. Also shown are the boiling temperature  $T_b$ , vapor pressure and melting temperature  $T_m$ .

Solvent	$E_T^N$	$T_b$ (°C)	Vapor Pressure (hPa) at 20 °C	$T_m$ (°C)
Cyclohexane	0,006	80,8	104	6,8
n-Hexane	0,009	68,7	160	-95,4
n-Octane <sup>a)</sup>	0,012	126,0	15	-56,8
Toluene	0,099	110,6	29	-95,0
1,4-Dioxane	0,164	101,3	41	11,8
Tetrahydrofuran (THF)	0,207	66,0	200	-108,4
o-Dichlorobenzene (o-DCB) <sup>b)</sup>	0,225	180,5	1.33	-17,1
Trichloromethane (CHCl <sub>3</sub> )	0,259	61,2	210	-63,6
Dichloromethane (DCM)	0,309	39,6	475	-94,9
Acetone	0,355	56,1	240	-94,7
N,N-Dimethylformamide (DMF)	0,386	153,1	3.5	-60,4
Isopropanol	0,546	82,2	44	-88,0
Ethanol	0,654	78,3	59	-114,5
Methanol	0,762	64,5	128	-97,9

a):  $T_m$  and  $T_b$  are taken from a different source.<sup>168</sup>, b): vapor pressure is taken from a different source.<sup>170</sup>

#### 5.1.4 Self-assembly of BTAs based on 1,3,5-triaminobenzene

In the following, the results of the self-assembly experiments will be discussed. At the beginning of the following subchapters, tables containing the self-assembly results are shown. Then, SEM images of the samples, which show fiber formation as well as the corresponding fiber diameter evaluation resulting in the fiber size distribution, can be seen.

Table 11 summarizes the results of the BTAs based on 1,3,5-triaminobenzene with side chains of three (**1a**), five (**1c**) and seven (**1e**) carbon atoms at different concentrations of 0.01 wt.% (top), 0.025 wt.% (middle) and 0.1 wt.% (bottom). The results are ordered by increasing solvent polarity (left side of the tables from top to bottom, followed by right side of the tables from top to bottom). The table shows if the fiber self-assembly was successful (green or red color) and with what kind of route the result was obtained (letters from A to F). The temperatures in parenthesis stand for the temperature of complete dissolution in the specific solvents.

Table 11: Results of the self-assembly studies from different solvents for the 1,3,5-benzenetrisamides based on 1,3,5-triaminebenzene **1a**, **1c** and **1e** at a concentration of 0.01 wt.% (top), 0.025 wt.% (middle) and 0.1 wt.% (bottom).

**BTA concentration: 0.01 wt.%**

	<b>1a</b>	<b>1c</b>	<b>1e</b>		<b>1a</b>	<b>1c</b>	<b>1e</b>
Cyclohexane	D	F (81 °C)	D	CHCl <sub>3</sub>	E	E	D
n-Hexane	D	E	D	DCM	D	F (40 °C)	D
n-Octane	D	B (125 °C)	D	Acetone	E	E	E
Toluene	B (80 °C)	F (80 °C)	B (110 °C)	DMF	E	E	E
1,4-Dioxane	E	E	F (70 °C)	Isopropanol	E	E	E
THF	E	E	E	Ethanol	E	E	E
o-DCB	C (90 °C)	B (100 °C)	B (130 °C)	Methanol	E	E	E

**BTA concentration: 0.025 wt.%**

	<b>1a</b>	<b>1c</b>	<b>1e</b>		<b>1a</b>	<b>1c</b>	<b>1e</b>
Cyclohexane	D	F (81 °C)	D	CHCl <sub>3</sub>	F (61 °C)	E	D
n-Hexane	D	E	D	DCM	D	D	D
n-Octane	D	D	D	Acetone	E	E	E
Toluene	B (90 °C)	F (90 °C)	B (110 °C)	DMF	E	E	E
1,4-Dioxane	E	E	F (70 °C)	Isopropanol	E	E	E
THF	E	E	E	Ethanol	E	E	E
o-DCB	B (100 °C)	B (100 °C)	B (130 °C)	Methanol	E	E	F (65 °C)

**BTA concentration: 0.1 wt.%**

	<b>1a</b>	<b>1c</b>	<b>1e</b>		<b>1a</b>	<b>1c</b>	<b>1e</b>
Cyclohexane	D	D	D	CHCl <sub>3</sub>	B (61 °C)	F (61 °C)	D
n-Hexane	D	F (60 °C)	D	DCM	D	D	D
n-Octane	D	D	D	Acetone	E	E	D
Toluene	B (100 °C)	F (90 °C)	B (110 °C)	DMF	E	A	E
1,4-Dioxane	E	E	F (70 °C)	Isopropanol	E	E	E
THF	E	E	E	Ethanol	E	E	E
o-DCB	B (120 °C)	B (120 °C)	B (130 °C)	Methanol	E	E	D

- A** Soluble at RT; fibers after solvent evaporation
- B** Soluble at elevated temperature (in parenthesis); fibers upon cooling at constant concentration
- C** Soluble at elevated temperature (in parenthesis); fibers after solvent evaporation
- D** BTA not soluble even at the boiling temperature of the solvent
- E** Soluble at RT; no fiber formation after solvent evaporation
- F** Soluble at elevated temperature; no fiber formation upon cooling and solvent evaporation

Fiber bundles could only be obtained from a few solvents. In most of the cases, the BTA could not be dissolved even at the boiling temperature of the solvent (**D**), or no fiber formation was observed (**E**, **F**). With only a few exceptions, the BTAs were not soluble in the solvents with low polarity such as cyclohexane, n-hexane and n-octane. In the solvents with the highest polarity acetone, DMF, isopropanol, ethanol and methanol, they could mostly be dissolved at room temperature but no fiber formation upon solvent evaporation was achieved. The best solvents for the self-assembly are toluene and o-DCB with an average polarity compared to the other solvents.

The BTA with the shortest side chains of three carbon atoms **1a** formed fiber bundles from toluene and o-DCB at all prepared concentrations, and from  $\text{CHCl}_3$  at the highest concentration of 0.1 wt.% by self-assembly upon cooling. The dissolution temperatures increased with increasing BTA concentration from 80 °C to 100 °C in toluene, from 90 °C to 120 °C in o-DCB, and from room temperature to the boiling temperature of  $\text{CHCl}_3$  at 61 °C. BTA **1c** with side chains of five carbon atoms self-assembled to fiber bundles from n-octane and o-DCB at the lowest concentration of 0.01 wt.%, while at 0.025 wt.% it was not soluble in n-octane, but fiber bundles could still be obtained from o-DCB. At the highest concentration, fiber bundles were formed from o-DCB upon cooling from 120 °C instead of 100 °C, which was the case at lower concentration. From DMF the BTA also formed fiber bundles but only from the highest concentrated solution. BTA **1e** bearing side chains of seven carbon atoms self-assembled to fiber bundles from toluene and o-DCB upon cooling at all concentrations from 110°C and 130 °C, respectively.

**Self-assembly from 0.01 wt.% concentrated BTA solutions**

Best solvents for the self-assembly to fibers and fiber bundles for nearly all three BTAs are toluene and o-DCB while **1c** bearing side chains of five carbon atoms did not form fiber or fiber bundles from toluene but from n-octane.

The fiber bundles from the 0.01 wt.% concentrated solutions from toluene and o-DCB formed by the BTA with side chains of three carbon atoms **1a** have a uniform surface, which can be seen in figure 88. From toluene, the fiber bundles are thin with an average fiber diameter of  $0.5 \pm 0.3 \mu\text{m}$  but also fiber bundles with about two micrometers in diameter are present. Thinner fiber bundles are roundly shaped with uniform surface and the thicker ones exhibit clean edges. Trisamide **1a** self-assembled from o-DCB to thick fiber bundles of about  $2.9 \mu\text{m}$  in diameter with a standard deviation of  $1.0 \mu\text{m}$ . The fiber surface is uniform, the morphology is edged, and some of the fiber bundles are twisted.

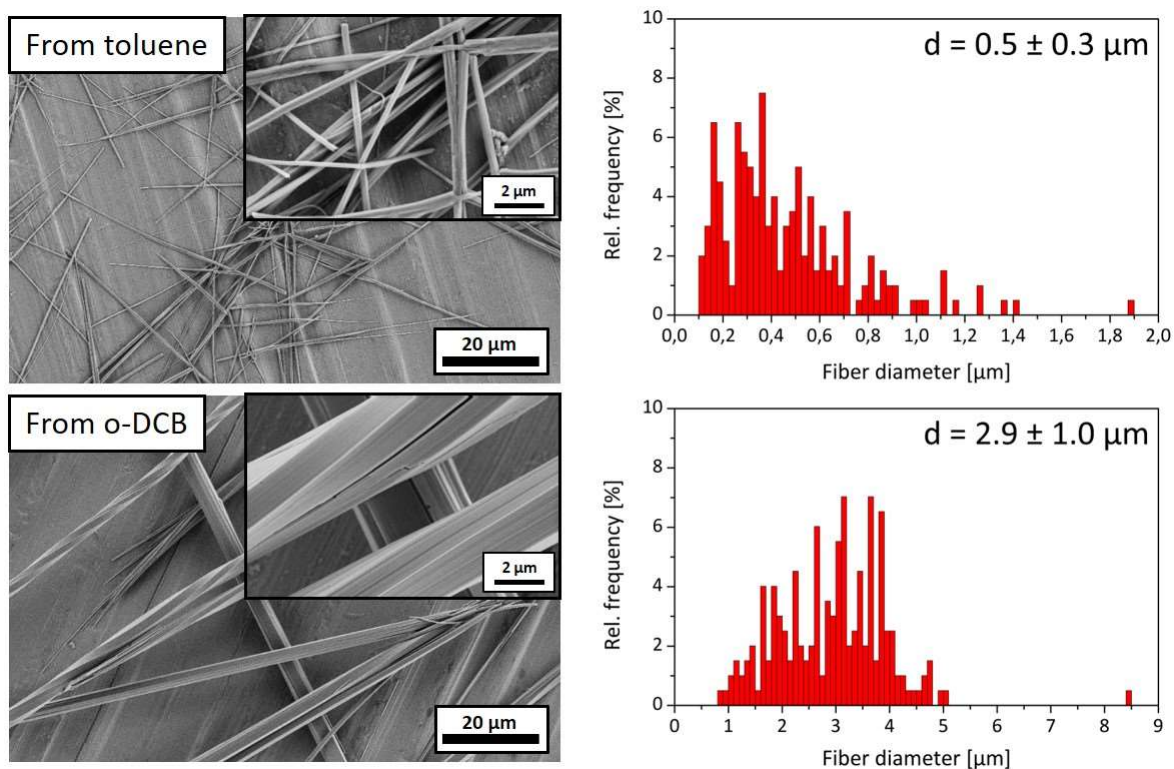


Figure 88: Scanning Electron Microscopy pictures (left) of the self-assembled supramolecular nanofiber bundles of **1a** bearing side chains of three carbon atoms from a 0.01 wt.% concentrated solution of toluene and ortho-dichlorobenzene, and the fiber size distribution (right) of the corresponding fiber samples. The bar diagrams show the fiber diameter dependent on the relative frequency of an evaluation of  $n = 200$  fiber diameters and the average value including standard deviation.

The self-assembly of **1c** bearing side chains of five carbon atoms from n-octane and o-DCB resulted in fiber bundles with uniform surface, which can be seen in figure 89 including the corresponding fiber size distribution. The picture of the fiber bundles from n-octane shows an edged fiber morphology with uniform surface, which form assemblies of fiber bundles and the fiber evaluation results in an average fiber diameter of  $1.1 \mu\text{m}$  with a standard deviation of  $0.4 \mu\text{m}$ . At some areas on the sample, a thin film surrounds and covers the fiber bundles, which may originate from the solvent evaporation process. The same could be found on the sample from o-DCB. The fibers have a uniform surface and edged morphology. In this case, the average fiber diameter is  $2.1 \mu\text{m}$  with a low standard deviation of  $0.8 \mu\text{m}$  resulting in a good fiber quality.

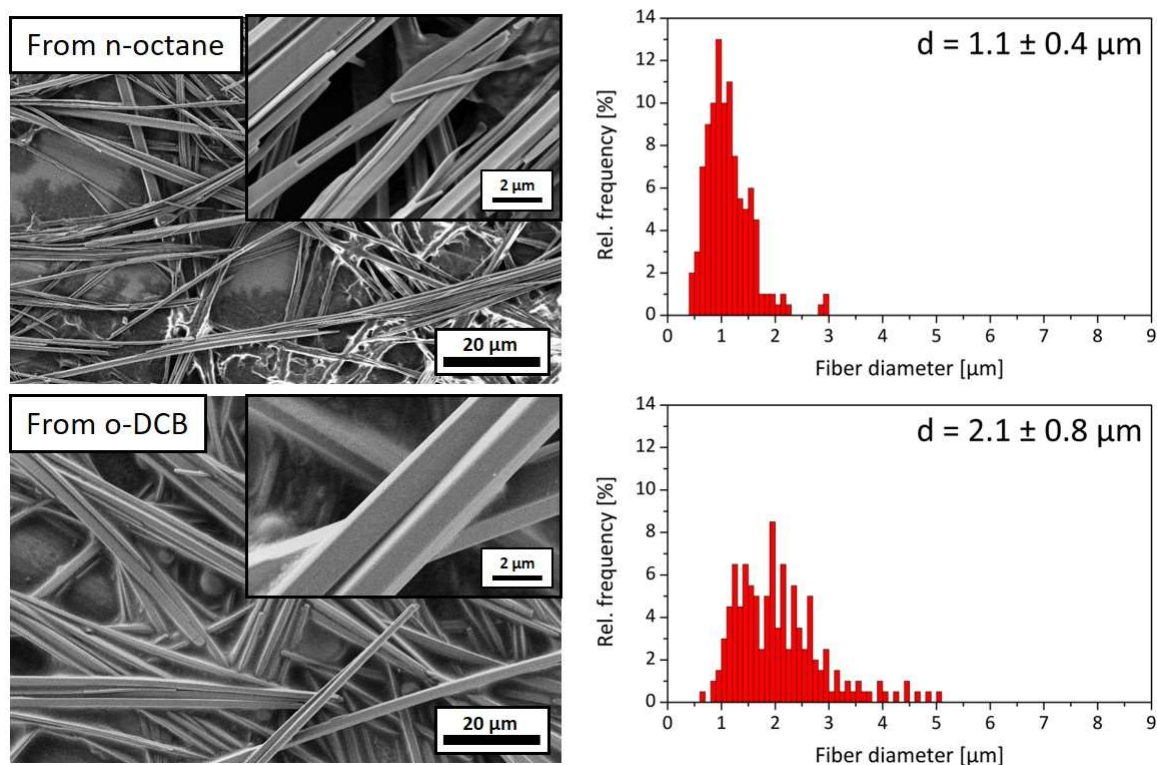


Figure 89: Scanning Electron Microscopy pictures (left) of the self-assembled supramolecular nanofiber bundles of **1c** bearing side chains of five carbon atoms from a 0.01 wt.% concentrated solution of n-octane and ortho-dichlorobenzene, and the fiber size distribution (right) of the corresponding fiber samples. The bar diagrams show the fiber diameter dependent on the relative frequency of an evaluation of  $n = 200$  fiber diameters and the average value including standard deviation.

The 1,3,5-benzenetrisamide with the longest side chains in this chapter of seven carbon atoms **1e** self-assembled to thin fiber bundles from toluene and o-DCB which can be seen in figure 90. The fiber bundles from toluene formed a dense network and assemblies of fiber bundles with uniform surface. The average fiber diameter is 0.2  $\mu\text{m}$  with a standard deviation of 0.1  $\mu\text{m}$ . Even thinner fiber bundles were obtained from o-DCB with an average fiber diameter of 0.12  $\mu\text{m}$  and a low standard deviation of 0.04  $\mu\text{m}$ .

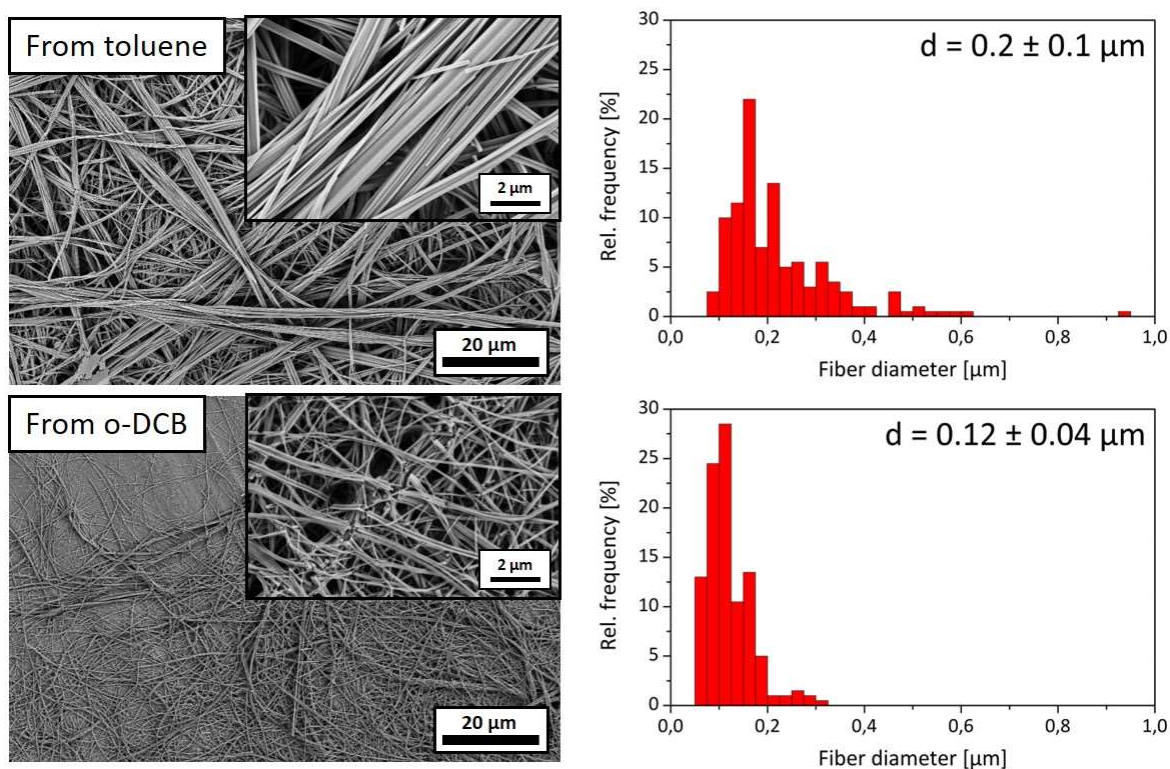


Figure 90: Scanning Electron Microscopy pictures (left) of the self-assembled supramolecular nanofiber bundles of **1e** bearing side chains of seven carbon atoms from a 0.01 wt.% concentrated solution of toluene and ortho-dichlorobenzene, and the fiber size distribution (right) of the corresponding fiber samples. The bar diagrams show the fiber diameter dependent on the relative frequency of an evaluation of  $n = 200$  fiber diameters and the average value including standard deviation.

### Self-assembly from 0.025 wt.% concentrated BTA solutions

The best solvents for the self-assembly from the 0.025 wt.% concentrated solutions for nearly all three selected BTAs are toluene and o-DCB. Only **1c** bearing side chains of five carbon atoms did not form supramolecular fibers or fiber bundles from toluene. It was also not dissolvable in n-octane although it was the case at lower concentration.

Self-assembled fiber bundles formed by **1a** bearing side chains of three carbon atoms from 0.025 wt.% concentrated solutions in toluene and o-DCB are displayed in figure 91. Thin fiber bundles of about  $0.4 \pm 0.3 \mu\text{m}$  were formed from toluene but the standard deviation of more than half of the actual average fiber diameter indicate that the fiber bundles differ in thickness. From o-DCB, the obtained average fiber diameter of about  $2.8 \pm 0.9 \mu\text{m}$  is higher than from toluene but the fiber quality is better. This can be seen in the SEM image by fiber bundles with uniform surface, as well as the narrow fiber size distribution.

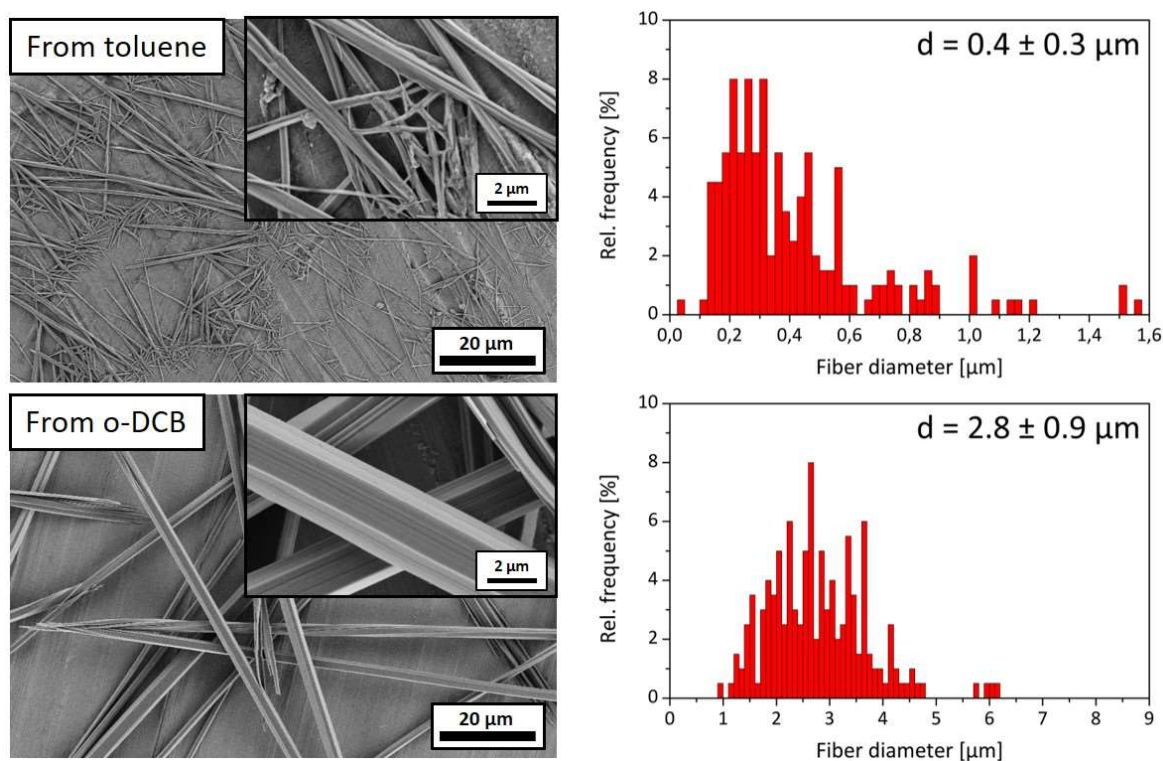


Figure 91: Scanning Electron Microscopy pictures (left) of the self-assembled supramolecular nanofiber bundles of **1a** bearing side chains of three carbon atoms from a 0.025 wt.% concentrated solution in toluene and ortho-dichlorobenzene, and the fiber size distribution (right) of the corresponding fiber samples. The bar diagrams show the fiber diameter dependent on the relative frequency of an evaluation of  $n = 200$  fiber diameters and the average value including standard deviation.

Trisamide **1c** with side chains of five carbon atoms self-assembled from a 0.025 wt.% concentrated solution in o-DCB to fiber bundles with uniform surface and edged morphology shown in figure 92. The fiber size distribution shows that the fiber bundles have an average fiber diameter of 2.2  $\mu\text{m}$  and a standard deviation of 1.1  $\mu\text{m}$ .

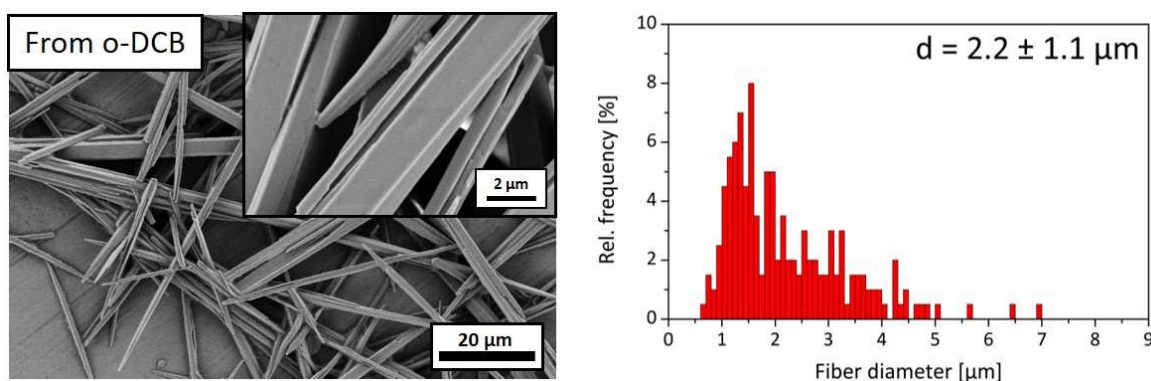


Figure 92: Scanning Electron Microscopy pictures (left) of the self-assembled supramolecular nanofiber bundles of **1c** bearing side chains of five carbon atoms from a 0.025 wt.% concentrated solution in ortho-dichlorobenzene, and the fiber size distribution (right) of the corresponding fiber samples. The bar diagrams show the fiber diameter dependent on the relative frequency of an evaluation of  $n = 200$  fiber diameters and the average value including standard deviation.

Trisamide **1e** with side chains of seven carbon atoms self-assembled to fiber bundles from toluene and o-DCB and both experiments resulted in good fiber quality. This can be seen in figure 93 by SEM pictures and the corresponding fiber size distributions. In both cases, the BTAs formed thin fiber bundles with an average fiber diameter of  $0.2 \pm 0.1 \mu\text{m}$  from toluene and  $0.11 \pm 0.05 \mu\text{m}$  from o-DCB mostly arranged to assemblies of fiber bundles. The fiber quality is high with a standard deviation half or below half of the average fiber diameters resulting from narrow fiber size distributions. Both samples exhibit very thin fiber bundles, most roundly shaped, but the typical edged fiber bundle morphology can also be found.

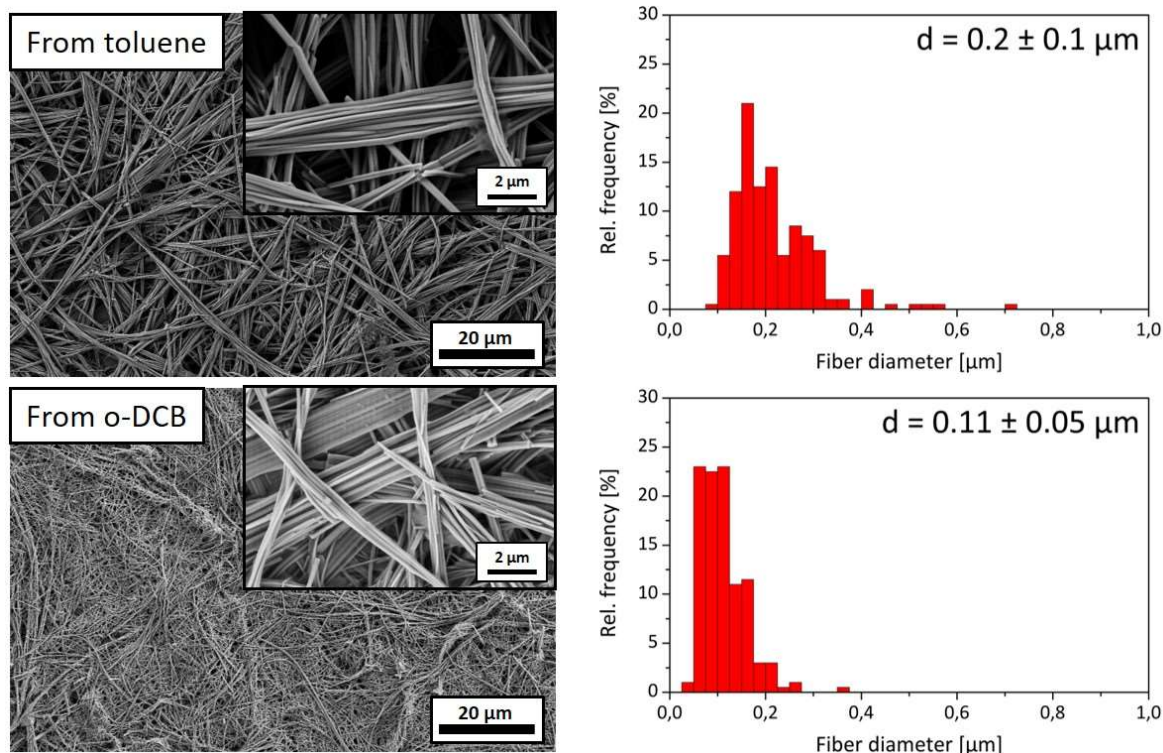


Figure 93: Scanning Electron Microscopy pictures (left) of the self-assembled supramolecular nanofiber bundles of **1e** bearing side chains of seven carbon atoms from a 0.025 wt.% concentrated solution in toluene and ortho-dichlorobenzene, and the fiber size distribution (right) of the corresponding fiber samples. The bar diagrams show the fiber diameter dependent on the relative frequency of an evaluation of  $n = 200$  fiber diameters and the average value including standard deviation.

### Self-assembly from 0.1 wt.% concentrated BTA solutions

The self-assembly investigations from the 0.1 wt.% concentrated solutions resulted in fiber bundles mostly formed from toluene and o-DCB but also from  $\text{CHCl}_3$  for **1a**, and from DMF for **1c**, where the BTAs were dissolvable at lower concentrations but did not form fibers.

The results for **1a** bearing side chains of three carbon atoms from toluene, o-DCB and  $\text{CHCl}_3$ , are shown in figure 94. The uniform surface and edged morphology of the formed nanofiber bundles is similar from all three solvents, but the average fiber diameter differs from about  $2.9 \pm 2.3 \mu\text{m}$  obtained from toluene to  $2.0 \pm 2.3 \mu\text{m}$  from o-DCB, down to  $1.5 \pm 1.6 \mu\text{m}$  from  $\text{CHCl}_3$ . In all cases, the standard deviations have a high value with about the same value as the fiber diameter itself. This means that the nanofiber bundles differ strongly in thickness. Possible explanations are different self-assembly techniques within the self-assembly process. For example, it is possible that the molecules, which did not self-assemble upon cooling, self-assembled upon solvent evaporation and increase of concentration. Another

possibility is a surface induced self-assembly at the air-liquid-surface or at the boundary surface to the aluminum DSC pan cap.

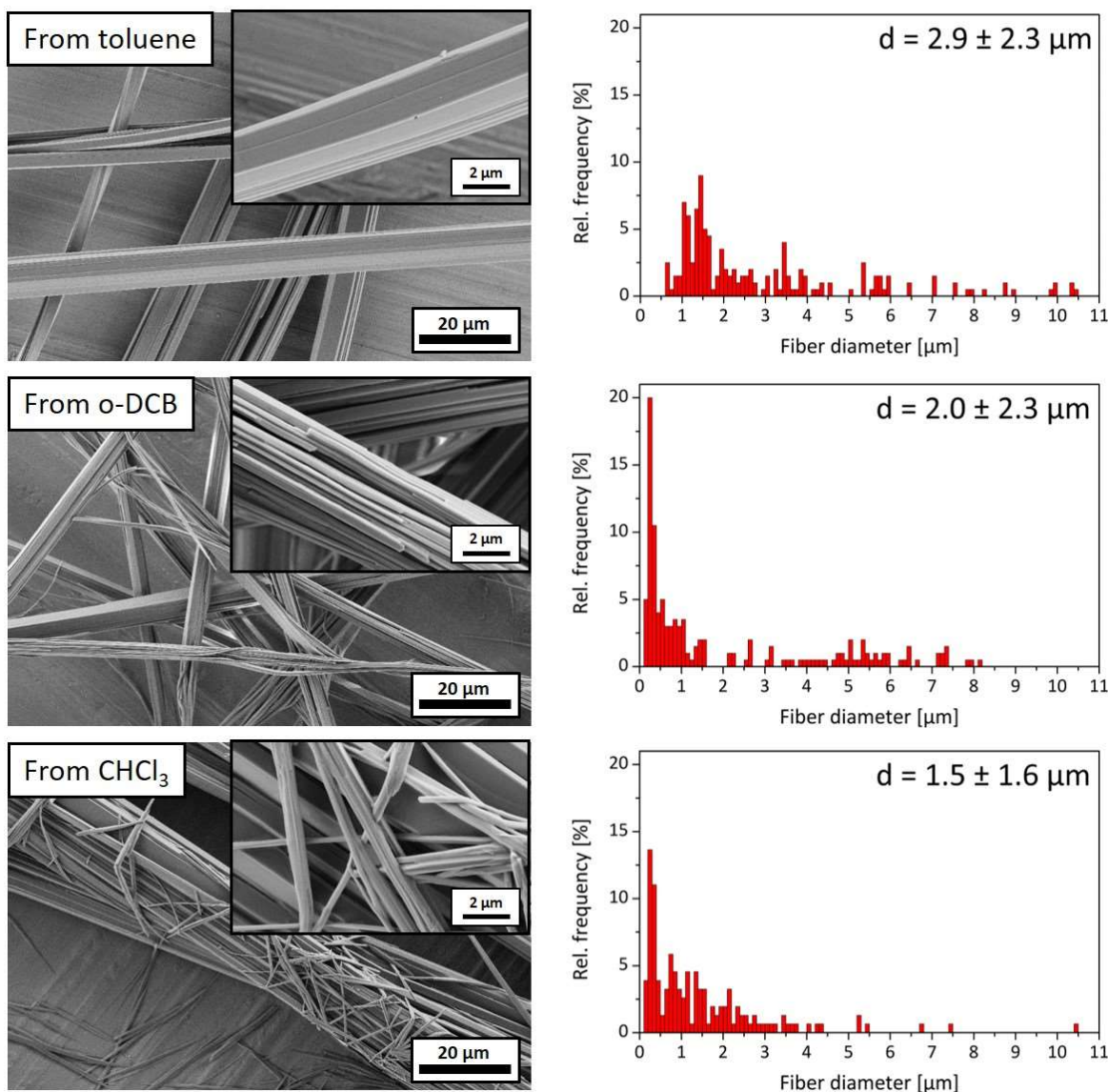


Figure 94: Scanning Electron Microscopy pictures (left) of the self-assembled supramolecular nanofiber bundles of **1a** bearing side chains of three carbon atoms from a 0.1 wt.% concentrated solution in toluene, *ortho*-dichlorobenzene and  $\text{CHCl}_3$ , and the fiber size distribution (right) of the corresponding fiber samples. The bar diagrams show the fiber diameter dependent on the relative frequency of an evaluation of  $n = 200$  fiber diameters and the average value including standard deviation.

Trisamide **1c** bearing side chains of five carbon atoms self-assembled to fiber bundles with uniform surface and edged morphology from *o*-DCB and DMF (figure 95), and the fiber bundles have an average fiber diameter of  $2.8 \pm 1.2 \mu\text{m}$  from *o*-DCB and  $4.2 \pm 2.7 \mu\text{m}$  from DMF, respectively. The fiber bundle quality from *o*-DCB is high with a standard deviation smaller than half of the average fiber diameter. The self-assembled fiber bundles from DMF are thicker and some band-shaped structures can be found. At higher magnification, it is also possible to find hollow fiber assemblies. It is possible that the BTA molecules self-assembled to hollow assemblies and then collapsed when the solvent was evaporated, resulting in band-like structures.

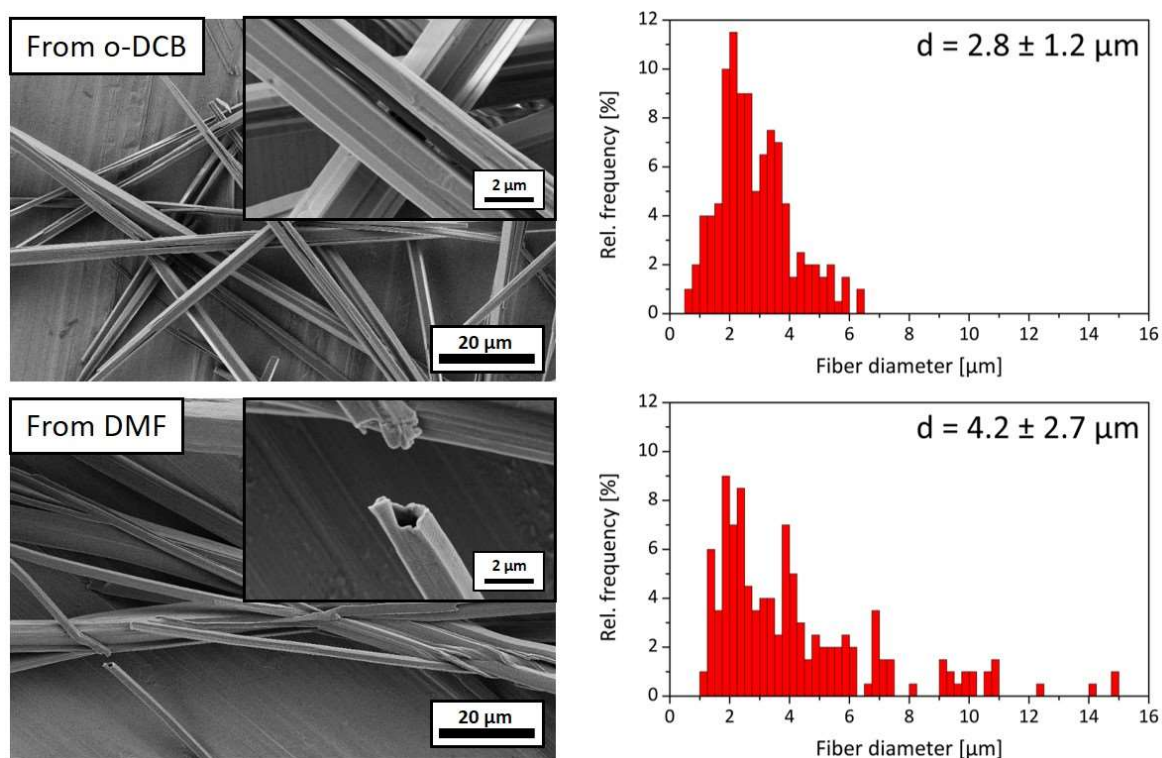


Figure 95: Scanning Electron Microscopy pictures (left) of the self-assembled supramolecular nanofiber bundles of **1c** bearing side chains of five carbon atoms from a 0.1 wt.% concentrated solution in *ortho*-dichlorobenzene and dimethylformamide, and the fiber size distribution (right) of the corresponding fiber samples. The bar diagrams show the fiber diameter dependent on the relative frequency of an evaluation of  $n = 200$  fiber diameters and the average value including standard deviation.

Fiber bundles with uniform surface of **1e** with side chains of seven carbon atoms, self-assembled upon cooling from toluene and *o*-DCB, can be seen in figure 96. The fiber bundles from toluene have a short and thick appearance with average fiber diameter of  $3.5 \pm 1.4 \mu\text{m}$ .

The fiber bundles are not hollowed, and the shape is inhomogeneous in thickness. Nevertheless, many fiber bundles with uniform surface can be found, and closer examination reveals fiber bundles with hexagonal edged morphology. The fiber bundles from *o*-DCB are thinner with an average fiber diameter of only  $0.17 \pm 0.06 \mu\text{m}$  and the fiber quality is high, proven by a low standard deviation of only about a third of the average fiber diameter.

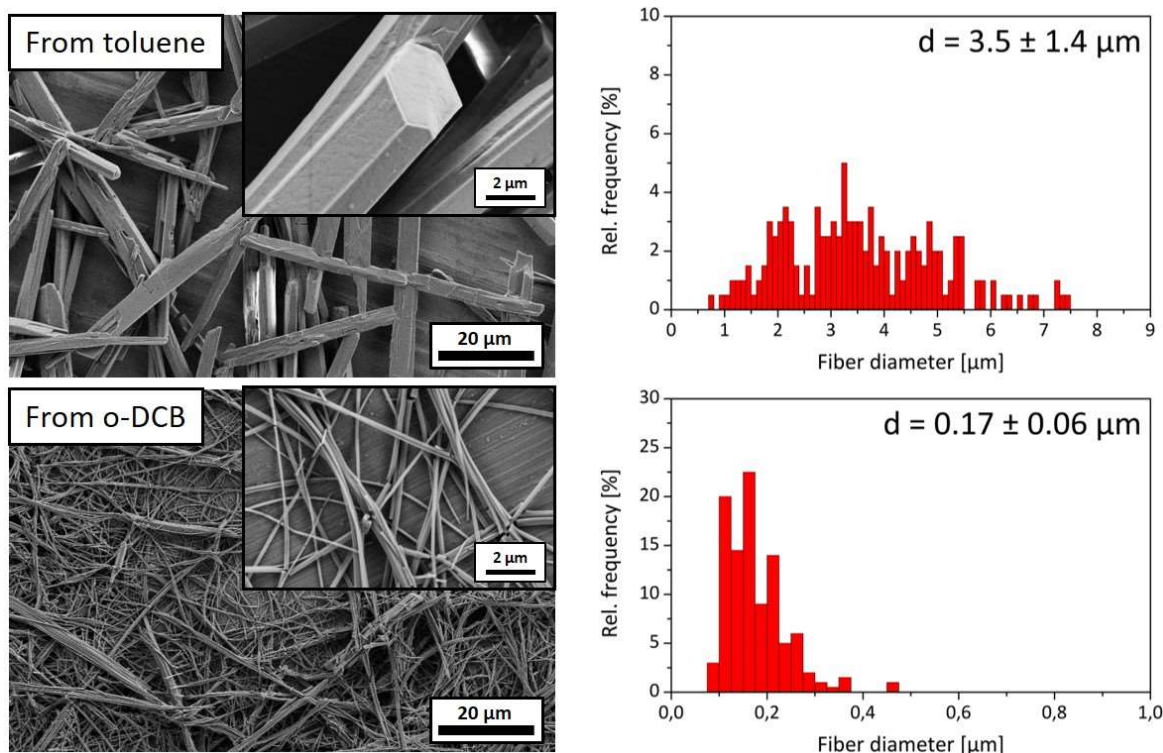


Figure 96: Scanning Electron Microscopy pictures (left) of the self-assembled supramolecular nanofiber bundles of **1e** bearing side chains of seven carbon atoms from a 0.1 wt.% concentrated solution in toluene and ortho-dichlorobenzene, and the fiber size distribution (right) of the corresponding fiber samples. The bar diagrams show the fiber diameter dependent on the relative frequency of an evaluation of  $n = 200$  fiber diameters and the average value including standard deviation.

### 5.1.5 Self-assembly of BTAs based on trimesic acid

The BTAs based on trimesic acid bearing side chains of three (**2a**), five (**2c**) and seven (**2e**) carbon atoms also self-assembled to fiber bundles. It was not possible to find a single solvent where all three BTAs with different side chain lengths formed fibers or fiber bundles. For a proper comparison of the BTAs with different side chain lengths, it is necessary to get fibers or fiber bundles from the same solvent. Therefore, a concentration of 0.1 wt.% had to be selected. The results are summarized in table 12, ordered by increasing solvent polarity (left side of the table from top to bottom, followed by right side of the table from top to bottom). The table shows if the fiber self-assembly was successful (green or red color) and with what kind of route the result was obtained (letters from A to F). The temperatures in parenthesis stand for the temperature of complete dissolution in the specific solvents.

Table 12: Results of the self-assembly investigations from different solvents for the 1,3,5-benzenetrisamides based on trimesic acid **2a**, **2c** and **2e** at a concentration of 0.1 wt.%.

	<b>2a</b>	<b>2c</b>	<b>2e</b>		<b>2a</b>	<b>2c</b>	<b>2e</b>
Cyclohexane	<b>D</b>	<b>D</b>	<b>D</b>	CHCl <sub>3</sub>	<b>D</b>	<b>D</b>	<b>D</b>
n-Hexane	<b>D</b>	<b>D</b>	<b>D</b>	DCM	<b>D</b>	<b>D</b>	<b>D</b>
n-Octane	<b>D</b>	<b>D</b>	<b>D</b>	Acetone	<b>E</b>	<b>E</b>	<b>A</b>
Toluene	<b>D</b>	<b>D</b>	<b>D</b>	DMF	<b>E</b>	<b>E</b>	<b>E</b>
1,4-Dioxane	<b>E</b>	<b>E</b>	<b>B</b> (80 °C)	Isopropanol	<b>E</b>	<b>F</b> (40 °C)	<b>D</b>
THF	<b>E</b>	<b>E</b>	<b>E</b>	Ethanol	<b>E</b>	<b>E</b>	<b>D</b>
o-DCB	<b>B</b> (170 °C)	<b>B</b> (170 °C)	<b>D</b>	Methanol	<b>E</b>	<b>A</b>	<b>D</b>

- A** Soluble at RT; fibers after solvent evaporation
- B** Soluble at elevated temperature (in parenthesis); fibers upon cooling at constant concentration
- C** Soluble at elevated temperature (in parenthesis); fibers after solvent evaporation
- D** BTA not soluble even at the boiling temperature of the solvent
- E** Soluble at RT; no fiber formation after solvent evaporation
- F** Soluble at elevated temperature; no fiber formation upon cooling and solvent evaporation

Similar to the BTAs based on 1,3,5-triaminobenzene, fiber bundles could only be obtained from a few solvents. In most of the cases, the BTA could not be dissolved even at the boiling temperature of the solvent (**D**), especially for the solvents with low polarity cyclohexane, n-hexane, n-octane and toluene, but also for CHCl<sub>3</sub> and DCM which have average polarity compared to the other solvents in the table above. In most other cases, the BTAs were dissolvable but no fiber formation could be observed (**E**, **F**). Trisamide **2a** with the shortest side chains of three carbon atoms only self-assembled to fiber bundles from o-DCB upon

cooling after the mixture was heated up to the boiling temperature for complete dissolution. The same result was obtained for **2c** bearing side chains of five carbon atoms, but it also formed fiber bundles from methanol after solvent evaporation. The BTA with the longest side chains in this chapter **2e** bearing side chains of seven carbon atoms self-assembled to fiber bundles from acetone after solvent evaporation and from 1,4-dioxane upon cooling. The best solvents for the self-assembly of BTAs **2a** and **2c** is *o*-DCB with a medium polarity compared to the other solvents in this chapter, while the BTA with the longest side chains **2e** self-assembled to fiber bundles from solvents with higher (acetone) and lower (1,4-dioxane) polarity. It is noticeable that the BTAs based on trimesic acid showed no fiber self-assembly from toluene, which is one of the best solvents for the self-assembly of the BTAs based on 1,3,5-triaminobenzene.

#### ***Self-assembly from 0.1 wt.% concentrated BTA solutions***

Figure 97 shows SEM pictures and the fiber size distribution of fiber bundles with high fiber quality of **2a** bearing side chains of three carbon atoms self-assembled from *o*-DCB. Fiber bundles with uniform surface and edged morphology with an average fiber diameter of  $1.6 \pm 0.8 \mu\text{m}$  were formed upon cooling.

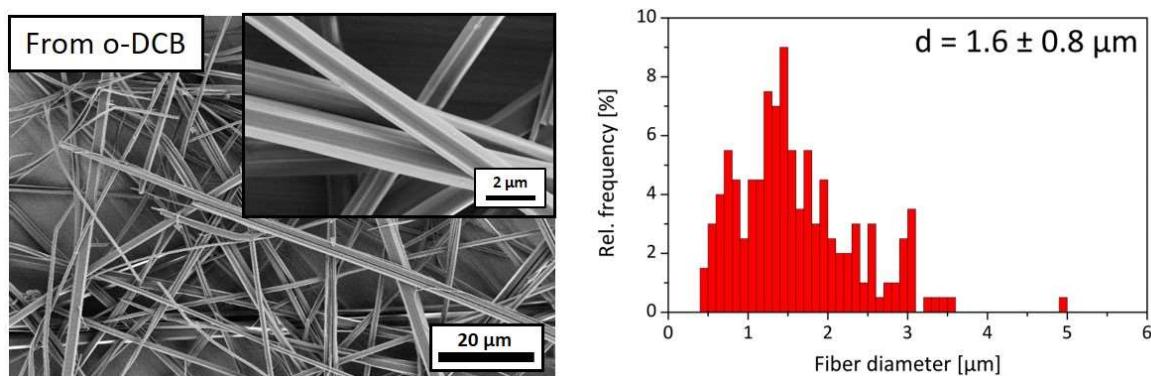


*Figure 97: Scanning Electron Microscopy pictures (left) of the self-assembled supramolecular nanofiber bundles of **2a** bearing side chains of three carbon atoms from a 0.1 wt.% concentrated solution in ortho-dichlorobenzene, and the fiber size distribution (right) of the corresponding fiber samples. The bar diagrams show the fiber diameter dependent on the relative frequency of an evaluation of  $n = 200$  fiber diameters and the average value including standard deviation.*

Fiber bundles formed by **2c** bearing side chains of five carbon atoms and the fiber diameter evaluations are shown in figure 98. From o-DCB, thin fiber bundles with an average fiber diameter of  $1.1\ \mu\text{m}$  and a low standard deviation of  $0.3\ \mu\text{m}$  could be obtained. From methanol, the average fiber diameter was found to be  $0.8\ \mu\text{m}$  with a high standard deviation of  $0.6\ \mu\text{m}$ . The resulting low fiber quality of the fiber bundles from methanol can be understood by observation of the SEM images of the formed fiber bundle network, where many thin fiber bundles cover longer and thicker fiber bundles. Self-assembly at different areas of the BTA solution, for example at the DSC pan cap surface or the air-liquid surface, is a possible explanation.

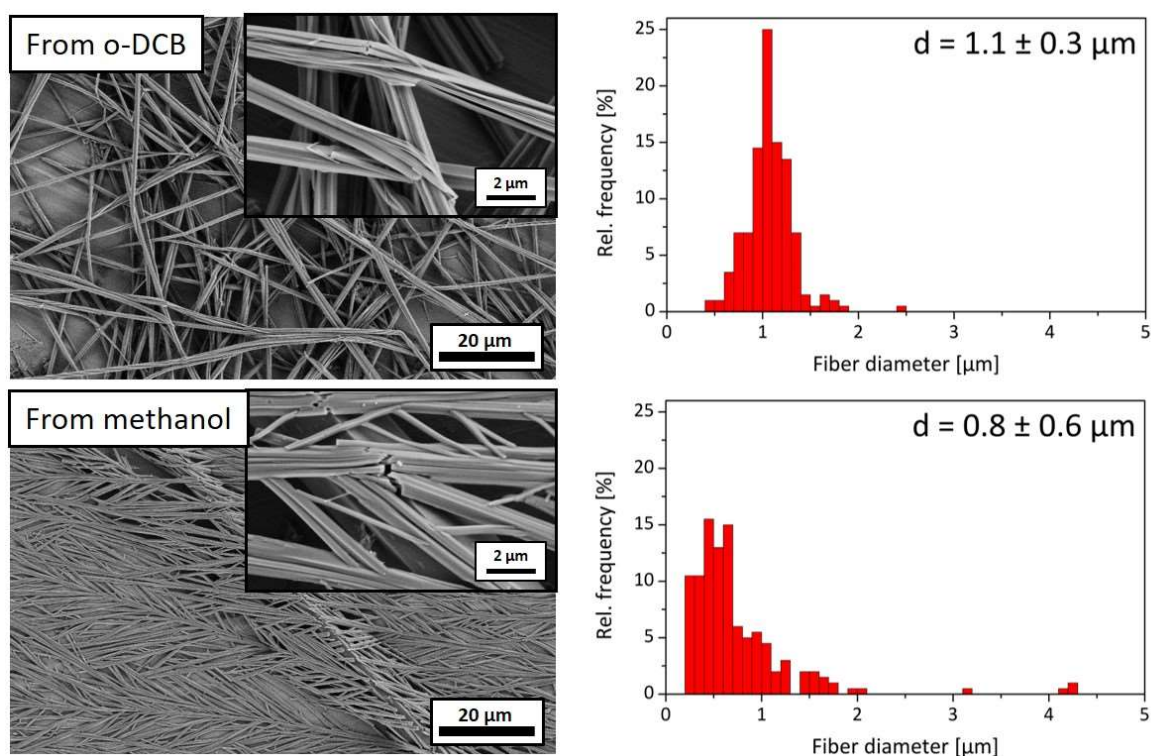


Figure 98: Scanning Electron Microscopy pictures (left) of the self-assembled supramolecular nanofiber bundles of **2c** bearing side chains of five carbon atoms from a 0.1 wt.% concentrated solution in ortho-dichlorobenzene and methanol, and the fiber size distribution (right) of the corresponding fiber samples. The bar diagrams show the fiber diameter dependent on the relative frequency of an evaluation of  $n = 200$  fiber diameters and the average value including standard deviation.

Regarding the self-assembly experiments with **2e** bearing side chains of seven carbon atoms, fiber diameter evaluations could be performed for the self-assembled fiber bundles from 1,4-dioxane and acetone, and the results can be seen in figure 99. In both cases, fiber bundles with small average fiber diameters of about  $0.15 \pm 0.06 \mu\text{m}$  from 1,4-dioxane and  $0.2 \pm 0.1 \mu\text{m}$  from acetone were formed. From 1,4-dioxane, band-like structures were developed but higher magnification reveals that they are build up by very thin fiber bundles, covering the surface of thicker fiber bundles.

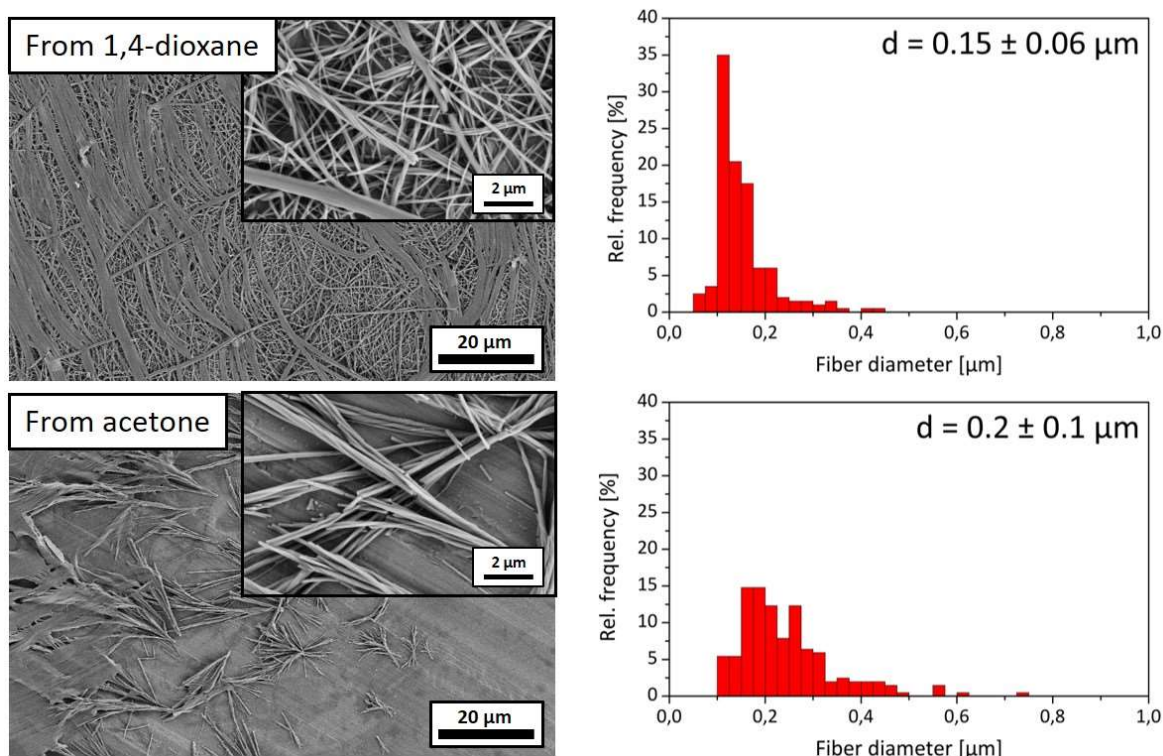


Figure 99: Scanning Electron Microscopy pictures (left) of the self-assembled supramolecular nanofiber bundles of **2e** bearing side chains of seven carbon atoms from a 0.1 wt.% concentrated solution in 1,4-dioxane and acetone, and the fiber size distribution (right) of the corresponding fiber samples. The bar diagrams show the fiber diameter dependent on the relative frequency of an evaluation of  $n = 200$  fiber diameters and the average value including standard deviation.

The self-assembly studies revealed that the selected BTAs with perfluorinated side chains can form fiber bundles with good quality, uniform surface and homogeneous fiber shape, which have average fiber diameters in the range of about two hundred nanometers up to a few micrometers. The next step is to mix a BTA with perfluorinated side chains with a structurally related BTA with alkyl side chains, which will be described next.

## 5.2 Co-self-assembly of two different 1,3,5-benzenetrisamides from solution

In this chapter, the simultaneous self-assembly (co-self-assembly) of two different structurally related 1,3,5-benzenetrisamides from solution from a solvent mixture is described. The term co-self-assembly is commonly used in the literature for the self-assembly of two different compounds, which can be connected via secondary bonds. For example Giasante et al. used the term co-self-assembly for their studies on three-component self-assembled nanofibers by using different anthracene derivatives as light emitting organogelators, resulting in fibers with tunable emissive properties.<sup>171</sup> Nie et al. reported on supramolecular, propeller-like architectures by co-assembly of achiral hexa-2-pyridyl-hexaazatriphenylene and different amino acid derivatives.<sup>172</sup> Fan et al. co-self-assembled vesicular nanoparticles by using structurally comparable amphiphilic boron-dipyrromethene dyes.<sup>173</sup> Co-self-assembly with derivatives based on a perylene core was also used to produce wide disk-like nanoparticles<sup>174</sup> and rod-like aggregates<sup>175</sup> or nanowires<sup>176</sup>.

In more detail and in view of this thesis, the four different possibilities how two trisamide molecules can self-assemble from solution are shown in figure 100.

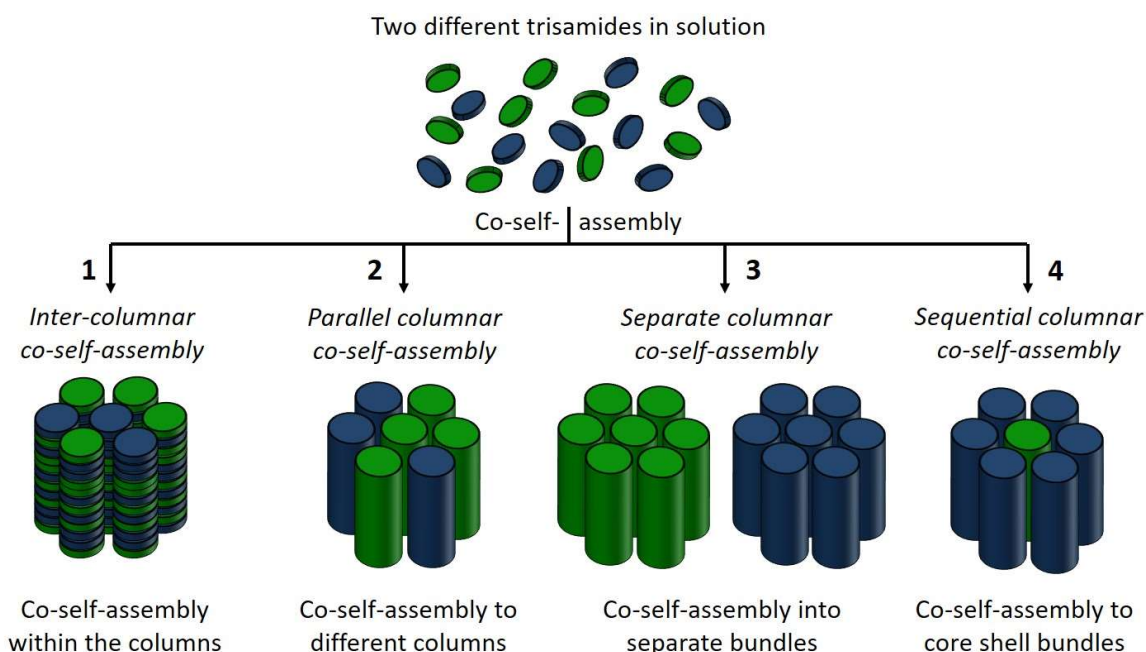


*Figure 100: Possible co-self-assembled structures of two structurally related trisamides from solution: 1 = Inter-columnar co-self-assembly (random self-assembly of the different molecules within the columns); 2 = Parallel columnar co-self-assembly (simultaneous self-assembly of columns built up by molecules of only one compound); 3 = Separate columnar co-self-assembly (different compounds self-assemble to separated fiber bundles); 4 = Sequential columnar co-self-assembly (the compounds self-assemble into a bundle with core shell structure).*

*Inter-columnar co-self-assembly* describes the co-self-assembly of two different compounds into one supramolecular fiber bundle where the molecules of both compounds are randomly distributed within a single column. This is difficult to achieve and was described if one of the materials has a chiral ability.<sup>165,177,178</sup> For example Smulders et al. used chiral and achiral 1,3,5-benzenetricarboxamides<sup>177</sup> and Helmich et al. porphyrin molecules<sup>178</sup> to co-self-assemble stacks with helical structures, and studied the chiral amplification phenomena of both systems. In 2012, van Houtem et al. studied the self-assembly of C<sub>3</sub>-symmetrical 3,3'-bis(acylamino)-2,2'-bipyridine discotics with achiral nine perfluoro-alkoxy tails and co-assembled it with derivatives bearing nine or six chiral, apolar dihydrocitronellyloxy tails.<sup>165</sup> The results were helical assemblies with the preference for alternating chiral and fluorinated discs up to an amount of 50 mol% of chiral discs. In 2019, de Windt et al. investigated the thermodynamically controlled, cooperative supramolecular copolymerization of two enantiomeric forms and an achiral analogue of 1,3,5-benzenetricarboxamides and 1,3,5-benzenetris(carbothioamides).<sup>179</sup> The results indicated that a nearly random copolymerization of the different monomers took place.

*Parallel columnar co-self-assembly* is the co-self-assembly of two different compounds into one supramolecular fiber bundle composed of single columns of only one compound.

*Separate columnar co-self-assembly* describes the co-self-assembly of two different compounds into separate fiber bundles only formed by compounds of the same kind. This can happen, when the single molecules only form aggregates with their own kind, or if both compounds have a different solubility in the applied solvent or solvent mixture and therefore will self-assemble at different times individually.

*Sequential columnar co-self-assembly* describes the co-self-assembly of two different compounds into one supramolecular fiber bundle exhibiting a core shell structure. This is a kind of co-self-assembly where the different compounds self-assemble not simultaneously. The one, which has the better solubility within the solution, will self-assemble later, on top of the first one, forming a shell around the bundles formed by the first compound.

The objective of this chapter is to investigate the self-assembly of two different BTAs from the same solvent mixture to supramolecular fibers or fiber bundles. Two BTAs, one with perfluorinated side chains and one with alkyl side chains were selected. It was important to find an appropriate solvent or solvent mixture, which provides good enough solubility for both BTAs and allows the formation of supramolecular fibers. The self-assembly experiments were carried out within polyamide and metal woven as support scaffolds.

### 5.2.1 Selected benzenetrisamides

Two structurally related BTAs, one perfluoroalkyl-substituted BTA (**A**) and one alkyl-substituted BTA (**B**) were selected and are shown in figure 101. Compound **A** is the BTA based on 1,3,5-triaminobenzene with three linear perfluorinated heptyl side chains connected to the amide group and was described in chapter 3 (designation **1e**). It was shown in 5.1.4 that this trisamide could be self-assembled to fiber bundles with a good fiber quality from two different solvents. Compound **B** is a BTA based on trimesic acid with three 6-methylheptyl side chains which was already described and characterized in detail by Timme et al.<sup>108</sup>, and was self-assembled successfully by Weiss et al.<sup>166</sup> This is the reason why it was chosen as the alkylated BTA. Nevertheless, **B** was already characterized before, a new synthesized batch was used for the experiments, which made it necessary to investigate it again for this work. The results are shown in the appendix (7.2 Appendix II: Additional data).

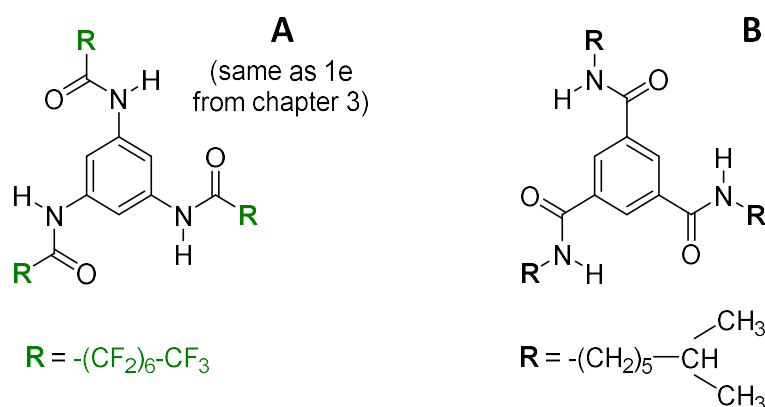


Figure 101: Selected trisamides for the co-self-assembly investigations: **A** (same as **1e** from chapter 3) = 1,3,5-benzenetrisamide based on 1,3,5-triaminobenzene with perfluorinated heptyl side chain; **B** = 1,3,5-benzenetrisamide based on trimesic acid with 6-methylheptyl side chains.

### 5.2.2 Support materials

Two support materials were used as scaffolds for the self-assembly experiments in order to obtain mechanical stable microfiber/supramolecular composites.

For most of the experiments, a polyamide (PA) woven from Buddeberg GmbH Laboratory Technology® with a mesh size of 100 μm was utilized as it is shown in figure 102. The woven was cut into pieces with edge lengths of about 1 cm and cleaned by washing in boiling methyl ethyl ketone (MEK) for 10 min, before it was subsequently dried at RT for at least 24 h. The woven microfibers show a characteristic rough and grooved surface.

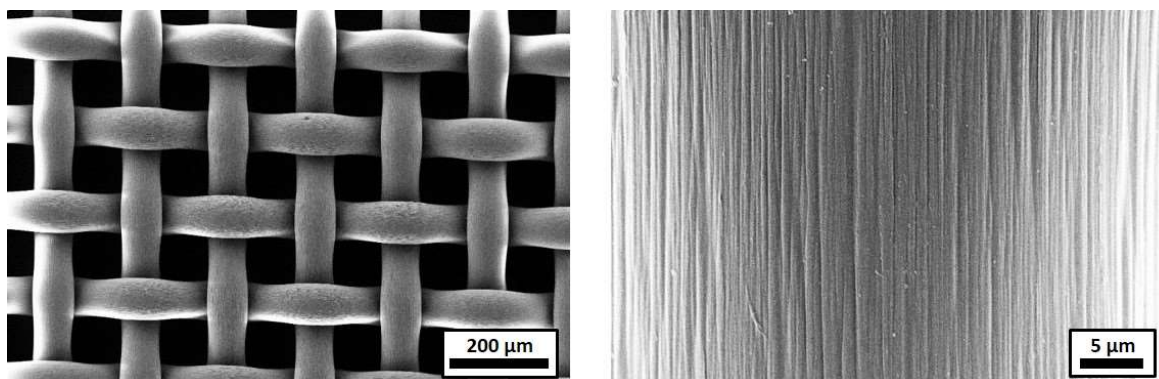


Figure 102: Polyamide woven from Buddeberg GmbH Laboratory Technology® with a mesh size of 100 µm utilized as support material for the self-assembly investigations.

The second support material was a metal woven with a mesh size of 68 µm from Bückmann GmbH for analysis by TGA. The metal woven was cut into pieces of about 1 cm edge length, cleaned with acetone in an ultrasonic sound bath for 15 min and subsequently dried at RT at least for 24 h. Figure 103 shows pictures of the cleaned metal woven. The surface of the woven microfibers was hurt mechanically originating from the storage process. The woven was stored in a reeled fashion where the different reeling layers had contact to each other.

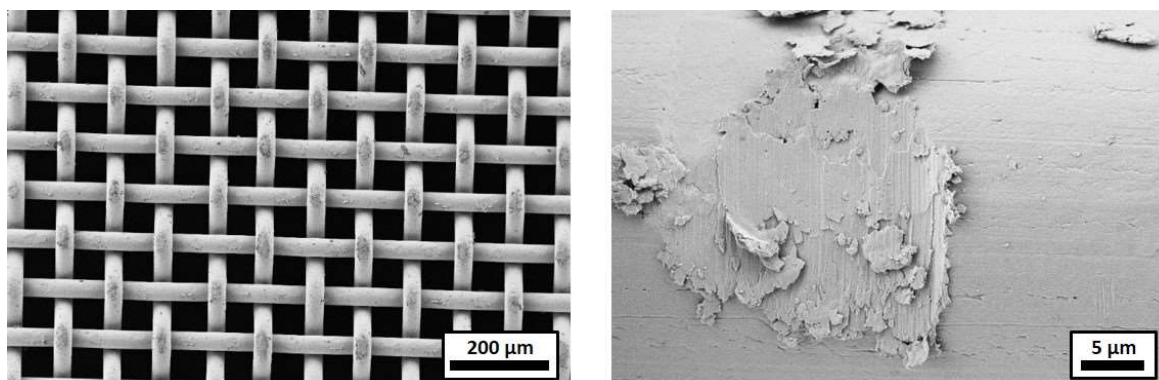


Figure 103: Metal woven from Bückmann GmbH with a mesh size of 68 µm utilized as support material for the self-assembly investigations.

### 5.2.3 Selected solvents

Two solvents were selected for the self-assembly experiments. The alkylated BTA **B** resulted in good fiber quality from MEK<sup>166</sup>, while the BTA with linear perfluorinated side chains **A** formed fibers with good quality from o-DCB. The boiling temperatures  $T_b$  of the selected solvents are:  $T_b(\text{MEK}) = 80\text{ °C}$  and  $T_b(\text{o-DCB}) = 179\text{ °C}$ .

It is important to know how fast the solvents evaporate from the woven. The vapor pressures of the solvents indicate that MEK evaporates first (vapor pressure of 96 mbar (20 °C)), and o-DCB stays a much longer time in the woven (vapor pressure of 1.3 mbar (20 °C)). For the investigation of the evaporation times from the PA woven, evaporation experiments were performed, and the weight loss was detected every six seconds at 40 °C with the help of a moisture analyzer. A moisture analyzer can be used for the determination of the moisture content of a material. In general, it is a scale including a heating element in the closure head and a cable-connected printer to record the data. The sample is placed on the scale, the temperature is adjusted, and the measurement is started. Over a determined time, the moisture analyzer measures the weight of the sample and gives out the results in fixed time intervals. After the measurement is done, the results can be plotted and a data curve for the evaporation of the contained liquid over time can be obtained. Figure 104 shows the results of the pure, as well as a 1:1 wt.% ratio mixture of the solvents MEK and o-DCB from a PA woven.

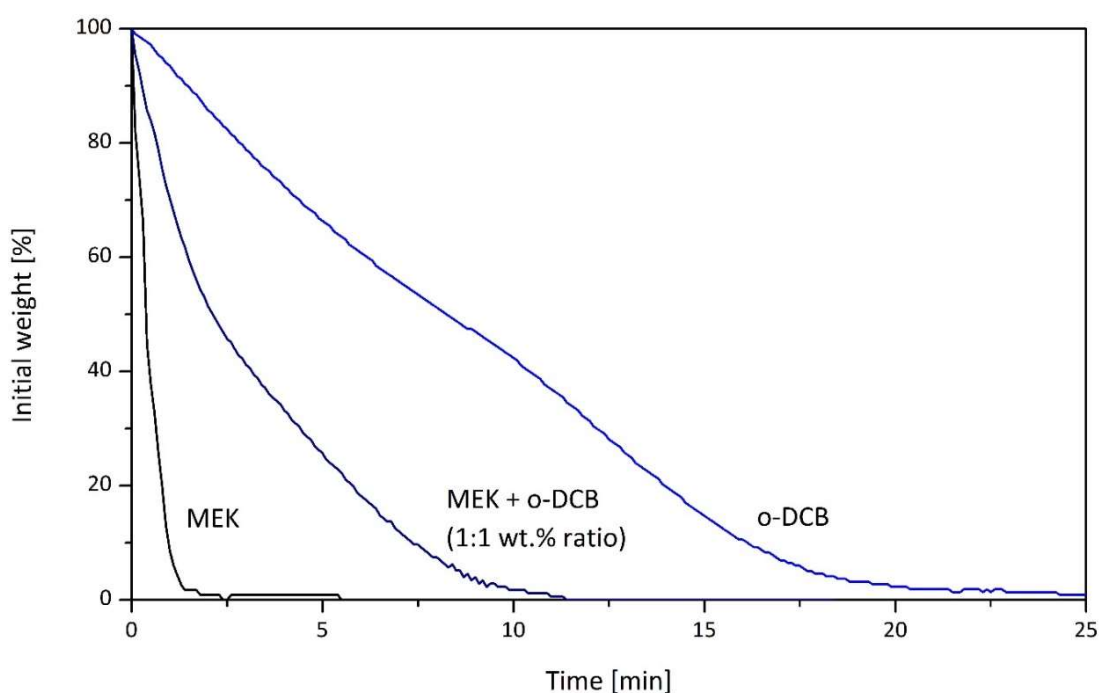
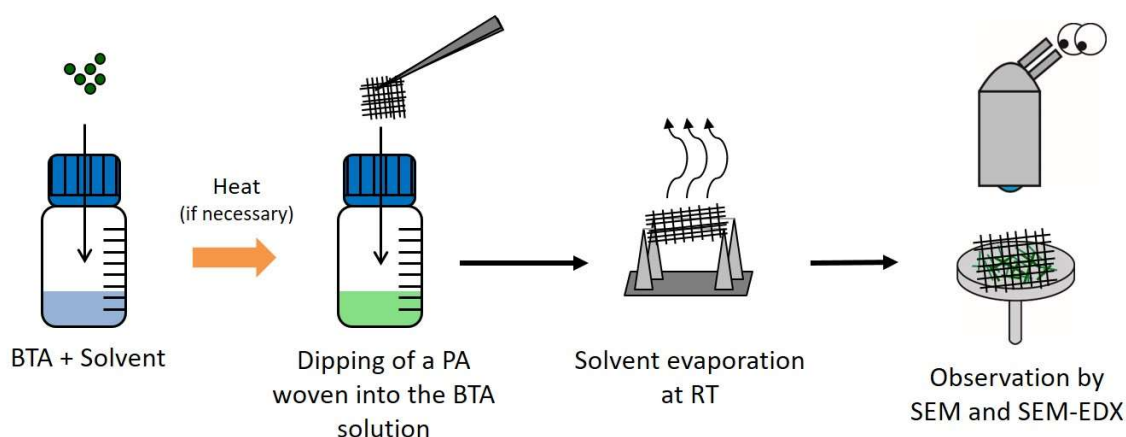


Figure 104: Evaporation curves (initial weight versus time) of methyl ethyl ketone (MEK), ortho-dichlorobenzene (o-DCB), and a 1:1 wt.% ratio mixture of both solvents in a polyamide woven scaffold. The curves originate from evaporation experiments by detection of the weight loss for every six seconds over time at 40 °C from a soaked polyamide woven until the solvents are completely evaporated.

The results of the moisture analyzer experiments show that pure MEK evaporates after 5 min while pure o-DCB needs an evaporation time of about 28 min to be removed completely. The evaporation curve of the solvent mixture shows a strong decrease in weight at first until about 50 % weight, then the slope is decreasing. This can be explained by the higher vapor pressure of MEK, which forces MEK to evaporate first. When most of MEK is removed, the remaining o-DCB is evaporating over a longer time period. The data also indicate that the solvents are mixable without phase separation, which can be seen by the curve progression of the mixture between the two single evaporation curves on the time scale. All the solvents are completely evaporated after about 13 minutes at 40 °C environment temperature. It had to be hold in mind that the measurements were executed at 40 °C but the drying of the self-assembled samples was done at RT. Therefore, the samples were dried at least for 2 h at RT to ensure complete solvent evaporation.

#### 5.2.4 Self-assembly procedure and parameters

All experiments were performed with the same procedure, which can be seen in figure 105. In the first step, one or two BTA powders were completely dissolved in the selected solvents or solvent mixture at three different concentrations (0.5, 1.0, and 1.5 wt.%). If necessary, the BTA/solvent mixtures were heated in steps of 5 °C with an equilibrium time of 15 min until the sample was completely dissolved. The dissolution was checked visually with a green laser.



*Figure 105: Experimental procedure for the self-assembly of two structurally related 1,3,5-benzenetrisamides from the same solvent or a solvent mixture. The 1,3,5-benzenetrisamides and solvents were mixed and heated if necessary, in 5 °C steps while stirring for 15 min for every step until a clear solution was obtained. A polyamide or metal woven was dipped into the solution and dried at room temperature on a self-made stand before the examination of the sample was performed.*

When the powder was completely dissolved, in the second step a polyamide (PA) or metal woven was dipped into the solution. The fully soaked woven was subsequently placed on a self-made stand, which had as less contact area as possible to the woven. The solvent was evaporated at least for half an hour at RT. After this step, the filled woven was directly used for further characterization by SEM and TGA. For DSC investigation, the self-assembly was directly carried out in the DSC pan by removing the solvents at RT for 24 h and further drying for another 24 h at 40 °C under vacuum.

### 5.2.5 Results of the self-assembly of individual compounds from a solvent or a solvent mixture

Dissolution experiments with **A** and **B** in MEK and o-DCB at concentrations of 0.5, 1.0, and 1.5 wt.% were performed as described before. In table 13, the results of the dissolution experiments are reported only for successful dissolution. The temperatures in parenthesis stand for the dissolution temperatures. In all cases, it was only heated to a temperature of 100 °C because in a mixture with MEK as second solvent, MEK would have been already evaporated at this temperature.

*Table 13: Dissolution results of the 1,3,5-benzenetrisamides **A** and **B** in methyl ethyl ketone and ortho-dichlorobenzene at 0.5, 1.0, and 1.5 wt.%. The temperatures in parenthesis stand for the temperature of complete dissolution.*

	Methyl ethyl ketone (MEK) Vapor Pressure: 96 mbar (20 °C)	o-Dichlorobenzene (o-DCB) Vapor Pressure: 1.3 mbar (20 °C)
<b>A</b> (-C <sub>7</sub> F <sub>15</sub> )	0.5 wt.% (RT) 1.0 wt.% (RT) 1.5 wt.% (RT)	0.5 wt.% (RT)
<b>B</b> (-C <sub>8</sub> H <sub>17</sub> )	0.5 wt.% (65 °C) 1.0 wt.% (75 °C) 1.5 wt.% (80 °C)	0.5 wt.% (RT)

The results of the dissolution experiments show that MEK is a very good solvent for the BTA with linear perfluorinated side chains **A**. It is possible to dissolve **A** at a concentration of 1.5 wt.% at room temperature. The mixture with **B** had to be heated, but it is also possible to dissolve up to 1.5 wt.% of **B**. In o-DCB, **A** and **B** could only be dissolved at RT at the lowest

concentration of 0.5 wt.%. At higher concentration, a temperature above 100 °C would be necessary.

### ***Self-assembly experiments of A from single solvents***

For the first experiments, **A** was mixed with MEK at a concentration of 0.5 wt.% at RT and the self-assembly was performed as described before. The results are shown in figure 106 by SEM images. Compound **A** self-assembled from MEK to a layer-like structure. The layer covers only the woven microfibrils and all the cavities stay uncovered. This means that for the self-assembly of **A** to supramolecular fibers, single solvent MEK is not sufficient. SEM images of the successful self-assembly of **A** from o-DCB was already shown in chapter 5.1.4. Here a higher concentration was used, but the fiber bundle shape stayed the same.

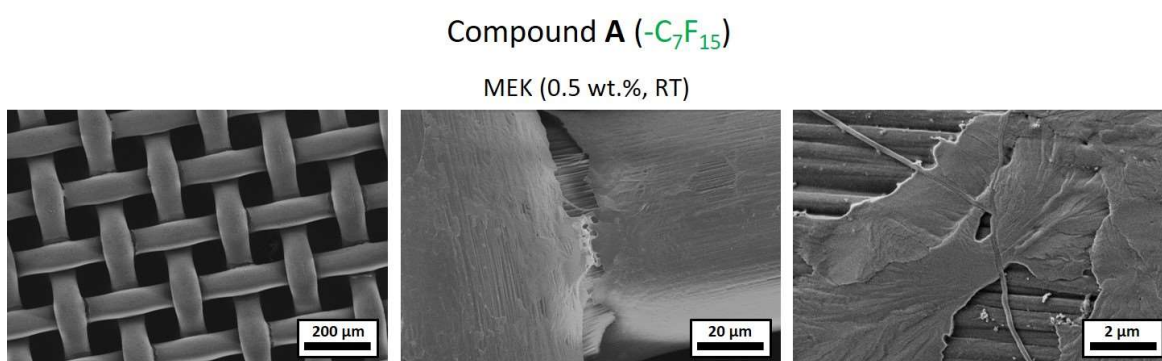


*Figure 106: Scanning Electron Microscopy pictures of the self-assembly results of **A** in the polyamide woven from a 0.5 wt.% concentrated solution at RT in methyl ethyl ketone.*

### ***Self-assembly experiments of B from single solvents***

Self-assembly experiments with **B** from MEK or o-DCB at a concentration of 0.5 wt.% were performed and the results are shown in figure 107 by SEM images. Compound **B** could be dissolved completely at RT at a concentration of 0.5 wt.%, while only in MEK it was necessary to heat the mixture up to 65 °C. Compound **B** forms homogeneous supramolecular fiber bundles with uniform surface from MEK with about one micrometer in diameter covering the woven cavities and forming a fiber net. In the case of o-DCB, thin fiber bundles arranged in a fiber net, which is completely covering the woven cavities, are formed.

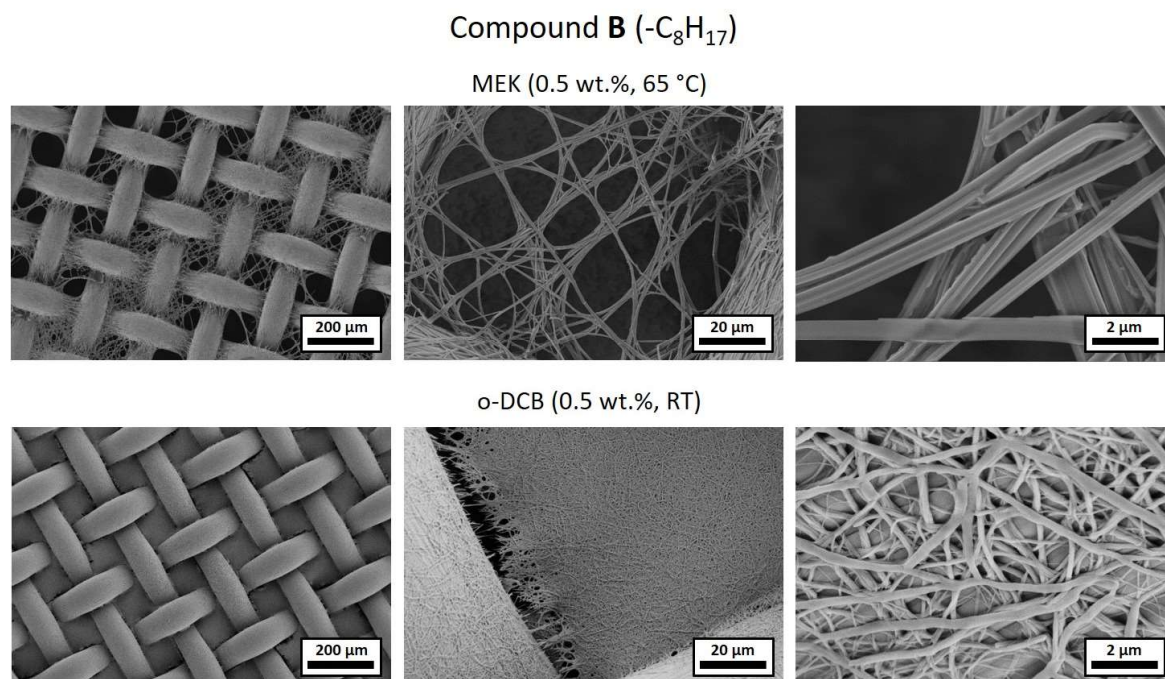


*Figure 107: Scanning Electron Microscopy pictures of the self-assembly results of **B** in the polyamide woven from a 0.5 wt.% concentrated solution at 65 °C of methyl ethyl ketone (top) and at RT of ortho-dichlorobenzene (bottom).*

The most promising self-assembled fiber bundles of **A** are formed from o-DCB, and of **B** from MEK. The results show that only one single solvent for the co-self-assembly experiments, in which both will self-assemble to fibers, is not sufficient. Therefore, it is necessary to use a solvent mixture with the premise that the BTAs are still self-assembling to fibers bundles and are also dissolvable at a temperature where none of the solvents already evaporate. MEK proved to be a good solvent for both BTAs, but it was not possible to dissolve them in o-DCB above a concentration of 0.5 wt.% without heating. Therefore, solvent mixtures with MEK were necessary for the dissolution of the compounds, even if **A** did not form fibers from MEK. In the following, a solvent mixture of MEK and o-DCB at a weight percent ratio of 1:1 was used to perform dissolubility and self-assembly experiments with the single BTAs at concentrations of 0.5, 1.0 and 1.5 wt.% to investigate the fiber formation from a solvent mixture.

**Self-assembly experiments of A from a solvent mixture**

Figure 108 shows the results of the self-assembly experiments of **A** from the solvent mixture at different concentrations. Therefore, the compound was completely dissolved already at RT at all concentrations. It self-assembles to thin fiber bundles at the lowest concentration. The fiber bundles could mostly be located near to the cross sections of the woven microfibers. The layer structure can be explained by a surface self-assembly process. It is possible that when MEK evaporates and the concentration increases high enough to start the self-assembly process, some material forms a layer at the surface in contact with the woven microfibers and remains there until the solvents are evaporated. This structure can also be seen in the images of the sample processed from a 1.5 wt.% concentrated solution, but in this case, no fibers were formed. The compound forms a sponge-like structure.

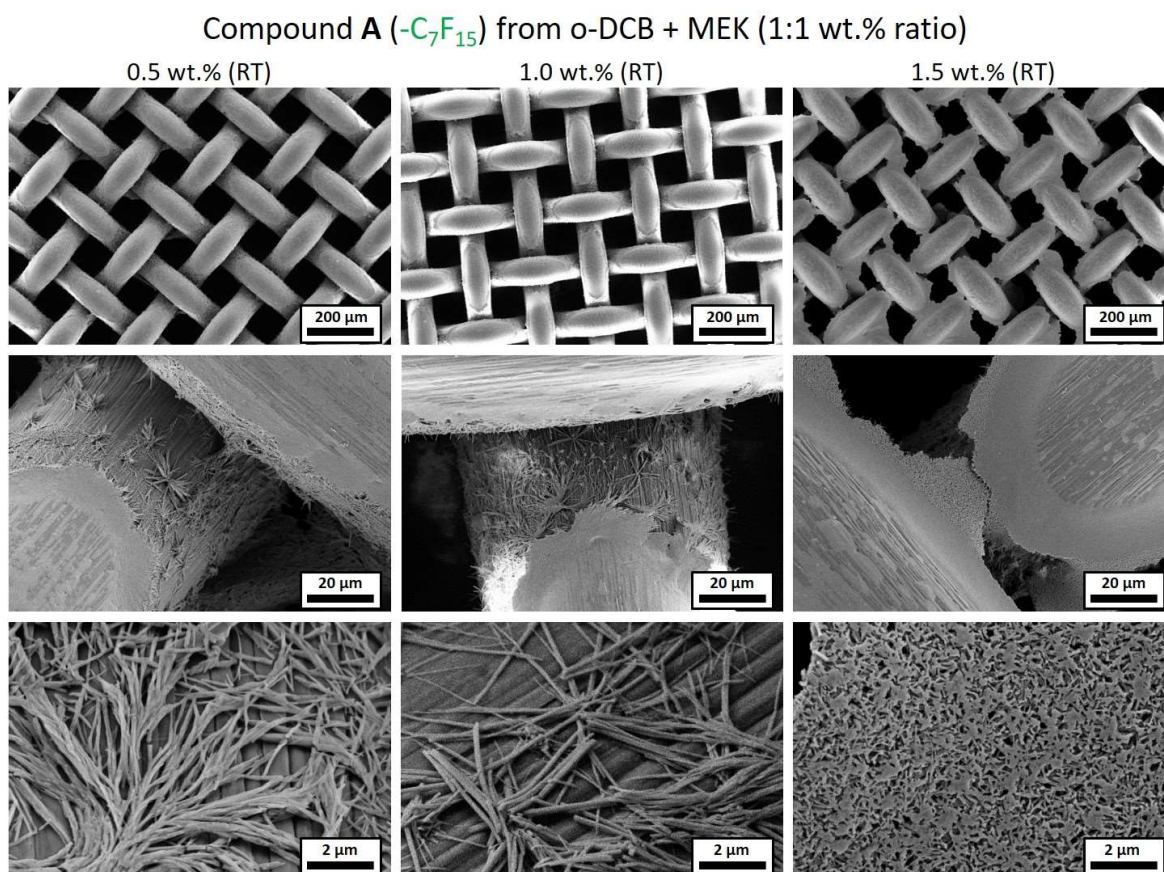


Figure 108: Scanning Electron Microscopy pictures of the self-assembly results of **A** in the polyamide woven from a 0.5 wt.% (left), 1.0 wt.% (middle) and 1.5 wt.% (right) concentrated solution of ortho-dichlorobenzene and methyl ethyl ketone (wt.% ratio: 1:1) The temperatures in parenthesis stand for the temperature of complete dissolution.

**Self-assembly experiments of B from a solvent mixture**

The self-assembly results of **B** from the o-DCB and MEK mixture can be seen in figure 109. It was not possible to dissolve the BTA at RT at all concentrations, the mixture with the lowest concentration of 0.5 wt.% had to be heated up to 60 °C, the 1.0 wt.% concentrated mixture up to 70 °C and the mixture with the highest concentration of 1.5 wt.% to a temperature of 75 °C. The shapes of the self-assembled fiber bundles of **B** from the MEK and o-DCB mixture are the same at all concentrations. The only difference is that more fiber bundles were formed with increasing concentration. The fiber bundles do not only cover the cavities of the woven but also the woven microfibers. They appear to be very thin with a diameter of about 100 nm to 200 nm. The fiber bundles form a dense fiber net with only small and randomly distributed cavities over the whole sample area.

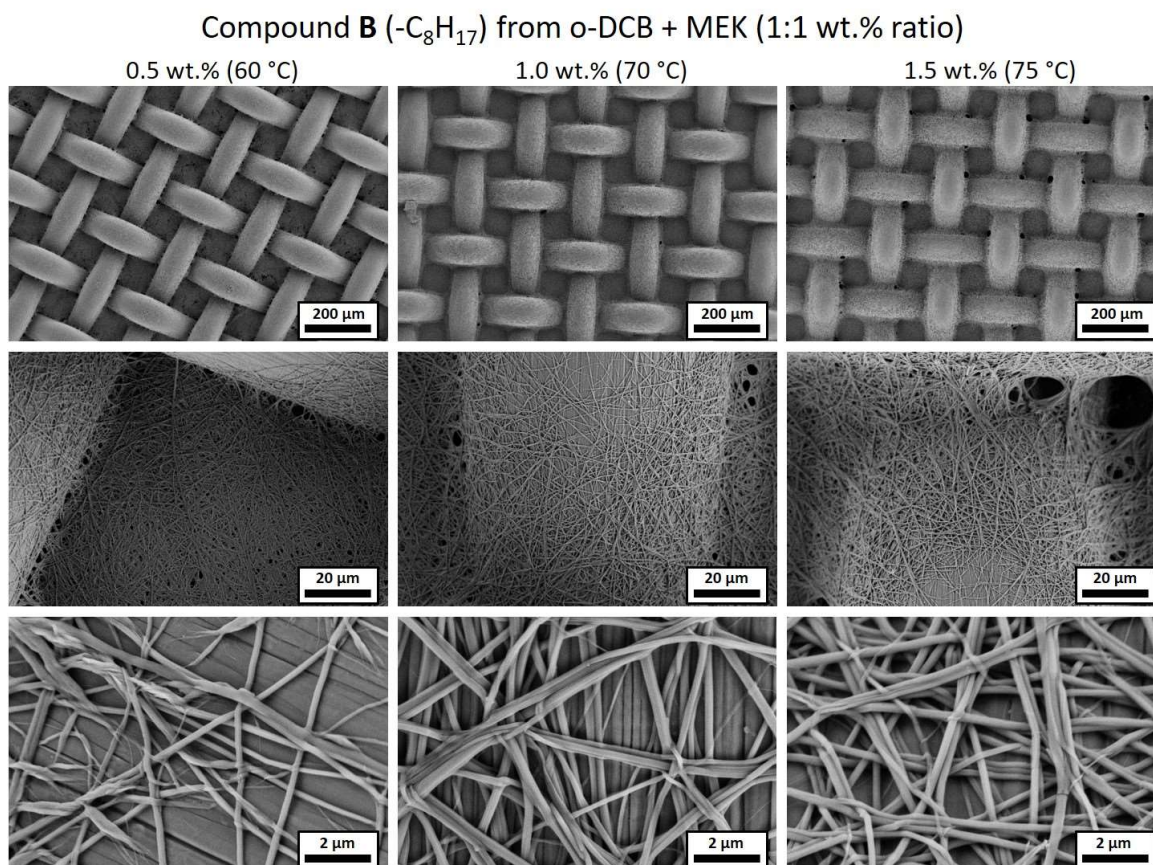


Figure 109: Scanning Electron Microscopy pictures of the self-assembly results of **B** in the polyamide woven from a 0.5 wt.% (left), 1.0 wt.% (middle) and 1.5 wt.% (right) concentrated solution of ortho-dichlorobenzene and methyl ethyl ketone (wt.% ratio: 1:1) The temperatures in parenthesis stand for the temperature of complete dissolution.

### 5.2.6 Results of the co-self-assembly from a solvent mixture

After the results of the self-assembly of the single BTAs **A** and **B** were shown, the results of the co-self-assembly from a solvent mixture is described in the following.

The experimental procedure for the co-self-assembly from a solvent mixture is the same as it was shown in figure 105 and described in chapter 5.2.4 with the difference, that not only one but two BTAs were mixed and dissolved together in the 1:1 solvent mixture of MEK and o-DCB. A BTA concentration of 1.0 wt.% was prepared which means that both single **A** and **B** were present with a concentration of 0.5 wt.% in the solvent mixture. The BTAs were completely dissolved at a temperature of 60 °C, which means that self-assembly upon cooling and solvent evaporation could take place. The resulting sample was characterized by SEM to investigate the fiber shape and by SEM-EDX to distinguish the supramolecular fiber bundles formed by the perfluorinated BTA **A** from the fiber bundles formed by the alkylated BTA **B**. TGA of the sample was performed to check if the initial weight percent ratio can also be found in the support scaffold, and DSC was carried out to find possible changes in the transition temperatures. For the thermal characterization methods, the co-self-assembly experiment was carried out in a metal woven.

#### *Self-assembly into the PA woven as support material*

The SEM pictures of the co-self-assembled fiber bundles of BTA mixture **A** and **B** (wt.% ratio: 1:1; mol% ratio: 1:2.4) from a 1.0 wt.% concentrated solution in MEK and o-DCB in a PA woven are displayed in figure 110 at different magnifications. At low magnification, the images show that the cavities of the PA woven are completely covered. At higher magnification, a dense fiber net can be identified which is partly covered by a patch-like layer formation. Comparison to the self-assembled fiber bundles of the single BTAs from the same solvent mixture reveals that the thin fiber bundles are similar to the fiber bundles formed by **B**. It is possible that one compound self-assembles first forming a fiber net, and in a second step, the other compound self-assembles on the fiber bundle net by formation of patch-like agglomerations. For a better determination of the different BTA compounds, SEM pictures combined with Energy-Dispersive X-Ray Spectroscopy (EDX) measurements were performed to distinguish the fluorinated from the alkylated compound.

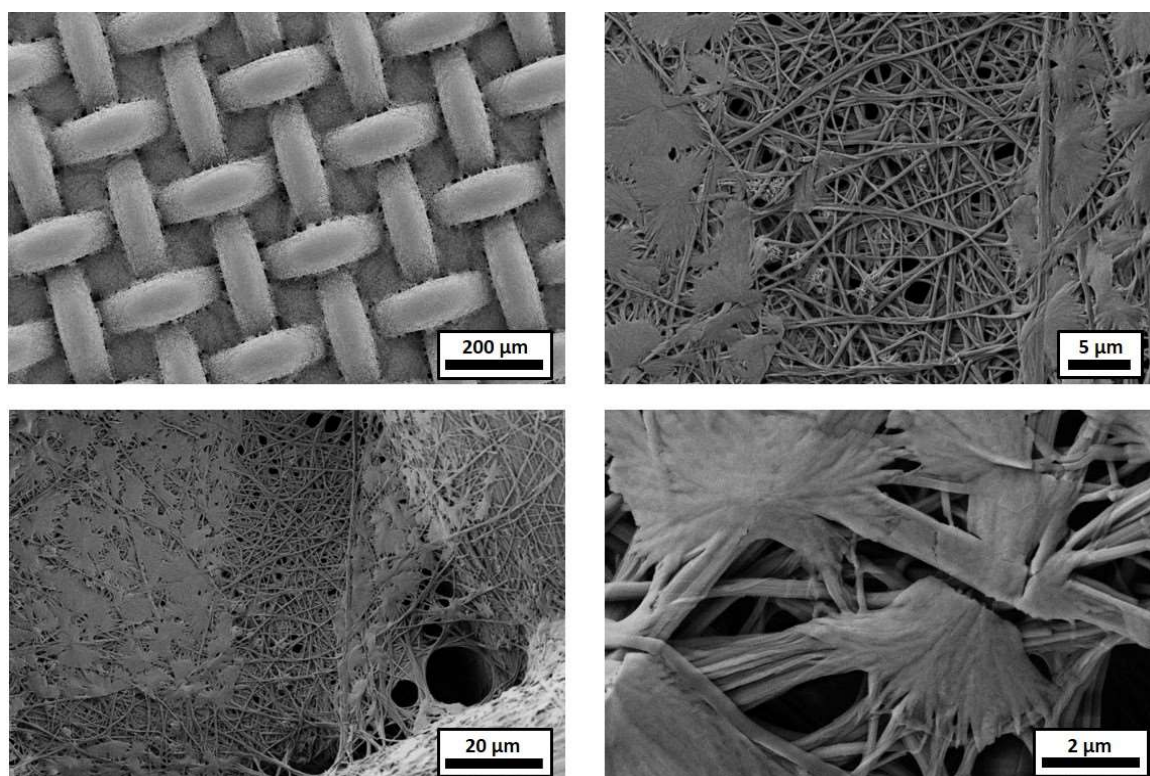
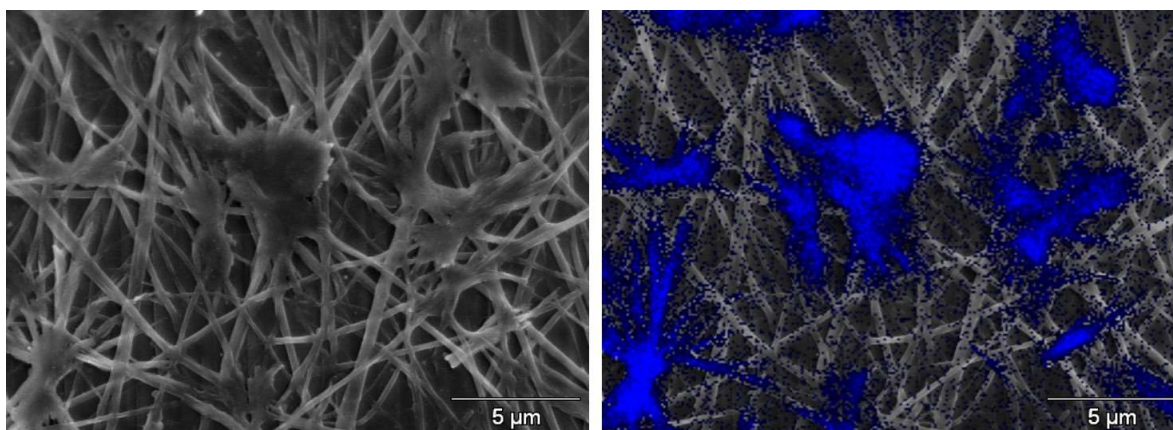


Figure 110: Scanning Electron Microscopy pictures of the self-assembled BTA mixture A and B at a concentration of 1.0 wt.% (wt.% ratio: 1:1; mol% ratio: 1:2.4) in a polyamide woven with a 100  $\mu\text{m}$  mesh size from a solvent mixture of methyl ethyl ketone and ortho-dichlorobenzene (wt.% ratio: 1:1).

### **Investigation by SEM-EDX**

Energy-Dispersive X-Ray Spectroscopy (EDX) allows the characterization of a sample by determination of the elemental composition in a particular area simultaneously with a usual SEM imaging. It is possible to include the EDX results into the SEM picture to make areas of high specific elemental appearance visible, which then can be recognized by a colored overlay. The EDX measurement is similar to the normal XRD as it was described in chapter 3 but it has two important differences. In a XRD measurement, the diffracted rays are detected at different angles to determine distances in an ordered molecular structure. Therefore, it is crucial that the X-rays of the incident beam have always the same energy level. In contrast to this, it is important to change the energy of the incident beam over a determined range in an EDX experiment. In an unexcited state, each electron of an atom has a discrete energy level or moves within an electron shell. An incident beam can excite an electron in an inner shell and an electron hole is generated, which will be automatically filled by an electron from an outer shell. This process releases energy of an amount similar to the difference between the two shells. Because this energy is characteristic for the atomic structure of every different

element, it is possible to get a spectrum showing signals for the counts of different emitting elements. The application of SEM-EDX makes it possible to highlight areas of high fluorine amount as it can be seen in figure 111. On the left side, a usual SEM picture is shown with the same fiber bundle shapes as it was the case in the SEM pictures in figure 110. The picture on the right side shows the same sample area but with an overlay of the EDX measurement which marks spots of fluorine presence by a blue color. The brighter the areas of blue color, the more fluorine atoms are present in this area. The EDX results verify that fluorinated compound **A** is mostly located at the spots of the patch-like agglomerations which leads to the conclusion that the fiber net is formed by **B**. This can be explained by a two-step self-assembly process where **B** self-assembled to fiber bundles first while **A** was still dissolved and after further removal of the solvent, the fluorinated compound self-assembled onto the already formed fiber net. The EDX results indicate that the different compounds form separate fiber bundle structures denoting a *separate columnar co-self-assembly* process.



*Figure 111: Scanning Electron Microscopy Energy-Dispersive X-ray Spectroscopy (SEM-EDX) pictures of the supramolecular fibers of co-self-assembled BTAs **A** and **B** (wt.% ratio 1:1, mol% ratio: 1:2.4) from a 1.0 wt.% concentrated solution of methyl ethyl ketone and ortho-dichlorobenzene (wt.% ratio: 1:1) in a polyamide woven. On the left side the SEM picture without EDX, on the right side the same SEM picture with an overlay of the local counts of detected X-rays with energy level characteristic for the fluorine element shown by a blue color.*

#### **Investigation by TGA of the self-assembled BTA mixture from a metal woven**

TGA was used to determine the amount of each BTA self-assembled into the support scaffold. For the measurements, the PA woven had to be replaced by a metal woven, which is stable to temperatures above 700 C. This ensures the decomposition of only the BTAs without falsify the results due to a decomposition of the woven itself. The results of the self-assembly into

a metal woven can be seen in figure 112 by SEM pictures. The self-assembled structures are the same as the ones formed in the PA woven.

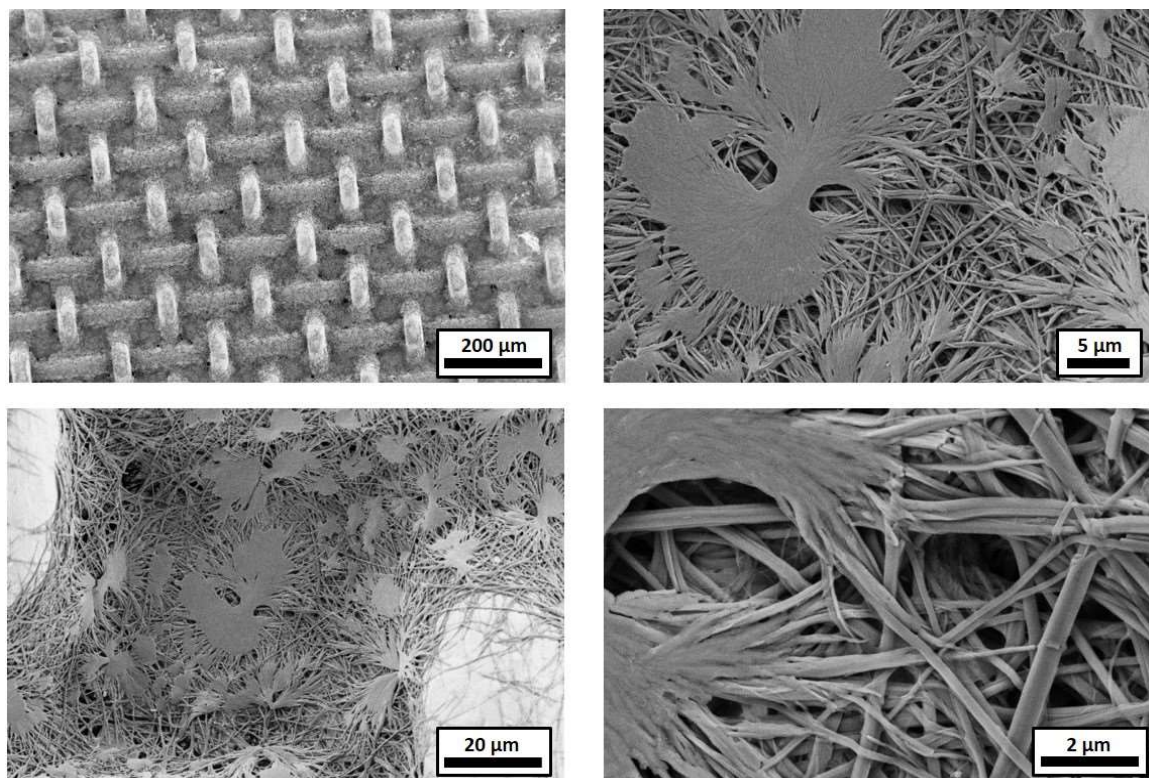


*Figure 112: Scanning Electron Microscopy pictures of the self-assembled mixture **A** and **B** at a concentration of 1.0 wt.% (wt.% ratio: 1:1; mol% ratio: 1:2.4) in a metal woven with a 63 μm mesh size from a solvent mixture of methyl ethyl ketone and ortho-dichlorobenzene (wt.% ratio: 1:1).*

The weight of the BTA materials in relation to the weight of the metal woven was about one part to ten parts. This ends in a higher random noise of the TGA data after the weight of the metal woven is subtracted to get the data for the pure BTAs. The TGA results of the single self-assembled compounds **A** and **B** and of the self-assembled compound mixture **A + B** in a metal woven can be seen in figure 113. The curve progression of the weight loss at increasing temperature of the self-assembled BTA mixture is the same as the data for single compound **A** until 50 % of the initial weight is removed. Afterwards, the weight remains constant for about 5 degrees and then the rest of the material begins to sublimate. The shoulder in the weight loss curve at exactly 50 % of initial weight proves the presence of the weight percent ratio of 1:1 of the compound mixture **A** and **B**.

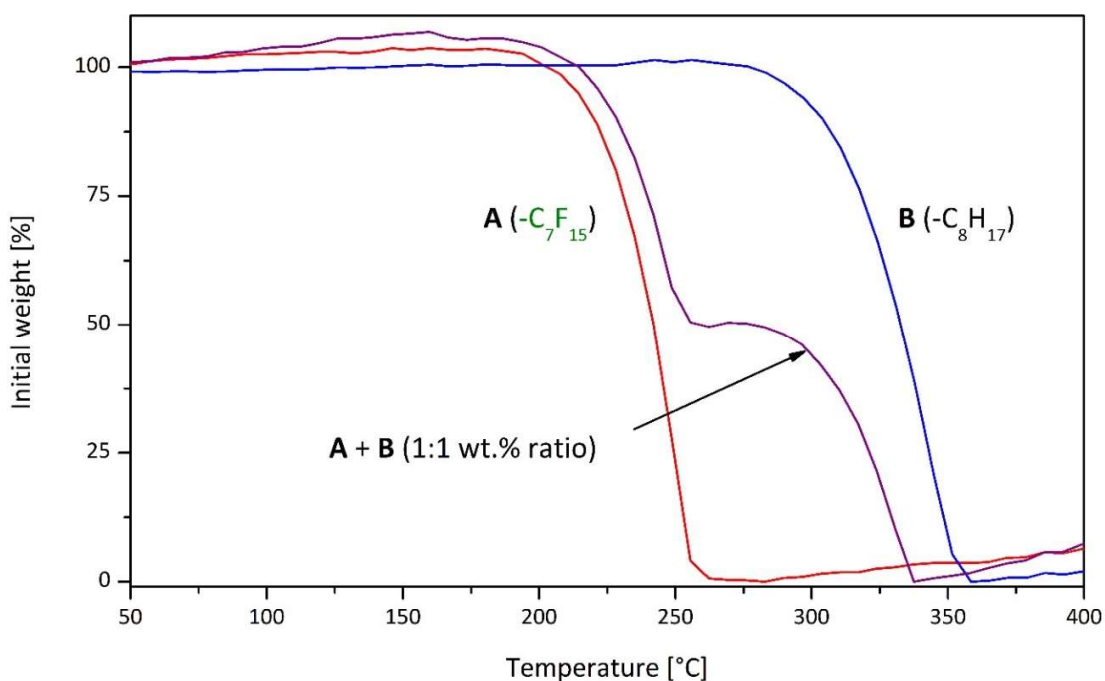


Figure 113: Thermogravimetric Analysis scans of the single self-assembled compounds **A** and **B**, and of the self-assembled compound mixture (wt.% ratio: 1:1; mol% ratio: 1:2.4) in a metal woven from a methyl ethyl ketone and ortho-dichlorobenzene solvent mixture (wt.% ratio: 1:1). The measurements of the 1,3,5-benzenetrisamides were executed in the metal woven (wt.%-ratio of the metal woven to the 1,3,5-benzenetrisamides material: ca. 10:1) and the weight of the metal woven was subtracted after the measurement.

### Investigation by DSC

DSC analysis of the mixed and self-assembled BTAs was performed to further determine the type of self-assembly. After drying, the resulting BTA powder was analyzed by DSC and the first heating scan, compared to the second heating scans of the pure compounds, was used to get conclusions on the self-assembly type. The second heating scan of the DSC of single compounds **A** and **B** compared to the first heating scan of the compound mixture of **A + B** (wt.% ratio: 1:1, mol% ratio 1:2.4) can be seen in figure 114. The DSC data of the compound mixture shows four transitions. The transition at the highest temperature of 273 °C can be assigned to the clearing temperature of **B** and the transition at 193 °C can be identified as the clearing temperature of **A**. The two remaining heat flow maxima at around 140 °C are the transitions from the crystalline state into the mesophase of **A**. Within the second heating scan of **A**, this transition shows only one heat flow maximum, but it is possible that the appearance of this transition changes after the first heating because of secondary recrystallization. All the

transitions of the single compounds can also be found at nearly the same temperatures in the DSC curves of the compound mixture, which indicates a *separate* or *sequential columnar co-self-assembly* process.

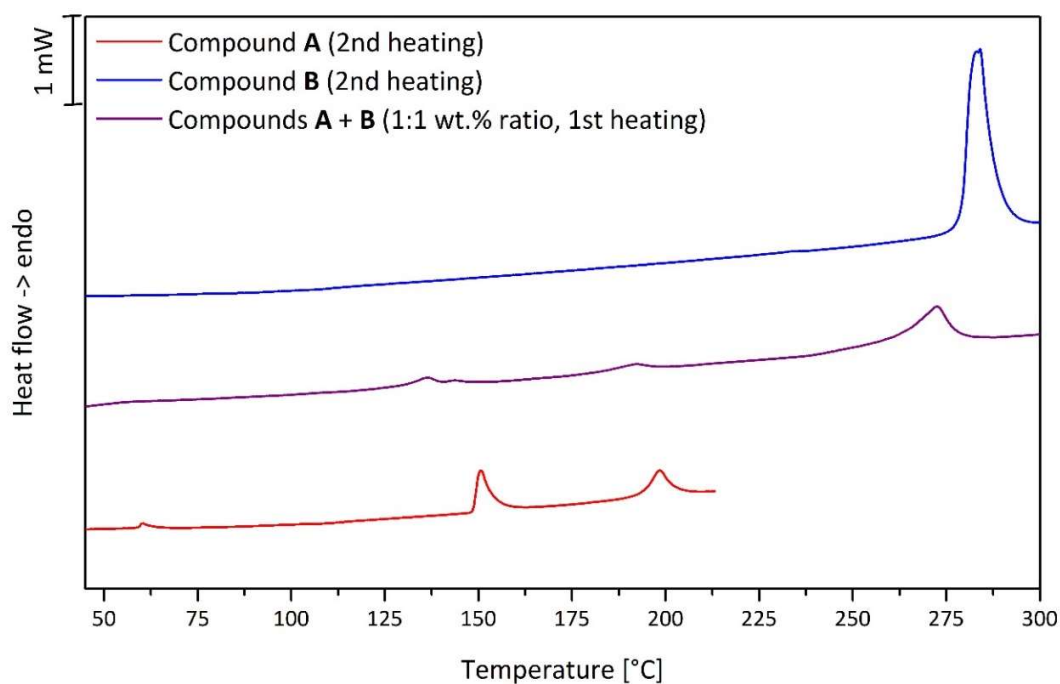


Figure 114: First heating scan of the Differential Scanning Calorimetry analysis of the self-assembled mixture **A + B** (wt.% ratio: 1:1; mol% ratio: 1:2.4) from a methyl ethyl ketone + ortho-dichlorobenzene mixture (wt.% ratio 1:1) in comparison to the data of the second heating from the Differential Scanning Calorimetry analysis of the single compounds.

### 5.3 Summary

In this chapter, the self-assembly of 1,3,5-benzenetrisamides with linear perfluorinated side chains from solution, as well as the co-self-assembly of two structurally related BTAs was investigated. Three BTAs based on 1,3,5-triaminobenzene (**1a**, **1c** and **1e**) and trimesic acid (**2a**, **2c** and **2e**) with different side chain lengths of three, five and seven carbon atoms were selected. One of them as well as a BTA with alkyl side chains were chosen for co-self-assembly experiments to investigate their self-assembly behavior in the presence of a different compound in the same solvent mixture.

Regarding the BTAs based on 1,3,5-triaminobenzene, supramolecular nanofiber bundles were formed from only a few solvents. Trisamide **1a** formed fiber bundles from toluene solutions of all three investigated concentrations (0.01, 0.025 and 0.1 wt.%) upon cooling. From *o*-DCB, fibers were formed upon cooling from solutions at concentrations of 0.025 and 0.1 wt.% while from the 0.01 wt.% concentrated solution, fibers were formed after solvent evaporation. From  $\text{CHCl}_3$  at the lowest concentration, **1a** also formed fiber bundles upon cooling. The best fiber quality was found from *o*-DCB with an average fiber diameter in the range of two to three micrometers. Second best results were achieved from toluene with lower average fiber diameters of about four hundred micrometers from 0.01 and 0.025 wt.% concentrated solutions.

The BTA **1c** bearing side chains of five carbon atoms self-assembled to fiber bundles from *o*-DCB at all concentrations and from *n*-octane at the lowest concentration upon cooling. The best fiber results were obtained from *o*-DCB with average fiber diameters between two and three micrometers.

Trisamide **1e** bearing side chains of seven carbon atoms self-assembled upon cooling to fiber bundles from toluene and *o*-DCB at all investigated concentrations. Here the best fiber quality was obtained from *o*-DCB with comparably thin average fiber diameters of between one hundred and two hundred nanometers. Second best results were achieved from 0.01 and 0.025 wt.% concentrated solutions from toluene with average fiber diameters of about two hundred nanometers.

The BTAs based on trimesic acid also self-assembled to fiber bundles. The BTA **2a** with side chains of three carbon atoms formed fiber bundles only from *o*-DCB upon cooling. The average fiber diameter was about 1.5 micrometers.

Trisamide **2c** bearing side chains of five carbon atoms self-assembled to fiber bundles upon cooling from *o*-DCB and after solvent evaporation from methanol, after it could be dissolved at room temperature. Fiber bundles with higher quality were obtained from *o*-DCB with an average fiber diameter of about one micrometer.

The BTA **2e** with the longest side chains of seven carbon atoms formed fibers from 1,4-dioxane upon cooling and from acetone after solvent evaporation. Both showed similar fiber quality with average fiber diameters of about 150 and 240 nanometers.

In conclusion, it is possible to self-assemble BTAs with linear perfluorinated side chains to supramolecular fiber bundles with average fiber diameters in the range of one hundred nanometers up to about four micrometers depending on the side chain length, the trisamide core, and the applied solvent. In most cases the BTAs with long side chains of seven carbon atoms form fiber bundles with lower average fiber diameters. The BTAs with shorter side chains of three carbon atoms self-assemble into comparably thicker fiber bundles. The self-assembled fiber bundles show always a uniform surface, the thinner fiber bundles are roundly shaped while the thicker fiber bundles mostly show edges and sometimes a twisted morphology.

For the co-self-assembly experiments, trisamide **1e** with perfluorinated side chains of seven carbon atoms and a structurally related BTA bearing three 6-methylheptyl side chains were co-self-assembled from a 1:1 mixture of methyl ethyl ketone (MEK) and o-dichlorobenzene (o-DCB) into a support scaffold. The co-self-assembly resulted in two different morphologies: fiber bundles and patch-like agglomerations. SEM-EDX and DSC studies indicated that the different morphologies are formed by only one particular compound, while TGA proved the presence of both compounds in the support scaffold at the initial weight ratio. This indicates that the self-assembly process is a *separated columnar co-self-assembly*, where no mixing of the BTA molecules within single supramolecular fibers or fiber bundles occur.

## 6. Summary

Supramolecular chemistry is the chemistry of molecular assemblies and intermolecular bonds. In contrary to the traditional chemistry, which deals with covalent chemical bonds, supramolecular chemistry is a matter of physical interactions between molecules. These non-covalent interactions determine the spatial organization of molecules, which can lead to the formation of larger well-defined supramolecular objects. In the supramolecular approach, molecules are able to self-assemble reversibly to defined supramolecular objects. The shape and functionality of these objects are imbedded in the molecular structure of the single molecules, which are influenced by the geometry of the molecule, side chains, and functional groups.

In this context, this thesis provides a systematic study of the (1) thermal properties, phase behavior and structure property relations of 1,3,5-benzenetrisamides with linear perfluorinated side chains, (2) melt electrospinning of trisamides with linear perfluorinated side chains, and (3) co-self-assembly studies of structurally different 1,3,5-benzenetrisamides from solution.

*1: Thermal properties, mesophase behavior and structure property relations of two series of 1,3,5-benzenetrisamides with linear perfluorinated side chains*

In a systematic evaluation, an insight into the structure property relations was obtained by investigation of the thermal properties and mesophase behavior of benzene trisamides (BTAs) with linear perfluorinated side chains of three up to eight carbon atoms, varying also in the connectivity of the amide linkage. In addition, one cyclohexane trisamide (CTA) was investigated. The transition temperatures were studied by Differential Scanning Calorimetry. Polarized Optical Microscopy investigations at different temperatures provided conclusions about the solid, liquid and mesophase properties by observation of the mesophase textures. For further clarification, temperature dependent X-Ray Diffraction measurements were performed and the resulting patterns were evaluated to get more information about the development of columnar phases and their degree of order. Temperature dependent Infrared Spectroscopy measurements were carried out to investigate the hydrogen bonding.

- *BTAs based on the 1,3,5-triaminobenzene core* pass through a plastic crystalline or liquid crystalline mesophase, which can mostly be identified as columnar phases. For example, the BTA bearing perfluorinated side chains of four carbon atoms first changes into a columnar hexagonal plastic mesophase upon heating at 177 °C, before it reaches the isotropic phase at 229 °C. The *BTAs based on the trimesic acid core* pass through one or more mesophases between the solid state and the isotropic phase, which are mostly of

liquid crystalline appearance, but could not be clearly identified as columnar phases. For example, the BTA bearing perfluorinated side chains of seven carbon atoms shows transition into an unidentified liquid crystalline mesophases upon heating at 166 °C, before it reaches the isotropic phase at 299 °C. All BTAs show an increase of the transition enthalpy at the melting temperature and a simultaneous decrease of the transition enthalpy at the clearing temperature with increasing side chain length. Comparison between the BTAs based on the different cores shows that the BTAs based on 1,3,5-triaminobenzene have lower clearing and melting temperatures than the BTAs based on trimesic acid. For both cores, the column-to-column distances of all BTAs increase linearly by a value of 0.1 nm for every additional CF<sub>2</sub> unit in the side chains indicating the presence of columnar phases.

- The *cyclohexane based trisamide* bearing perfluorinated side chains of seven carbon atoms passes through an unidentified liquid crystalline mesophase upon heating, changes into an unidentified liquid crystalline mesophase, and passes through a columnar nematic phase before the isotropic phase is reached.
- A comparison of the BTAs with perfluorinated side chains to BTAs with the same architecture and side chains lengths but bearing *alkyl side chains* revealed that the BTAs with perfluorinated side chains pass through plastic crystalline and liquid crystalline mesophases. The BTAs bearing alkyl side chains rarely show liquid crystalline mesophases. BTAs with linear perfluorinated side chains show about 40 degrees higher transition temperatures into the isotropic phase. A decrease in the molecular order with increasing side chain length was found for both BTAs bearing alkyl and perfluorinated side chains. In addition, a similar increase of the intercolumnar distance with about 0.1 nm for every additional CH<sub>2</sub> or CF<sub>2</sub> unit in the side chains was revealed.
- A comparison of cyclohexane based trisamides bearing perfluorinated or alkyl side chains of seven carbon atoms show that both develop a columnar nematic phase but the mesophase range differs strongly. With regard to the clearing temperature, the CTA with linear perfluorinated side chains shows a value of about 30 degrees higher than the CTA bearing alkyl side chains. Both trisamides show an intermolecular distance of about 0.47 nm indicating that the formed columns are arranged in a similar way of stacking.

## 2: Melt electrospinning of trisamides with linear perfluorinated side chains

A selection of two BTAs based on 1,3,5-triaminobenzene with different side chain length and the cyclohexane based trisamide were processed by melt electrospinning to supramolecular fibers. The electrospinning parameters were varied to find the best parameter set in terms of electrospinning temperature and applied electric field for the production of thin high-quality supramolecular fibers.

- The best results for the melt electrospinning of the BTAs with linear perfluorinated side chains could be achieved at applied electric fields with strength of 5.0 kV/cm and 6.7 kV/cm, resulting in fibers with average fiber diameters of  $0.5 \pm 0.2 \mu\text{m}$  for the BTA with shorter side chains, and of  $0.4 \pm 0.2 \mu\text{m}$  for the BTA with longer side chains. The most challenging problem for the melt electrospinning is the high sublimation tendency of the highly fluorinated compounds.
- The cyclohexane-based trisamide was successfully melt electrospun from the isotropic phase as well as from the nematic phase. Best results were obtained from the nematic phase with comparably thin fibers of about  $1.7 \mu\text{m}$  in diameter.

Furthermore, the melt electrospinning of comparably thick fibers in the range of  $5 \mu\text{m}$  to  $15 \mu\text{m}$  for direct force measurements within a collaboration with the chair of Physical Chemistry II at the University of Bayreuth was successfully performed. It could be shown that all compounds can be processed to fibers of the desired thickness in an electric field with a strength of 2.5 kV/cm up to 5.0 kV/cm. Two of them were used for direct force measurements. This work resulted already in a publication. Wettability measurements with a polar and a nonpolar liquid of fiber mats of BTAs with perfluorinated and alkyl hexyl side chains resulted in an about 20 degrees higher contact angle for the fluorinated BTA type with the polar liquid, and an about 70 degrees higher contact angle with the nonpolar liquid.

### *3: Self-assembly of 1,3,5-benzenetrisamides with perfluorinated side chains and co-self-assembly of structurally related 1,3,5-benzenetrisamides from solution*

In a bottom-up self-assembly approach, six BTAs with linear perfluorinated side chains, varying in the side chain length and core architecture, were selected and self-assembled to supramolecular fibers from solution. Two BTAs, one bearing linear perfluorinated and one bearing alkyl side chains, were chosen for the co-self-assembly studies with the aim to determine the type of self-assembly by means of the molecular composition of single fibers in the self-assembled morphologies.

- BTAs based on 1,3,5-triaminobenzene form thin fiber bundles with uniform surface mostly upon cooling from different solvents at concentrations of 0.1 wt.% and below. The best results were obtained from o-DCB. Fiber bundles with average fiber diameters of about two micrometers for the BTAs based on 1,3,5-triaminobenzene with side chains of three and five carbon atoms, as well as fiber bundles with average fiber diameters in the range of only  $0.1 \mu\text{m}$  up to  $0.2 \mu\text{m}$  formed by the BTA with side chains of seven carbon were obtained. Overall, thinner fiber bundles were often roundly shaped while thicker fibers showed an edged, often a hexagonal shaped, and sometimes a twisted morphology.

- BTAs based on trimesic acid formed fiber bundles from only a few solvents at a concentration of 0.1 wt.%. It is not possible to obtain fiber bundles for all three BTAs from the same solvent, which is necessary for a proper comparison.
- Pre-experiments showed that a mixture of methyl ethyl ketone and ortho-dichlorobenzene was necessary, in terms of solubility and fiber formation, to perform the co-self-assembly experiments with the selected BTAs. The co-self-assembly resulted in formation of two different morphologies, which indicate that a separate columnar co-self-assembly process takes place where each of the compounds form single fibers.

## **7. Appendix**

### **7.1 Appendix I: Analytical equipment and procedures**

#### ***Thermogravimetric Analysis (TGA)***

TGA/SDTA851<sup>e</sup> from Mettler-Toledo GmbH. All measurements were performed with a heating rate of 10 K/min in a temperature range of 30-700 °C.

#### ***Differential Scanning Calorimetry (DSC)***

Diamond DSC from PerkinElmer or DSC 2 STAR<sup>e</sup> System from Mettler-Toledo GmbH. All measurements were performed with a heating and cooling rate of 10 K/min under inert gas atmosphere (N<sub>2</sub> gas flow 50 ml/min) by using reusable high-pressure pans (steel) as sample container.

#### ***Optical Polarization Microscopy (POM)***

Nikon Diaphot 300 with heating table Mettler-Toledo FP 82 HT and Control unit Mettler-Toledo FP 90. The trisamide samples were prepared by placing the powders between two glass slides. Deformation experiments were carried out by moving the upper glass slide carefully.

#### ***X-Ray Diffractometry (XRD)***

Huber Guinier Diffractogram 600 with a Huber Germanium Monochromator 611, Cu-Anode (CuK<sub>α1</sub>-rays,  $\lambda = 0,155051$  nm, X-Ray generator from Seifert), Huber SMC 9000 Stepping Motor Controller with self-made cover system and primary beam detector, self-made heating oven allows heating up to 250 °C. The construction is also explained in the literature.<sup>180</sup> Sample preparation in glass tubes from Hilgenberg GmbH with an inner diameter of 1.0, 1.5 or 2.0 mm.

#### ***IR Spectroscopy***

Bio-Rad Digilab FTS-40 with a heating unit for KBr preforms. The preforms were prepared by mixing 1.5 mg of trisamide powder with 200 mg of dried KBr, before the mixture was filled into a metal tool and pressed for 2 min with a mass of 13 tons to preforms of 1.3 cm in diameter.

### ***Scanning Electron Microscopy (SEM)***

The sample was mounted on a standard sample holder by conductive adhesion graphite-pad (Plano GmbH) and examined with a LEO 1530 from Carl Zeiss AG (FE-SEM with Schottky-field-emission cathode; in-lens detector, SE2 detector, or Back Scattered Detector) using an accelerating voltage of 3 kV.

The samples were sputtered with platinum (2 nm using a Cressington HR208 sputter coater and a Cressington mtm20 thickness controller) prior to SEM imaging.

### ***Energy Dispersive X-Ray Spectroscopy (EDX; combined with SEM)***

*Ultra plus:* The sample was mounted on a standard sample holder by conductive adhesion graphite-pad (Plano GmbH) and examined with a Ultra plus from Carl Zeiss AG (FE-SEM with Schottky-field-emission cathode; in-lens detector, SE2 detector, EsB, AsB ) using an accelerating voltage of 5 kV.

The samples were sputtered with platinum (2 nm using a Cressington HR208 sputter coater and a Cressington mtm20 thickness controller) or vapor coated with carbon (using a Balzers Union MED 010) prior to SEM imaging.

The EDX detector was an Ultradry 30 mm<sup>2</sup> (SDD) from Thermo Fisher Scientific with a “Noran System 7 Spectral Imaging System” software (NSS).

### ***Melt Electrospinning Device***

For the melt electrospinning experiments, a custom designed equipment was used as it was described by Singer et al.<sup>83</sup> Glass syringes from Poulten & Graf (Fortuna Optima with luer glass tip) with a volume of 1 mL and a shortened hypodermic needle (length about 1 mm) were used for the experiments. The syringe was placed in an electrically heated block, which can be heated up to 350 °C at maximum with a fluctuation of  $\pm 0.5$  °C at 250 °C. The temperature at the needle tip is about 5 % lower than the adjusted temperature at the heated block. A precision motor with gear system can move a piston, equipped with a pressure transducer, which is connected to the plunger of the syringe, and responsible for the adjusted flow rate. The entire drive unit can be tilted by 90° for an easy replacement of the syringes between the experiments. The syringe needle and all attached electronic components are earthed. A high voltage power supply from Schulz Electronic (high voltage units AK0175 and AK1026, +60 and -60 kV, respectively) is connected to the collector plate in the base plate below the needle.

***Wettability Measurements***

For the measurement of the wettability of a surface, a Drop Shape Analyzer (model DSA25S) from Krüss GmbH was used to measure the contact angle with demineralized water or diiodomethane. The surface for investigation was placed under a syringe with the particular liquid, a droplet released on the surface, and the contact angle was measured automatically by the device corresponding software.

***Moisture Analyzer***

The evaporation behavior of the solvents and the solvent mixtures was analyzed by a Moisture Analyzer MA 145 from Sartorius AG at a temperature of 40 °C. The weight of the remaining solvent was detected in six second steps until the weight remained constant for five minutes.

## 7.2 Appendix II: Additional data

### 7.2.1 Additional data to chapter 3

#### Results of the IR analysis of BTAs with linear perfluorinated side chains

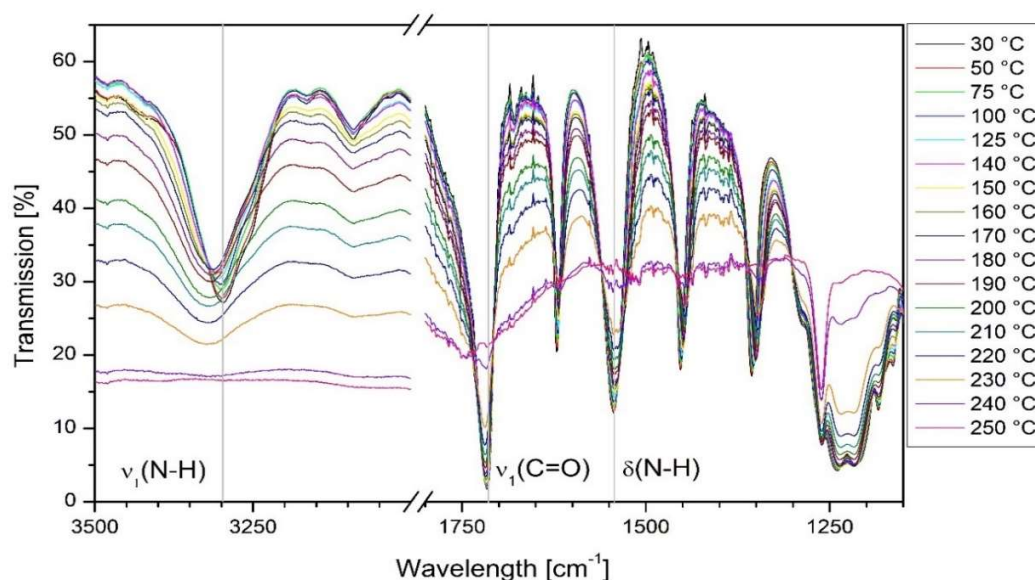


Figure 115: Infrared Spectroscopy spectra of **1a** at different temperatures upon heating; vertical grey lines: band positioning of the specific vibrational and deformational signals in the solid state at 30 °C.

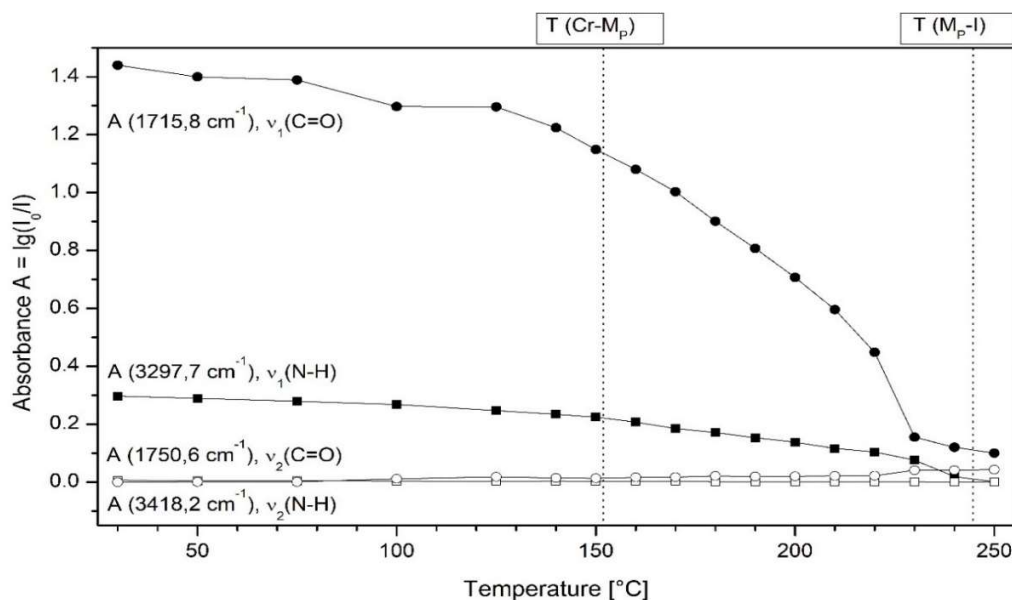


Figure 116: Infrared Spectroscopy absorbance of **1a** as a function of the temperature; circles:  $\nu(\text{C=O})$ , square:  $\nu(\text{N-H})$ , filled symbols: hydrogen bonded form  $\nu_1$ , unfilled symbols: non-hydrogen bonded form  $\nu_2$ ; vertical dashed lines: transition temperatures (second heating of DSC).

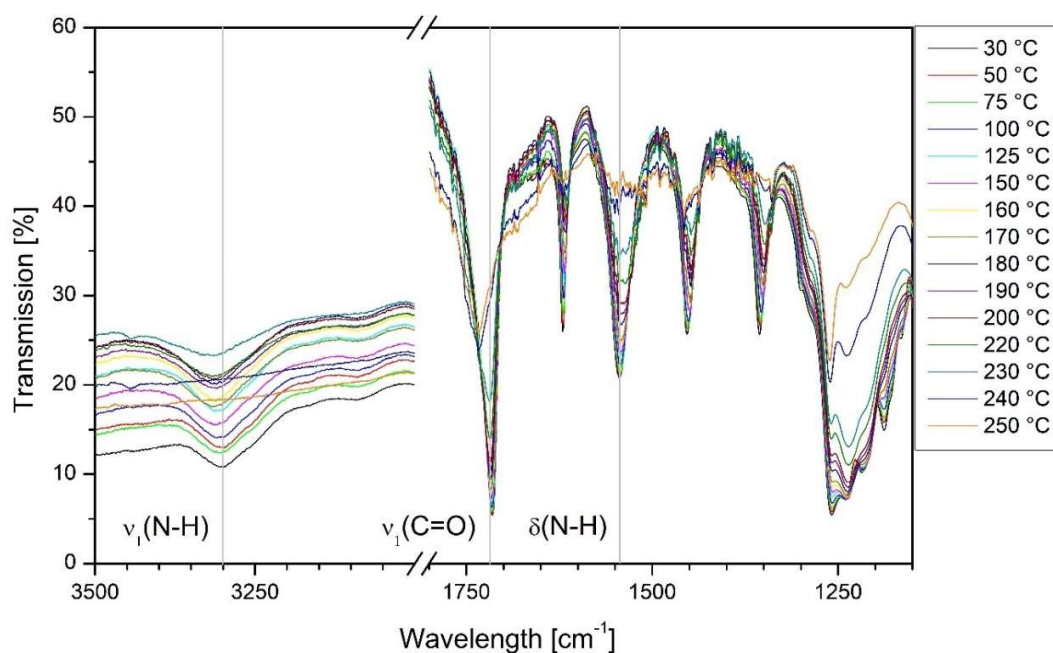


Figure 117: Infrared Spectroscopy spectra of **1b** at different temperatures upon heating; vertical grey lines: band positioning of the specific vibrational and deformational signals in the solid state at 30 °C.

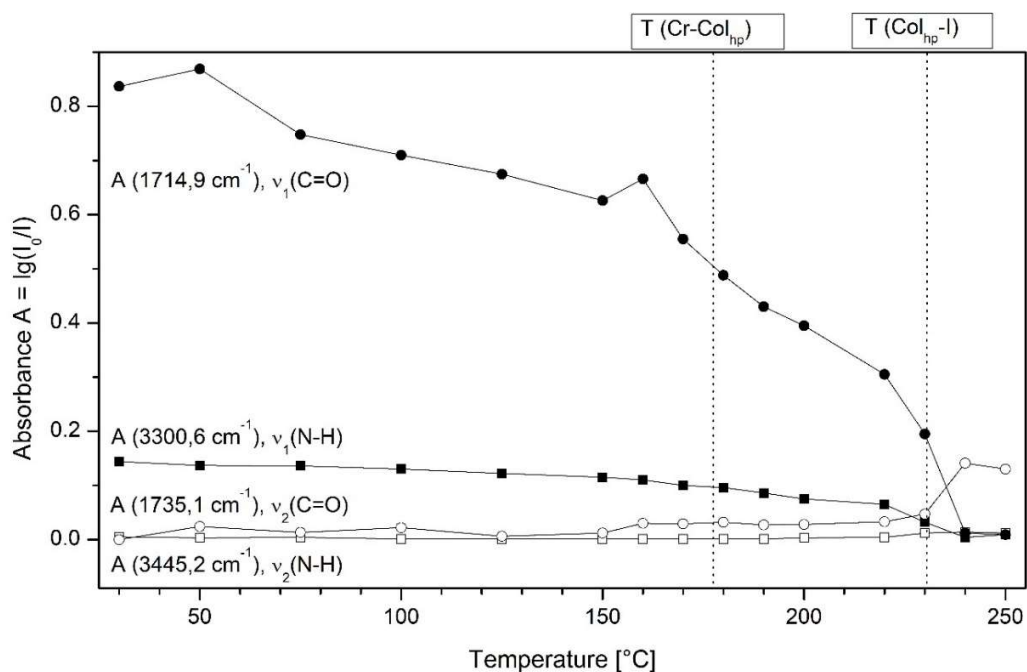


Figure 118: Infrared Spectroscopy absorbance of **1b** as a function of the temperature; circles:  $\nu(\text{C=O})$ , square:  $\nu(\text{N-H})$ , filled symbols: hydrogen bonded form  $\nu_1$ , unfilled symbols: non-hydrogen bonded form  $\nu_2$ ; vertical dashed lines: transition temperatures (second heating of DSC).

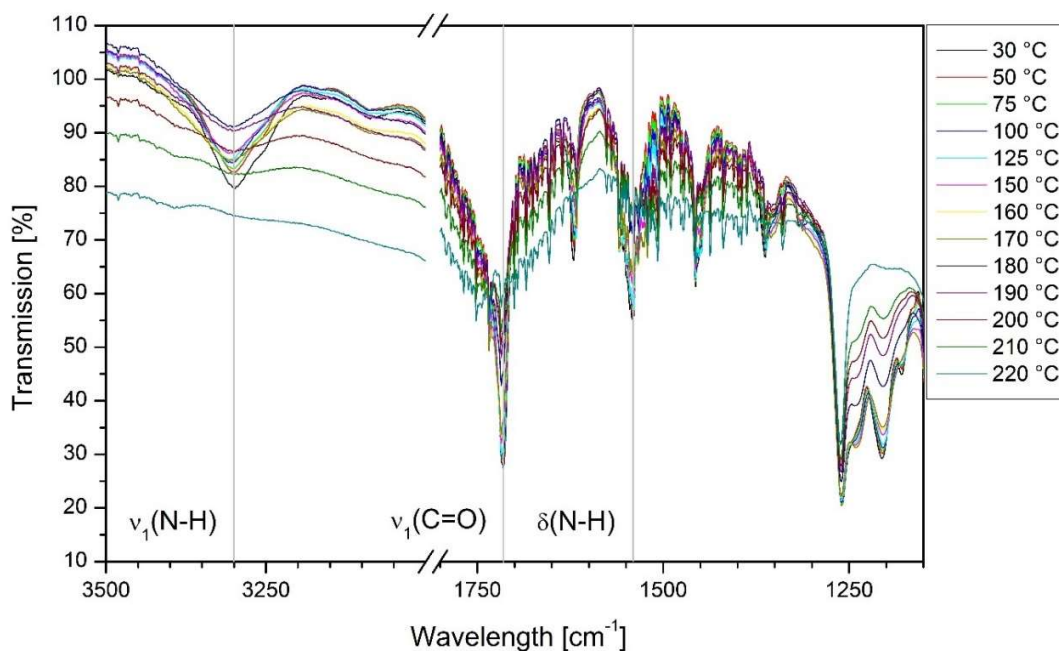


Figure 119: Infrared Spectroscopy spectra of **1c** at different temperatures upon heating; vertical grey lines: band positioning of the specific vibrational and deformational signals in the solid state at 30 °C.

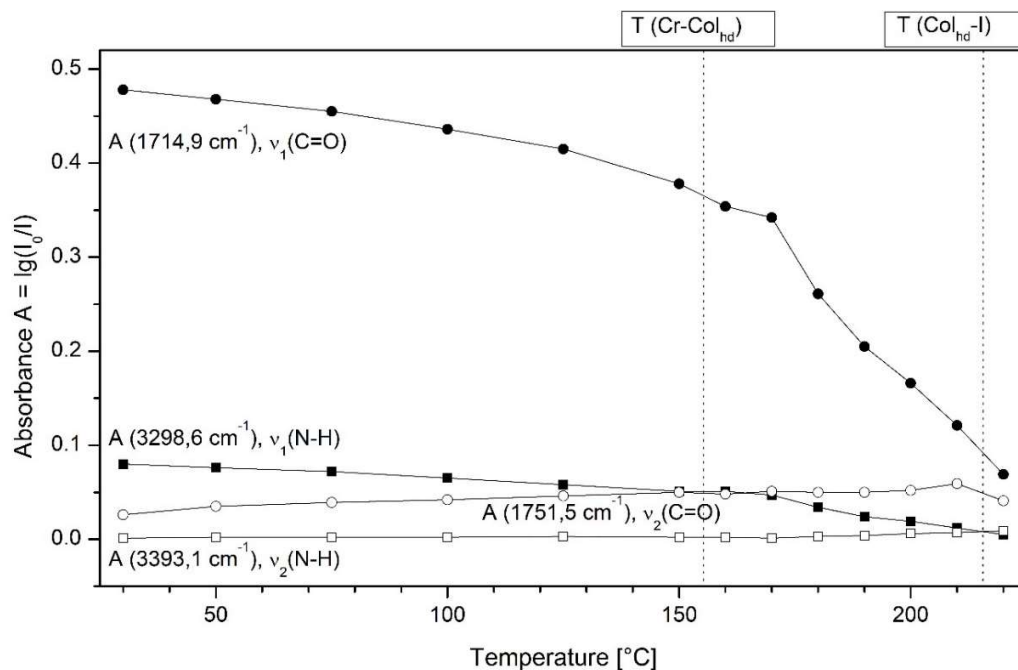


Figure 120: Infrared Spectroscopy absorbance of **1c** as a function of the temperature; circles:  $\nu(\text{C=O})$ , square:  $\nu(\text{N-H})$ , filled symbols: hydrogen bonded form  $\nu_1$ , unfilled symbols: non-hydrogen bonded form  $\nu_2$ ; vertical dashed lines: transition temperatures (second heating of DSC).

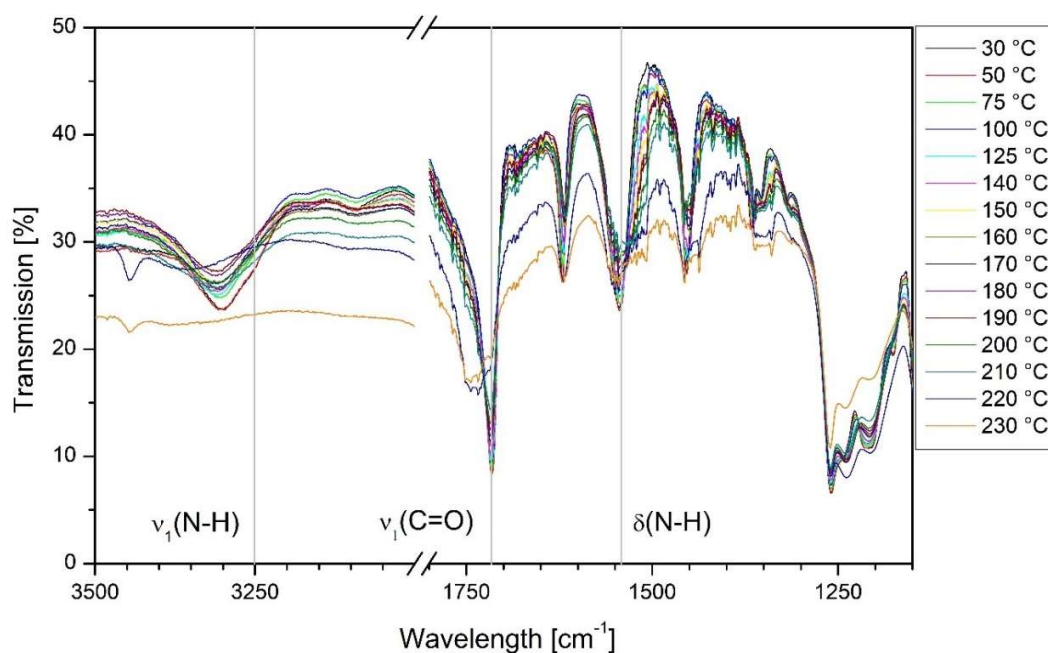


Figure 121: Infrared Spectroscopy spectra of **1d** at different temperatures upon heating; vertical grey lines: band positioning of the specific vibrational and deformational signals in the solid state at 30 °C.

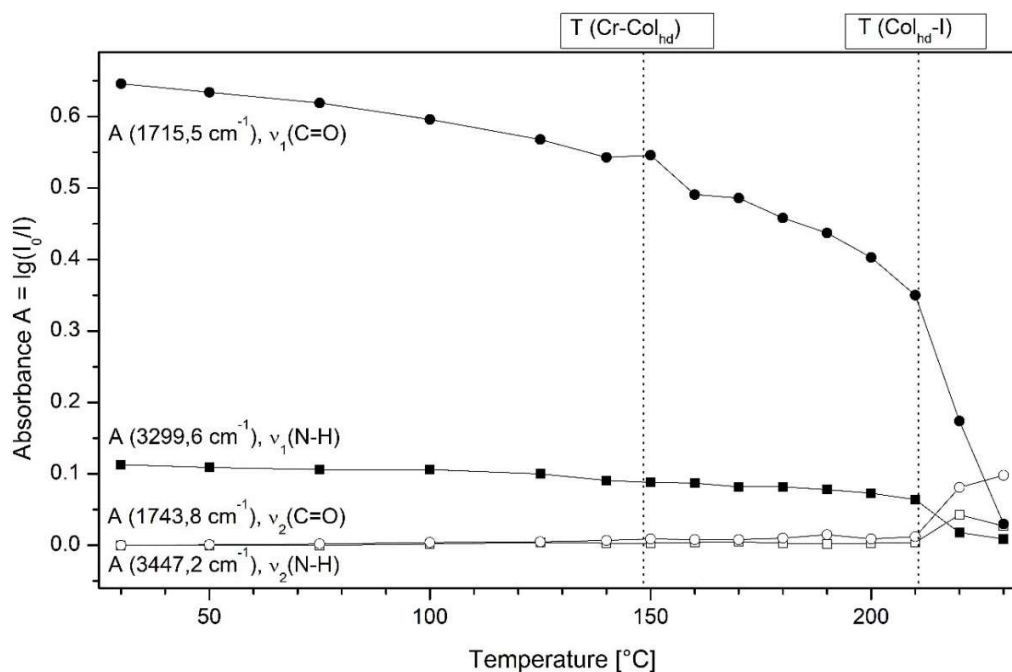


Figure 122: Infrared Spectroscopy absorbance of **1d** as a function of the temperature; circles:  $\nu(\text{C}=\text{O})$ , square:  $\nu(\text{N}-\text{H})$ , filled symbols: hydrogen bonded form  $\nu_1$ , unfilled symbols: non-hydrogen bonded form  $\nu_2$ ; vertical dashed lines: transition temperatures (second heating of DSC).

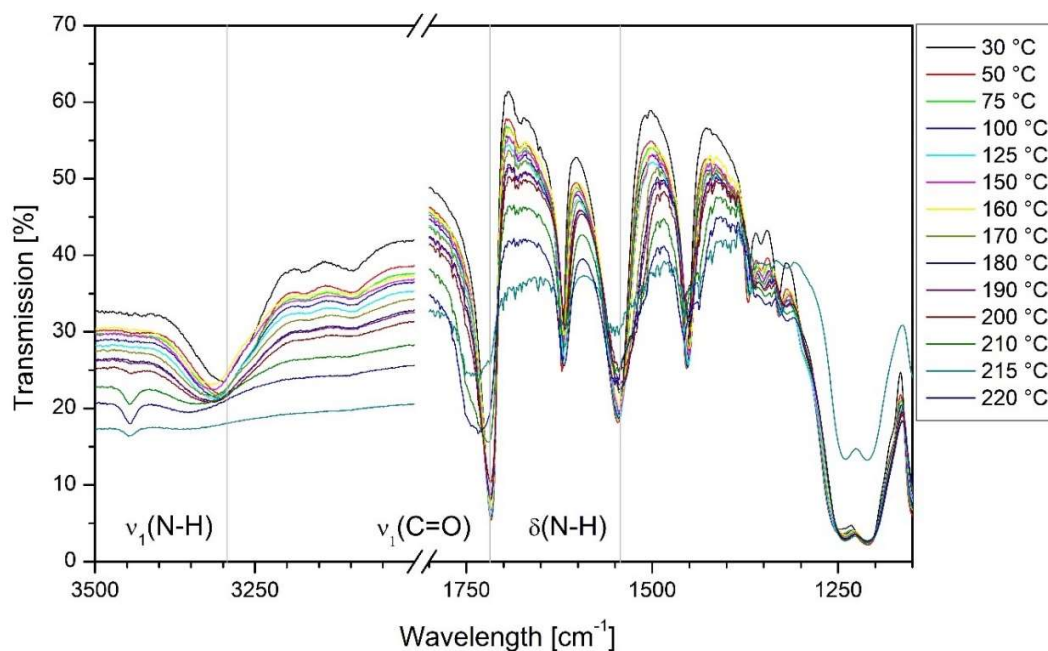


Figure 123: Infrared Spectroscopy spectra of **1f** at different temperatures upon heating; vertical grey lines: band positioning of the specific vibrational and deformational signals in the solid state at 30 °C.

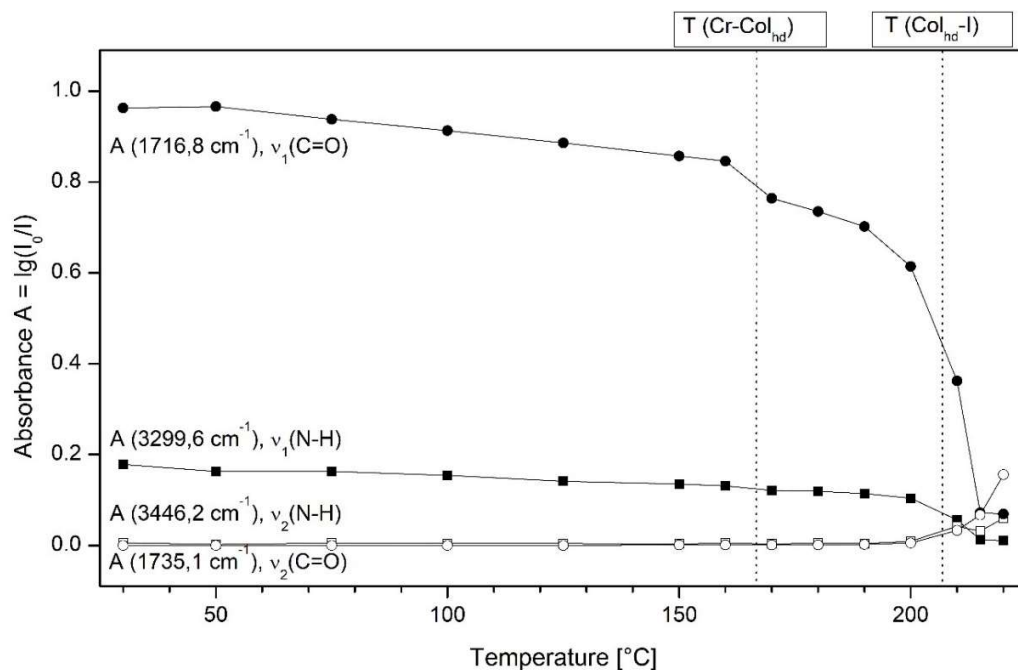


Figure 124: Infrared Spectroscopy absorbance of **1f** as a function of the temperature; circles:  $\nu(\text{C=O})$ , square:  $\nu(\text{N-H})$ , filled symbols: hydrogen bonded form  $\nu_1$ , unfilled symbols: non-hydrogen bonded form  $\nu_2$ ; vertical dashed lines: transition temperatures (second heating of DSC).

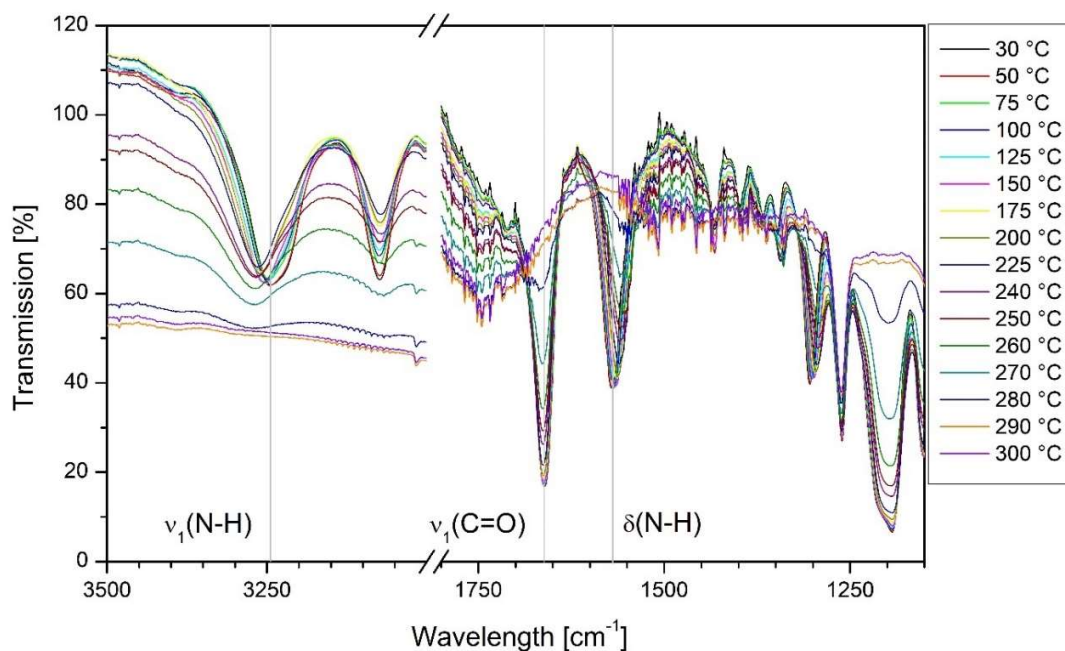


Figure 125: Infrared Spectroscopy spectra of **2a** at different temperatures upon heating; vertical grey lines: band positioning of the specific vibrational and deformational signals in the solid state at 30 °C.

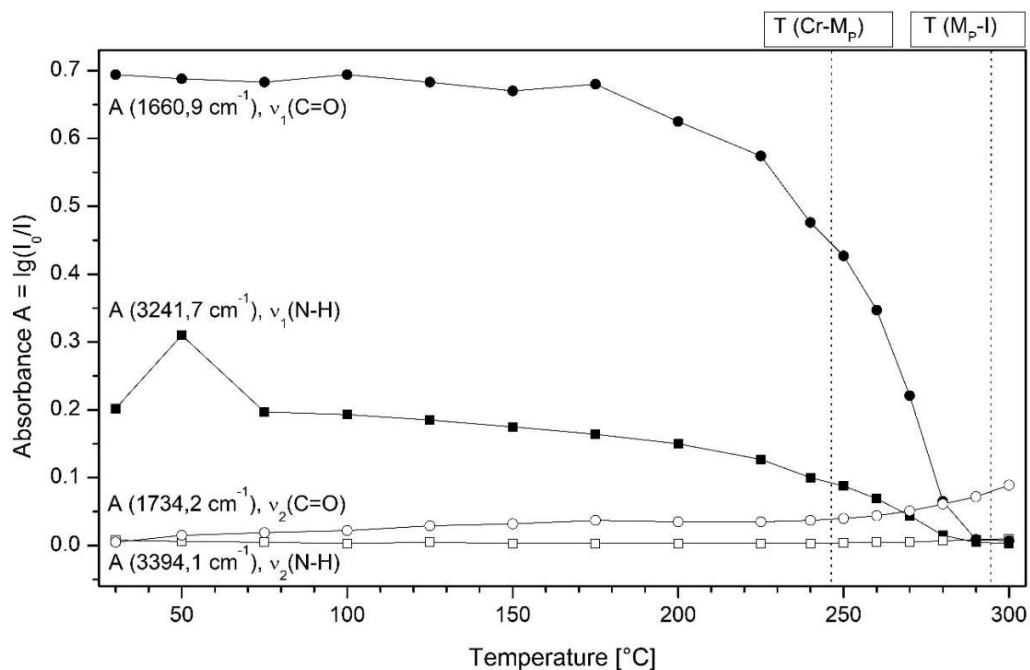


Figure 126: Infrared Spectroscopy absorbance of **2a** as a function of the temperature; circles:  $\nu(\text{C=O})$ , square:  $\nu(\text{N-H})$ , filled symbols: hydrogen bonded form  $\nu_1$ , unfilled symbols: non-hydrogen bonded form  $\nu_2$ ; vertical dashed lines: transition temperatures (second heating of DSC).

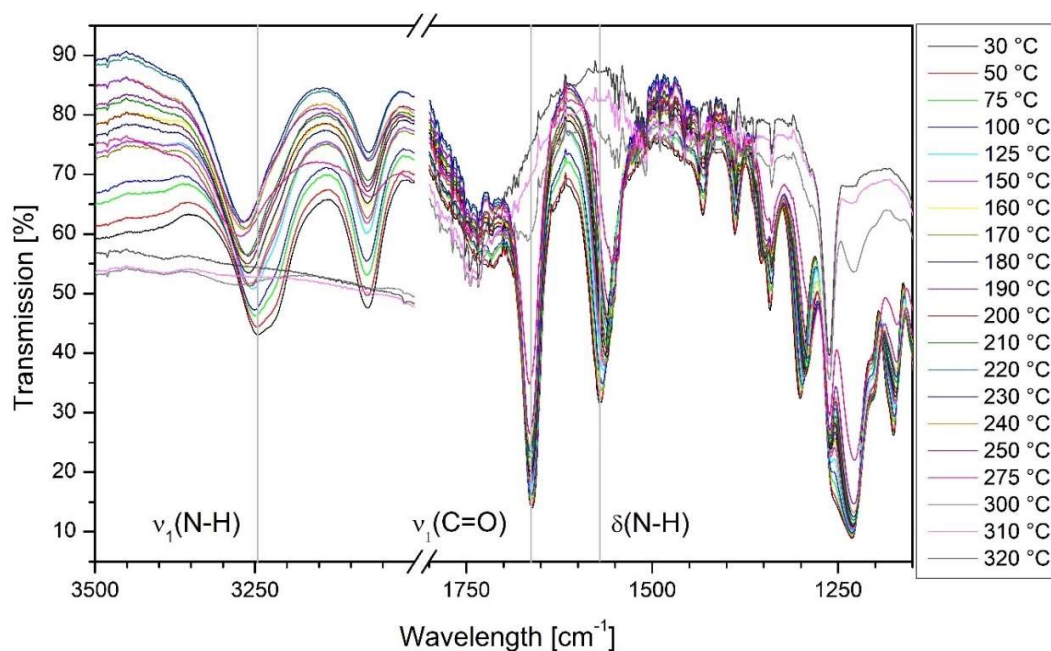


Figure 127: Infrared Spectroscopy spectra of **2b** at different temperatures upon heating; vertical grey lines: band positioning of the specific vibrational and deformational signals in the solid state at 30 °C.

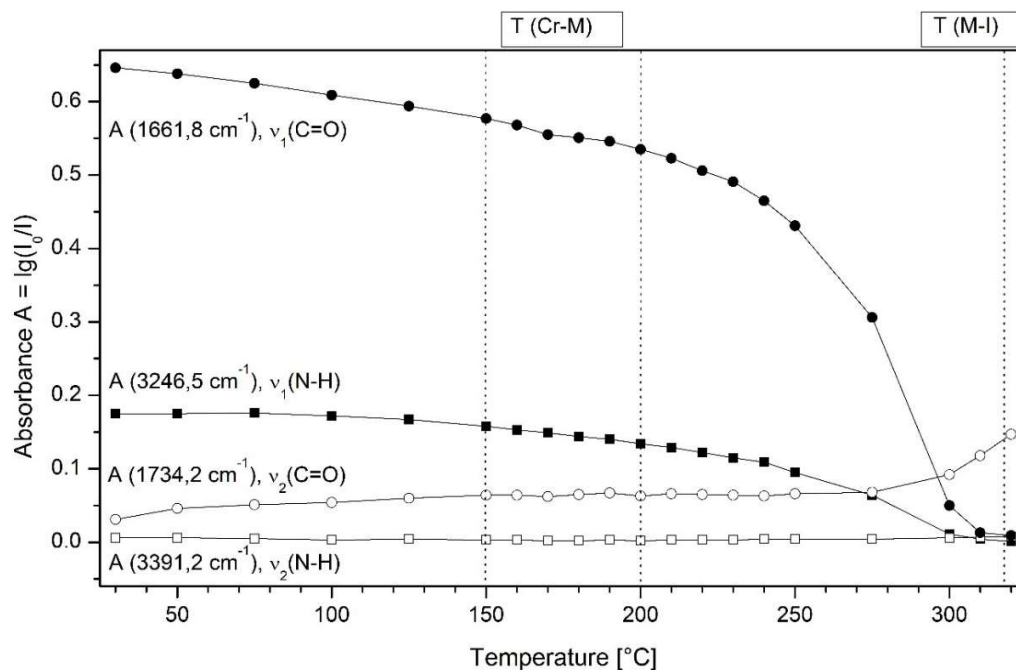


Figure 128: Infrared Spectroscopy absorbance of **2b** as a function of the temperature; circles:  $\nu(\text{C}=\text{O})$ , square:  $\nu(\text{N}-\text{H})$ , filled symbols: hydrogen bonded form  $\nu_1$ , unfilled symbols: non-hydrogen bonded form  $\nu_2$ ; vertical dashed lines: transition temperatures (second heating of DSC).

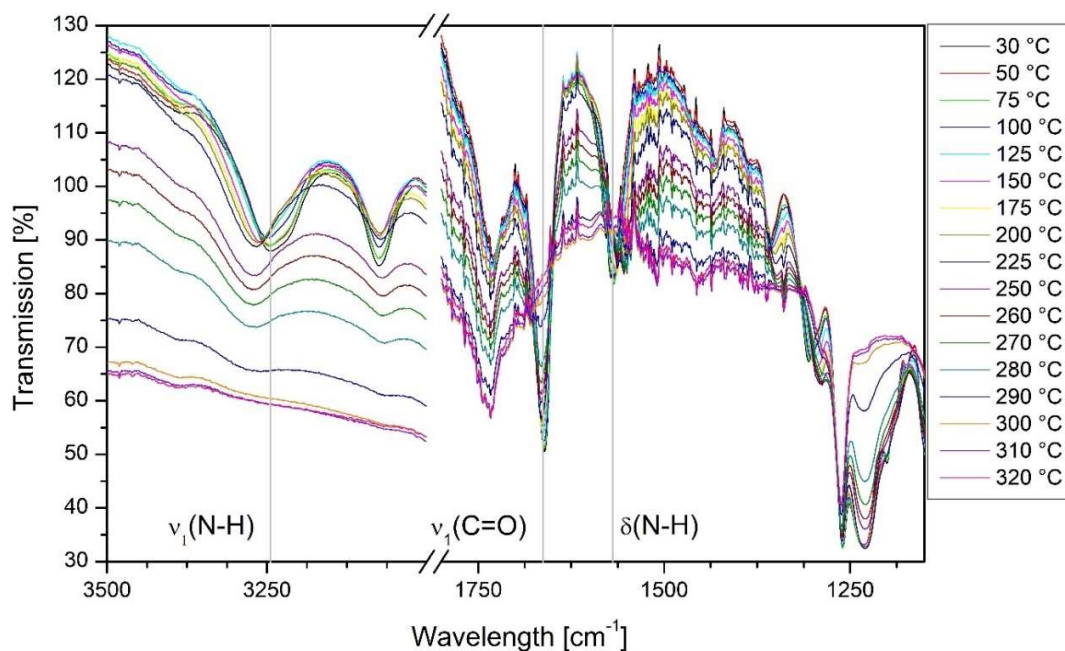


Figure 129: Infrared Spectroscopy spectra of **2c** at different temperatures upon heating; vertical grey lines: band positioning of the specific vibrational and deformational signals in the solid state at 30 °C.

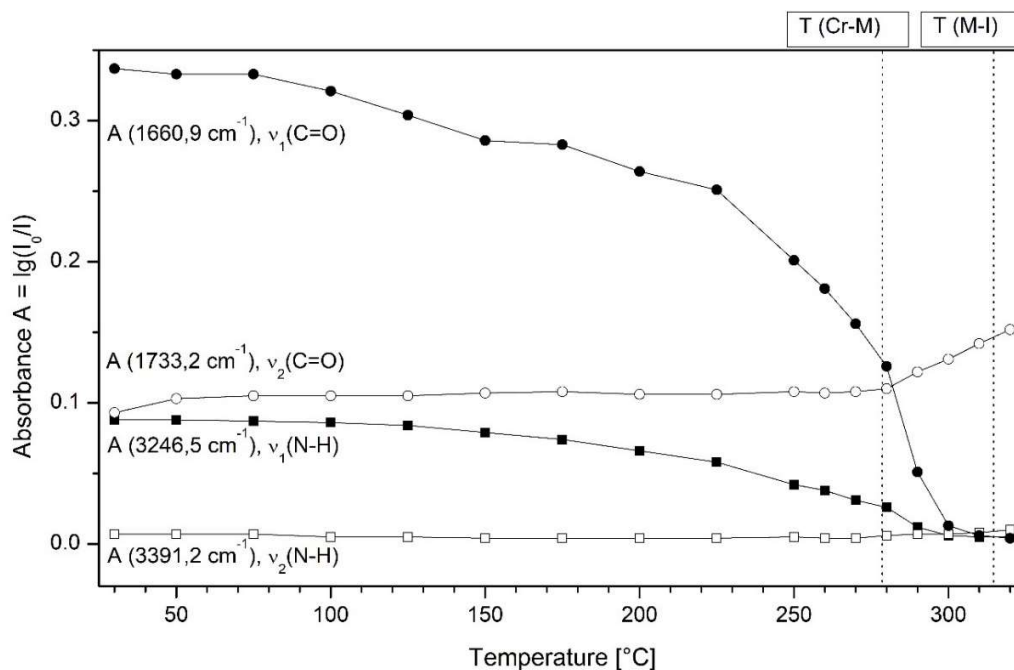


Figure 130: Infrared Spectroscopy absorbance of **2c** as a function of the temperature; circles:  $\nu(\text{C=O})$ , square:  $\nu(\text{N-H})$ , filled symbols: hydrogen bonded form  $\nu_1$ , unfilled symbols: non-hydrogen bonded form  $\nu_2$ ; vertical dashed lines: transition temperatures (second heating of DSC).

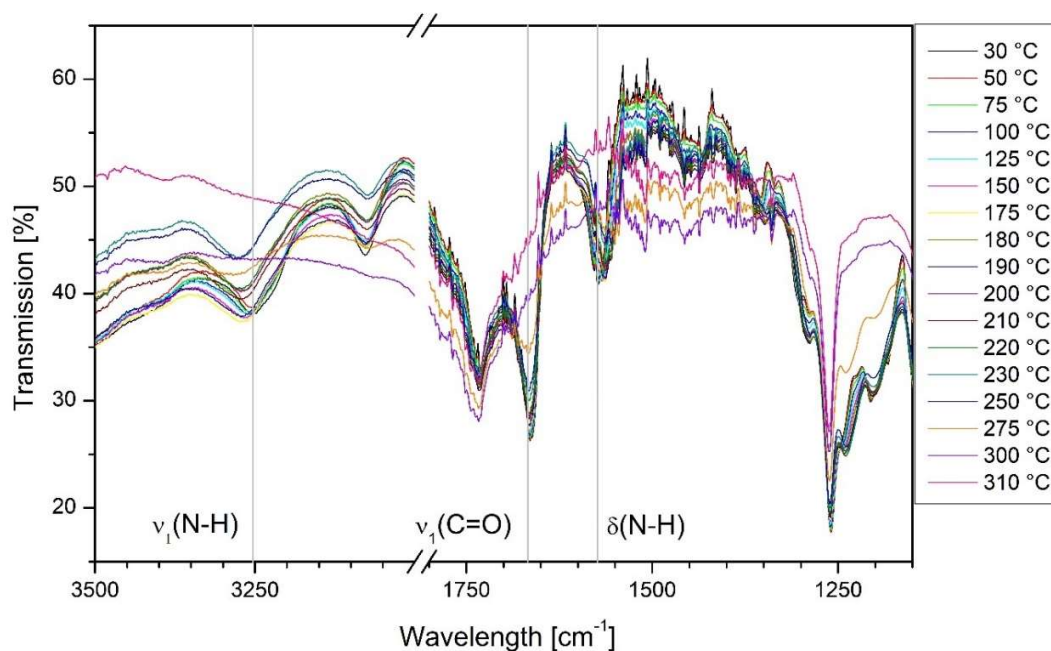


Figure 131: Infrared Spectroscopy spectra of **2d** at different temperatures upon heating; vertical grey lines: band positioning of the specific vibrational and deformational signals in the solid state at 30 °C.

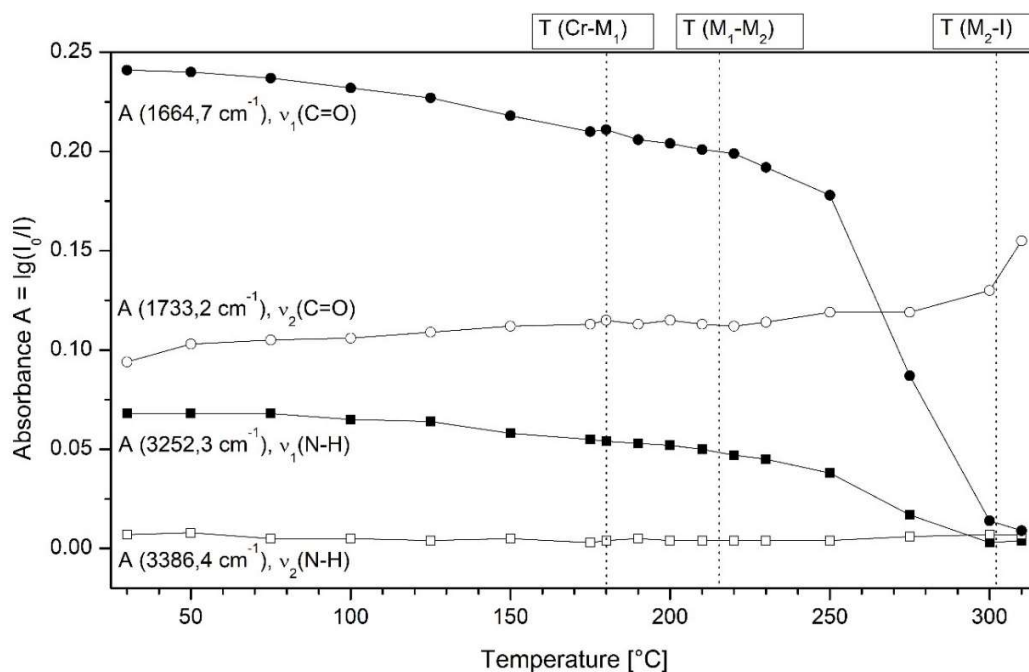


Figure 132: Infrared Spectroscopy absorbance of **2d** as a function of the temperature; circles:  $\nu(\text{C}=\text{O})$ , square:  $\nu(\text{N}-\text{H})$ , filled symbols: hydrogen bonded form  $\nu_1$ , unfilled symbols: non-hydrogen bonded form  $\nu_2$ ; vertical dashed lines: transition temperatures (second heating of DSC).

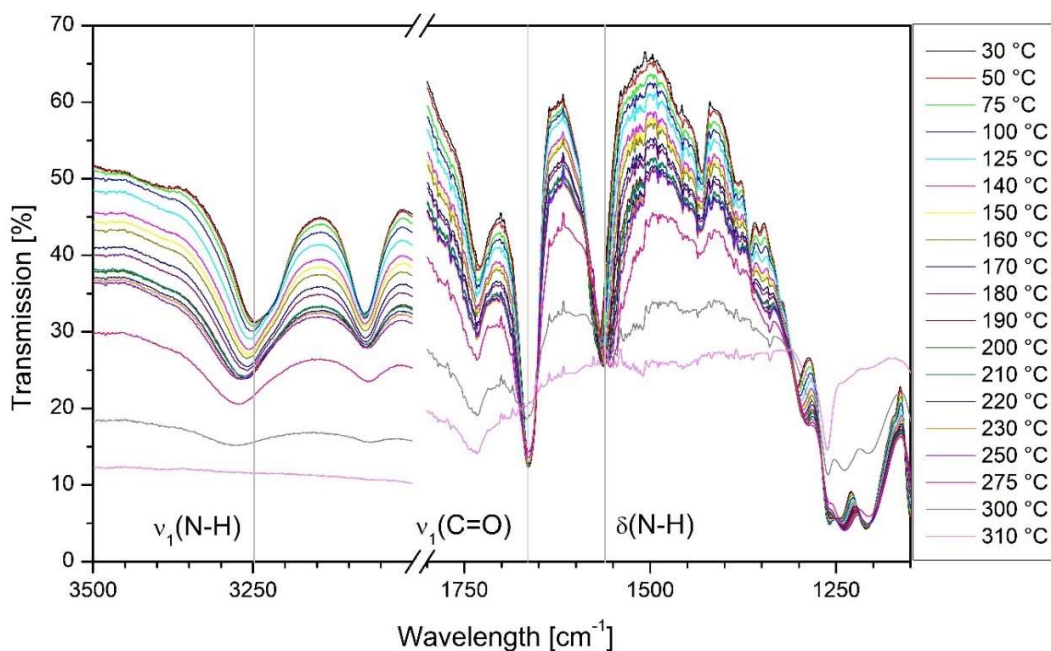


Figure 133: Infrared Spectroscopy spectra of **2f** at different temperatures upon heating; vertical grey lines: band positioning of the specific vibrational and deformational signals in the solid state at 30 °C.

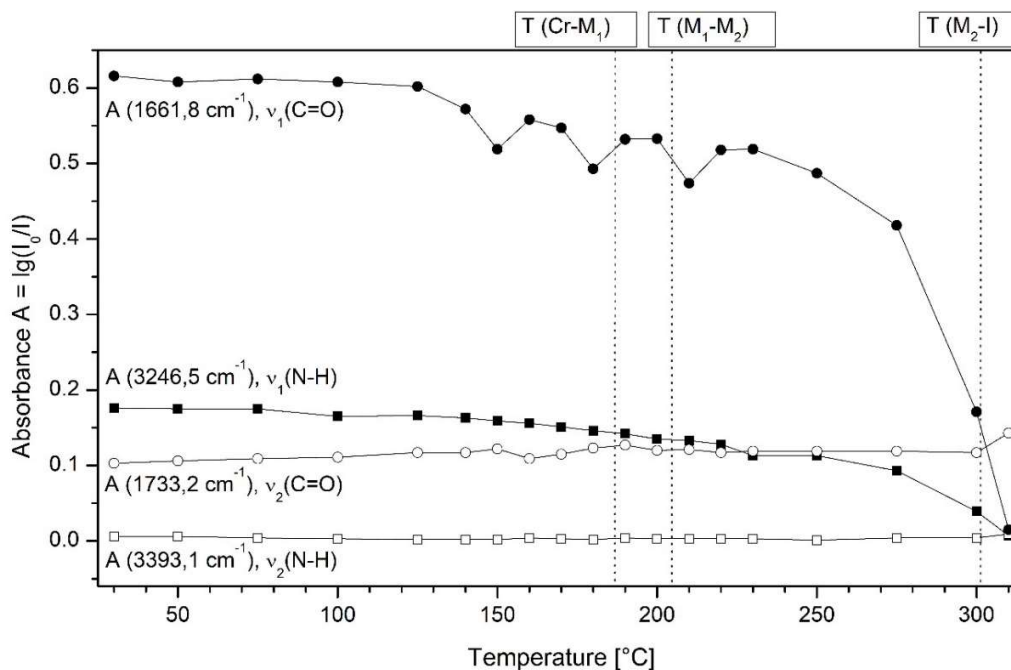


Figure 134: Infrared Spectroscopy absorbance of **2f** as a function of the temperature; circles:  $\nu(\text{C=O})$ , square:  $\nu(\text{N-H})$ , filled symbols: hydrogen bonded form  $\nu_1$ , unfilled symbols: non-hydrogen bonded form  $\nu_2$ ; vertical dashed lines: transition temperatures (second heating of DSC).

### 7.2.2 Additional data to chapter 4

#### *Electrospinning of the BTA with pentadecafluoroheptyl side chains (1e)*

In the following, the electrospinning results of **1e** are shown, beginning with the determination of the different electrospinning temperatures. Therefore, the phase behavior, already discussed in chapter 3, including the temperature of 10% initial weight loss determined by TGA, and the first heating and cooling curve of the DSC are shown in figure 135.  $T_{\text{Spin}1}$  was selected 20 °C above  $T_c$  at 227 °C.  $T_{\text{Spin}2}$  and  $T_{\text{Spin}3}$  were selected at ten (217 °C) and twenty (207 °C) degrees below  $T_{\text{Spin}1}$ , respectively. The material still resides in the isotropic phase at all spinning temperatures after equilibration and cooling down from 227 °C.

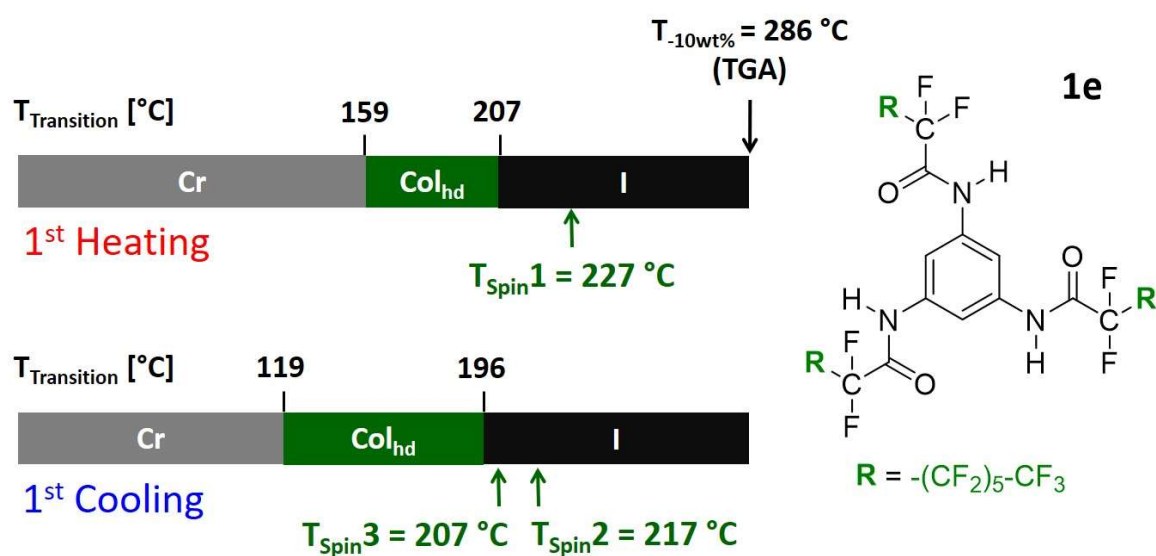


Figure 135: Trisamide **1e** with phase transition temperatures at first heating and cooling (Differential Scanning Calorimetry, heating and cooling rate 10 K/min), type of mesophase (Cr: crystalline, Col: columnar mesophase, h: hexagonal, d: disordered, I: isotropic), temperature of 10% weight loss, and the selected spinning temperatures  $T_{\text{Spin}1}$ ,  $T_{\text{Spin}2}$  and  $T_{\text{Spin}3}$  in green.

### Electrospinning results of **1e** at a spinning temperature of 227 °C

For different working distances of 4 cm (figure 136), 6 cm (figure 137), and 9 cm (figure 138), the electrospinning results of **1e** obtained at a spinning temperature of 227 °C at different applied voltages, including the average fiber size and fiber size distributions are shown.

At a *working distance of 4 cm* (figure 136), it was possible to spin fibers at -20 and -30 kV corresponding to electrical field strengths of 5.0 and 7.5 kV/cm, and with average fiber diameters of  $1.8 \pm 1.7 \mu\text{m}$  and  $1.2 \pm 1.2 \mu\text{m}$ , respectively. Considering the fiber quality, a high standard deviation in both cases indicate a broad fiber size distribution, proven by observation of the SEM images. Nevertheless, the optical evaluation of the fibers leads to a good fiber quality when only the fiber shape is taken in account. Long and homogeneous fibers with uniform surface can be found which are only rarely discontinued by beads.

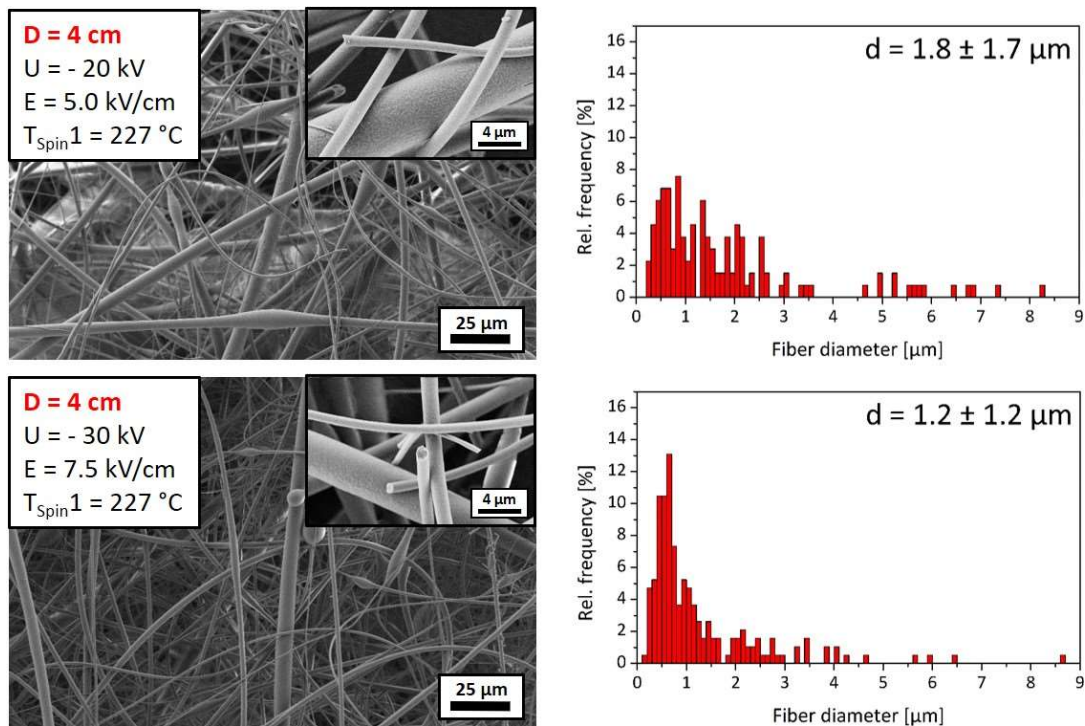


Figure 136: Scanning Electron Microscopy images (left) of electrospun fibers of **1e** produced at  $T_{\text{Spin}1}$  of 227 °C, **working distance D of 4 cm** and an electrospinning applied voltage  $U$  of -20 (top) and -30 kV (bottom). The bar diagrams (right) show the fiber diameter dependent on the relative frequency of an evaluation of  $n = 150$  fiber diameters and the average value including standard deviation.

The images in figure 137 show the results of **1e** at a *working distance of 6 cm* and applied voltages of -20, -30, and -40 kV corresponding to electrical field strengths of 3.3, 5.0 and

6.7 kV/cm, respectively. The results in fiber quality and average fiber diameter of the two lower applied voltages are similar with  $1.8 \pm 1.3 \mu\text{m}$  at -20 kV and  $1.7 \pm 1.2 \mu\text{m}$  at -30 kV, respectively. Fibers processed at -40 kV are thinner with an average fiber diameter of only  $0.6 \pm 0.5 \mu\text{m}$ . All samples show fibers with uniform surface. The high standard deviations are caused by the presence of a few thicker fibers.

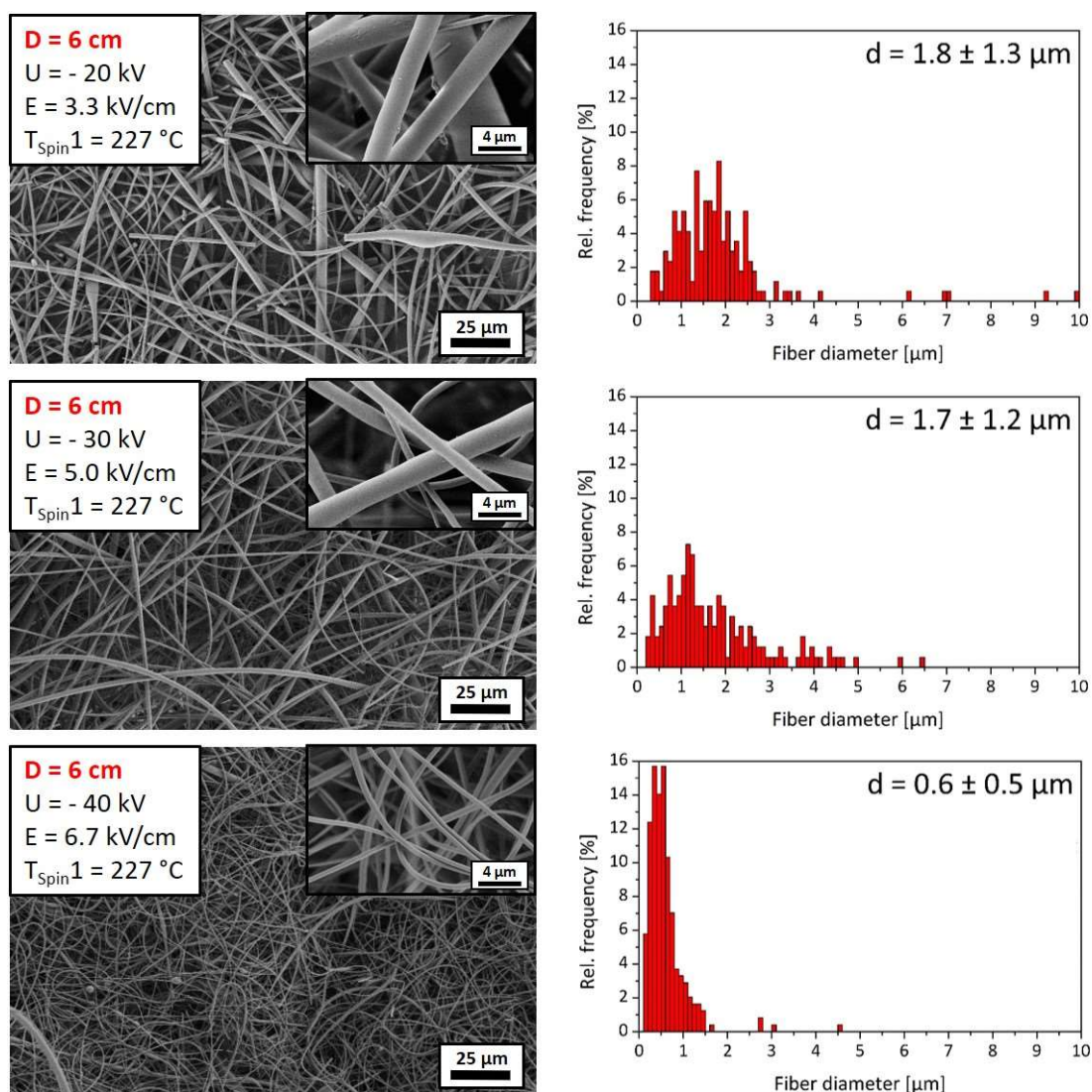


Figure 137: Scanning Electron Microscopy images (left) of electrospun fibers of **1e** produced at  $T_{Spin1}$  of 227 °C, **working distance D of 6 cm** and an electrospinning applied voltage  $U$  of -20 (top), -30 (middle), and -40 kV (bottom). Bar diagrams (right) show the fiber diameter dependent on the relative frequency of an evaluation of  $n = 150$  fiber diameters and the average value with standard deviation.

At a *working distance of 9 cm* (figure 138), it was possible to electrospin fibers at applied voltages of -30, -40 and -50 kV corresponding to electrical field strengths of 3.3, 4.4 and 5.6 kV/cm, respectively. The average fiber diameters are in the range of one up to two micrometers with  $1.4 \pm 0.7 \mu\text{m}$  processed at -30 kV,  $1.3 \pm 0.7 \mu\text{m}$  processed at -40 kV, and  $1.7 \pm 0.7 \mu\text{m}$  processed at -50 kV. The standard deviations stay below half of the actual average fiber diameters at least for the samples produced at -30 kV and -50 kV. The fibers have uniform surface and are roundly shaped.

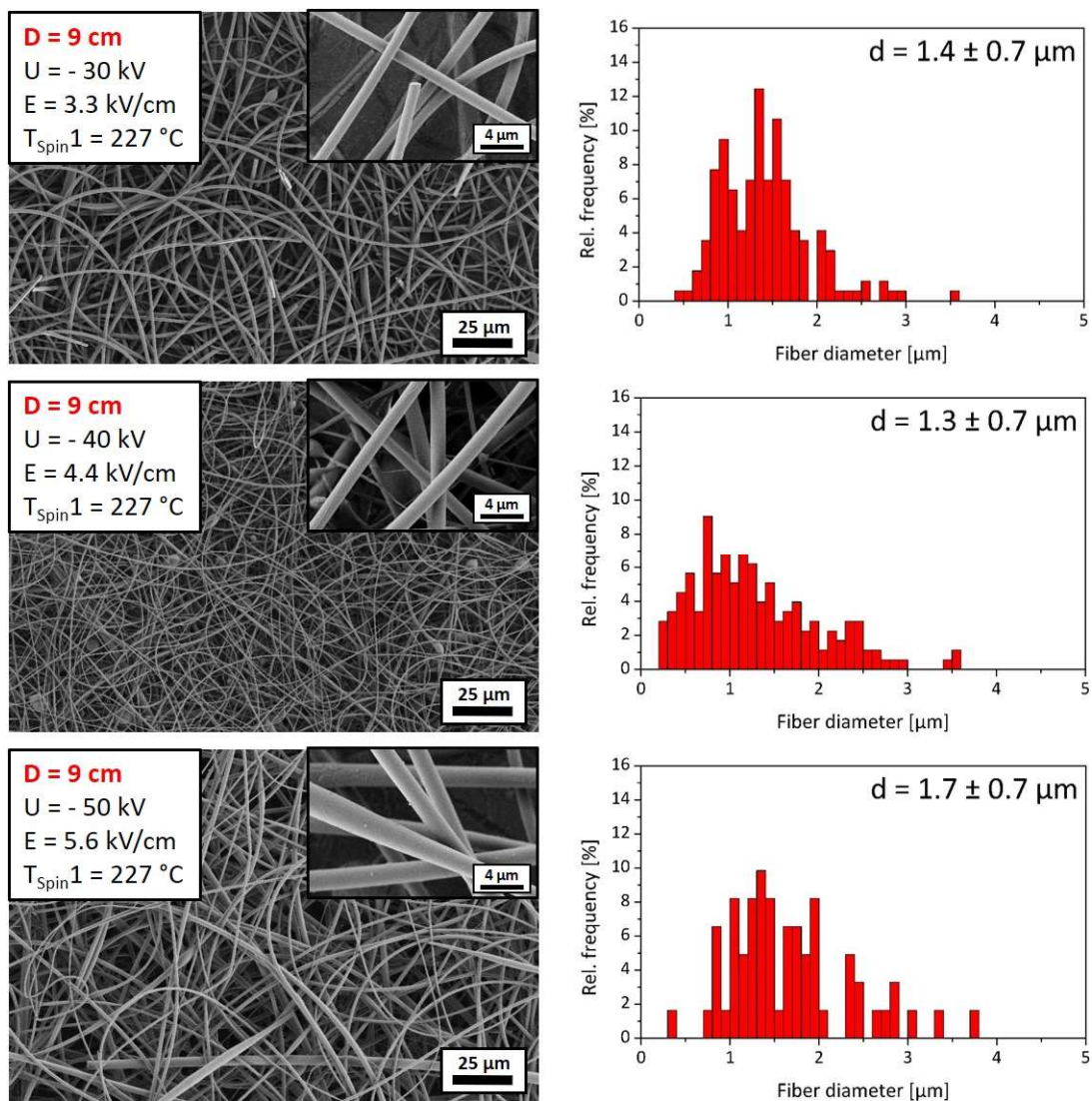


Figure 138: Scanning Electron Microscopy images (left) of electrospun fibers of **1e** produced at  $T_{\text{Spin}1}$  (of  $227 \text{ }^\circ\text{C}$ , *working distance D of 9 cm* and an electrospinning applied voltage  $U$  of -30 (top), -40 (middle), and -50 kV (bottom)). Bar diagrams (right) show the fiber diameter dependent on the relative frequency of an evaluation of  $n = 150$  fiber diameters and the average value with standard deviation.

### Electrospinning results of **1e** at a spinning temperature of 217 °C

For different working distances of 4 cm (figure 139), 6 cm (figure 140), and 9 cm (figure 141), the electrospinning results of **1e** obtained at a spinning temperature of 217 °C at different applied voltages, including the average fiber size and fiber size distributions, are shown.

At a *working distance of 4 cm* (figure 139), electrospinning to fibers was possible at -15, -20, and -30 kV corresponding to electrical field strengths of 3.8, 5.0 and 7.5 kV/cm, respectively.

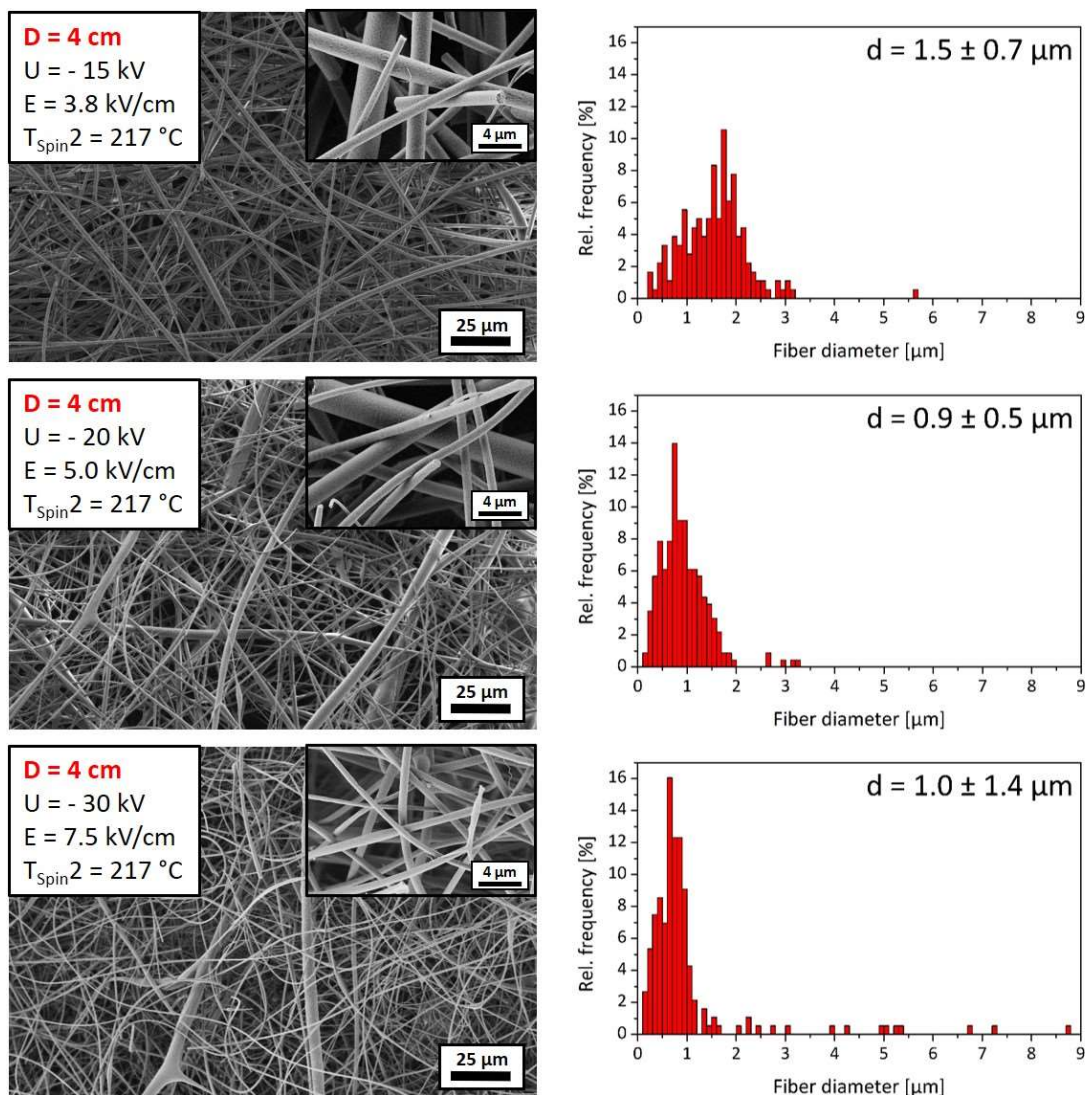


Figure 139: Scanning Electron Microscopy images (left) of electrospun fibers of **1e** produced at  $T_{\text{Spin}2}$  of 217 °C, **working distance D of 4 cm** and an electrospinning applied voltage U of -15 (top), -20 (middle), and -30 kV (bottom). Bar diagrams (right) show the fiber diameter dependent on the relative frequency of an evaluation of  $n = 150$  fiber diameters and the average value with standard deviation.

At the lower applied voltages, the resulting fibers have a good quality with standard deviations of around half of the actual average fiber diameters ( $1.5 \pm 0.7 \mu\text{m}$  at  $-15 \text{ kV}$  and  $0.9 \pm 0.5 \mu\text{m}$  at  $-20 \text{ kV}$ ). The quality of the fibers produced at  $-30 \text{ kV}$  is poor with standard deviation higher than the average fiber diameter ( $1.0 \pm 1.4 \mu\text{m}$ ) and many different shaped fibers and agglomerations can be found.

At a *working distance of 6 cm* (figure 140), it was possible to produce fibers at applied voltages of  $-30$  and  $-40 \text{ kV}$  corresponding to electrical field strengths of  $5.0$  and  $6.7 \text{ kV/cm}$ , respectively. Thin fibers with an average fiber diameter of  $0.4 \pm 0.2 \mu\text{m}$  were obtained at an applied voltage of  $-30 \text{ kV}$  while the fibers produced at  $-40 \text{ kV}$  have a fiber diameter of  $0.9 \pm 0.5 \mu\text{m}$ , which is in the range of the fiber diameters produced at a working distance of  $4 \text{ cm}$ . The standard deviations are slightly above half of the actual average fiber diameters, but the SEM images show that beads are present on the sample produced at the lower applied voltage. The samples electrospun at  $-40 \text{ kV}$  include a few thicker fibers between mostly thin fibers.

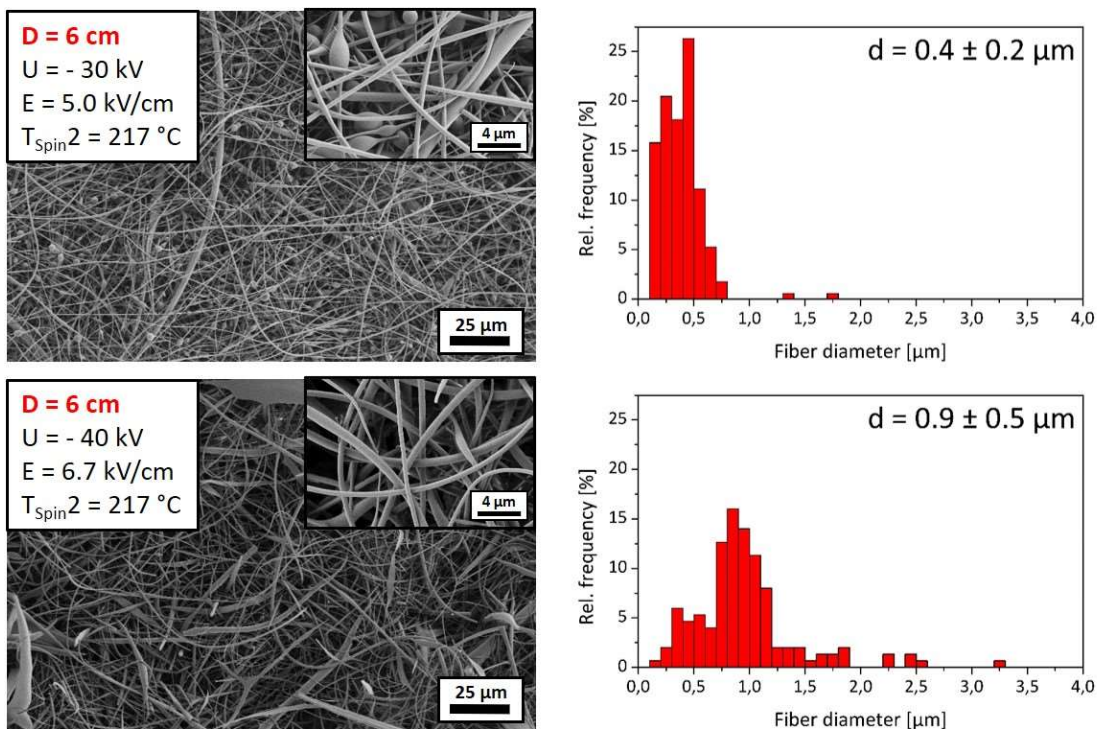


Figure 140: Scanning Electron Microscopy images (left) of electrospun fibers of **1e** produced at  $T_{\text{Spin}2}$  of  $217 \text{ }^\circ\text{C}$ , **working distance D of 6 cm** and an electrospinning applied voltage  $U$  of  $-30$  (top) and  $-40 \text{ kV}$  (bottom). The bar diagrams (right) show the fiber diameter dependent on the relative frequency of an evaluation of  $n = 150$  fiber diameters and the average value including standard deviation.

At a *working distance of 9 cm*, (figure 141) fibers were produced at applied voltage of -40 and -50 kV corresponding to electrical field strengths of 4.4 and 5.6 kV/cm, respectively. At applied voltage of -40 kV, fibers with an average fiber diameter of 2.1  $\mu\text{m}$  and a high standard deviation of 1.4  $\mu\text{m}$  were obtained. Most of the fibers have diameters in the range of one to two micrometers but also a few thicker ones with about four to six micrometers can be found. The average fiber diameter decreased by increasing applied voltage to -50 kV, but the standard deviation remains above half of the actual average fiber diameter ( $1.3 \pm 0.8 \mu\text{m}$ ). Here, most of the fibers have diameters up to two micrometers but a few thicker ones cause the high standard deviation. In both cases, homogeneously shaped fibers with uniform surface were obtained.

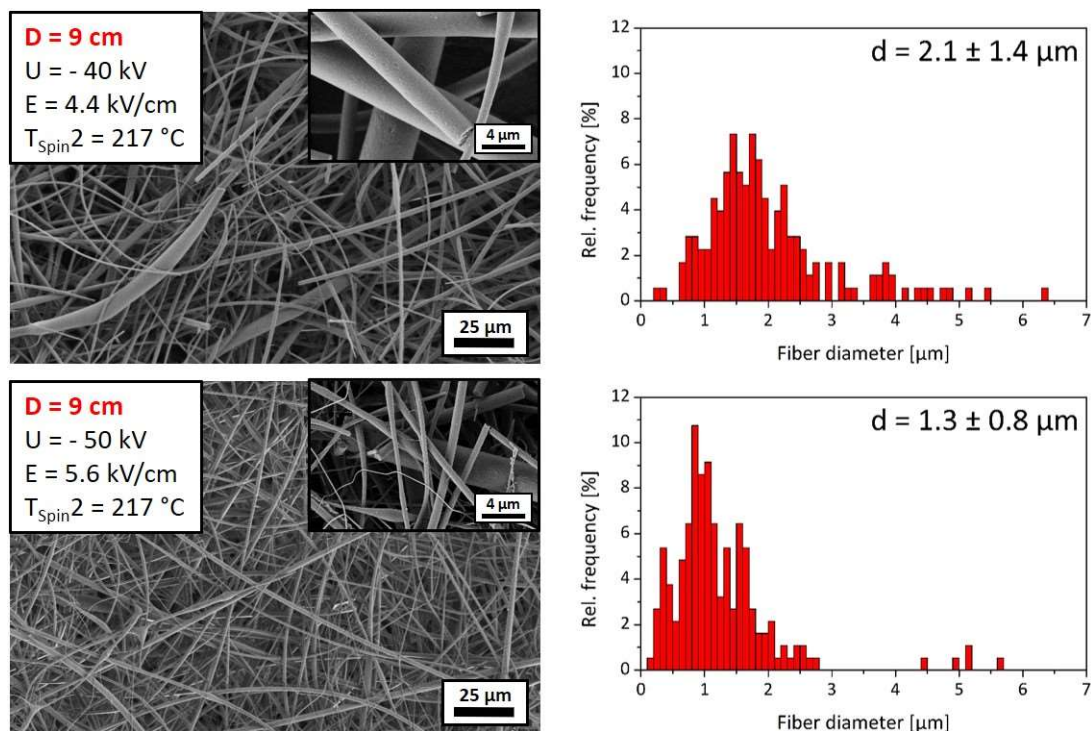


Figure 141: Scanning Electron Microscopy images (left) of electrospun fibers of **1e** produced at  $T_{\text{Spin}2}$  of 217  $^{\circ}\text{C}$ , **working distance D of 9 cm** and an electrospinning applied voltage  $U$  of -40 (top) and -50 kV (bottom). The bar diagrams (right) show the fiber diameter dependent on the relative frequency of an evaluation of  $n = 150$  fiber diameters and the average value including standard deviation.

### **Electrospinning results of 1e at a spinning temperature of 207 °C**

In the following, the results of the electrospinning at 207 °C are described. Only two parameter combinations allowed fiber formation: at a working distance of 6 cm and applied voltage of -40 kV ( $E = 6.7$  kV/cm), and a working distance of 9 cm at applied voltage of -30 kV ( $E = 3.3$  kV/cm). Both are shown in figure 142 including their fiber size and fiber size distributions. All other parameter combinations resulted in a flashover at higher electric fields or droplets of melt on the collector at lower electric fields.

At a *working distance of 6 cm* (figure 142 top), a narrow fiber size distribution with thin fibers of high quality and an average fiber diameter of  $0.4 \pm 0.2$   $\mu\text{m}$  was obtained. The SEM images show homogeneous fibers with uniform surface. The fibers produced at a *working distance of 9 cm* (figure 142 bottom) and an applied voltage of -30 kV resulted in a narrow fiber size distribution with fibers rarely thicker than 2  $\mu\text{m}$ . The average fiber diameter of  $0.8 \pm 0.4$   $\mu\text{m}$  proves the high quality of the fibers in addition to their uniform surface and homogeneous thickness over the whole sample.

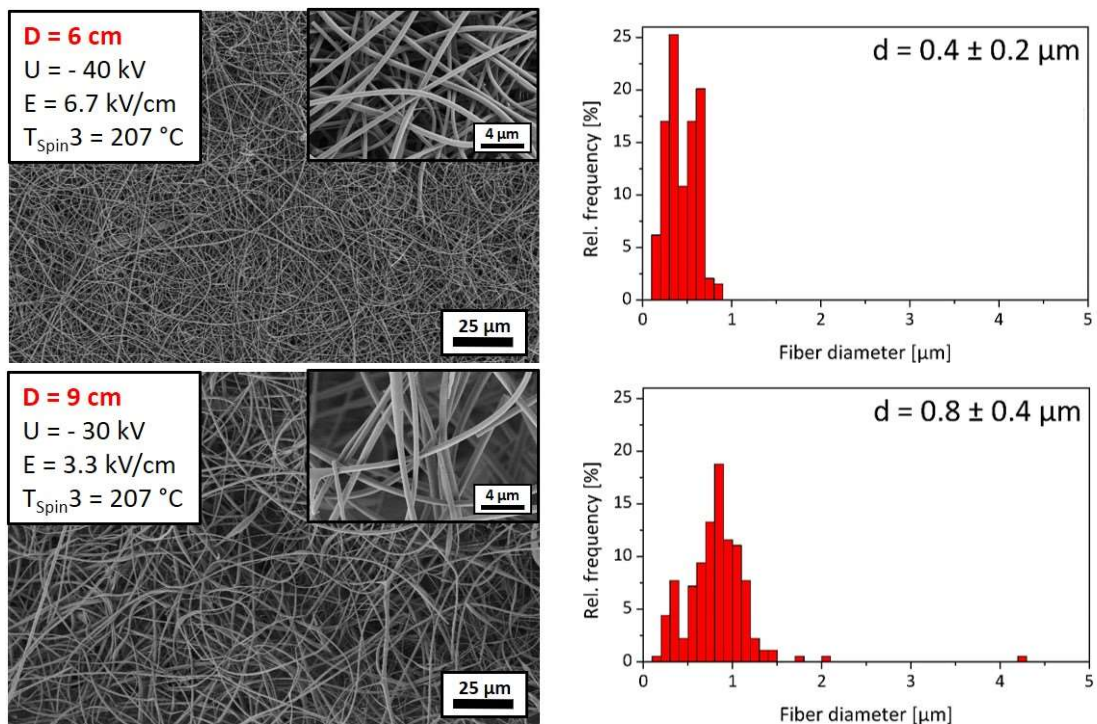


Figure 142: Scanning Electron Microscopy images (left) of electrospun fibers of **1e** produced at  $T_{\text{Spin}3}$  of 207 °C, **working distance D of 6 cm** and an electrospinning applied voltage  $U$  of -40 kV (top), as well as fibers produced at a working distance **D of 9 cm** and an electrospinning applied voltage  $U$  of -30 kV. The bar diagrams (right) show the fiber diameter dependent on the relative frequency of an evaluation of  $n = 150$  fiber diameters and the average value including standard deviation.

The results of all electrospinning experiments of **1e** are summarized in table 14 including the average fiber diameters and the standard deviation values.

In summary, the electrospinning of **1e** was successfully performed resulting in fibers with uniform surface and average fiber diameters in the range of 0.4  $\mu\text{m}$  up to 1.8  $\mu\text{m}$ . Most of the successful experiments were performed at the highest electrospinning temperature  $T_{\text{Spin}1}$  of 227  $^{\circ}\text{C}$ . At the lowest temperature, only two parameter combinations allowed fiber formation. Regarding the fiber size distributions and average fiber diameters, it stands out that a lot of uniform and thin fibers were fabricated but the existence of a few very thick fibers causes high standard deviation values.

*Table 14: Average fiber diameters including standard deviations of the electrospinning results of **1e** dependent on the electrospinning temperature  $T_{\text{Spin}}$  and the applied electric field strength  $E$  (with the corresponding parameter combination of working distance  $D$  and applied high voltage  $U$ ). The best results are shown in green.*

$T_{\text{Spin}}$ ( $^{\circ}\text{C}$ )		$T_{\text{Spin}1} = 227$	$T_{\text{Spin}2} = 217$	$T_{\text{Spin}3} = 207$
$E$ (kV/cm)				
<b>3.3</b>	D = 6 cm; U = -20 kV	1.8 $\pm$ 1.3 $\mu\text{m}$		droplet formation
	D = 9 cm; U = -30 kV		droplet formation	0.8 $\pm$ 0.4 $\mu\text{m}$
<b>3.8</b>	D = 4 cm; U = -15 kV	droplet formation	1.5 $\pm$ 0.7 $\mu\text{m}$	droplet formation
<b>4.4</b>	D = 9 cm; U = -40 kV	1.3 $\pm$ 0.7 $\mu\text{m}$	2.1 $\pm$ 1.4 $\mu\text{m}^*$	droplet formation
<b>5.0</b>	D = 4 cm; U = -20 kV	1.8 $\pm$ 1.7 $\mu\text{m}^*$	0.9 $\pm$ 0.5 $\mu\text{m}$	droplet formation
	D = 6 cm; U = -30 kV	1.7 $\pm$ 1.2 $\mu\text{m}$	0.4 $\pm$ 0.2 $\mu\text{m}^*$	
<b>5.6</b>	D = 9 cm; U = -50 kV	1.7 $\pm$ 0.7 $\mu\text{m}$	1.3 $\pm$ 0.8 $\mu\text{m}$	droplet formation
<b>6.7</b>	D = 6 cm; U = -40 kV	<b>0.6 <math>\pm</math> 0.5 <math>\mu\text{m}</math></b>	0.9 $\pm$ 0.5 $\mu\text{m}^*$	<b>0.4 <math>\pm</math> 0.2 <math>\mu\text{m}</math></b>
<b>7.5</b>	D = 4 cm; U = -30 kV	1.2 $\pm$ 1.2 $\mu\text{m}^*$	1.0 $\pm$ 1.4 $\mu\text{m}$	flashover

\*fibers of this sample have beads or show high thickness inhomogeneity alongside the fiber direction

Only for a few experiments, the standard deviations remain below half of the actual average fiber diameter caused by the lack of thicker fibers. In these cases, fibers with good fiber

quality were found. The fibers with best overall quality are obtained at  $T_{\text{Spin}3}$  of 207 °C, a working distance of 6 cm and an applied voltage of -40 kV ( $E = 6.7$  kV/cm) resulting in an average fiber diameter of  $0.4 \pm 0.2$   $\mu\text{m}$ . Second best results were obtained at  $T_{\text{Spin}1}$  of 227 °C, at the same working distance and applied voltage, with average fiber diameter of  $0.6 \pm 0.5$   $\mu\text{m}$ . In both cases, the standard deviation is at least half of the actual average fiber diameter, but the bar diagrams of the fiber size distributions show that this is caused by only a few thicker fibers on the sample. A possible explanation for the formation of much thicker fibers on nearly all of the fiber samples can be the very low surface tension of highly fluorinated compounds.<sup>3</sup> In comparison to **1c**, compound **1e** has longer linear perfluorinated side chains resulting in a higher fluorine density of the material and thus it is possible that it has a lower surface tension. Therefore, it is possible that at the start of the electrospinning process, meaning the enabling of the electric field, some material, which has wetted the syringe tip, is just elevated to the collector without forming a jet or is not elongated in the electric field. Another explanation can be the sublimation of the material right after it leaves the syringe tip and therefore disturbing the proper electrospinning process.

### Analytical data of the BTAs for the melt electrospinning to thick fibers for direct force measurements

#### *N*<sup>1</sup>,*N*<sup>3</sup>,*N*<sup>5</sup>-tris(decyl)-1,3,5-cyclohexanetricarboxamide **4a**

##### DSC:

- First heating: One transition at 111 °C (3 kJ/mol) with low, two transitions at 161 °C (23 kJ/mol) and 246 °C (26 kJ/mol) with medium, and another transition at 307 °C (6 kJ/mol) with low enthalpy.
- Second heating: Two transitions at 79 °C (1 kJ/mol) and 130 °C (3 kJ/mol) with low, one transition at 238 °C (19 kJ/mol) with medium, and another transition at 297 °C (3 kJ/mol) with low enthalpy.

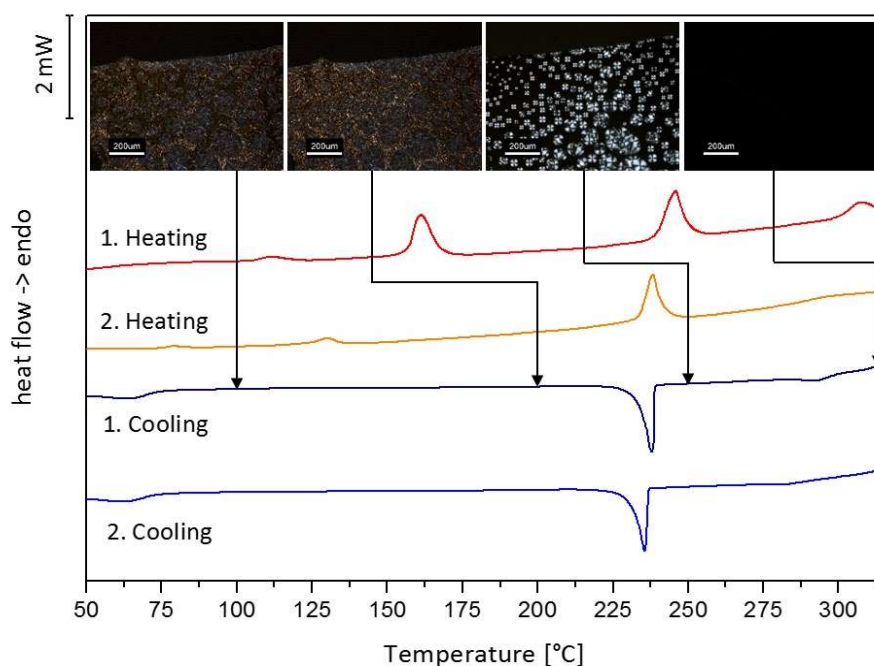


Figure 143: Differential Scanning Calorimetry heating and cooling scans of **4a** (heating and cooling rate: 10 K/min, N<sub>2</sub> atmosphere). Polarized Optical Microscopy pictures were taken at the marked temperatures within the first cooling scan, scale of the pictures: 200 μm.

##### POM:

- First and second transition cannot be observed optically (crystalline → crystalline).
- Third transition (crystalline → mesophase) 130 °C to 135 °C.
- Fourth transition (mesophase → nematic phase) 240 °C to 245 °C.
- Fifth transition (nematic phase → isotropic phase) 310 °C to 315 °C.

- Cooling: Below 275 °C slow development of a nematic *schlieren* texture. The nematic phase changes into a mesophase with high viscosity at 238 °C indicating a Col<sub>hp</sub> phase, which remains until 60 to 50 °C. At this temperature, the texture breaks under deformation in a crystalline fashion.

The combination of the results of DSC and POM lead to the following phase characteristics at first heating:

Cr<sub>1</sub> 111 °C (3 kJ/mol) Cr<sub>2</sub> 161 °C (23 kJ/mol) Col<sub>hp</sub> 246 °C (26 kJ/mol) N 307 °C (6 kJ/mol) I

**(1*s*,3*s*,5*s*)-N<sup>1</sup>,N<sup>3</sup>,N<sup>5</sup>-triheptyl-1,3,5-cyclohexanetricarboxamide 4b**

DSC:

- First heating: Two overlapping transitions at 191 °C and 207 °C (combined 14 kJ/mol) with low, and two transitions at 280 °C (22 kJ/mol) and 308 °C (11 kJ/mol) with medium enthalpy.
- Second heating: Two transitions at 169 °C (7 kJ/mol) and 273 °C (14 kJ/mol) with medium enthalpy.

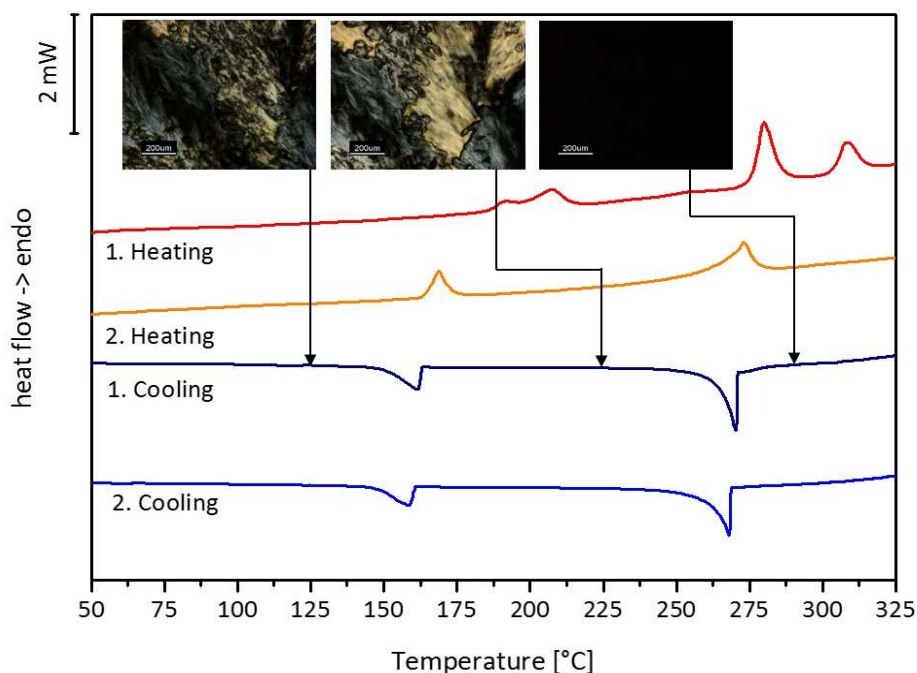


Figure 144: Differential Scanning Calorimetry heating and cooling scans of **4b** (heating and cooling rate: 10 K/min, N<sub>2</sub> atmosphere). Polarized Optical Microscopy pictures were taken at the marked temperatures within the first cooling scan, scale of the pictures: 200 μm.

*POM:*

- First transition (crystalline → crystalline) 200 °C to 220 °C.
- Second transition (crystalline → plastic crystalline) 250 °C to 260 °C.
- Third transition (plastic crystalline → nematic phase) 280 °C to 290 °C.
- Fourth transition (nematic phase → isotropic phase) 305 °C.
- Cooling: At 270 °C the plastic crystalline mesophase is developed, the nematic phase could not be observed. At 160 °C to 150 °C, the plastic crystalline mesophase changes into the crystalline state.

*The combination of the results of DSC, and POL lead to the following phase characteristics at first heating:*

Cr<sub>1</sub> 191 °C Cr<sub>2</sub> 207 °C (combined 14 kJ/mol) M<sub>p</sub> 280 °C (22 kJ/mol) N 308 °C (11 kJ/mol) I

***N<sup>1</sup>,N<sup>3</sup>,N<sup>5</sup>-trihexyl-1,3,5-benzenetricarboxamide 5a****DSC:*

- First heating: Four transitions at 61 °C (5 kJ/mol), 72 °C (3 kJ/mol), 91 °C (2 kJ/mol) and 166 °C (0.2 kJ/mol) with low, and one transition at 207 °C (14 kJ/mol) with medium enthalpy.
- Second heating: Two transitions at 72 °C (0.5 kJ/mol) and 164 °C (0.1 kJ/mol) with low, and one transition at 207 °C (11 kJ/mol) with medium enthalpy.

*POM:*

- First and second transition: No change in the texture observable.
- Third transition: Brightening of the powder between 80 to 90 °C indicates a change from the crystalline state into a mesophase.
- Fourth transition (first mesophase → second mesophase) 160 °C to 170 °C.
- Fifth transition (second mesophase → isotropic phase) 210 °C to 215 °C.
- Cooling: At 200 °C, the material forms a dendritic and spherulitic texture indicating a columnar phase, which is deformable under stress and is fully developed at 175 °C. Below 175 °C, the viscosity of the material slowly decreases with decreasing temperature until 70 °C is reached. Then the texture is not deformable any more indicating the transition from the mesophase into the crystalline state.

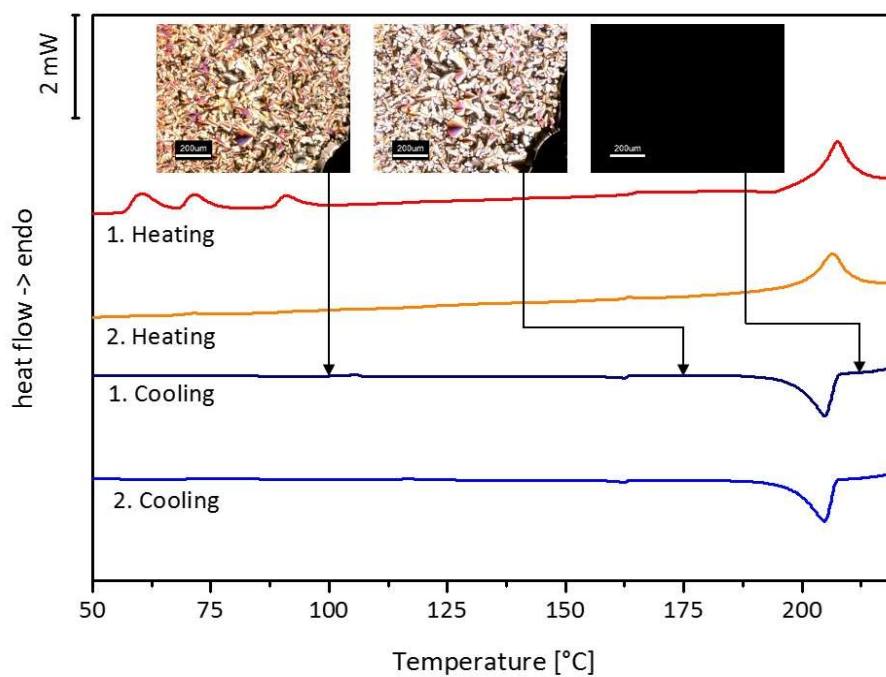


Figure: 145: Differential Scanning Calorimetry heating and cooling scans of **5a** (heating and cooling rate: 10 K/min,  $N_2$  atmosphere). Polarized Optical Microscopy pictures were taken at the marked temperatures within the first cooling scan, scale of the pictures: 200  $\mu m$ .

The combination of the results of DSC and POM lead to the following phase characteristics at first heating:

Cr 61-91 °C (combined 10 kJ/mol) Col<sub>hp</sub> 166 °C (0.2 kJ/mol) Col<sub>h</sub> 207 °C (14 kJ/mol) I

***N*<sup>1</sup>,*N*<sup>3</sup>,*N*<sup>5</sup>-tributyl-1,3,5-benzenetricarboxamide **5b****

DSC:

- First heating: One transition at 118 °C (7 kJ/mol) with low, and one transition at 236 °C (25 kJ/mol) with high enthalpy.
- Second heating: One transition at 103 °C (8 kJ/mol) with low, and one transition at 235 °C (20 kJ/mol) with high enthalpy.

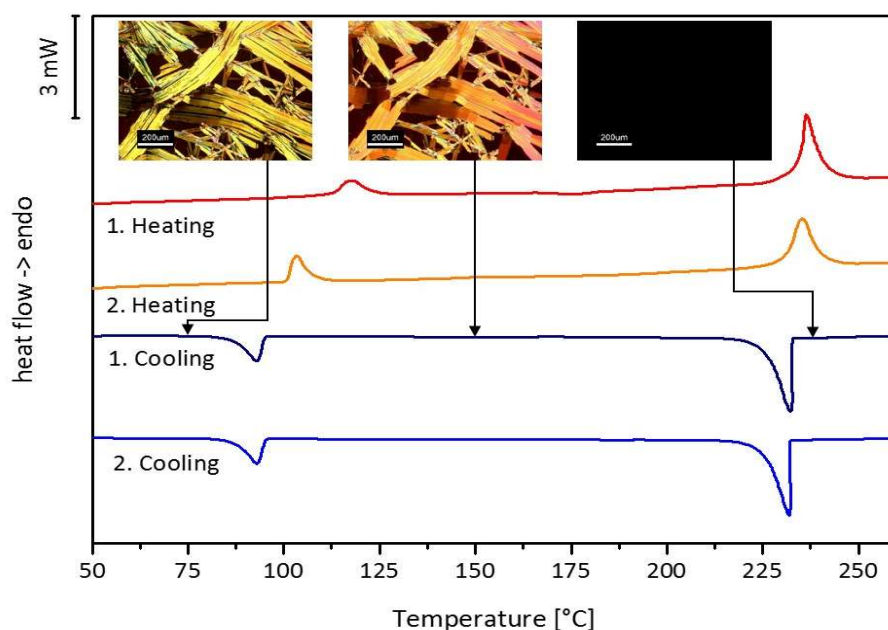


Figure 146: Differential Scanning Calorimetry heating and cooling scans of **5b** (heating and cooling rate: 10 K/min, N<sub>2</sub> atmosphere). Polarized Optical Microscopy pictures were taken at the marked temperatures within the first cooling scan, scale of the pictures: 200 μm.

POM:

- First transition (crystalline → plastic crystalline) 100 °C to 110 °C.
- Second transition (plastic crystalline → isotropic phase) 230 °C to 240 °C.
- Cooling: At 225 °C, the material begins to develop band textures, which are bending under deformation indicating a plastic mesophase. Beside the band textures, there is still liquid material present until about 95 °C. Below this temperature the liquid material gets solid and deformation causes crystalline breaking of the textures.

The combination of the results of DSC and POM lead to the following phase characteristics at first heating:

Cr 118 °C (7 kJ/mol) M<sub>p</sub> 236 °C (25 kJ/mol) I

***N<sup>1</sup>,N<sup>3</sup>,N<sup>5</sup>-tris(2-methoxyethyl)-1,3,5-benzenetricarboxamide 5c***

DSC:

- First heating: One transition at 149 °C (36 kJ/mol) with high enthalpy.
- Second heating: One transition at 148 °C (31 kJ/mol) with high enthalpy.

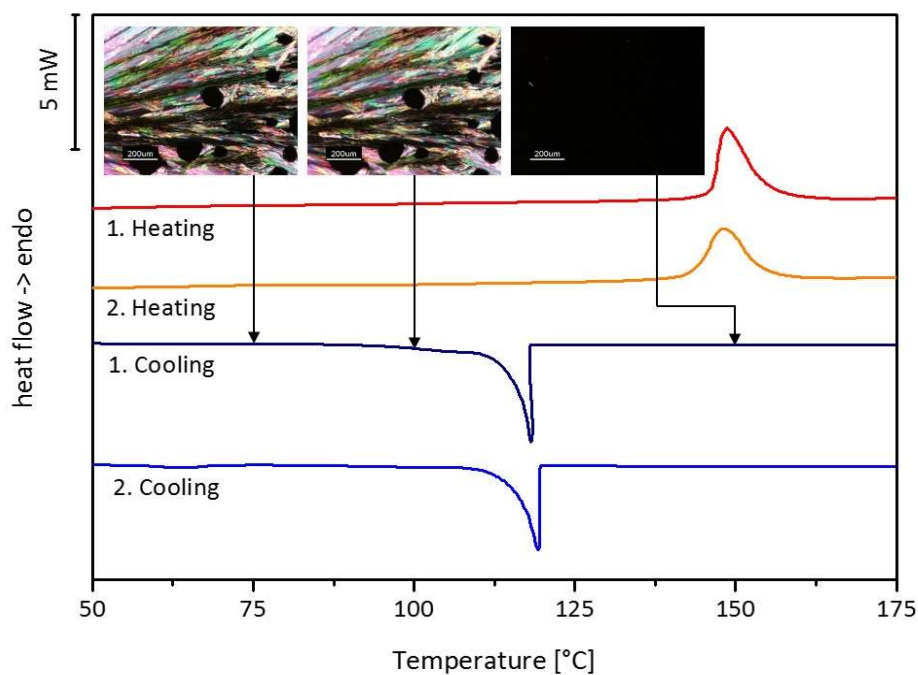


Figure 147: Differential Scanning Calorimetry heating and cooling scans of **5c** (heating and cooling rate: 10 K/min, N<sub>2</sub> atmosphere). Polarized Optical Microscopy pictures were taken at the marked temperatures within the first cooling scan, scale of the pictures: 200 μm.

POM:

- First transition (crystalline → isotropic phase) 148 °C to 150 °C
- Cooling: Fast recrystallization at 192 °C to a layer structure, which breaks under deformation.

The combination of the results of DSC and POM lead to the following phase characteristics at first heating:

Cr 149 °C (36 kJ/mol) I

***N*<sup>1</sup>,*N*<sup>3</sup>,*N*<sup>5</sup>-tris(4-methoxyphenyl)-1,3,5-benzenetricarboxamide **5d****

DSC:

- First heating: One transition at 266 °C (0.6 kJ/mol) with low, and one transition at 275 °C (33 kJ/mol) with high enthalpy.
- Second heating: One transition at 274 °C (31 kJ/mol) with high enthalpy.

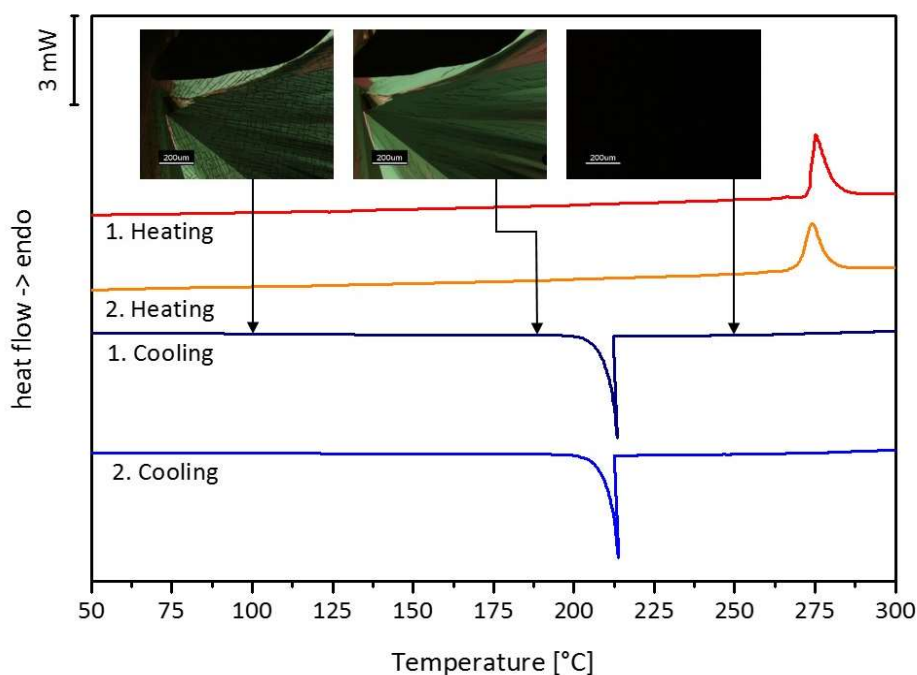


Figure 148: Differential Scanning Calorimetry heating and cooling scans of **5d** (heating and cooling rate: 10 K/min, N<sub>2</sub> atmosphere). Polarized Optical Microscopy pictures were taken at the marked temperatures within the first cooling scan, scale of the pictures: 200 μm.

POM:

- First transition (crystalline → isotropic phase) 279 °C to 281 °C.
- Cooling: Fast recrystallization at 188 °C to a crystalline layer structure, which breaks under deformation. Thermal crack development by further cooling.

The combination of the results of DSC and POM lead to the following phase characteristics at first heating:

Cr<sub>1</sub> 266 °C (0.6 kJ/mol) Cr<sub>2</sub> 275 °C (33 kJ/mol) I

***N,N,N'*-(1,3,5-benzenetriyl)triheptanamide 6a**

DSC:

- First heating: One transition at 166 °C (16 kJ/mol) with high enthalpy.
- Second heating: One transition at 166 °C (16 kJ/mol) with high enthalpy.

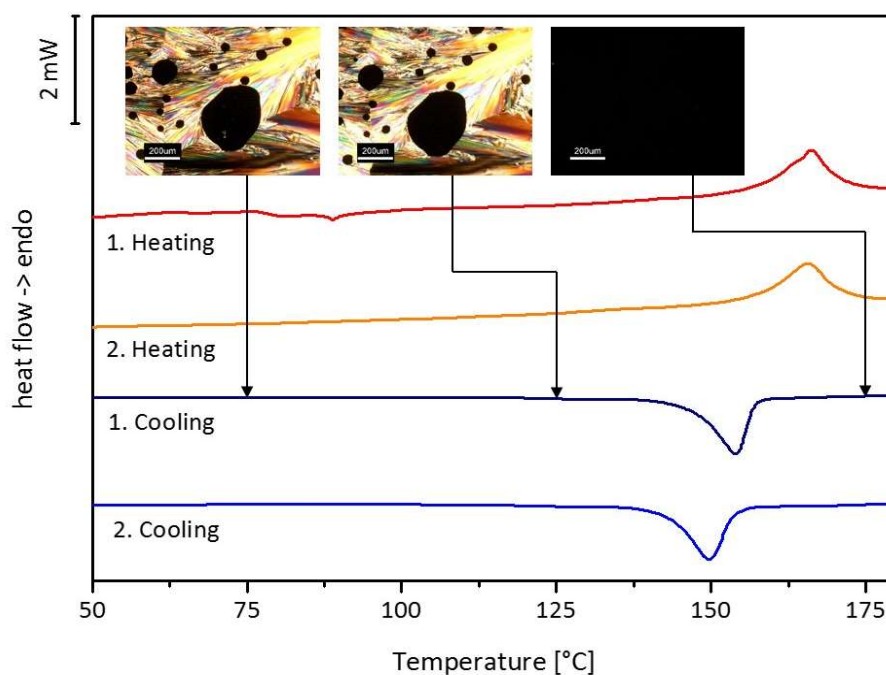


Figure 149: Differential Scanning Calorimetry heating and cooling scans of **6a** (heating and cooling rate: 10 K/min,  $N_2$  atmosphere). Polarized Optical Microscopy pictures were taken at the marked temperatures within the first cooling scan, scale of the pictures: 200  $\mu\text{m}$ .

POM:

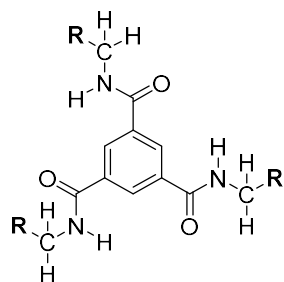
- First transition (crystalline  $\rightarrow$  isotropic phase) 175 °C.
- Cooling: Recrystallization at 163 °C to a layer texture, which is breaking crystalline under deformation.

The combination of the results of DSC and POM lead to the following phase characteristics at first heating:

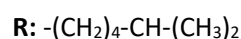
Cr 166 °C (16 kJ/mol) I

### 7.2.3 Additional data to chapter 5

#### Characterization of $N^1, N^3, N^5$ -tris(6-methylheptyl)-1,3,5-benzenetricarboxamide (**B**)



$N^1, N^3, N^5$ -tris(6-methylheptyl)-1,3,5-benzenetricarboxamide



**DSC:** In figure 150 the first and second heating and cooling scans of the DSC analysis of  $N^1, N^3, N^5$ -tris(6-methylheptyl)-1,3,5-benzenetricarboxamide (**B**) are shown.

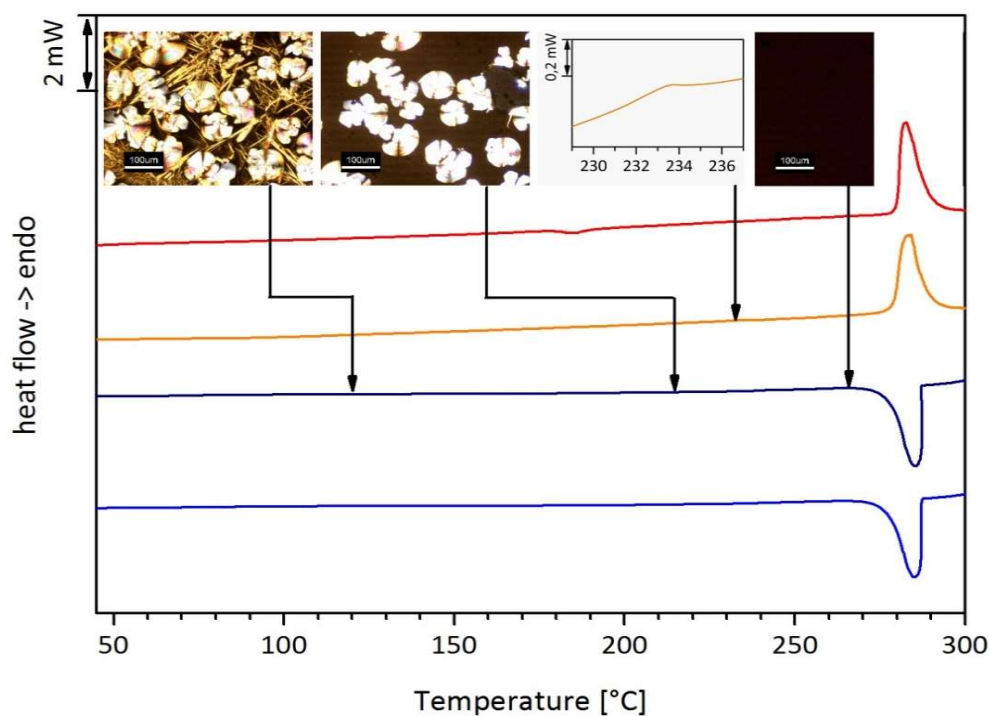


Figure 150: First and second Differential Scanning Calorimetry heating and cooling scans of **B**. The mesophase textures of the Polarized Optical Microscopy pictures were taken at the marked temperatures within the first cooling scan. The data curve shortcut is a magnification of the second heating scan.

Based on the second heating scan, only one clear transition at 284 °C with high enthalpy of 48 kJ/mol can be found indicating the transition into the isotropic phase. By taking a closer look at the heating scan, another transition at 234 °C with low enthalpy of 0.1 kJ/mol is present. This can be explained by a small change in the molecular order and can originate from the change of one into another crystalline state, or the transition from a columnar plastic into a lesser ordered columnar phase.

**POM:** Upon first heating, the powder under the crossed polarizers slowly begins to brighten above 220 °C, indicating a transition into a different phase. Above 266 °C, the picture turns black which means that the compound resides in the isotropic phase. Upon cooling, a spherulitic texture starts to develop at 237 °C indicating a columnar hexagonal phase, while a liquid phase is still present surrounding the formed textures. Shearing causes bending and folding, which indicates the presence of a plastic crystalline mesophase. Needles are formed when the temperature falls below 215 °C, and the textures do not change again until RT is reached. It can be assumed that the plastic mesophase freezes below 215 °C and no crystalline structure is developed at RT. Combined with the DSC results, the transition with low enthalpy at 234 °C can be identified as a transition from a plastic crystalline into a liquid crystalline mesophase, while the transition with high enthalpy at 284 °C stands for the clearing temperature.

**XRD:** In figure 151, the XRD patterns of the first heating at RT, 100 °C and 250 °C are shown. Based on the patterns at RT and 100 °C, it is possible to find most of the important signals for the identification of a Col<sub>h</sub> phase ([100], [110], [200], and [210]) and additional signals which prove the presence of a Col<sub>hp</sub> phase or a crystalline state. The signal for [001], standing for the intermolecular distance within the columns formed by the BTA molecules, can be found. At 250 °C the pattern changes, only the [100] signal can be clearly identified and calculated to a column-to-column distance of 1.53 nm. Combination with the POM results indicate that a Col<sub>h</sub> phase is still present. The lack of other signals for the clear identification of a Col<sub>h</sub> phase is due to the transition into a lower ordered phase by the cease of the 3D order. It is not possible to identify the phase as an ordered or disordered Col<sub>h</sub> phase because there is also an overall decrease in signal intensity compared to the patterns at lower temperature.

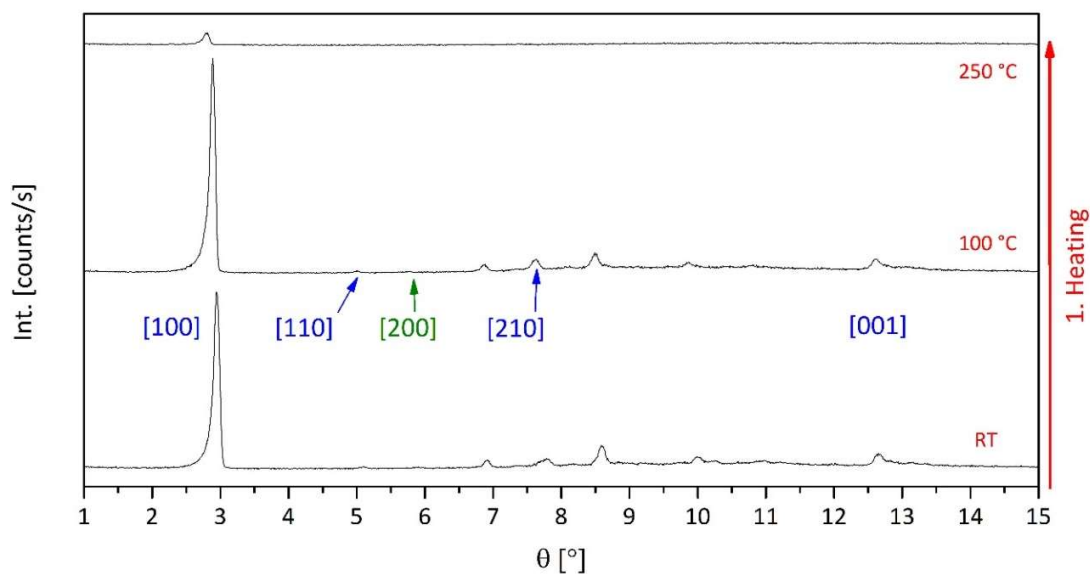


Figure 151: X-Ray Diffraction patterns of the different phases of **B** at different temperatures at heating. It shows a  $Col_{hp}$  pattern at room temperature and a transition between the  $Col_{hp}$  and a second mesophase between 100 °C and 250 °C. The green and blue numerics stand for the signals indicating a columnar hexagonal pattern. Blue = signal found, green = signal not found.

The combination of the results of DSC, POM and XRD lead to the following phase characteristics for **B** at second heating:

$$Col_{hp} \ 234 \text{ °C} \ (0.1 \text{ kJ/mol}) \ Col_h \ 284 \text{ °C} \ (48 \text{ kJ/mol}) \ I$$

Compared to the results of Timme, only a small temperature shift of the transitions to lower values of about six degrees for the transition with low enthalpy, and seven degrees for the clearing temperature can be found, but he was able to identify the mesophase just below the clearing temperature as a  $Col_{ho}$  phase.<sup>45</sup>

## 8. References

- (1) Cardoso, V. F.; Correia, D. M.; Ribeiro, C.; Fernandes, M. M.; Lanceros-Méndez, S. Fluorinated Polymers as Smart Materials for Advanced Biomedical Applications. *Polymers* **2018**, *10*.
- (2) Berger, R.; Resnati, G.; Metrangolo, P.; Weber, E.; Hulliger, J. Organic fluorine compounds: a great opportunity for enhanced materials properties. *Chem. Soc. Rev.* **2011**, 3496–3508.
- (3) Kirsch, P. *Modern Fluoroorganic Chemistry*; WILEY-VCH Verlag GmbH & Co. KGaA: Weinheim, 2004.
- (4) Krafft, M. P.; Riess, J. G. Chemistry, Physical Chemistry, and Uses of Molecular Fluorocarbon–Hydrocarbon Diblocks, Triblocks, and Related Compounds—Unique “Apolar” Components for Self-Assembled Colloid and Interface Engineering. *Chem. Rev.* **2009**, 1714–1792.
- (5) Li, Z.; Whu, L.-Z., Eds. *Hydrogen Bonded Supramolecular Structures*; Springer-Verlag: Berlin, Heidelberg, 2015.
- (6) O'Hagan, D. Understanding organofluorine chemistry. An introduction to the C-F bond. *Chem. Soc. Rev.* **2008**, 308–319.
- (7) Smart, B. E. Fluorine substituent effects (on bioactivity). *J. Fluorine Chem.* **2001**, 3–11.
- (8) Vincent, J. M. Recent advances of fluorine chemistry in material sciences. *Chem. Commun.* **2012**, 11382–11391.
- (9) Roesky, H. A flourish of fluorine. *Nat. Chem.* **2010**, 240.
- (10) Wang, J.; Sanchez-Rosello, M.; Acena, J. L.; Pozo, C. D.; Sorochinsky, A. E.; Fustero, S.; Soloshonok, V. A.; Liu, H. Fluorine in pharmaceutical industry: fluorine-containing drugs introduced to the market in the last decade. *Chem. Rev.* **2014**, 2432–2506.
- (11) Sen, K. D.; Jorgensen, C. K., Eds. *Electronegativity*; Springer-Verlag: New York, 1987.
- (12) Tschierske, C. *Liquid Crystals Materials Design and Self-Assembly*; Springer-Verlag: Berlin, Heidelberg, 2012.
- (13) Peng, H. Synthesis and application of fluorine-containing polymers with low surface energy. *Polymer Reviews* **2019**, *59*, 739–757.
- (14) Albrecht, T.; Elben, H.; Jaeger, R.; Kimmig, M.; Steiner, R.; Strobl, G.; Stühn, B.; Schwickert, H.; Ritter, C. Molecular dynamics in perfluoro-n-eicosane. II. Components of disorder. *J. Chem. Phys.* **1991**, 2807–2816.
- (15) Bunn, C. W.; Howells, E. R. Structures of Molecules and Crystals of Fluoro-Carbons. *Nature* **1954**, 549–551.
- (16) Schwickert, H.; Strobl, G. R.; Kimmig, M. Molecular-Dynamics in Perfluoro-n-Eicosane. 1. Solid-Phase Behavior and Crystal-Structures. *J. Chem. Phys.* **1991**, 2800–2806.
- (17) Kirsch, P.; Bremer, M. Nematic Liquid Crystals for Active Matrix Displays: Molecular Design and Synthesis. *Angew. Chem.* **2000**, 4284–4405.
- (18) Campos-Vallette, M.; Rey-Lafon, M. Vibrational spectra and rotational isomerism in short chain n-perfluoroalkanes. *J. Mol. Struct.* **1983**, 23–45.
- (19) Marchionni, G.; Ajroldi, G.; Righetti, C. M.; Pezzin, G. Molecular interactions in perfluorinated and hydrogenated compounds: linear paraffins and ethers. *Macromolecules* **1993**, 1751–1757.
- (20) Corbierre, M. K.; Cameron, N. S.; Lennox, R. B. Polymer-stabilized gold nanoparticles with high grafting densities. *Langmuir* **2004**, 2867–2873.
- (21) Ionita, P.; Volkov, A.; Jeschke, G.; Chechik, V. Lateral diffusion of thiol ligands on the surface of Au nanoparticles: an electron paramagnetic resonance study. *Anal. Chem.* **2008**, 95–106.

- (22) Smart, B. E.; Tatlow, J. C., Eds. *Organofluorine Chemistry: Principles and Commercial Applications: Characteristics of C-F Systems*; Plenum Press: New York, 1994.
- (23) Watanabe, N.; Nakajima, T.; Touhara H., Eds. *Studies in Inorganic Chemistry: Graphite Fluorides* Vol. 8; Elsevier: Oxford, 1988.
- (24) Young, C. L. Upper critical solution temperature of perfluoro-n-alkane and n-alkane mixtures. *Trans. Faraday Soc.* **1969**, 2639–2644.
- (25) Binks, B. P.; Fletcher, P.D.I.; Sager, W.F.C.; Thompson, R. L. Semifluorinated alkanes as primitive surfactants in apolar hydrocarbon and fluorocarbon solvents. *J. Mol. Liq.* **1997**, 177–190.
- (26) Shimoni, L.; Glusker, J. P. The geometry of intermolecular interactions in some crystalline fluorine-containing organic compounds. *Struct. Chem.* **1994**, 383–397.
- (27) Dunitz, J. D.; Taylor, R. Organic Fluorine Hardly Ever Accepts Hydrogen Bonds. *Chem. Eur. J.* **1997**, 89–98.
- (28) Reichenbacher, K.; Süß, H. I.; Hulliger, J. Fluorine in crystal engineering--"the little atom that could". *Chem. Soc. Rev.* **2005**, 22–30.
- (29) Collings, P. J.; Hird M., Eds. *Introduction to liquid crystals chemistry and physics*; Taylor and Francis: London, 1997.
- (30) Kato, T.; Mizoshita, N.; Kishimoto, K. Functional liquid-crystalline assemblies: self-organized soft materials. *Angew. Chem. Int. Ed.* **2006**, 38–68.
- (31) Tschierske, C. Liquid crystal engineering – new complex mesophase structures and their relations to polymer morphologies, nanoscale patterning and crystal engineering. *Chem. Soc. Rev.* **2007**, 1930–1970.
- (32) Goodby, J. W.; Saez, I. M.; Cowling, S. J.; Görtz, V.; Draper, M.; Hall, A. W.; Sia, S.; Cosquer, G.; Lee, S. E.; Raynes, E. P. Transmission and amplification of information and properties in nanostructured liquid crystals. *Angew. Chem. Int. Ed.* **2008**, 2754–2787.
- (33) Tschierske, C. Non-Conventional Soft Matter. *Ann. Rep. Progr. Chem. Ser.* **2001**, 191–268.
- (34) Demus, D.; Goodby, J. W.; Gray, G. W.; Spiess, H.-W.; Vill, V., Eds. *Handbook of Liquid Crystals: Vol. 1: Fundamentals*; WILEY-VCH Verlag GmbH: Weinheim, 1998.
- (35) Wang, H.; Bisoyi, H. K.; Urbas, A. M.; Bunning, T. J.; Li, Q. The Halogen Bond: An Emerging Supramolecular Tool in the Design of Functional Mesomorphic Materials. *Chemistry (Weinheim an der Bergstrasse, Germany)* **2019**, 25, 1369–1378.
- (36) Arkas, M.; Kitsou, I.; Gkouma, A.; Papageorgiou, M. The role of hydrogen bonds in the mesomorphic behaviour of supramolecular assemblies organized in dendritic architectures. *Liquid Crystals Review* **2019**, 7, 60–105.
- (37) Hunter, L. The C–F bond as a conformational tool in organic and biological chemistry. *Beilstein J. Org. Chem.* **2010**, No. 38.
- (38) Hird, M. Fluorinated liquid crystals--properties and applications. *Chem. Soc. Rev.* **2007**, 2070–2095.
- (39) Chandrasekhar, S.; Sadashiva, B. K.; Suresh, K. A. Liquid crystals of disc-like molecules. *Pramana* **1977**, 471–480.
- (40) Kopitzke, J.; Wendorff, J. H. Discotic liquid crystals: Materials for optoelectronics. *Chem. Unserer Zeit* **2000**, 4–16.

- (41) Laschat, S.; Baro, A.; Steinke, N.; Giesselmann, F.; Hägele, C.; Scalia, G.; Judele, J.; Kapatsina, E.; Sauer, S.; Schreivogel, A.; *et al.* Discotic liquid crystals: from tailor-made synthesis to plastic electronics. *Angew. Chem. Int. Ed.* **2007**, 4832–4887.
- (42) Glüsen, B.; Heitz, W.; Kettner, A.; Wendorff, J. H. A plastic columnar discotic phase Dp. *Liq. Cryst.* **1996**, 627–633.
- (43) Kumar, S. *Chemistry of discotic liquid crystals*; CRC Press Inc.: Boca Raton FL, 2010.
- (44) Wicklein, A. *Self-Organizing n-type Perylene Derivatives for Organic Photovoltaics – Synthesis, Characterization and Application*. Dissertation; University of Bayreuth, 2010.
- (45) Timme, A. *Flüssigkristalline supramolekulare Systeme*. Dissertation; University of Bayreuth, 2012.
- (46) Chandrasekhar, S. Discotic liquid crystals: a brief review. *Liq. Cryst.* **1993**, 3–14.
- (47) Dahn, U.; Erdelen, C.; Ringsdorf, H.; Festag, R.; Wendorff, J. H.; Heiney, P. A.; Maliszewskyj, N. C. Fluoroalkylated discotic liquid crystals. *Liq. Cryst.* **1995**, 759–764.
- (48) Terasawa, N.; Monobe, H.; Kiyohara, K.; Shimizu, Y. Strong tendency towards homeotropic alignment in a hexagonal columnar mesophase of fluoroalkylated triphenylenes. *Chem. Commun.* **2003**, 1678–1679.
- (49) Boden, N.; Bushby, R. J.; Cammidge, A. N.; Duckworth, S.; Headdock, G. J.  $\alpha$ -Halogenation of triphenylene-based discotic liquid crystals: towards a chiral nucleus. *J. Mater. Chem.* **1997**, 601–605.
- (50) Aebischer, A.; Aebischer, O. F.; Donnio, B.; Alameddine, B.; Dadras, M.; Güdel, H. U.; Guillon, D.; Jenny, T. A.; J. Controlling the lateral aggregation of perfluoroalkylated hexa-peri-hexabenzocoronenes. *J. Mater. Chem.* **2007**, 1262–1267.
- (51) Alameddine, B.; Aebischer, O. F.; Amrein, W.; Donnio, B.; Deschenaux, R.; Guillon, D.; Savary, C.; Scanu, D.; Scheidegger, O.; Jenny, T. A. Mesomorphic Hexabenzocoronenes Bearing Perfluorinated Chained. *Chem. Mater.* **2005**, 4798–4807.
- (52) Kouwer, P.H.J.; Picken, S. J.; Mehl, G. H. Local lamellar organisation of discotic mesogens carrying fluorinated tails. *J. Mater. Chem.* **2007**, 4196–4203.
- (53) Jung, B. J.; Tremblay, N. J.; Yeh, M.-L.; Katz, H. E. Molecular Design and Synthetic Approaches to Electron-Transporting Organic Transistor Semiconductors. *Chem. Mater.* **2011**, 568–582.
- (54) An, Z.; Yu, J.; Domercq, B.; Jones, S. C.; Barlow, S.; Kippelen, B.; Mader, S. R. Room-temperature discotic liquid-crystalline coronene diimides exhibiting high charge-carrier mobility in air. *J. Chem. Mater.* **2009**, 6688–6698.
- (55) Sakurai, T.; Tashiro, K.; Honsho, Saeki, A.; Seki, S.; Osuka, A.; Muranaka, A.; Uchiyama, M.; Kim, J.; Ha, S.; Kato, K.; *et al.* Electron- or Hole-Transporting Nature Selected by Side-Chain-Directed  $\pi$ -Stacking Geometry: Liquid Crystalline Fused Metalloporphyrin Dimers. *J. Am. Chem. Soc.* **2011**, 6537–6540.
- (56) Zhou, X.; Kang, S. W.; Kumar, S.; Li, Q. Self-assembly of discotic liquid crystal porphyrin into more controllable ordered nanostructure mediated by fluorophobic effect. *Liq. Cryst.* **2009**, 269–274.
- (57) Luca, G. de; Liscio, A.; Melucci, M.; Schnitzler, T.; Pisula, W.; Clark, C. G.; Jr; Scolaro, L. M.; Palermo, V.; Müllen, K.; *et al.* Phase separation and affinity between a fluorinated perylene diimide dye and an alkyl-substituted hexa-peri-hexabenzocoronene. *J. Mater. Chem.* **2010**, 71–82.
- (58) Li, Y.; Tan, L.; Wang, Z.; Qian, H.; Shi, Y.; Hu, W. Air-stable n-type semiconductor: core-perfluoroalkylated perylene bisimides. *Org. Lett.* **2008**, 529–532.

- (59) Schmidt R., Ling, M.M.; Oh, J. H.; Winkler, M.; Könemann, M.; Bao, Z. N.; Würthner, F. Core-Fluorinated Perylene Bisimide Dyes: Air Stable n-Channel Organic Semiconductors for Thin Film Transistors with Exceptionally High On-to-Off Current Ratios. *Adv. Mater.* **2007**, 3692–3695.
- (60) Katz, H. E.; Lovinger, A. J.; Johnson, J.; Kloc, C.; Siegrist, T.; Li, W.; Lin, Y. Y.; Dodabalapur, A. A soluble and air-stable organic semiconductor with high electron mobility. *Nature* **2000**, 478–481.
- (61) See, K. C.; Landis, C.; Sarjeant, A.; Katz, H. E. Easily Synthesized Naphthalene Tetracarboxylic Diimide Semiconductors with High Electron Mobility in Air. *Chem. Mater.* **2008**, 3609–3616.
- (62) Zheng, Q. D.; Huang, J.; Sarjeant, A.; Katz H.E. Pyromellitic Diimides: Minimal Cores for High Mobility n-Channel Transistor Semiconductors. *J. Am. Chem. Soc.* **2008**, 14410–14411.
- (63) Lehn, J.-M. Cryptates: inclusion complexes of macropolycyclic receptor molecules. *Pure Appl. Chem.* **1978**, 851–892.
- (64) Vögtle, F. *Supramolekulare Chemie*, 2nd Edition; Teubner: Stuttgart, 1992.
- (65) Nyrkova, I. A.; Semenov, A. N. The concept of strongly interacting groups in self-assembly of soft matter. *The European Physical Journal E* **2018**, *41*, 1–27.
- (66) Steed, J. W.; Atwood, J. L., Eds. *Supramolecular Chemistry*, 2nd Edition; John Wiley & Sons, Ltd.: Chichester UK, 2009.
- (67) Lehn J.-M. *Supramolekulare Chemie - Chemische Grundlagenforschung auf neuen Wegen*; Picus: Wien, 2007.
- (68) Brunsveld, L.; Folmer, B.J.B.; Meijer, E. W.; Sijbesma, R. P. Supramolecular polymers. *Chem. Rev.* **2001**, 4071–4097.
- (69) Abraham, F.; Ganzleben, S.; Hanft, D.; Smith, P.; Schmidt, H.-W. Synthesis and Structure-Efficiency Relations of 1,3,5-Benzenetrisamides as Nucleating Agents and Clarifiers for Isotactic Poly(propylene). *Macromol. Chem. Phys.* **2010**, 171–181.
- (70) Stals, P.J.M.; Haveman, J. F.; Martín-Rapún, R.; Fitié, C.F.C.; Palmans, A.R.A.; Meijer, E. W. The influence of oligo (ethylene glycol) side chains on the self-assembly of benzene-1, 3, 5-tricarboxamides in the solid state and in solution. *J. Mater. Chem.* **2009**, 124–130.
- (71) Lightfoot, M. P.; Mair, F. S.; Pritchard, R. G.; Warren, J. E. New Supramolecular packing motifs: pi-stacked rods encased in triply helical hydrogen bonded amide strands. *Chem. Commun.* **1999**, 1945–1946.
- (72) Kristiansen, M.; Smith, P.; Chanzy, H.; Bärlocher, C.; Gramlich, V.; McCusker, L.; Weber, T.; Pattison, P.; Blomenhofer, M.; Schmidt, H.-W. Structural Aspects of 1,3,5-Benzenetrisamides-A New Family of Nucleating Agents. *Cryst. Growth Des.* **2009**, 2556–2558.
- (73) Bernet, A.; Albuquerque, R. Q.; Behr, M.; Hoffmann, S. T.; Schmidt, H.-W. Formation of a supramolecular chromophore: a spectroscopic and theoretical study. *Soft Matter* **2012**, 66–69.
- (74) Shikata, T.; Kuruma, Y.; Sakamoto, A.; Hanabusa, K. Segment sizes of supramolecular polymers of N,N',N''-tris(3,7-dimethyloctyl)benzene-1,3,5-tricarboxamide in n-decane. *J. Phys. Chem. B* **2008**, 16393–16402.
- (75) Saunders, L.; Ma, P. X. Self-Healing Supramolecular Hydrogels for Tissue Engineering Applications. *Macromolecular bioscience* **2019**, *19*, e1800313.
- (76) Mohmeyer, N.; Behrendt, N.; Zhang, X.; Smith, P.; Altstädt, V.; Sessler, G. M.; Schmidt H.-W. Additives to improve the electret properties of isotactic polypropylene. *Polymer* **2007**, 1612–1619.

- (77) Blomenhofer, M.; Ganzleben, S.; Hanft, D.; Schmidt, H.-W.; Kristiansen, M.; Smith, P.; Stoll, K.; Mäder, D.; Hoffmann, K. "Designer" Nucleating Agents for Polypropylene. *Macromolecules* **2005**, 3688–3695.
- (78) Abraham, F.; Schmidt H.-W. 1,3,5-Benzenetrisamide based nucleating agents for poly(vinylidene fluoride). *Polymer* **2012**, 913–921.
- (79) Richter, F.; Schmidt, H.-W. Supramolecular Nucleating Agents for Polybutylene Terephthalate based on 1,3,5-Benzenetrisamides. *Macromo. Mater. Eng.* **2013**, 190–200.
- (80) Rajput, L.; Mukherjee, G.; Biradha, K. Influence of Solvents in Assembling Tris(4-halophenyl)benzene-1,3,5-tricarboxamides: Interplay of N–H···O and Halogen···Halogen Interactions. *Cryst. Growth Des.* **2012**, 5773–5782.
- (81) Stals, P.J.M.; Everts, J. C.; Bruijn, R. de; Filot, I.A.W.; Smulders, M.M.J.; Martín-Rapún, R.; Pidko, E. A.; Greef, M.M.J. de; Palmans, A.R.A.; Meijer, E. W. Dynamic Supramolecular Polymers Based on Benzene-1,3,5-tricarboxamides: The Influence of Amide Connectivity on Aggregate Stability and Amplification of Chirality. *Chem. Eur. J.* **2010**, 810–821.
- (82) Lee, S.; Oh, S.; Lee, J.; Malpani, Y.; Jung, Y.-S.; Kang, B.; Lee, J. Y.; Ozasa, K.; Isoshima, T.; Lee, S. Y.; *et al.* Stimulus-responsive azobenzene supramolecules: fibers, gels, and hollow spheres. *Langmuir* **2013**, 5869–5877.
- (83) Singer, J. C.; Giesa, R.; Schmidt, H.-W. Shaping self-assembling small molecules into fibres by melt electrospinning. *Soft Matter* **2012**, 9972–9976.
- (84) Matsunaga, Y.; Nakayasu, Y.; Sakai, S.; Yonenaga, M. Liquid Crystal Phases Exhibited by N,N',N''-Trialkyl-1,3,5-Benzenetricarboxamides. *Mol. Cryst. Liq. Cryst.* **1986**, 327–333.
- (85) Palmans, A.R.A.; Vekemans, J.A.J.M.; Kooijman, H.; Spek, A. L.; Meijer, E. W. Hydrogen bonded porous solid derived from trimesic amide. *Chem. Commun.* **1997**, 2247–2248.
- (86) Rajput, L.; Biradha, K. J. Crystalline forms of 1,3,5-benzene-tri(pyridinyl)carboxamides: Isolated site hydrates as polymorphs and solvates. *J. Mol. Struct.* **2011**, 97–102.
- (87) Jiminéz, C. A.; Belmar, J. B.; Ortíz, L.; Hidalgo, P.; Fabelo, O.; Pasán, J.; Ruiz-Pérez, C. Influence of the Aliphatic Wrapping in the Crystal Structure of Benzene Tricarboxamide Supramolecular Polymers. *Cryst. Growth Des.* **2009**, 4987–4989.
- (88) Rochefort, A.; Bayard, É.; Hadj-Messaoud, S. Competitive Hydrogen Bonding in  $\pi$ -Stacked Oligomers. *Adv. Mater.* **2007**, 1992–1995.
- (89) Timme, A.; Kress, R.; Albuquerque, R. Q.; Schmidt, H.-W. *Chem. Eur. J.* **2012**, 8329–8339.
- (90) Nguyen, T.-Q.; Bushey, M. L.; Brus, L. E.; Nuckolls, C. Tuning Intermolecular Attraction to Create Polar Order and One-Dimensional Nanostructures on Surfaces. *J. Am. Chem. Soc.* **2002**, 15051–15054.
- (91) Albuquerque, R. Q.; Timme, A.; Kress, R.; Senker, J.; Schmidt, H.-W. Theoretical investigations of macrodipoles in supramolecular columnar stackings. *Chem. Eur. J.* **2013**, 1647–1657.
- (92) Korlepara, D. B.; Henderson, W. R.; Castellano, R. K.; Balasubramanian, S. Differentiating the mechanism of self-assembly in supramolecular polymers through computation. *Chemical communications* **2019**, 55, 3773–3776.
- (93) Stals, P.J.M.; Smulders, M.M.J.; Martín-Rapún, R.; Palmans, A.R.A.; Meijer, E. W. Asymmetrically substituted benzene-1,3,5-tricarboxamides: self-assembly and odd-even effects in the solid state and in dilute solution. *Chem. Eur. J.* **2009**, 2071–2080.

- (94) Jonkheijm, P.; van der Schoot, P.; Schenning, A.P.J.H.; Meijer, E. W. Probing the solvent-assisted nucleation pathway in chemical self-assembly. *Science* **2006**, 80–83.
- (95) Oosawa, F.; Kasai, M. A theory of linear and helical aggregations of macromolecules. *J. Mol. Biol.* **1962**, 10–21.
- (96) Pilot, I.A.W.; Palmans, A.R.A.; Hilbers, P.A.J.; van Santen, R. A.; Pidko, E. A.; Greef, T.F.A. de. Understanding cooperativity in hydrogen-bond-induced supramolecular polymerization: a density functional theory study. *J. Phys. Chem. B.* **2010**, 13667–13674.
- (97) Kulkarni, C.; Reddy, S. K.; George, S. J.; Balasubramanian, S. Cooperativity in the stacking of benzene-1, 3, 5-tricarboxamide: the role of dispersion. *Chem. Phys. Let.* **2011**, 226–230.
- (98) Stals, P.J.M.; Korevaar, P. A.; Gillissen, M.A.J.; Greef, T.F.A. de; Fitié, C.F.C.; Sijbesma, R. P.; Palmans, A.R.A.; Meijer, E. W. Symmetry Breaking in the Self-Assembly of Partially Fluorinated Benzene-1, 3, 5-tricarboxamides. *Angew. Chem. Int. Ed.* **2012**, 11297–11301.
- (99) Stumpf, M.; Spörrer, A.; Schmidt, H.-W.; Altstädt, V. Influence of supramolecular additives on foam morphology injection-molded i-PP. *Journal of Cellular Plastics* **2011**, 519–534.
- (100) Singer, J. C. *Controlling the Morphology of Supramolecular Nano- and Microfibers by Self-Assembly and Electrospinning*. Dissertation; University of Bayreuth, 2014.
- (101) Schmidt, M.; Wittmann, J. J.; Kress, R.; Schneider, D.; Steuernagel, S.; Schmidt, H.-W.; Senker, J. Crystal Structure of a Highly Efficient Clarifying Agent for Isotactic Polypropylene. *Cryst. Growth Des.* **2012**, 2543–2551.
- (102) Wegner, M.; Dudenko, D.; Sebastiani, D.; Palmans, A.R.A.; Greef, T.F.A. de; Graf, R.; Spiess, H. W. The impact of the amide connectivity on the assembly and dynamics of benzene-1,3,5-tricarboxamides in the solid state. *Chem. Sci.* **2011**, 2040–2049.
- (103) Abraham, F. *Synthesis and structure property relations on benzene-1,3,5-tricarboxamides: The influence of amide connectivity on aggregate stability and amplification of chirality*. Dissertation; University of Bayreuth, 2009.
- (104) Zehe, C. S.; Hill, J. A.; Funnell, N. P.; Kreger, K.; van der Zwan, K. P.; Goodwin, A. L.; Schmidt, H.-W.; Senker, J. Mesoscale Polarization by Geometric Frustration in Columnar Supramolecular Crystals. *Angew. Chem. Int. Ed.* **2017**, 4432–4437.
- (105) Zehe, C.; Schmidt, M.; Siegel, R.; Kreger, K.; Daebel, V.; Ganzleben, S.; Schmidt, H.-W.; Senker, J. Influence of fluorine side-group substitution on the crystal structure formation of benzene-1,3,5-trisamides. *CrystEngComm* **2014**, 9273–9283.
- (106) Fan, E.; Yang, J.; Geib, S. J.; Stoner, T. C.; Hopkins, M. D.; Hamilton. Hydrogen-bonding control of molecular aggregation: self-complementary subunits lead to rod-shaped structures in the solid state. *J. Chem. Soc.; Chem. Commun.* **1995**, 1251–1252.
- (107) Tomatsu, I.; Fitié, C.F.C.; Byelov, D.; Jeu, W. H. de; Magusin, P.C.M.M.; Wübbenhorst, M.; Sijbesma, R. P. Thermotropic phase behaviour of trialkyl cyclohexanetriamides. *J. Phys. Chem. B.* **2009**, 14158–14164.
- (108) Timme, A.; Kress, R.; Albuquerque, R. Q.; Schmidt, H.-W. Phase behavior and mesophase structures of 1,3,5-benzene- and 1,3,5-cyclohexanetricarboxamides: towards an understanding of the losing order at the transition into the isotropic phase. *Chem. Eur. J.* **2012**, 8329–8339.
- (109) Eisenmann A. *Flüssigkristalline supramolekulare Systeme*, 2012.
- (110) Prasad S.K.; Rao D.S.S.; Chandrasekhar, S.; Kumar, S. X-Ray studies on the columnar structures of discotic liquid crystals. *Mol. Cryst. Liq. Cryst.* **2003**, 121–139.

- (111) Hesse M.; Meier H.; Zeeh B., Eds. *Spektroskopische Methoden in der organischen Chemie*, 5th Edition; Georg Thieme Verlag: Stuttgart, New York, 1995.
- (112) Volkmann H., Ed. *Handbuch der Infrarot-Spektroskopie*; Verlag Chemie: Weinheim, 1972.
- (113) Fitié, C.F.C.; Tomatsu, I.; Byelov, D.; de Jeu W.H.; Sijbesma, R. P. Nanostructured materials through orthogonal self-assembly in a columnar liquid crystal. *Chem. Mater.* **2008**, 2394–2404.
- (114) Stals, P.J.M.; Haveman, J. F.; Martín-Rapún, R.; Fitié, C.F.C.; Palmans, A.R.A.; Meijer, E. W. The influence of oligo(ethylene glycol) side chains on the self-assembly of benzene-1,3,5-tricarboxamides in the solid state and in solution. *J. Mater. Chem.* **2009**, 124–130.
- (115) Harada Y.; Matsunaga, Y. New Mesomorphic Compounds: N,N',N''-Trialkanoyl-2,4,6-trimethyl-1,3,5-benzenetriamines. *Bull. Chem. Soc. Jpn.* **1988**, 2739–2741.
- (116) Mahoney S.J.; Ahmida M.M.; Kayal H.; Fox N.; Shimizuc Y.; Eichhorn S.H. Synthesis, mesomorphism and electronic properties of nonaflate and cyano-substituted pentyloxy and 3-methylbutyloxy triphenylenes. *J. Mater. Chem.* **2009**, 9221–9232.
- (117) Bognitzki M.; Hou H.; Ishaque M.; Frese T.; Hellwig M.; Schwarte C.; Schaper A.; Wendorff, J. H.; Greiner A. Polymer, Metal, and Hybrid Nano- and Mesotubes by Coating Degradable Polymer Template Fibers (TUFT Process). *Adv. Mater.* **2000**, 637–640.
- (118) Ramakrishna S.; Fujihara K.; Teo W.-E.; Lim T.-C., Eds. *An Introduction to Electrospinning and Nanofibers*; World Scientific Publishing Co. Pte. Ltd.: Singapore, 2005.
- (119) Ding, B.; Wang, X.; Yu, J. *Electrospinning: Nanofabrication and Applications*; Elsevier: Amsterdam' Netherlands, 2019.
- (120) Wendorff, J. H.; Agarwal S.; Greiner A., Eds. *Electrospinning: Materials, Processing and Applications*; WILEY-VCH Verlag GmbH & Co. KGaA: Weinheim, 2012.
- (121) Greiner A.; Wendorff, J. H. Electrospinning: a fascinating method for the preparation of ultrathin fibers. *Angew. Chem. Int. Ed.* **2007**, 5670–5703.
- (122) Agarwal S.; Burgard M.; Greiner A.; Wendorff, J. H., Eds. *Electrospinning - A Practical Guide To Nanofibers*; Walter de Gruyter GmbH: Berlin/Boston, 2016.
- (123) Yoon K.; Kim K.; Wang X.; Fang D.; Hsiao B.S.; Chu B. High flux ultrafiltration membranes based on electrospun nanofibrous PAN scaffolds and chitosan coating. *Polymer* **2006**, 2434–2441.
- (124) Appel W.P.J.; Meijer, E. W.; Dankers P.Y.W. Enzymatic activity at the surface of biomaterials via supramolecular anchoring of peptides - the effect of material processing. *Macromol Biosci.* **2011**, 1706–1712.
- (125) Tayi A.S.; Pashuck E.T.; Newcomb C.J.; McClendon M.T.; Stupp S.I. Electrospinning bioactive supramolecular polymers from water. *Biomacromolecules* **2014**, 1323–1327.
- (126) Mollet B.B.; Comeras-Aragonès M.; Spiering A.J.H.; Söntjens S.H.M., Meijer E.W., Dankers P.Y.W. A modular approach to easily processable supramolecular bilayered scaffolds with tailorable properties. *J. Mater. Chem. B* **2014**, 2483.
- (127) Morikawa, K.; Green, M.; Naraghi, M. A Novel Approach for Melt Electrospinning of Polymer Fibers. *Procedia Manufacturing* **2018**, 26, 205–208.
- (128) Hunley M.T.; Harber A.; Orlicki J.A.; Rawlett A.M.; Long T.E. Effect of hyperbranched surface-migrating additives on the electrospinning behavior of poly(methyl methacrylate). *Langmuir* **2008**, 654–657.
- (129) McKee M.G.; Layman J.M.; Cashion M.P.; Long T.E. Phospholipid nonwoven electrospun membranes. *Science* **2006**, 353–355.

- (130) Wang K.; Wang C.-Y.; Wang Y.; Li H.; Bao C.-Y.; Liu J.-Y.; Zhang S.X.-A.; Yang Y.-W. Electrospun nanofibers and multi-responsive supramolecular assemblies constructed from a pillar[5]arene-based receptor. *Chem. Commun.* **2013**, 10528.
- (131) Yan X.; Zhou M.; Chen J.; Chi X.; Dong S.; Zhang M.; Ding X.; Yu Y.; Shao S.; Huang F. Supramolecular polymer nanofibers via electrospinning of a heteroditopic monomer. *Chem. Commun.* **2011**, 7086–7088.
- (132) Chae S.K.; Park H.; Yoon J.; Lee C.H.; Ahn D.J.; Kim J.-M. Polydiacetylene supramolecules in electrospun microfibers: Fabrication, micropatterning, and sensor applications. *Adv. Mater.* **2007**, 521–524.
- (133) Wang X.; Pellerin C.; Bazuin C.G. Enhancing the Electrospinnability of Low Molecular Weight Polymers Using Small Effective Cross-Linkers. *Macromolecules* **2016**, 891–899.
- (134) Yoon J.; Kim, J.-M. Fabrication of Conjugated Polymer Supramolecules in Electrospun Micro/Nanofibers. *Macromol. Chem. Phys.* **2008**, 2194–2203.
- (135) Burgard, M.; Weiss, D.; Kreger, K.; Schmalz, H.; Agarwal, S.; Schmidt, H.-W.; Greiner, A. Mesostructured Nonwovens with Penguin Downy Feather-Like Morphology—Top-Down Combined with Bottom-Up. *Adv. Funct. Mater.* **2019**, 29, 1903166.
- (136) Poss, A. J.; Nalewajek, D.; Cantlon, C. L.; Lu, C.; Wo, S. Electrospinning of Fluoropolymers. *Appl. Phys. Lett.* **2002**, 80, 15 / 802, 673.
- (137) Guangming G.; Juntao W.; Yong Z.; Jingang L.; Xu J.; Lei J. A novel fluorinated polyimide surface with petal effect produced by electrospinning. *Soft Matter* **2014**, 549.
- (138) Agarwal S.; Horst S.; Bognitzki M. Electrospinning of Fluorinated Polymers: Formation of Superhydrophobic Surfaces. *Macromo. Mater. Eng.* **2006**, 592–601.
- (139) Grignard B.; Vaillant A.; de Coninck J.; Pines M.; Jonas A.M.; Detrembleur C.; Jerome C. Electrospinning of a functional perfluorinated block copolymer as a powerful route for imparting superhydrophobicity and corrosion resistance to aluminum substrates. *Langmuir* **2011**, 335–342.
- (140) Xuefei C.; Yang Hu.; Zhen-Liang X. Poly(vinyl alcohol)–perfluorinated sulfonic acid nanofiber mats prepared via electrospinning as catalyst. *Material Letters* **2011**, 1719–1722.
- (141) Zhang L.; Li Y.; Yu J.; Ding B. Fluorinated polyurethane macroporous membranes with waterproof, breathable and mechanical performance improved by lithium chloride. *RSC Adv.* **2015**, 79807–79814.
- (142) Zhao J.; Yuan W.Z.; Xu A.; Ai F.; Lu Y.; Zhang Y. Perfluorinated Sulfonic Acid Ionomer/Poly(N-vinylpyrrolidone) Nanofibers Membranes: Electrospinning Fabrication, Water Stability, and Metal Ion Removal Applications. *React. Funct. Polym.* **2011**, 1102–1109.
- (143) Zhao, P.; Soin, N.; Prashanthi, K.; Chen, J.; Dong, S.; Zhou, E.; Zhu, Z.; Narasimulu, A. A.; Montemagno, C. D.; Yu, L. Emulsion electrospinning of polytetrafluoroethylene (PTFE) nanofibrous membranes for high-performance triboelectric nanogenerators. *ACS Appl. Mater. Interfaces* **2018**, 10, 5880–5891.
- (144) Kim H.-W.; Kim H.-E. Nanofiber generation of hydroxyapatite and fluor-hydroxyapatite bioceramics. *J. Biomed. Mater. Res. Part B Appl. Biomater.* **2006**, 323–328.
- (145) Govinna, N.; Sadeghi, I.; Asatekin, A.; Cebe, P. Thermal properties and structure of electrospun blends of PVDF with a fluorinated copolymer. *J. Polym. Sci. Part B: Polym. Phys.* **2019**, 57, 312–322.

- (146) Spasova, M. G.; Manolova, N. E.; Markova, N. D.; Rashkov, I. B. Electrospun fibrous fluor-containing polymer materials decorated with ZnO nanoparticles: Preparation and properties. *Scientific Works of the Union of Scientists in Bulgaria-Plovdiv, Series C. Technics and Technologies* **2017**, Vol. XV., 162–165.
- (147) Ducheyne, P.; Healy, K.; Hutmacher, D. W.; Grainger, D. W.; Kirkpatrick, C. J. *Comprehensive Biomaterials II: Electrospinning With Polymer Melts - State of the Art and Future Perspectives*; Elsevier: Amsterdam, Netherlands, 2017.
- (148) Singer, J. C.; Ringk A.; Giesa, R.; Schmidt, H.-W. Melt Electrospinning of Small Molecules. *Macromol. Mater. Eng.* **2015**, 259–276.
- (149) Kluge D.; Singer, J. C.; Neubauer J.W.; Abraham, F.; Schmidt, H.-W.; Fery A. Influence of the Molecular Structure and Morphology of Self-Assembled 1,3,5-Benzenetrisamide Nanofibers on their Mechanical Properties. *Small* **2012**, 2563–2570.
- (150) Kluge D.; Singer, J. C.; Neugirg B.R.; Neubauer J.W.; Schmidt, H.-W.; Fery A. Top–down meets bottom–up: A comparison of the mechanical properties of melt electrospun and self-assembled 1,3,5-benzenetrisamide fibers. *Polymer* **2012**, 5754–5759.
- (151) Thandavamoorthy S.; Gopinath N.; Ramkumar S.S. Self-assembled honeycomb polyurethane nanofibers. *J. Appl. Polym. Sci.* **2006**, 3121–3124.
- (152) Tong H.-W.; Wang M. Negative voltage electrospinning and positive voltage electrospinning of tissue engineering scaffolds: a comparative study and charge retention on scaffolds. *Nano LIFE* **2012**, 1250004-1-16.
- (153) Butt H.-J.; Cappella B.; Kappl M. Force measurements with the atomic force microscope: Technique, interpretation and applications. *Surf. Sci. Rep.* **2005**, 1–152.
- (154) Neugirg B.R.; Helfricht N.; Czich S.; Schmidt, H.-W.; Papastavrou G.; Fery A. Long-range interaction forces between melt-eletrospun 1,3,5-cyclohexanetrisamide fibers in crossed-cylinder geometry. *Polymer* **2016**, 363–371.
- (155) Owens, D. K.; Wendt, R. C. Estimation of the surface free energy of polymers. *J. Appl. Polym. Sci.* **1969**, 1741–1747.
- (156) Reichardt C., Ed. *Solvents and Solvent Effects in Organic Chemistry*, 3rd Updated and Enlarged Edition; WILEY-VCH Verlag GmbH & Co. KGaA: Weinheim, 2003.
- (157) Zeng, W.; Liu, Y.; Li, X.; Jin, W.; Zhang, D. Synthesis and self-assembly of chiral Gemini-shaped hexabenzocoronene amphiphiles. *Dyes and Pigments*, 107624.
- (158) Soler R.; Badetti E.; Moreno-Mañas M.; Vallribera A.; Sebastián R.N.; Vera F.; Serrano J.L.; Sierra T. Wide temperature range mesomorphic behaviour of highly fluorinated 15-membered macrocycles and their open trisulphonamide precursor. *Liquid Crystals* **2007**, 235–240.
- (159) Sasada Y.; Monobe, H.; Ueda Y.; Shimizu Y. Drastic enhancement of discotic mesomorphism induced by fluorination of the peripheral phenyl groups in triphenylene mesogens. *Chem. Commun.* **2008**, 1452–1454.
- (160) Johansson G.; Percec V.; Ungar G.; Zhou J.P. Fluorophobic Effect in the Self-Assembly of Polymers and Model Compounds Containing Tapered Groups into Supramolecular Columns. *Macromolecules* **1996**, 646–660.
- (161) Dupuy N.; Pasc A.; Parant S.; Fontanay S.; Duval R.E.; Gérardin C. Amino-ethoxilated fluorinated amphiphile: Synthesis, self-assembling properties and interactions with ssDNA. *J. Fluorine Chem.* **2012**, 330–338.

- (162) Krieg E.; Weissman H.; Shimoni E.; Ustinov A.B.O.; Rybtchinski B. Understanding the effect of fluorocarbons in aqueous supramolecular polymerization: ultrastrong noncovalent binding and cooperativity. *J. Am. Chem. Soc.* **2014**, 9443–9452.
- (163) Aebischer, O. F.; Aebischer, A.; Tondo P.; Alameddine, B.; Dadras, M.; Güdel, H.-U.; Jenny, T. A. Self-aggregated perfluoroalkylated hexa-peri-hexabenzocoronene fibers observed by cryo-SEM and fluorescence spectroscopy. *Chem. Commun.* **2006**, 4221–4223.
- (164) Steinlein, C.; Kreger, K.; Schmidt, H.-W. Controlling the Aspect Ratio of Supramolecular Fibers by Ultrasonication. *Macromol. Mater. Eng.* **2019**, 304, 1900258.
- (165) van Houtem M.H.C.J.; Benaskar F.; Fitié, C.F.C.; Martín-Rapún, R.; Vekemans, J.A.J.M.; Meijer, E. W. Helical self-assembly and co-assembly of fluorinated, preorganized discotics. *Org. Biomol. Chem.* **2012**, 5898–5908.
- (166) Weiss D.; Skrybeck D.; Misslitz H.; Nardini D.; Kern A.; Kreger K.; Schmidt, H.-W. Tailoring Supramolecular Nanofibers for Air Filtration Applications. *ACS Appl. Mater. Interfaces* **2016**, 14885–14892.
- (167) Weiss, D.; Skrybeck, D.; Misslitz, H.; Nardini, D.; Kern, A.; Kreger, K.; Schmidt, H.-W. Tailoring Supramolecular Nanofibers for Air Filtration Applications. *ACS Appl. Mater. Interfaces* **2016**, 8, 14885–14892.
- (168) Sigma Aldrich, Ed. *Handbook of Fine Chemicals*; MO: St. Louis, 2007-2008.
- (169) Dimroth, K.; Reichardt, C.; Siepmann, T.; Bohlmann, F. Über Pyridinium-N-phenol-betaine und ihre Verwendung zur Charakterisierung der Polarität von Lösungsmitteln. *Liebigs Ann. Chem.* **1963**, 661, 1–37.
- (170) Wiley Online Library. <http://onlinelibrary.wiley.com/doi/10.1002/3527600418.mb9550e0001/pdf> (accessed August 13, 2016).
- (171) Giasante C.; Schäfer C.; Raffy G.; Guerzo A.D. Exploiting direct and cascade energy transfer for color-tunable and white-light emission in three-component self-assembled nanofibers. *J. Phys. Chem.* **2012**, 21706–21716.
- (172) Nie B.; Zhan T.-G.; Zhou T.-Y.; Xiao Z.-Y.; Jiang G.-F.; Zhao X. Self-assembly of chiral propeller-like supermolecules with unusual "sergeants-and-soldiers" and "majority-rules" effects. *Chem. Asian J.* **2014**, 754–758.
- (173) Fan G.; Lin Y.-X.; Yang L.; Gao F.-P.; Zhao Y.-X.; Qiao Z.-Y.; Zhao Q.; Fan Y.-S.; Chen Z.; Wang H. Co-self-assembled nanoaggregates of BODIPY amphiphiles for dual colour imaging of live cells. *Chem. Commun.* **2015**, 12447–12450.
- (174) Olive A.G.L.; Guerzo A.D.; Schäfer C.; Belin C.; Raffy G.; Giasante C. Fluorescence amplification in self-assembled organic nanoparticles by excitation energy migration and transfer. *J. Phys. Chem. C* **2010**, 10410–10416.
- (175) Zhang, X.; Chen Z.; Würthner, F. Morphology Control of Fluorescent Nanoaggregates by Co-Self-Assembly of Wedge- and Dumbbell-Shaped Amphiphilic Perylene Bisimides. *J. Am. Chem. Soc.* **2007**, 4886–4887.
- (176) Görl F.; Zhang, X.; Stepanenko V.; Würthner, F. Supramolecular block copolymers by kinetically controlled co-self-assembly of planar and core-twisted perylene bisimides. *Nat. Commun.* **2015**, 7009.

- (177) Smulders, M.M.J.; Filot, I.A.W.; Leenders J.M.A.; van der Schoot, P.; Palmans, A.R.A.; Schenning, A.P.J.H.; Meijer, E. W. Tuning the extent of chiral amplification by temperature in a dynamic supramolecular polymer. *J. Am. Chem. Soc.* **2010**, 611–619.
- (178) Helmich F.; Smulders, M.M.J.; Lee C.C.; Schenning, A.P.J.H.; Meijer, E. W. Effect of stereogenic centers on the self-sorting, depolymerisation, and atropisomerisation kinetics of porphyrin-based aggregates. *J. Am. Chem. Soc.* **2011**, 12238–12246.
- (179) Windt, L. N. J. de; Kulkarni, C.; Eikelder, H. M. M. ten; Markvoort, A. J.; Meijer, E. W.; Palmans, A. R. A. Detailed Approach to Investigate Thermodynamically Controlled Supramolecular Copolymerizations. *Macromolecules* **2019**, 52, 7430–7438.
- (180) Schmidt H.-W.; Smith P.; Blomenhofer M. Polypropylene Resin Compositions. (WO 200246300A2).



## **(Eidesstattliche) Versicherungen und Erklärungen**

(§ 8 Satz 2 Nr. 3 PromO Fakultät)

*Hiermit versichere ich eidesstattlich, dass ich die Arbeit selbstständig verfasst und keine anderen als die von mir angegebenen Quellen und Hilfsmittel benutzt habe (vgl. Art. 64 Abs. 1 Satz 6 BayHSchG).*

(§ 8 Satz 2 Nr. 3 PromO Fakultät)

*Hiermit erkläre ich, dass ich die Dissertation nicht bereits zur Erlangung eines akademischen Grades eingereicht habe und dass ich nicht bereits diese oder eine gleichartige Doktorprüfung endgültig nicht bestanden habe.*

(§ 8 Satz 2 Nr. 4 PromO Fakultät)

*Hiermit erkläre ich, dass ich Hilfe von gewerblichen Promotionsberatern bzw. –vermittlern oder ähnlichen Dienstleistern weder bisher in Anspruch genommen habe noch künftig in Anspruch nehmen werde.*

(§ 8 Satz 2 Nr. 7 PromO Fakultät)

*Hiermit erkläre ich mein Einverständnis, dass die elektronische Fassung der Dissertation unter Wahrung meiner Urheberrechte und des Datenschutzes einer gesonderten Überprüfung unterzogen werden kann.*

(§ 8 Satz 2 Nr. 8 PromO Fakultät)

*Hiermit erkläre ich mein Einverständnis, dass bei Verdacht wissenschaftlichen Fehlverhaltens Ermittlungen durch universitätsinterne Organe der wissenschaftlichen Selbstkontrolle stattfinden können.*

.....  
Ort, Datum, Unterschrift